Energy Efficient PWM Induction Machine Drives for Electric Vehicles

By

Zhan-Yuan Wu

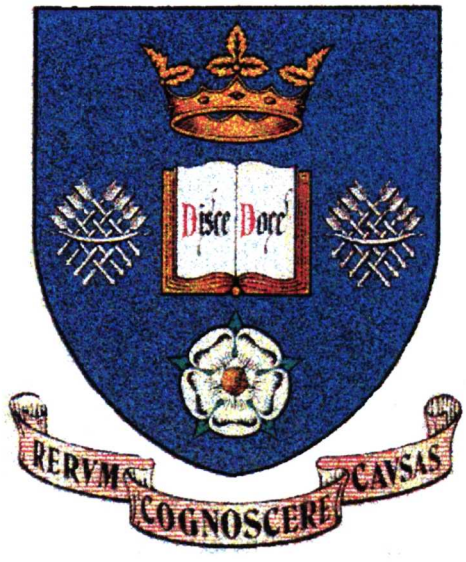

A thesis submitted for the degree of Doctor of Philosophy in the Department of Electronic and Electrical Engineering, The University of Sheffield

October, 1999

To my parents

Summary

The viability of any electric vehicle is critically dependent on it having an acceptable range between charges, a feature which is ultimately dictated by the capacity of the battery energy store. Considerable improvements in vehicle range are possible, however, by ensuring the most effective use of this limited energy resource through the minimisation of the losses in the electric drive-train, i.e. the combined machine and power electronic controller. A particular consideration is that, for the majority of the time, the electric drive-train will be operating at part load.

The thesis investigates the operation of induction motor based electric traction drive-trains, with a view to minimising the system loss over typical driving cycles. The study is based around a 26kW induction motor and IGBT inverter drive, which is typical of the technology used to power a small urban vehicle.

A potential advantage of an induction motor based drive-train is the ability to vary the level of excitation field in the motor, and therefore the balance of iron and copper loss. The control of the supply voltage magnitude necessitates the use of some form of modulation on the output of the power converter. The method of modulation employed will influence the harmonic content of the supply to the motor, the level of parasitic harmonic loss in the machine and the switching losses of the power semiconductors.

A theoretical study supported by experimental work on a DSP controlled drive is presented and used to determine the most appropriate modulation strategy at a given operating point to achieve an optimal balance between the motor copper, iron and harmonic loss and inverter switching and conduction loss. It is shown that compared to the established method of constant flux and fixed inverter switching frequency control, a significant reduction in the traction system loss can be achieved. Some different modulation schemes involve varying amounts of computational overhead in a DSP, the implementation of candidate modulation and control schemes has also been investigated to ensure the defined scheme is practically realisable.

Acknowledgements

The author wishes to thank his supervisors, Dr. P H Mellor and Prof. D Howe for their continuous guidance and encouragement during the course of the research, and deeply appreciates their interest in this work. He is also grateful to Dr. B Boholo for the use of his calorimeter test rig, and Dr. N Powell for the advice during the development of FPGA.

Special thanks are also due to the technical staff, Mr. J Wilkinson and Mr. R Garraway, for their help in setting-up the test facility, and all the members of the Electric Machines & Drives Group for their help and friendship, among whom Dr. Z Q Zhu must be mentioned.

The author greatly appreciate the financial assistance of the University of Sheffield and the European Communities, without which this work could not have taken place.

Finally, the author is very grateful to his wife, Ying, for her consistent support, tolerance and sacrifice in these many years. He also acknowledges his daughter, Michelle, for the joy she brought to the family.

Nomenclature

Modulation

PWM	pulse width modulation
RPWM	random PWM
PDM	pulse density modulation
m(t)	modulating signal
ω	modulating wave frequency (rad/s)
ω_s	carrier wave frequency (rad/s)
f	machine supply frequency (Hz)
f_n	machine harmonic frequency (Hz)
f_s	inverter switching frequency (Hz)
R	modulation frequency ratio
M	modulation depth
δ	modulating wave phase angle (rad)
θ	phase shift in PWM output fundamental voltage (rad)
$\Delta\theta$	angle step for vector space PWM implementation (degree)
β	third harmonic factor in sub-optimal PWM
ε	sampling factor in adjustable PWM
α_k	kth pulse angle in the pulse pattern of optimal PWMs (degree)
$\vec{V}$	machine stator rotating voltage vector
$\vec{V_a}$, $\vec{V_b}$, $\vec{V_c}$	machine phase voltage vectors
$\vec{V_0} \rightarrow \vec{V_7}$	inverter switching voltage vectors

V_n	magnitude of nth harmonic in PWM output (V)
J_n	Bessel function of first kind

Harmonic distortion

THD	total harmonic distortion
THDI	total harmonic distortion related to motor iron loss
THD^*	normalised THD in optimal harmonic minimisation PWM

Power electronics

GTO	gate turn-off thyristor
BJT	bipolar junction transistor
MOSFET	Metal Oxide Semiconductor Field Effect Transistor
IGBT	isolated gate transistor
MCT	mos-controlled thyristor

Rectifier

R_c	charging resistor in the rectifier (Ω)
R_d	discharging resistor in the rectifier (Ω)
C_d	d.c. link smoothing capacitor (μF)

Inverter

R	gate resistance (Ω)
R_p	polarised gate resistance for turn-on (Ω)
R_n	

	polarised gate resistance for turn-off (Ω)
R_L	load resistance (Ω)
L	load inductance (H)
T_{R_L}	load inductor temperature (^oC)
P_{cond}	conduction power loss (W)
P_T	conduction power loss in power component (W)
P_D	conduction power loss in diode (W)
P_{sw}	switching power loss (W)
P_{Tsw}	switching power loss in power component (W)
P_{Dsw}	switching power loss in diode (W)
P_{swPWM}	switching power loss for PWM operation (W)
P_{PWM}	total power loss for PWM operation (W)
P_{IN}	inverter input power (W)
P_{INV}	inverter power loss (W)
P_{R_L}	load resistive loss (W)
V_{ce} , V_T	conduction voltage drop across power component (V)
V_D	conduction voltage drop across diode (V)
v_{AO}	inverter output phase fundamental voltage for phase A (V)
v_{AB}	inverter output line fundamental voltage between phase A and B (V)
V_d	d.c. link voltage (V)
I_d	d.c. link current (A)
i_L , I_L	load current (A)
I_m	inverter output fundamental current amplitude in sinusoidal PWM mode (A)

I_c	power component collector current (A)
t_{on}	turn-on time (ns)
t_{off}	turn-off time (ns)
λ	duty cycle for inverter d.c. mode operation
$\alpha_1 \rightarrow \alpha_4$	coefficients in inverter switching loss model

Microelectronics

DSP	digital signal processor
FPGA	field programmable gate array

Electrical Machines

IM	induction machine
SRM	switched reluctance motor
PM	permanent magnet machine

Induction machine

$\cos \varphi$	machine power factor
R_s	stator resistance (Ω)
$R_{s,dc}$	stator d.c. resistance (Ω)
R_r	rotor resistance (Ω)
$R_{r,dc}$	rotor d.c. resistance (Ω)
L_l	machine leakage inductance (H)
$L_{l,nom}$	machine nominal leakage inductance (H)
X_{nom}	nominal leakage reactance (Ω)

H_s	stator slot depth (mm)
H_r	rotor conductor height (mm)
C_s	stator resistance variation factor
C_r	rotor resistance variation factor
C_i	machine iron loss coefficient
σ	machine leakage inductance variation factor
v_a , v_b , v_c	machine three phase voltages (V)
V	machine fundamental supply voltage (V)
V_e	machine rated fundamental supply voltage (V)
i_a , i_b , i_c	machine three phase currents (A)
i_A , i_B , i_C	machine three line currents (A)
I	machine fundamental current (A)
I_e	machine rated fundamental current (A)
I_n	rms value of machine nth harmonic phase current (A)
i_n	ratio of harmonic current and fundamental current
T_{em}	machine electromagnetic torque (Nm)
$T_{em,n}$	machine nth torque ripple (Nm)
T_m	machine output torque (Nm)
T_{me}	machine rated output torque (Nm)
f	machine supply frequency (Hz)
f_e	machine rated supply frequency (Hz)
f_r	machine rotor frequency (Hz)
s	machine speed slip
s_e	

	machine rated speed slip
Φ	machine air-gap flux
Φ_e	machine rated air-gap flux
k_v	machine per-unit supply voltage
k_T	machine per-unit torque
k_f	machine stator per-unit frequency
k_{f_r}	machine rotor per-unit frequency
k_w	per-unit switching frequency
ω_m	machine rotor rotating frequency (rad/s)
P_{out}	machine output power (W)
P_R	machine copper loss (W)
$P_{R,har}$	machine harmonic copper loss (W)
P_{R_e}	machine copper loss at rated condition (W)
P_s	stator harmonic copper loss (W)
P_{sT}	stator total harmonic copper loss (W)
P_r	rotor harmonic copper loss (W)
P_{rT}	rotor total harmonic copper loss (W)
P_I	machine iron loss at rated condition (W)
$P_{I,c}$	machine core loss at rated condition (W)
$P_{I,s}$	machine stray load iron at rated condition (W)
$P_{i,nom}$	machine nominal iron loss (W)
P_{iT} , $P_{I,har}$	machine total harmonic iron loss (W)
P_{IM}	induction machine total power loss (W)

$P_{IM,har}$	induction machine harmonic power loss (W)
$P_{IM,fund}$	induction machine fundamental power loss (W)

Drive system

P_{sys}	machine drive system loss (W)
EMC	electromagnetic compatibility

Vehicles

EV	electric vehicle
HEV	hybrid electric vehicle
ZEV	zero emission vehicle
m	vehicle mass (Kg)
v	vehicle speed (m/s)
P	vehicle machine power (W)
r	wheel radius (m)
n_g	vehicle overall gear ratio
A_f	vehicle front area (m^2)
η	transmission efficiency
θ	vehicle inclination (degree)
F	force produced by vehicle (N)
F_d	force due to aerodynamic drag (N)
F_r	force due to tyre rolling resistance (N)
F_g	vehicle climbing force (N)

Contents

1. Introduction

Environmental concerns on urban emissions from diesel and petrol engines have led to a renewed interest in battery powered passenger and commercial electric vehicles. The successful introduction of electric vehicles will be largely dependent on the realisation of an acceptable range between battery charges. A critical requirement of an electric drive train is therefore high efficiency in order to ensure the most effective use of the limited energy source of the traction battery. State-of-art electric vehicle traction drives are generally a.c. machine based, supplied from a pulse width modulated (PWM) voltage source inverter. Although efficient designs for the inverter and machine are necessary requirement, an overall high efficiency can only be achieved by appropriate control of the traction system.

Industrial electrical machines are generally designed to operate at a single rated point where the machine excitation field is specified so that the machine has the highest efficiency. However, in the case of an electric vehicle traction drive, which must be capable of operating over a wide range of speeds and loads, to retain a relatively high efficiency the excitation field needs to be controlled to give an optimal balance between the machine iron loss and copper loss. For example, at high machine speeds and light loads, iron loss in an induction machine can be the largest component of motor loss and improvements in efficiency over the established practice of fixed field operation can be gained by reducing the supply voltage and increasing the frequency, when the torque requirement of the load can be met with less than full motor excitation field. The control of the supply voltage necessitates the use of some form of modulation on the output of the power converter.

From the perspective of the electric drive a high battery voltage is beneficial because of the lower working currents and a corresponding higher efficiency and the smaller size power converter. However, a high battery voltage has safety implication and is less reliable than a lower voltage battery. The need for an increased number of series connected battery cells can dramatically increase the likelihood of cell imbalance and result in string failure; and there is increased

difficulty in achieving a balanced battery charge across the cells. As a result, the battery supply is usually limited to moderate voltages, typically 200 - 300V and therefore, to realise high traction powers, the inverter power electronics must be rated at high currents. In such cases the semiconductor switching loss can form a substantial part of the overall drive loss and the use of relatively low PWM frequencies are necessary to retain an acceptable system efficiency. Whereas a low inverter switching frequency has implications on motor harmonic loss, the use of sophisticated PWM control strategies offer the possibility to reduce the harmonic distortion in the machine current, whilst retaining a low switching frequency. Thus the choice of PWM method has a major influence on system efficiency.

Although electrically the inverter control and machine control are effectively two independent systems, they need to be considered together to achieve an optimal balance between the major loss components, viz. motor copper, iron and harmonic loss and the inverter switching and conduction loss. The research described in the thesis assesses various PWM techniques and inverter control methods to determine a methodology of maximising the efficiency of an electric traction system over typical vehicle driving cycles.

1.1 Electric vehicles

In the early 1900s, three types of automobiles - electric, steam, and gasoline - were competing against each other. Yet within little more than a decade, technology innovation and the public's thirst for speed and power on the road sealed transportation future behind the wheels of gasoline-powered automobiles for nearly the next hundred years. However, environmental concerns are now demanding a reassessment of transport technologies and gasoline-powered vehicles have been targeted as a major source of the emissions that create urban air pollution. For example, in the UK it was estimated [Adcock 1995] that road transport was responsible for 90 per cent of the carbon monoxide (CO) released, 37 per cent of the non methane organic gases (NMOG), 47 per cent of the particulate matter (PM) and 50 per cent of the nitrogen oxides (NOx). In the urban environment the contribution of road transport is even higher.

Over the years, notwithstanding the profusion of gasoline vehicle, the interest in electric vehicles has been maintained, and with recent concern of the global environment and improvements in the technologies of electric machines, power semiconductors and batteries, once again the zero emission battery powered vehicle has remerged as a serious contender. Since October 1990 when the California Air Resources Board (CARB) mandated that by 2003 10% of all vehicles lighter than 1700kg sold in the State must be classified as zero emission, large numbers of electric vehicles have been developed in USA, Europe and Asia. Today Ford, General Motors, Toyota and Honda have introduced electric cars in volume production. Every evidence indicates that the revival of electric vehicles is becoming more and more definite.

It should be noted that emissions associated with EVs come from generating the electricity to charge EV batteries, rather than from operating the vehicle, and it is always easier to control and monitor the emissions for fixed generating plant than for a large number of mobile sources (internal combustion engines). It is believed that replacing a conventional vehicle with an EV can greatly reduce emissions - NMOG by 98%, NOx by 92%, and CO by 99% [Chen 1995].

Another key issue that is forcing the rethink of vehicle technology is the need to reduce global energy usage and the associated greenhouse emissions. It was calculated [Shimizu 1998] that from a base supply of crude oil, the total energy efficiency of an electric vehicle is better than that of an internal combustion engine. At constant speed, the electric vehicle delivers a 21% overall efficiency versus 14% for the gasoline vehicle. The energy losses and the final overall efficiencies assumed in this analysis are shown in Fig 1.1.

Although the electric vehicle has the benefits of zero emissions, low fuel costs and high efficiency, given the capabilities of current battery technologies, its range is limited on a single charge. The gasoline engined vehicle benefits from its small size, a long range between refuelling and the existence of an extensive network of gasoline refuelling stations. As a result, vehicle manufacturers are currently more interested in the hybrid electric vehicles (HEV), in which an internal combustion engine is added to a pure EV to either drive the same transmission or to

charge the batteries [Wouk 1995]. Since the engine is reduced in size and by constraining it to run at the speed and load conditions at which it operates most efficiently and emits the least emissions, with the electric traction system operating in other conditions, the hybrid electric vehicles can certainly offer improved fuel consumption and emissions. However, this kind of vehicles can only be regarded as low emission or ultra low emission vehicles, and it is still in doubt that this type of vehicle will be approved by CARB and others [Baker 1997].

Encouragingly, the advancements in the technologies of electrical energy storage is fast. Besides the batteries, other electrochemical and electromechanical energy storage techniques, such as fuel cells, ultracapacitors and flywheels [Howe 1996], are under development. It is certain that the zero-emission pure electric vehicles have a very promising future, although their usage may be restricted to urban operations and specialised sectors.

Table 1.1 gives details of some commercial developments of electric vehicles. The relevant drivetrain technologies will be discussed briefly in the following sections.

1.2 Electric vehicle drives

The modern electric vehicle contains a diverse range of technologies which includes electrical and electronic engineering, mechanical automotive engineering, and chemical engineering. The functional diagram of an EV propulsion system is shown in Fig 1.2, and the power flow and losses in the system are indicated in Fig 1.3.

The battery is a crucial component of electric vehicles. In principle, most modern batteries are capable of producing sufficient power and energy for urban driving. Battery technologies include lead-acid (Pd-Acid), nickel-cadmium (NiCd), sodium-nickel-chloride (NaNiCl2), lithium (Li) and nickle-metal-hydride (NiMH). However, a decision on the type to employ is a compromise based on energy density, power density, energy efficiency, charging rate, cycle life, operating environment, weight, cost and recyclability. For example $Na\ Ni\ Cl_2$ batteries may not be suitable

Table 1.1 Typical electric vehicles and their characteristics

Vehicle	Electrovair GM	ETV-1 GE	ETX-II Ford	FEV Nissan	Honda Honda EV	CitySTROMer Volkswagen	ZIC Electric Fiat	EV1 GM
Year	1966	Late 1970	Late 1980	1991	1995	1995	1995	1996
Range km km/h	50	87 city cycle	227 80	160 70	210	80 80	230 50	145 highway
Top speed km/h	128	96	96	130	130	100	100	130
Gross weight kg	1530	1793	2310	1010	1615	1860	1190	1350
Load kg	-	270	260	4 passengers	4 passengers	346	340	2 passengers
Acceleration km/h	15.6 s 0 - 96	8.8 s 0 - 50	20 s 0 - 80	3.6 s 0 - 40	18.7 s 0 - 80	13 s 0 - 50	7 s 0 -50	8.5 s 0 - 96
Gradeability%	-	-	30	35	25	20	25	
Motor	IM	DC	PMSM	IM	BDCM	Synch. Motor	IM	IM
Converter	SCR inverter	Transistor chopper	Transistor inverter	IGBT inverter	inverter	inverter	IGBT inverter	IGBT inverter
Battery Voltage	Silver-Zinc 512 V	lead-Acid 96 V	Na-S 200 V	Ni-Cd 160 V	NiMH 288 V	Lead-Acid 96 V	NaNiCl2 -	Lead-acid 312V

for electric vehicles since they require a high temperature liquid electrolyte. Widespread use of NiCd batteries may not be acceptable because of recycling difficulties and containment of cadmium which is known toxic pollutant. Lithium (Li) based batteries need several more years of development before safe and high capacity cells become commercially available. The NiMH battery is emerging as the preferred high energy battery for electric vehicles with a good cycle life, although its cost is likely to remain high. However, the century-old lead-acid battery is still a major contender. In the light of the current capabilities and the development history of lead-acid technology, future lead-acid batteries are expected to meet the following goals [ALABC 1995]:

- Improved energy to weight ratio - 50 Wh/kg at a three-hour discharge rate.
- Improved power to weight ratio - 150 W/kg at 80% depth of discharge.
- Improved battery life - three years or over 500 cycles of the urban driving schedule with less than 20% capacity loss.
- Improved cost per battery pack - £100 per kilowatt-hour.
- Improved rapid charging - 100 per cent in four hours, 80 per cent in 15 minutes, and 50 per cent in five minutes.

Two alternative energy sources to batteries are now under development, flywheel energy storage and ultracapacitors. Both promise ample power and cycle life, and if coupled with batteries they can be used as a second source to meet the peak power requirements of an electric vehicle during both acceleration and regenerative braking. Such energy sources can extend the driving range of a vehicle for given battery capability whilst increasing the life cycle of the batteries. Ultracapacitors, which store energy in a polarised liquid layer that forms when an electric potential is created between two electrodes in an electrolyte, are now commercially available. For example, the ultracapacitor modules developed by Siemens are rated at 100 farads and 56 volts [Michel 1999]. However, the voltage level of a single cell is not high enough yet for effective use in an electric vehicle system. Flywheel energy storage, where energy is stored in a rotating mass of composite material connected to a motor/generator, can be scaled for different power requirements and is also environmental benign since there are no disposal problems at end of

useful life. Further developments are needed in high strength fibre composite materials, containment and safety issues, and high speed magnetic bearing systems before flywheels are likely to be viable in electric vehicles.

Ideally the electric traction drive would be designed with a torque/speed characteristic that could use a single gear ratio for the total vehicle speed range, and this seems to be one of the major advantages of the electric motor as compared to the combustion engine. However, with a single gear ratio, the peak torque rating and hence the size and weight of the motor would be determined by the requirements of acceleration and gradability. Utilisation of variable gear ratios can reduce the size of motor and power electronics, as well as improve the transmission efficiency, however, this involves penalties in first cost and weight. Thus, an optimal transmission system should be designed on consideration of overall cost, weight and efficiency [Bitsche 1994].

As far as the control of the vehicle traction system is concerned, satisfactory performance and efficiency can be achieved by suitable design of motors and power converters, and by the adoption of a suitably sophisticated control system.

1.2.1 Electric vehicle traction machines

The electrical traction machine is a vital component of an electric vehicle. It is the main energy consuming component, and its characteristics will determine the design of the power electronic controller and the control strategies. The following diagram illustrates the issues involved in the design or selection of a traction machine.

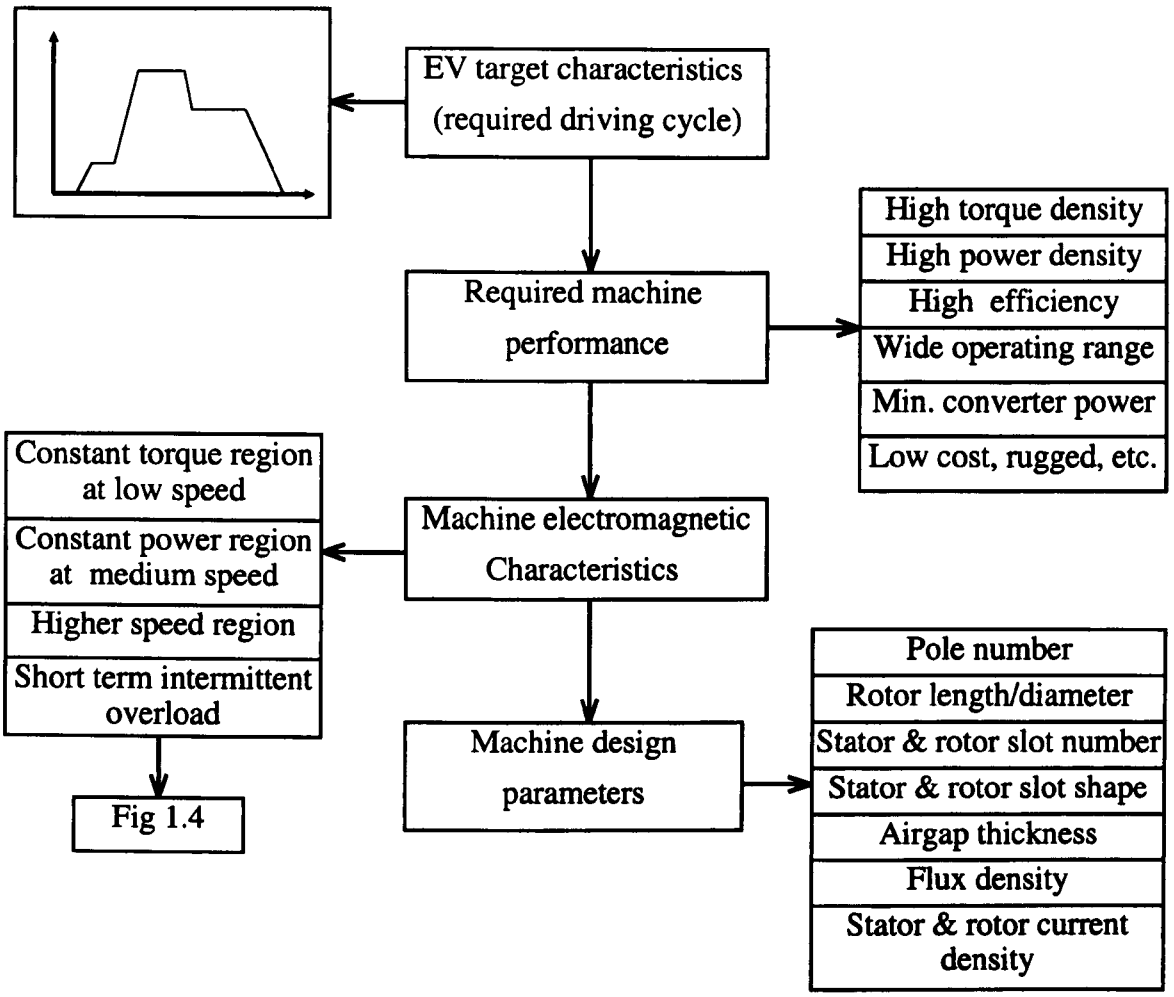

Traditionally d.c. commutator motors, loosely named as d.c. motors, have been prominent in traction applications. By replacing the field winding and pole structure with high-energy permanent magnets, permanent magnet d.c. motors permit a considerable reduction in stator diameter. However, the principle problem of d.c. motors arises from their commutators and brushes, which limits their maximum speed and also makes them less reliable and unsuitable for maintenance-free operations.

With recent developments in power electronic control methods and magnetic materials a.c. motors can now outperform the d.c. motor in most aspects. However, there is still a considerable debate on the relative merits of various forms of a.c. motors.

Induction motors are well established in the industrial sector and are attractive, because they are simple, inexpensive and robust, and can be manufactured in the large volumes needed for automotive applications. When controlled as variable speed drives, induction machines are capable of operating over the torque-speed envelope required by an electric vehicle, i.e. the constant torque region till the base speed, the constant power region, and the high speed region. The main drawback of an induction machine is its lower efficiency in the low speed high torque region. To achieve a good performance it must be controlled using complex vector control methods which require an accurate measurement of rotor slip speed.

By replacing the rotor winding with high-energy permanent magnets, brushless a.c. motors and brushless d.c. motors are formed. The advantages of brushless PM motors are their high peak torque capability, high efficiency, and low weight. In the full flux operating range, the permanent magnet motors have the highest efficiency and specific output of all a.c. motors. However, to achieve a wide operating range at constant power, a field weakening technique must be employed where the phase angle of the driving current is adjusted to act against the permanent magnet excitation field. This production of a counter magnetic motive force involves complex vector control strategies and leads to poor efficiency at high speed. Moreover, permanent magnet machines are subject to limitations imposed by the permanent magnets themselves. These include the risk of demagnetisation during fault conditions of excessive currents in the motor windings or overheating of the magnets. Also, high energy permanent magnets are still expensive. Compared to induction machines, the development of permanent magnet machines is still in its infancy.

In recent years switched reluctance motors [SRM] have seen a revival of interest. These types of machines are simple in structure and rugged. In a typical switched reluctance machine, the magnetic loading is about 80% of the comparable induction machine, while the electric loading is a factor of twice higher [Buckley 1995]. This implies that an SRM can theoretically deliver about 160% of the output of a conventional induction machine in the same frame size, and that the weight and cost can be lower when using a SRM. However, the machines are inherently

noisy, and to produce the sufficient torque a narrow high tolerance air gap is needed, thus increasing the manufactuering costs. Although the principle of operation of an SRM is simple, to achieve satisfactory torque control complex control techniques are needed. The SRM has yet to establish itself in electric vehicle traction applications.

Some of the applications of the various machines in electric vehicles are given in Table 1.2.

Table 1.2 Electrical machine type used in prototype electric vehicles

Motor	Vehicle	Max. kW@rpm	Max. Nm@rpm	Max. rpm
DC machine	ETV-I	30	163	5000
Induction machine	ZIC Elettrica	21.5@8000	100@1600	8000
Synch. machine	CitySTRORMer	17.5	-	-
PM synch. machine	ETX-II	52	110	11000
Brushless d.c. machine	BWM-EI	32 rated	150@2400	8000
SRM	Chloride Lucas	-	-	-

Up to now, most American vehicle manufacturers have tended to use the a.c. induction machine, whilst in Europe brushless permanent magnet machines are favoured because of their particular advantage of efficiency in european city cycles. Nevertheless, induction machines have also been used in European electric vehicle drives, e.g. in Fiat Elettra.

1.2.2 Converters

In the design of a power electronic converter, the circuit topology and power semiconductor devices need to be considered.

Following the two types of machines (d.c. or a.c.), the converter topologies can be divided into d.c./d.c. converters (d.c. choppers) and d.c./a.c. converters (inverters), and each can be configured in the hard-switched or soft-switched mode. Conventional hard-switched converters have the advantages of simplicity and reliability. Soft-switched converters combine the main power semiconductor switches with either parallel or series resonant circuits to provide either a zero-voltage-switching or a zero-current-switching capability. The potential of the soft-switched

inverter include: zero switching loss and high efficiency, smaller heat sink requirement and a high power density, less severe EMI and low acoustic noise through ultrasonic switching. The disadvantages include a complex circuit structure and control, higher voltage or current stresses on the devices, and greater harmonic content in the output because of the limitations of integral half-cycle modulation methods (PDM). Although soft switching inverter topologies have received a lot of attention in the literature, more effort is needed to establish viability of this technology for electric vehicle applications [Chen 1997]. For example, recent research has shown that the hard-switched inverter is as efficient as a soft-switched inverter when employed for high power electric vehicle drives [Rendell 1996]. Here an IGBT hard-switched inverter and a resonant link soft-switched inverter were developed for a 26 kW traction machine, the two circuits being shown schematically in Fig 1.5 and Fig 1.6, respectively. A comparison of the corresponding switching losses (resonant link circuit loss is included in the soft-switched inverter) given in Fig 1.7 indicates an advantage for the soft-switched inverter at switching frequencies above ~8 kHz.

The selection of power semiconductor devices for EV propulsion is generally based on the requirements of the voltage rating, current rating, switching frequency, and efficiency. Most power semiconductors, viz. GTO, BJT, power MOSFET, IGBT and MCT, are suitable for EV drives. Ideally these devices should have the following characteristics,

- A large forward and reverse voltage blocking capability with minimal leakage current.
- A large current capability when on, with a minimal conduction voltage drop.
- Very fast switching speeds.
- Minimal level of injected energy from the control source to trigger the switch.

A comparison of the characteristics and performances of the principal power semiconductors is given in Table 1.3.

Table 1.3. Performance comparison of power semiconductor devices

Device	GTO	BJT	MOSFET	IGBT	MCT
Power rating	4500V,3000A	1800V,1000A	100V,40A 800V, 5A	1700V,1200A	1500V,50A
Switching freq	1- 10 kHz	10kHz	30 - 100 kHz	>20 kHz	20 kHz
Control	current	current	voltage	voltage	voltage
Voltage drop	2 - 3 V	1 - 2 V	R_{DS}->$V^{2.5}$	2 - 4 V	1-2 V
Turn on /off times	4/10 μs	1.7/5	0.09/0.14	0.9/1.4	1.0/2.0
Temperature coef.	negative	negative	positive	negative	negative
Ruggedness	snubber	snubber	snubberless	snubberless	snubberless
Availability	Good	Good	Good	Good	Rare
Cost	Low	Low	Low	Low	High

Note a voltage-controlled device requires a simple drive circuit and small control power. Devices with positive temperature coefficient can be easily paralleled and will share current equally, although those with negative temperature coefficient can operate in parallel with careful design. Ruggedness refers to the capability of a device to withstand rated voltage and rated current simultaneously while switching and whether external circuits (snubber) are required.

The IGBT provides the most favourable overall performance, though the power MOSFET has also been accepted for many electric propulsion systems, especially for relatively low-voltage low-power electric bicycles, scooters and tricycles. The MCT, a relatively new device, would appear to be competitive because of its lower conduction voltage drop and satisfactory switching characteristics. However, available MCT devices still have only relatively low power ratings, and it seems that MCTs are not very suitable for paralleling. The power semiconductors used in three example electric vehicle drives are given in Table 1.4.

The progress in power semiconductor technologies has been very rapid. However, improvements of switching performance are usually accompanied by a decrease in conduction performance,

Table 1.4. Examples of power devices used in electric vehicle drives

Power devices	Vehicles	Power rating	Switching frequency
IGBT	Nissan FEV	60 kVA	10 kHz
MCT	Ford/GE ETX-II	87.3 kVA	5 kHz
MOSFET	Sheffield Go-Kart	12 kVA	16 kHz

and vice versa. Table 1.5 summaries the performance of a range of IGBTs manufactured by International Rectifier, which are available in TO3P packages. The table shows that the Standard IGBT has the lowest conduction voltage drop but the worst switching performance and would be a good choice for electric vehicle applications where a relatively low switching frequency is beneficial for the vehicle energy efficient operation.

Table 1.5. Comparison of International Rectifier IGBTs (parameters are given for a current density of $1A/mm^2$ of active area, 100^oC, typical values)

IGBT	Standard	Fast	Ultrafast
Voltage drop	1.3 V	1.5 V	1.9 V
Switching energy	0.54 mJ/A mm^2	0.16 mJ/A mm^2	0.055 mJ/A mm^2
Conduction losses (50% duty)	0.625 W	0.75 W	0.95 W

Currently there is a trend of using integrated circuit modules instead of the discrete components. The improved packing of the power module can reduce the circuit stray inductance and thus limit over voltage and ringing. However, it seems that using discrete power components is still more cost-effective. In addition, discrete components are available in a wide range of characteristic and from many different manufacturers, and thus offer a more flexible choice of characteristics. Stray inductance can be limited by careful circuit layout of discrete components to guarantee the operation of the devices to remain within their snubberless safe switching operation areas. Nevertheless, custom-specific packaging is an essential requirement for volume manufacture [Locher 1996], which is tailored to meet customs' requirements for high peak power during acceleration, light weight and reliability.

1.2.3 Control

The adequate control of the functions of an electric vehicle and the management of the energy can be a complex process, and thus in many aspects control can be considered as a separate component of the EV powertrain. Corresponding to the development in electrical machines and power converters, various control methods have been proposed, from the most basic to the complex field oriented control and direct torque control methods [Casadei 1995]. In many cases the dynamic performance of the drive system is emphasised, particularly for the applications in machine tools and robotics. However, for an EV drivetrain, the key issue is to achieve the demanded vehicle operation with a maximum efficiency, and there is a moderate requirement in terms of system dynamic response. Thus, a simple feedforward control method may be sufficient in practice. A digital implementation of the control strategies using digital signal processors (DSP) may also be necessary.

1.2.4 Summary

Following the preceding discussion, a cost effective traction drive system with suitable performance for an electric vehicle would contain the components given in Table 1.6,

Table 1.6. A suitable drive system for electric vehicles.

Battery	Motor	Converter			Control
		Topology	Power device	Modulation	
Lead-Acid	Induction machine	Voltage source hard-switched	IGBT	Feedforward PWM	Loss minimisation strategy

1.3 Realisation of an energy efficient induction machine traction drive

The viability of an all-electric vehicle is critically dependent upon it having an acceptable range between charges, a feature which is dictated ultimately by the capacity of the battery energy store. However, a significant factor in improving vehicle range is the effective use of the limited energy resource through minimisation of the total losses in the electric drive-train, i.e. the combined machine and power electronic design and control.

1.3.1. Machine design

The requirement for a traction machine is that it should meet the vehicle target performance characteristics with an overall high efficiency. On consideration of this and the necessary operation from a converter, the machine will be designed based on a number of compromises. For example, to achieve the high speed motor pull-out torque, a low motor leakage inductance is required. However, a low inductance may lead to significantly higher harmonic currents or demand a higher converter switching rate. To increase the machine efficiency, large machine size may seem appropriate, however, the machine will be heavier; high pole number implies the necessity of increased inverter switching frequency and thus increased switching loss.

1.3.2 Inverter design

A hard-switched inverter exhibits both conduction loss and switching loss. Its efficiency can be improved by careful selection of power components so that there is an optimal balance between conduction loss and switching loss. Inverter efficiency can also be improved by adoption of an inverter topology with paralleled discrete power components to decrease the conduction loss as well as the switching loss, although the inverter cost will be increased.

1.3.3 PWM strategy

Pulse-Width-Modulation (PWM) is an established method of generating variable voltage and variable frequency a.c. supply from a fixed d.c. power source (e.g. batteries). Several PWM strategies have been proposed over the past two decades with a variety of performances and complexities. When the inverter switching frequency is sufficiently high, these different PWM methods behave very similarly and will not greatly influence the machine performance. However, the potentially high switching current in an electric vehicle drive necessitates the adoptions of relatively low switching frequencies to retain system efficiency. The switching characteristics of PWM will ultimately introduce harmonic losses in the machine, and the extent of these losses will depend upon the PWM strategy. In many existing electric vehicle drives, relatively high switching frequencies have been used with no particular consideration of the modulation strategy. In one particularly study, an optimal harmonic minimisation PWM has been proposed as the

most suitable method [Vezzini 1994]. However, the most appropriate PWM modulation technique should be the one that for a particular level of inverter losses and machine fundamental losses, the machine harmonic losses are the minimum. Additionally, the PWM method should be relatively easily implemented in a digital controller.

1.3.4 System control

In an induction machine traction drive, the major losses are machine copper, iron and harmonic losses, and inverter switching and conduction losses. These losses are dependent upon the three control variables: machine fundamental supply voltage magnitude and frequency and inverter switching frequency. For example, for a given machine load, supply frequency and inverter switching frequency, decreasing the machine supply voltage will cause a reduction in iron loss, an increase of machine copper loss and harmonic loss, and increased inverter switching loss and conduction loss. Alternatively, an increase in inverter switching frequency with the other two variables fixed will result in a higher inverter switching loss and lower machine harmonic loss. Thus, the three control variables should be carefully adjusted to give an optimal balance between these major loss components. Since for the majority of time the vehicle traction drive is operating at partial load, it is believed that the system energy efficiency can be considerably improved by dynamically changing the operating point to suit load conditions.

The optimum efficient operation of an induction machine has received much attention over the years. For constant speed operation, the use of power factor controllers was proposed to vary the input voltage according to the load level [Nola 1979]. In the case of a variable speed drive, the machine flux level can be controlled by adjusting the supply voltage and frequency for optimal efficiency operation at the required working points [Kirschen 1984]. In many of the published energy efficient induction machine control schemes, either the effect of the power electronic controller is not considered or the inverter switching loss is assumed to have a negligible effect on the system efficiency [Boglietti 1994]. To avoid the difficulty of including the inverter losses and the resulted machine harmonic losses in the optimisation procedure, feedback control systems with direct measurement of drive system input power have been proposed [Kirschen

1987, Garcia 1994, Boys 1988]. However, these systems involve on-line searching techniques to determine the optimal control variables, which may not be suitable for continually changing loads such as in a traction drive. Although the control of the inverter and the machine can be effectively decoupled, their combined operation should be considered if maximum efficiency is to be achieved. One method would be to find a loss function, which includes all major losses in the system and, based upon the three principal control variables. Then an optimisation procedure can be applied to determine the three control variables that would give maximum efficiency for every vehicle drive operating condition. Knowledge based artificial intelligence may be included in such a system to compensate for the machine parameter variations and any modelling errors.

1.3.5 Summary

The considerations needed in the efficient design and operation of induction machine traction drive for an electric vehicle are summarised in Fig 1.8, which also gives an overall guide to the research.

1.4 Structure of thesis and contribution to the knowledge

Starting from a recognition of the need for electric vehicles, Chapter 1 reviews the main components of an electric vehicle traction system. The research area of the thesis is then identified.

In Chapter 2, a prototype drive system is described, which is used for experimental work in the thesis and includes a discussion of the instrumentation and various performance measurement techniques used. In the development of the prototype inverter an investigation of parallel operation of IGBTs has been undertaken.

In Chapter 3, various PWM control strategies are reviewed, with particular emphasis on the detailed analysis of the feedforward PWM methods and their practical implementations. Then, a DSP based digital PWM modulator is developed, and the implementation of the PWM strategies

described. A series of tests are undertaken to validate the earlier analysis, and to investigate the spectral errors that occur in a practical inverter system.

Chapter 4 considers the effect of PWM operation on an inverter fed induction machine drive system performance and identifies the most suitable PWM strategy for an induction machine drive. Models of the machine harmonic loss and the inverter loss are developed and verified by experiments. Machine torque ripple and acoustic noise are also addressed.

Chapter 5 presents a vector space gear changing PWM control algorithm, which features easy digital implementation and flexible on-line adjustment of control parameters to obtain a good harmonic performance whilst allowing smooth transition over changes of switching frequency.

In Chapter 6, analytical and experimental results are used to investigate the influence of the three control variables, viz. machine fundamental voltage and frequency and inverter switching frequency, on the drive system efficiency. An overall system loss model is developed as a function of these three control variables and is used to develop an optimal minimal loss control strategy. This loss minimisation strategy is then validated through experiment.

In Chapter 7, the above developed loss minimisation control strategy is applied to a representative 26kW electric vehicle over a standard urban driving cycle (ECE15). The benefits of the proposed control method over the conventional constant flux control mode are demonstrated.

Finally, the research results are summarised in Chapter 8, and suggestions for future research are made.

The major contribution of the thesis may be summarised as follows:

(a) The development of a complete system loss model for an induction machine driven by an efficient IGBT voltage source inverter based on previously published work and the validation of

this model through extensive testing of a 3kW prototype drive system (Chapter 2 and Chapter 4).

(b) A detailed assessment of various feedforward PWM strategies and influence of modulation frequency ratio on the drive system total loss (Chapter 3, Chapter 4 and Chapter 6).

(c) Development of a novel implementation strategy for vector space PWM (Chapter 5).

(d) Development of an optimal minimal loss control strategy for inverter fed induction machine drives. This strategy predicts that by applying it to a 26kW electric vehicle over a standard urban driving cycle (ECE15), the total loss can be reduced by 30% and driving range increased by over 5%, when compared with the conventional constant flux and constant switching frequency control (Chapter 6 and Chapter 7)

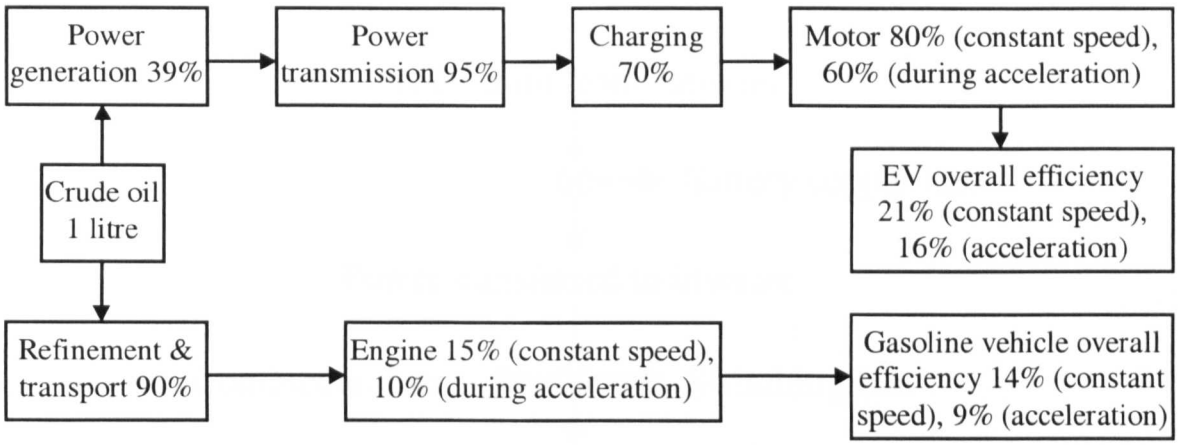

Fig 1.1 Comparison of energy losses and final overall efficiency in electric vehicle and gasoline vehicle.

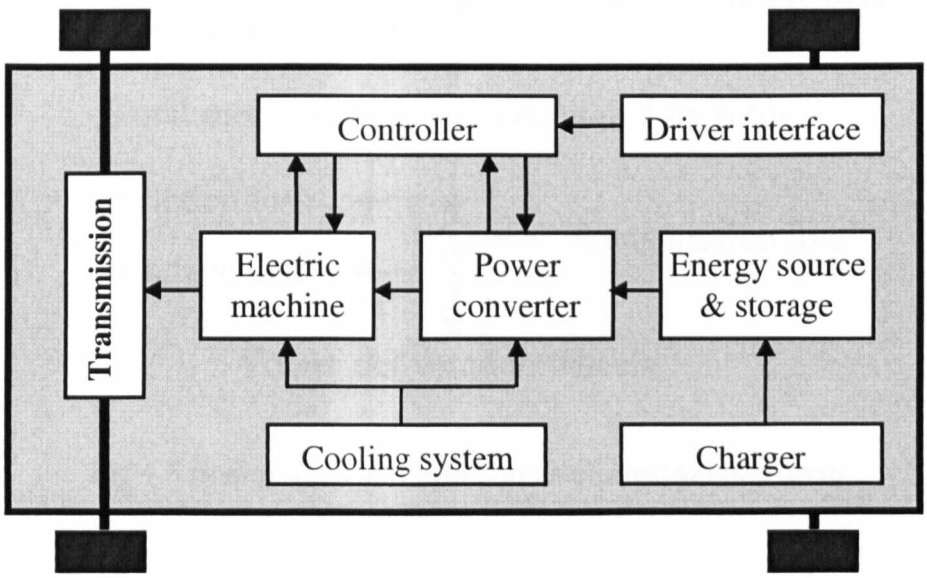

Fig 1.2 Diagram of electric vehicle drive system.

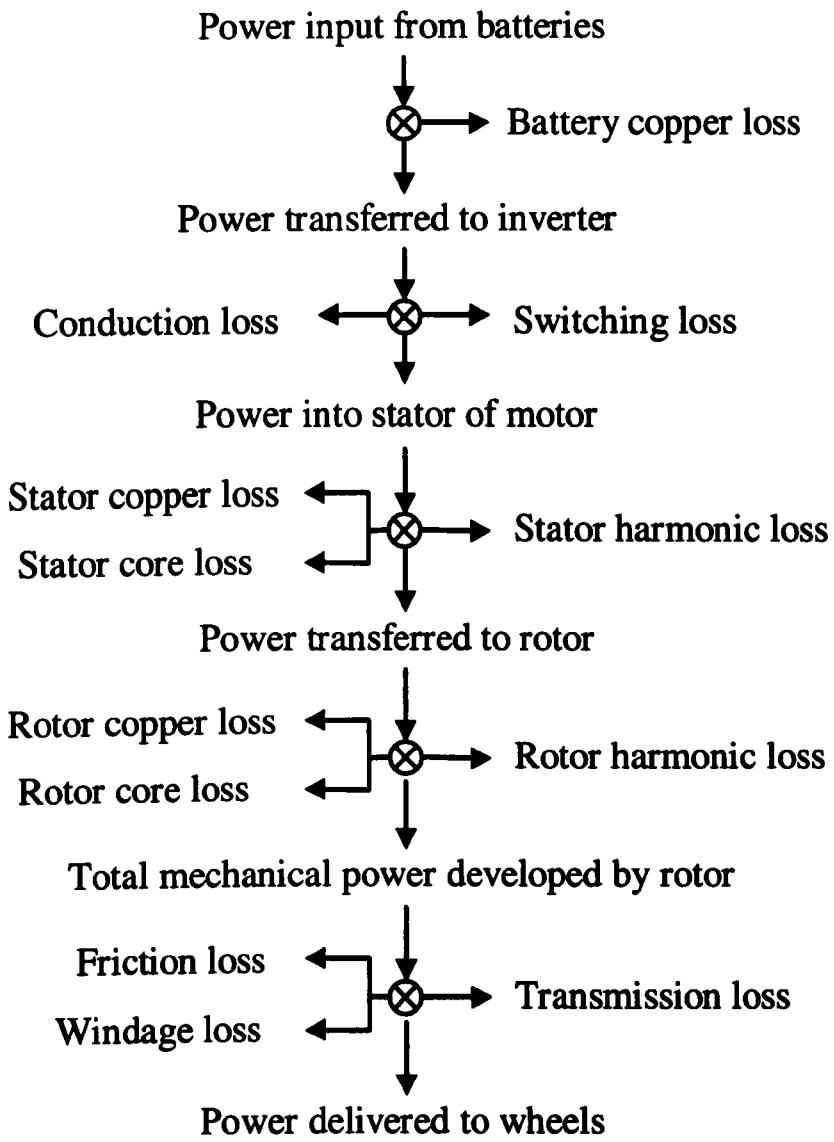

Fig 1.3 Energy flow and losses in an electric vehicle drive.

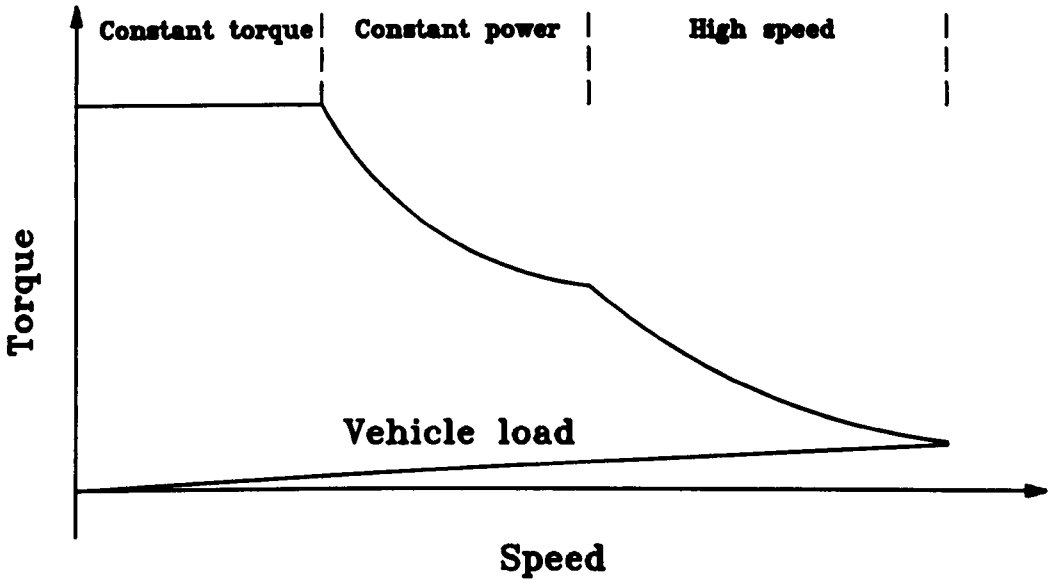

Fig 1.4 Practical torque speed characteristic of a traction machine.

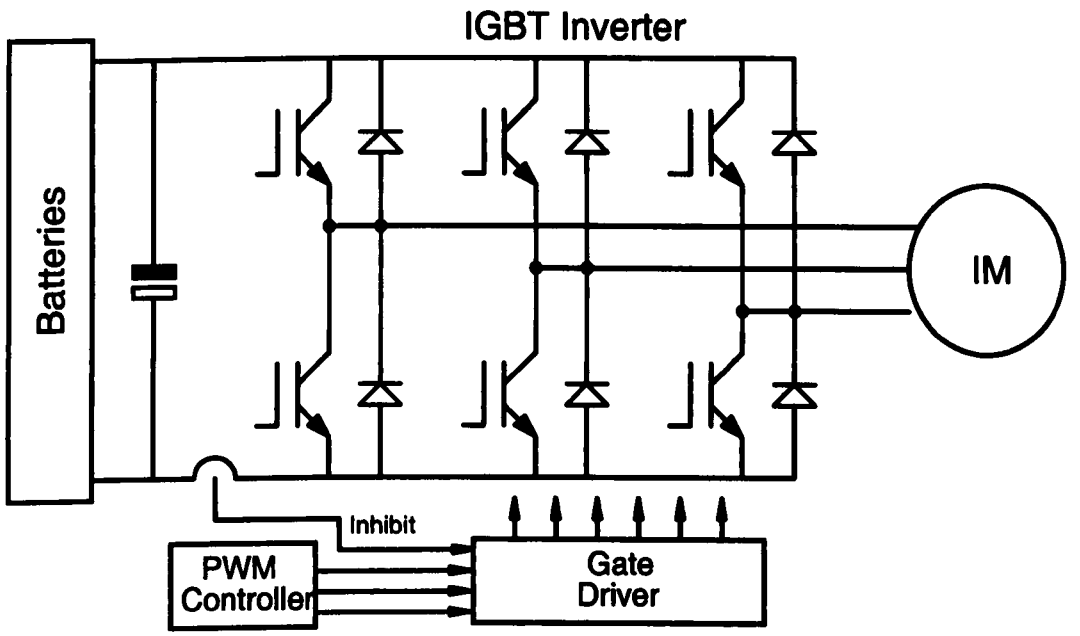

Fig 1.5 Voltage source hard-switched inverter IM drive.

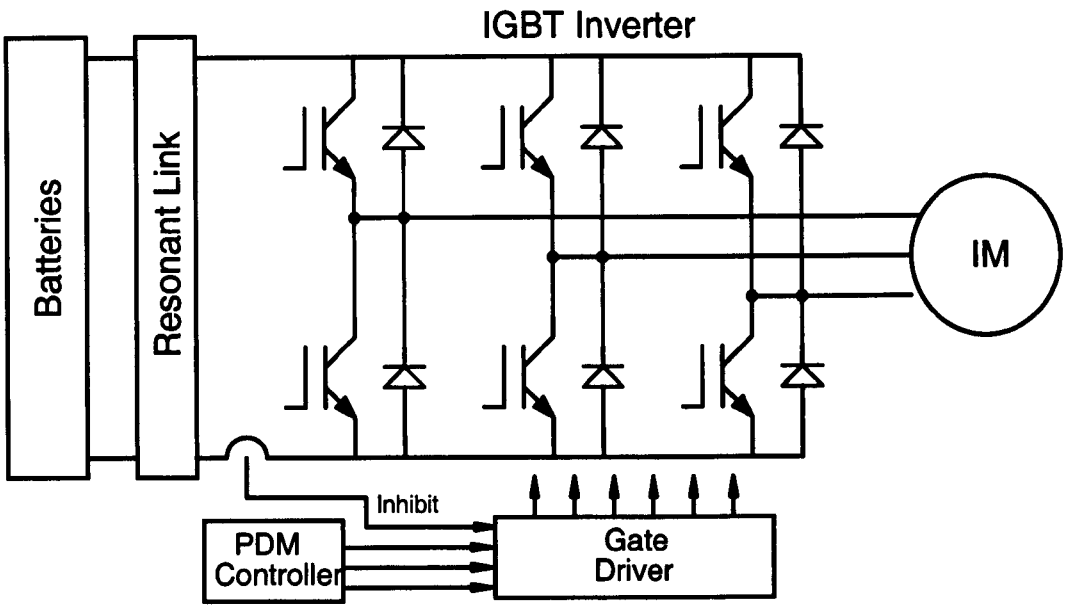

Fig 1.6 Resonant link soft-switched inverter IM drive.

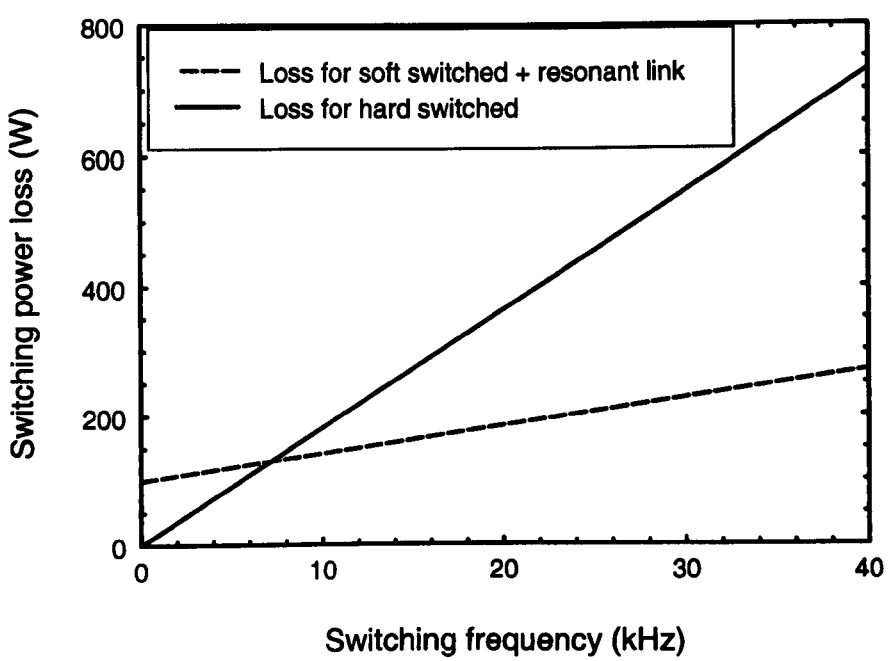

Fig 1.7 Comparison of switching losses with two inverter topologies (resonant link loss is included in the soft-switched inverter).

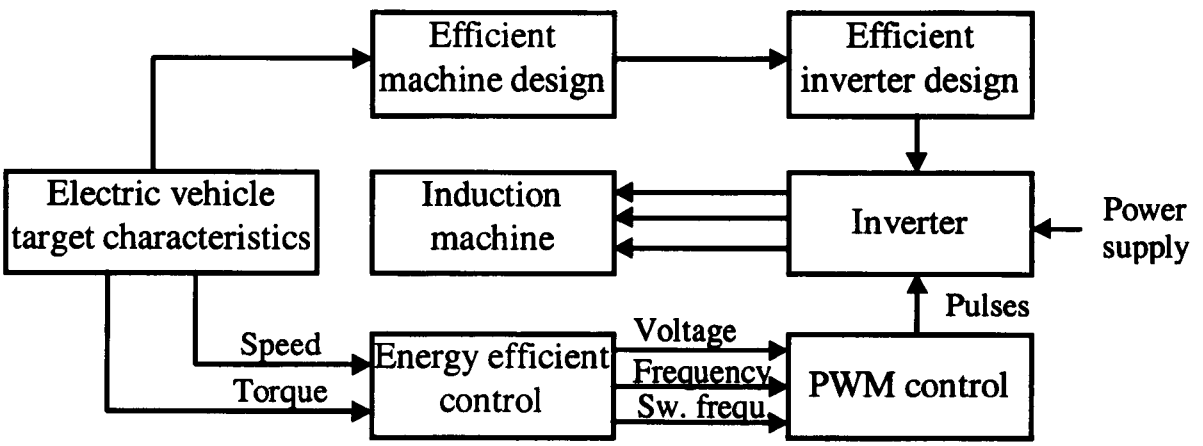

Fig. 1.8 A design rule for energy efficient usage in electric vehicles.

2. Experimental Induction Machine Drive System

To evaluate the performance of an induction machine traction drive and its optimal energy efficiency control strategies, a representative drive system was constructed. In addition the test bed has been used to provide an environment for the development of models of the various components in the system and their experimental validation. In this chapter the main components of the experimental system will be described, including the design of a high efficiency power electronic inverter. A description of the various measurement techniques used on the test bed is also given.

2.1 System construction

A schematic of the full experimental system is shown in Fig. 2.1(a), which consists of a 340V d.c. power supply, an IGBT power inverter and its DSP controller, a test induction machine and dynamometer and measurement system. Fig. 2.1(b) is a photograph of the system.

2.1.1 Power supplies

For test purposes, a representative d.c. link power supply was derived by rectifying the a.c. main supply (Fig.2.2). Three phase isolation transformers with a 1:1 turn ratio were connected in a Y/Δ configuration and the output was fed to a standard three phase rectifier. The output of the rectifier was then connected to a 2×4700 μF smoothing capacitor bank. With a standard 415V a.c. supply input to the isolation transformers, the d.c. link output voltage at no load would be 340V. Contactors, time relays and other control circuitry have been arranged to provide a safe switch-on and -off operation. Contactors C1 and C2 are initially open to allow the voltage across the d.c. link capacitor bank to build up gradually. After a preset time set by the timer, the charging resistor R_c is shorted by closing C1, and the power supply is in its normal operational state. At switch-off of the power supply, the contactor C2 connects the resistor R_d across the capacitor bank to discharge the d.c. link. The design capacity of the rectifier supply is 6kW.

2.1.2 Test induction machines

A 26kW induction machine has been specially designed at the University of Sheffield for an electric vehicle application [Harson 1995]. This machine was used as a basis for the original development of the drive system and will be used later to benchmark the optimal energy efficiency control strategies developed in this thesis. A detailed description of the specification and performance of the machine is given in section 2.2. However, due to the early unavailability of this large machine, initially a standard industrial three-phase 3kW induction machine has been employed for experimental purposes. The machine was configurable in "Δ" to work at low, 240V, line voltage. The specification and electrical parameters of this machine are given in Appendix A.

2.1.3 Three-phase IGBT inverter

The three-phase voltage source hard-switched converter topology used in the investigation employs IGBT power semiconductors, with low conducting voltage and medium switching speed characteristics. Device paralleling techniques have been applied so as to extend the inverter maximum current handling capability whilst using relatively low cost standard TO3P packaged devices, as well as to improve the inverter efficiency. The inverter is rated at 40kVA, and has been sized to be capable of driving the 26kW induction machine.The detailed design of the inverter and an investigation of device paralleling are given in section 2.3.

2.1.4 DC dynamometer

A shunt d.c. generator with a swinging frame has been used as a flexible load to the 3kW induction machine. Its field and armature currents can be controlled in a manner that allows the test induction machine to be loaded at a constant torque or at a constant output power. The d.c. generator, being an old University laboratory machine, has a relatively large size and a high rotor inertia. Its specifications are given in Appendix A.

2.1.5 Drive system controller

A digital DSP based drive system controller was developed to control the switching of the inverter power devices, and thus to define the switching frequency of the inverter, and the voltage and frequency of the a.c. supply to the machine. A separate controller was used to define the operating mode of the experimental rig, and to vary the loading of the test machine. These controllers will be discussed in detail in later chapters.

2.1.6 Protection

The d.c. link current was monitored to detect abnormal operating states. If a fault occurs that causes the d.c. link current to exceed prescribed limits, a protection circuit is triggered which disables the gate drive signals of the converter. This blocking signal was also applied whilst d.c. link capacitor is charged on initial turn-on. The DSP controller operating mode and control parameter settings were protected by a enable/disable switch.

Since the machine regenerative braking process was controlled, there was no risk of overvoltage in the d.c. link, thus eliminating the need of d.c. link dump circuit. Other protection, such as systems' power component thermal protection, were not implemented at this experimental stage.

2.2 Design features of the 26kW induction traction motor

The high efficiency, 26kW induction traction motor was developed to be capable of powering a small passenger vehicle as part of an European Commission funded research project. The power train required a single traction machine, which drove the vehicle wheels through a fixed gear and a mechanical differential. The machine base speed and output power were specified with regard to maximum torque to overcome a 10% gradient and acceleration performance of 0-50 km/h in 8s. The maximum speed of the motor was dictated by the maximum road speed and the gear ratio of the available transmission, requiring the machine to ideally have a constant power characteristic up to a maximum speed of approximately 4 times the base

speed. A prime requirement in the machine design was high efficiency. Table 2.1 gives some details of the machine design requirements.

Table 2.1 Principal ratings of 26kW traction induction motor.

Output power	Base speed	Max. speed	Max. torque	Pull-out torque at max. speed
26 kW	2000 rpm	7500 rpm	122 Nm	14.5 Nm

The machine design process involved three stages and required a number of interactions before a satisfactory design was realised [Harson 1995]:

(a) Making appropriate choices for the pole number and slot number, etc.

(b) Designing the machine dimensions and winding parameters to provide the required power at base speed within a specified space envelope.

(c) Evaluating the machine performance over its full speed range.

The choice of pole number involves a compromise between machine weight and overall efficiency, and eventually a pole number of 6 was chosen. The stator winding was a conventional double layer fractional slot type in 45 slots with a coil pitch of 6 slots. The rotor winding was made up of low resistance copper bars braced to endrings, with 38 tapered unskewed bars. The winding was designed to alleviate the undesirable effects of harmonic fluxes such as, iron loss, noise and vibration, cogging, crawling and synchronous torques. The stator slots were semi-closed, round bottomed shapes with tapered sides. The rotor slots were fully closed "pear" shaped. These slot shapes, together with a reasonably large number of slots per pole per phase of the stator, resulted in a low leakage reactance, and thus operation over a wide field weakening range was possible. The machine performance was evaluated using the classical equivalent circuit approach, which used both fundamental and harmonic circuit elements.

The electrical specification of the designed machine is given in Table 2.2, and some of its electrical parameters in Table 2.3.

The characteristic of the machine is shown in Fig.2.3. The evaluated machine efficiency is given in Fig.2.4, which indicates an acceptable maximum in excess of 90% over a wide speed range. The machine torque-speed envelope is shown in Fig.2.5, and meets the original specification given in Table 2.1.

Table 2.2. Electrical specifications of the 26kW induction machine

Output power	P_{out}	26	kW
Base speed (full load speed)	n	2022	rpm
Base frequency	f	103.2	Hz
Efficiency	η	92	%
Power factor	cos φ	0.85	
Phase voltage	U	153	V
Phase current	I	75	
pole pairs	p	3	
Rated torque	T_s	122	Nm
Pull out torque	T_m	260	%
Connection		Δ	

Table 2.3. Electric parameters of the 26kW induction machine

Stator resistance	$R_{s,dc}$	0.053	Ω
Rotor resistance	$R_{r,dc}$	0.053	Ω
Nominal leakage reactance	X_{nom}	0.445	Ω

2.3 Design of the experimental inverter

2.3.1 Inverter topology

When operating at relatively low switching frequency, conventional hard-switched voltage source inverters will have a higher efficiency compared to the more complex resonant d.c. link topologies. Therefore, a standard six-switch topology was chosen for the inverter design.

Although many developments have occurred in power semiconductors to increase their switching performance, an improvement in component switching speed is often accompanied by an increase of component conduction loss. A comparison of the conduction and switching performance of a manufacturer's Standard IGBT, Fast IGBT and Ultrafast IGBT, as given in Table 1.5, clearly illustrates this. Therefore, a careful selection of the power semiconductor devices used is necessary as it can significantly affect the inverter operating efficiency.

Observations from power component data sheets and experimental measurements show that the conduction voltage drop of a typical power device increases with conducting current, and that the switching times of the device are also influenced by the conducting current in such a way that higher conducting current intends to increase the switching times, especially the turn-off time in the case of an IGBT. These phenomenon suggest that if the conducting current can be kept small then the power component will have low conduction loss and switching loss. Components paralleling operation is a potential solution to the problem. This paralleling technique can also bring other benefits to the system, for example, increasing the power handling capability of smaller and cheaper components, whilst increasing the power dissipation capability. This technique for reducing inverter losses has also been recommended by [Schmid, 1995], where an optimal number of ten paralleled MOSFETs was used for a hybrid electric vehicle inverter drive to balance the improvement in inverter efficiency and the increase of the cost and weight. However, the advantages of IGBT paralleling operation can only be guaranteed if the current sharing among the paralleled devices is good.

The IXYS manufactured Standard IGBTs, IXSH40N60, were chosen for the experimental inverter design. This device has a relatively high power handling capability of 600V and 75A, and has a medium switching speed (maximum 30kHz) but relatively a low conduction voltage drop. The data sheet of this component is attached in Appendix A. In the experimental inverter only two IGBTs have been paralleled as a single switch in the inverter, although more can be used to achieve a higher rating. The selected freewheeling/flyback diodes were DSE12X61-06C devices (Appendix A), which have a power handling capability of 600V and 120A, and a fast reverse recovery of 35ns. Since the forward voltage drop of a diode does not change significantly with variation of conducting current, a single diode was used for each switch. The schematic diagram of the inverter is shown in Fig 2.6(a). Switching aided circuits were not employed as these would increase the overall inverter switching loss.

A cubic forced air heatsink was used for cooling the semiconductor devices. The paralleled devices were placed close to each other to ensure similar operating temperatures. To reduce stray inductance, copper strips were used for d.c. link buses, for component inter connections and for connections to the filter capacitors. The collectors of the paralleled IGBTs were led through copper strips to individual terminals to allow individual current monitoring, however, in normal operation, the corresponding terminals were shorted by copper bars. Two 2200 μF electrolytic de-couple capacitors were connected to the d.c. link buses, one close to the positive bus whilst another to the negative bus. Similarly, two 0.2 μF metallised polypropylence capacitors were connected to the d.c. link buses to suppress high frequency ripple in the d.c. link. To ease the manufacturing and replacement of components, and to provide a good electrical contact, most of the connections were made using bolts.

2.3.2 Design of inverter gate drive circuit

The inverter gate drive circuit is shown in Fig 2.6(b). The low device drive circuits were powered from a commercial 15V d.c. supply and three individual isolated 15V d.c. supplies were used for the upper devices. The inputs to the driver were digital PWM signals generated from the DSP controller. The PWM signal for each phase output was buffered and inverted

before passing through a 3 μs leading edge delay circuit, and then was opto-coupled and buffered before driving the IGBT gates. This opto-coupler (H11L1) has a response of 1MHz and therefore introduced a minimal time delay. To protect the IGBTs, the gates were fitted with 18V zener diodes to clamp transients. Low value resistors were put in series between the driving signals and IGBTs gates to prevent voltage ringing in the inverter during switching. This arrangement, together with some diodes, has also been used to improve the transient current sharing among paralleled IGBTs, as will be discussed in the next section. A protection feature was included in the gate driver which enabled the gate signals to be blocked if a fault condition occurred. The gate signals can also be disabled and enabled by two push buttons.

A photograph of the experimental inverter is shown in Fig. 2.7.

2.3.3 Investigation of IGBT current sharing

Almost all types of power semiconductors, viz. Thyristors, Darlington transistors, BJTs, MOSFETs and IGBTs, have been configured in parallel, with the MOSFET being particularly suitable because of the positive temperature coefficient of its channel resistance. In the early years, the main purpose was to extend the power capability of the components. More recently, it seems that the paralleling operation may also have benefit in improving a converter efficiency and reducing cooling requirements. When hard paralleling a number of devices, to ensure a good current sharing considerable care must be taken in the geometric layout of the devices on the common heatsink, with them being driven from a common control signal [Mohan 1995]. In addition, the device characteristics may need to be closely matched. Another approach is to use active and passive snubbers which overcome the constraints of hard paralleling by improving the dynamic load sharing of the individual devices [Mellor 1991]. Since the transient current sharing is more sensitive to unequal switching times across a batch of nominally similar devices, and since the turn-on and turn-off times in an IGBT device are significantly influenced by the gate resistance, a further approach is to use the gate turn-on and turn-off resistances to balance the difference between the device switching characteristics. The latter method has been adopted in the design of the prototype inverter used in the thesis.

Due to the different current sharing behaviour of IGBT in its conduction state and during switching, these will be discussed separately. As a comparison, the current sharing performance of two paralleled MOSFETs, BUK455 (60V, 20A), has also been experimentally investigated [Appendix B].

2.3.3.1 Steady state current sharing performance

The circuit layout of paralleled IGBTs is very important for a satisfactory current sharing. Since IGBTs usually have a negative temperature coefficient of saturation voltage, it is necessary to ensure they are mounted properly on a common heat sink to minimise any temperature variation between the individual devices.

The test circuit used for measuring the steady state current sharing of devices is shown in Fig 2.8. For the tests the two paralleled devices IGBTs were of the same type but arbitrarily selected from the batch supplied. The gate terminals of the two IGBTs were hard-connected, and driven from a standard gate circuit, comprising of a low impedance totem pole transistor drive and a series 10Ω resistance. A laboratory pulse generator with variable frequency and duty capability was adopted as the control source. The specification of the load inductor used in the test circuit is given in Appendix A.

The current sharing between two random selected devices was measured by observing the difference in the device current after it had settled following a switching transient. The results of the test are shown in Table 2.4. The first row of the table gives the total load current, the second row gives the maximum current difference between the two devices, and the third row is the difference expressed as a percentage of the total current. The measured current sharing waveform of the two devices in the case of a 60A total load current is shown in Fig 2.9.

Table. 2.4 Test results for steady state current sharing

Total current (A)	5	10	20	30	40	50	60	70	80	100	128
Current difference (A)	0.6	1.2	2.0	2.3	2.4	2.4	2.3	2.2	2.1	2.0	2.0
Percentage of difference	12.0	12.0	10.0	7.7	6.0	4.8	3.8	3.1	2.6	2.0	1.6

The observed steady state current difference between the two IGBTs is very small, representing only around 2% when the combined load current is close to the rated value. The unbalanced current remains approximately constant regardless of total load current. Although at low current levels an IGBT has a negative temperature coefficient like a BJT, when the current is high the IGBT tends to exhibit a positive temperature coefficient, acting similar to a MOSFET. This feature, together with the thermal feedback provided by the heatsink, support the successful paralleling operation of IGBTs in steady state.

The observed differences in current sharing transients during turn-on and turn-off however were large, even at relatively low d.c. supply voltages, illustrating that the device switching characteristics can be significantly different.

2.3.3.2 Transient current sharing performance

The main factor that influences the transient current sharing is the variation in switching times of the individual paralleled devices. The switching behaviour of an IGBT may be expressed as a function of the device parameters and the drive circuit parameters [Letor 1992],

$$\frac{di}{dt} = f(V_g, R_g, V_{th}, C_{ge}, C_{gc}, g_{fs}, L_s) \qquad (2.1)$$

where

V_g – *gate voltage*

V_{th} – *thresh hold voltage*

R_g – *gate series resistance*

C_{ge} – *gate–emitter capacitance*

C_{gc} – *gate–collector capacitance*

g_{fs} – *forward transconductance*

L_s – *emitter–ground wiring stray inductance*

For a given device, the switching behaviour of an IGBT is closely related to its gate drive. The turn-on event of an IGBT is predominantly a majority carrier phenomenon as in a MOSFET, and is thus greatly affected by the gate drive. By contrast the turning-off for the IGBT is a minority carrier phenomenon and is more dependent on the bipolar characteristics, and thus the turn-off behaviour of the IGBT is only marginally influenced by the gate drive. A high value for the gate drive voltage and low value for the series gate resistance are desirable, because they would ensure minimum turn-on losses. However, the use of a higher gate resistance is recommended to suppress the opposing freewheel diode recovery voltage transients and the unacceptable ringing during recovery at turn-on, and to restrict the high voltage overshoot at turn-off. Since the turn-off energy in an IGBT, especially in a standard IGBT, is significantly greater than the turn-on energy [International Rectifier 1994], the total switching losses in the device could be considered to be relatively insensitive to gate drive parameters, thus enabling the gate resistance to be used for transient current sharing control.

A simple scheme to improve the transient current sharing between paralleled IGBTs is to vary the gate drive series resistances for each device. Initially, this concept was tested on two paralleled IGBTs, with a single fixed value of turn-on and turn-off resistance used for one IGBT, and two polarised variable resistors used for the turn-on and turn-off drive of the second IGBT, as shown in Fig 2.10. The reason for this circuit arrangement is that the IGBT switching behaviour at turn-on and turn-off are different, and the current sharing performance must be adjusted for each case.

The current sharing performance of a randomly selected pair of IGBTs was measured with variable gate resistance drive circuit, and over a range of conducting currents and supply voltages. Fig 2.11, in comparison with Fig 2.9, shows how the transient current sharing

performance can be improved by using the proposed technique. The investigations also showed that it is difficult to achieve a good current sharing at small nominal gate resistances (Fig 2.12), and a medium value, of around 40 Ω, is preferable (Fig 2.13). Once the gate resistances are tuned, satisfactory current sharing performance is maintained over a wide range of conducting currents and supply voltages. Fig 2.14(a),(b) and (c) show the typical measured conducting currents in the two paralleled components and their difference when operated as an inverter switch. To illustrate the trimming range, the optimal values of the gate resistances of the six pairs of IGBTs used in the prototype full bridge inverter are given in Table. 2.5.

The effectiveness of this IGBT paralleling scheme under variable duties has also been investigated. The current sharing between the devices are shown in Fig 2.15 (a) and (b) when the inverter pole is controlled under variable duty PWM to produce a sinusoidal current output.

Table 2.5 Range of trimming of gate resistances for six matched pairs of IGBTs.

Inverter switch		T_1	T_2	T_3	T_4	T_5	T_6
IGBT2 gate resistance, R (Ω)		47	47	47	47	47	47
IGBT1 gate resistances	R_p (Ω)	45	44	41	47	35	55
	R_n (Ω)	41	44	51	45	52	47

It is believed that this current sharing technique can also be used for the case where more than two IGBTs are to be paralleled (Fig 2.16). Here, the strategy would be to use the IGBT with fixed gate resistance as a reference and to tune the turn-on and turn-off resistances of the other IGBTs so that their switching behaviour follows that of the base IGBT.

2.3.4 Improvement in inverter efficiency by device paralleling

The energy dissipation within a power semiconductor device is usually classified in terms of conduction losses and switching losses, which are expressed in general terms as,

$$P_{cond} = V_{ce} I \tag{2.2}$$

$$P_{sw} = \int v(t)\, i(t)\, dt \tag{2.3}$$

where V_{ce} is the conduction voltage drop, I the conducting current, v(t) the transient switching voltage, i(t) the transient switching current.

In its saturated on state, the conduction voltage drop of an IGBT will increase with the conduction current. For example, for IXSH40N60 IGBT investigated, the variation of voltage drop with the conducting current can be approximated by a linear relationship at a gate voltage of 12V,

$$V_{ce} = 0.0528 * I + 0.895 \tag{2.4}$$

It should be noted that, the constant "junction" element of the saturation voltage represents only around 20% of the saturation voltage at rated current.

The turn-off time of an IGBT also increases with the forward current. The relationship can again be obtained from the data sheet at a 12V, 47Ω gate drive,

$$t_{off} = 3.692 * I + 244.6 \ \ ns \tag{2.5}$$

Equations (2.4) and (2.5) imply that conduction loss and the switching loss of an IGBT will increase with the square of load current. The parallel operation of two matched devices will effectively halve the conducting current in each device, and thus halve the current dependent element of conduction voltage drop. The potential of conduction loss reduction is indicated in Fig 2.17. A similar argument can be applied to the turn-off switching losses.

Further improvement of inverter efficiency could be achievable by paralleling more devices. However, this will be penalised by the increased weight and cost. Thus, in practice, the number of devices used will be dictated by silicon costs, cooling requirements and desired system efficiency. The recent development in high-rating packaged modules, in which several

silicon devices are paralleled, may eliminate the need of using discrete paralleled components for high power applications. Nevertheless, the paralleling technique described in the thesis is useful in cases where, due to unavailability of packaged modules or for reasons of cost, it is prefered to parallel discrete components.

2.4 Measurement methods employed in the experimental tests

A capability of high accuracy is an important feature of experimental measurement. Since the principal purpose of the experimental drive was to develop accurate models of the system efficiency, in most cases the measurements were taken in the steady state after the system had fully settled. The section discusses the various measurement techniques employed on the test rig.

2.4.1 Measurement of currents and voltages

Moving iron and moving coil analogue Ampere and Volt meters can be used to accurately measure current and voltage, provided that the waveforms are not distorted and within the instrument frequency range. However, in an inverter drive system, waveforms which contain high level of harmonic distortions are common, and hence wide bandwidth digital meters need to be employed. A 100kHz high bandwidth power analyser (Voltech PM3000A) was also used to measure current and voltage. This instrument not only gives higher accuracy, but also is capable of computing both RMS and fundamental values. High bandwidth digital oscilloscopes were used to measure current and voltage waveforms. The detailed specifications of these instruments are given in Appendix A.

2.4.2 Measurement of harmonics

The harmonic content of a signal can be evaluated by its spectrum distribution or its total harmonic distortion. The measurement of harmonics was usually achieved by employing a dynamic signal analyser (HP 35660A). However, a good performance from the transducers used to obtain the signals for the analyser is critical if accuracy is to be obtained. In the case of current measurements a 60MHz hall effect current probe (Tektronix TM502A) was used to

obtain the current signal. Standard matched oscilloscope probes were used directly for harmonic measurements of grounded low voltage signals. Initially, a differential voltage probe was used to isolate the high voltage signals and to scale it into a low level signal. However, early experiments showed that the available device introduced unacceptable distortion onto the signal measured. An alternative was to convert the voltage into a current, and then use the current probe to perform the measurement. The technique applied to the measurement of the output voltage from the inverter is shown in Fig 2.18, and employed three balanced thick film non-inductive resistors of sufficiently high values so as not to affect the operation of the machine and the overall system loss measurement. The spectrum distributions of the signals measured were obtained directly from the analyser. The voltage based total harmonic distortion (THD), which is a very useful term in modulation processes, was then indirectly calculated from acquired spectrum data,

$$THD = \sqrt{\sum_{n=2}^{\infty} \left(\frac{V_n}{n\,V_1}\right)^2} \qquad (2.6)$$

2.4.3 Measurement of speed

There are a variety of methods which can be used to measure the speed of a rotating shaft. Commercially available optical encoders offer high accuracy but are costly, whereas standard analogue tachogenerators normally have an error of 1 - 2 %. A simple but accurate speed measurement method was adopted (Fig 2.19) for the test rig, in which a disc having 36 equally spaced holes was constructed and attached to the machine shaft. An optical sensor was mounted so that the disc passed between the transmitting and the receiving diodes and the generated pulse train from the optical sensor was fed to the signal analyser. The frequency f_1 of the dominant fundamental harmonic was then measured and used to determine the machine speed using,

$$n = \frac{60}{36} f_1 \qquad (2.7)$$

By setting a very narrow frequency span of the analyser, a high measurement accuracy was possible. For example, with the analyser frequency span set at 25Hz, the speed measurement error was within 0.2rpm. The influence of speed fluctuation on the measurement can be eliminated by using the "average" function available on the analyser.

2.4.4 Measurement of torque

Torque reaction can be translated into force and measured using strain gauges arranged within a load cell. A commercial load cell was used in the experiments (Maywood D2000). Its specification, together with the specification of its strain gauge amplifier is also given in Appendix A. The method of installation of the load cell is very important to the torque measurement. A standard way is to use a swinging frame dynamometer, where the d.c. machine is mounted on gimbals with an arm extending perpendicular to the shaft to act on a load cell. To ensure that the mounting surface is stiff enough and the load is applied centrally to the cell, a piece of hard steel plate was mounted on top of the cell and a convex load ball was used. The torque measurement scheme is shown in Fig 2.20. The load cell when calibrated had a linear measuring range of 0 - 17Nm. The accuracy of measurement is estimated to be 0.1Nm.

Torque fluctuations were observed in the load cell measurement, the largest being caused by eccentricity of the load machine, which varied at about twice the machine rotational frequency. A low pass filter was employed to insulate the fluctuations from the torque measurements in steady state, as shown in Fig. 2.20.

2.4.5 Assessment of torque ripple

Due to the inertia of dynamometer and the limited bandwidth of the instrument, the load cell method is only suitable for steady state and low frequency torque measurement. Advanced in-line torque transducers could be used to measure the torque dynamic response and to detect the torque ripple [Schofield 1993a], however, the instalment of these devices are critical and highly sensitive to mechanical resonances. As a result meaningful measurements of torque

ripple from in-line transducers are difficult to achieve. An indirect method was used in thesis for guaging torque ripple levels, by inferring it from the level of ripple in the inverter d.c. link current. The principle of the method is described below.

2.4.5.1 Current harmonics on the inverter d.c. link

In the ideal operation of a three phase inverter at a fixed supply voltage, the output currents are purely sinusoidal with no ripple and are balanced across the three phases. Similarly the inverter d.c. link current will be a smooth d.c. component. However, in practice, the switching operation will cause harmonics in the output voltages and currents. Since the inverter itself has no energy storage elements (the filter capacitor is here assumed to be external to the inverter), the instantaneous power input must equal the instantaneous power output. Thus, the inverter d.c. link current can be determined from,

$$I_d = \frac{1}{V_d} [\, v_a(t)\, i_a(t) + v_b(t)\, i_b(t) + v_c(t)\, i_c(t) \,] \tag{2.8}$$

where v_a , v_b , v_c , i_a , i_b , and i_c are the phase voltages and currents, and V_d and I_d is the d.c. link voltage and current.

Considering the fundamental and odd harmonic components of phase voltages and currents, e.g. for phase "a",

$$v_a(t) = V_1 \sin(\omega t) + \sum_{k=1}^{\infty} V_{6k\pm1} \sin (6k\pm1)(\, \omega t + A_{6k\pm1}) \tag{2.9}$$

$$i_a(t) = I_1 \sin(\omega t - \varphi) + \sum_{k=1}^{\infty} I_{6k\pm1} \sin (6k\pm1)(\, \omega t + \varphi_{6k\pm1}) \tag{2.10}$$

the major components of the product $v_a(t)\, i_a(t)$ are,

$$v_a(t)\, i_{a(6)} = V_1 \sin\omega t \;\; I_1 \sin(\omega t - \varphi) +$$

$$V_1 \sin\omega t \cdot \sum_{k=1}^{\infty} I_{6k\pm1} \sin(6k\pm1)(\omega t + \varphi_{6k\pm1}) + I_1 \sin(\omega t - \varphi) \cdot \sum_{k=1}^{\infty} V_{6k\pm1} \sin(6k\pm1)(\omega t + A_{6k\pm1}) \tag{2.11}$$

Accordingly,

$$I_d \approx \frac{3}{2} V_1 I_1 \cos\varphi +$$

$$\frac{3}{2} V_1 \sum_{k=1}^{\infty} (I_{6k+1} - I_{6k-1}) \cos(6k\omega t + \alpha_{6k}) + \frac{3}{2} I_1 \sum_{k=1}^{\infty} (V_{6k+1} - V_{6k-1}) \cos(6k\omega t + \beta_{6k}) \tag{2.12}$$

Since

$$V_{6k+1} - V_{6k-1} = ((6k+1)\, I_{6k+1} - (6k-1)\, I_{6k-1})\, x = cx\, (I_{6k+1} - I_{6k-1}) \tag{2.13}$$

where

$$c = (6k-1) \rightarrow (6k+1) \tag{2.14}$$

$$I_d \approx \frac{3}{2} V_1 I_1 \cos\varphi + c_1 V_1 \sum_{k=1}^{\infty} (I_{6k+1} - I_{6k-1}) \cos(6k\omega t + \gamma_{6k}) \tag{2.15}$$

Thus, the d.c. link current is composed of a constant and harmonics at multiples of six times the fundamental frequency.

2.4.5.2 Machine torque ripple due to source current harmonics

The total instantaneous torque is the sum of the torque produced by phases a, b and c,

$$T_{em}(t) = \frac{1}{\omega_m} [\, e_a(t)\, i_a(t) + e_b(t)\, i_b(t) + e_c(t)\, i_c(t) \,] \tag{2.16}$$

The calculation of the torque fluctuations can be done by considering the fundamental flux and the harmonic currents [Robertson 1971]. Therefore, assuming the speed is constant,

$$T_{em} \approx T_{em0} + c_2 E_1 \sum_{k=1}^{\infty} (I_{6k+1} - I_{6k-1}) \cos(6k\omega t + \psi_{6k}) \qquad (2.17)$$

Torque therefore consists of a constant component and sextant harmonics. Comparison of Eqns (2.15) and (2.17) indicates that the torque ripple components can be evaluated by the harmonic content in the d.c. link current. However, it must be noted that this direct comparison is based on the assumption that all input current frequency components produce corresponding torque ripple and there is no high frequency change in stored energy in the system. This assumption may be applicable to the system where relatively low switching frequencies are used. When the switching frequency is high, the method of using the d.c. link current to indicate torque ripple magnitude will be less accurate.

2.4.6 Measurements of power

Direct power measurements were used to determine the machine input and output power, the inverter input power and the power losses in the inverter and machine.

2.4.6.1 Measurement of machine output power

The machine output power was calculated from the measurements of machine speed and torque,

$$P_{out} = \omega_m T_{em} \qquad (2.18)$$

The torque ripple and speed fluctuation due to the PWM inverter drive do not contribute to the machine output power. In addition, the torque ripple induced speed fluctuation is small because of the large inertia of the load dynamometer.

2.4.6.2 Measurement of inverter input power and machine input power

The inverter d.c. input will contain an element of current ripple due to the inverter switching action. The machine input waveforms are even more complex, consisting of a mixture of high frequency components due to the switching and low frequency harmonics of the fundamental.

Traditional methods of measuring voltage and current using analogue meters, or measuring power directly using moving coil Wattmeters, are not suitable. An appropriate way is to use a high bandwidth digital power analyser, such as Voltech PM3000, which samples the currents and voltages at a high rate and then processes them to obtain a real time measurement. The arrangement of independent channels and isolations in the analyser allow the measurements of inverter input power and machine input power simultaneously. Besides the measurement of the total values of voltage, current and power, the fundamental values that contribute to work in the machine can also be isolated. The scheme for these measurements is shown in Fig 2.21.

In Fig 2.21, two channels of the power analyser CH1 and CH2 were connected to two phases of the machine input in the standard two wattemeter configuration, and the third channel, CH3, was connected to the inverter d.c. link to measure the inverter input power. To ensure reliable measurements, output current waveform was used as a trigger source for CH1 and CH2, and voltage was selected as the trigger source of CH3. The power analyser can be programmed working in various modes, however, the "PWM drive" mode was found to be very useful in this case.

2.4.7 Measurement of power loss

There are commonly two loss measurement techniques: input/output measurement, and calorimeter based measurement [Boholo 1997].

2.4.7.1 Input/output loss measurement

The system loss is deduced by subtracting the output power measurement from the input power measurement. In a typical inverter fed machine drive, the input is the d.c. link power, whereas the output power is obtained from the speed and torque sensors mounted on the dynamometer. Thus, the resulted total loss is composed of inverter loss, machine loss and the driving machine windage and friction loss. The accuracy is largely dependent on how good the input and output power measurement instruments are. The Voltech power analyser has a voltage and current measurement accuracy of 0.05%, and for a d.c. link of 340V and 12A, the

system input power measurement has an error of about 4W. The system output power measurement from the 3kW machine speed measurement ($1500 \pm 0.2\ rpm$) and torque measurement ($20 \pm 0.1\ Nm$) has an error of about 16W. Thus, the input/output loss measurement gives an accuracy of 2% in the system loss of 1000W. A measurement error of below 4% has also been evaluated in the experimental system.

2.4.7.2 Measurement using a balance calorimeter

Since all the power losses within a machine or an inverter appear as generated heat, the most accurate way to determine loss is to directly measure the heat output from the power loss source. In the calorimeter method the system to be measured (e.g. inverter and machine), accompanied by a heater, is installed within an insulated enclosure, that has an inlet and an outlet ports for heat exchange. Air is input to the calorimeter enclosure at a constant inlet temperature and flow rate, and the temperature rise of air at the outlet is used to evaluate the power loss. This evaluation is performed over two operations. Initially, the machine is loaded and operated at the required load until the temperature rise in the air flowing through the calorimeter is constant. The unexcited machine is subsequently rotated by some external means at arranged fix speed and the test conditions are replicated by applying an electrical input to a heater mounted inside, to give a temperature rise in the air flow which is the same as that measured during the first test. The second operation is normally referred to as a balance test, and the input power to the heater is the required measurement, which is equal to the inverter and machine loss, but excludes machine friction and windage loss.

A calorimeter measurement facility was available at the University of Sheffield which was designed for measuring loss in induction machines up to 30kW rating [Boholo 1997]. This computer controlled facility was highly accurate, being capable of distinguishing 5W within 1000W of loss.

2.4.7.3 Assessment of loss measurement methods

A 4-pole 4kW induction machine was set-up in the calorimeter, and the machine was fed from the inverter described earlier and loaded by a d.c. dynamometer. The inverter was controlled by a digital PWM modulator, as will be described later, allowing adjustment of the machine supply voltage and frequency. Fig 2.22 shows a photograph of the test.

During the test the electrical machine was operated at rated flux, rated load and rated speed slip, but with reduced supply voltage and speed. The working condition of the machine and the calorimeter are summarised in Table 2.6.

Table 2.6 Working conditions for the calorimeter based drive system loss measurement

IM, 4kW, 4-pole, 240V, 50Hz, 1420rpm				Calorimeter	
Frequency	Voltage	Torque	Speed	Air flow rate	Inlet temp.
34 Hz	168 V (70%)	26.9 Nm (100%)	940 rpm	3.2 m/s	25 ^oC

During the test, the calorimeter inlet and outlet temperatures were continuously recorded, together with the inverter input and the machine output power measurements from the power analyser using a computer. When the system reached a thermal equilibrium, the final values were also recorded. In the balance test, the machine was driven to the same speed by the d.c. dynamometer and the power supplied to the heater was adjusted to give the same temperature rise in the outlet. Again after the thermal equilibrium was achieved the power supplied to the heater was recorded.

Two sets of calorimetric measurements have been carried out, with the inverter being controlled using two different modulation techniques. Firstly, the system was controlled by the sub-optimal PWM modulation. Fig 2.23(a)-(c) show the variations of inlet temperatures during the first and balance tests, the variations of outlet temperatures for the same tests, and the input and output powers of the system during the first test, respectively. To illustrate the

variation with time of the loss measurement derived from the input and output powers, the loss difference between the input and output powers is plotted with a supressed average during a period of 4 hours, as shown in the inset of Fig. 2.23(c). This indicates a variation of $\pm 20\ W$ which is within ± 2 % of the averaged value. It should be noted that the data logged by the computer from the power analyser given in the figure was only to three significant figures. However, in all tests, once the operation condition had settled the data was recorded to the nearest 0.1W directly from the instrument display using its internal averaging function. Therefore, the accuracy of final measurement would be equal to that of the instrument which is specified as 0.1% of the product of the maximum voltage and current scales. For example, for the test results in Table 2.7 a voltage scale of 500V and a current scale of 20A would be used, and this would give an accuracy of input power measurement within 10W. Similarly, the accuracy of output power measurement was found within 20W. The measured data at thermal equilibrium are given in Table 2.7.

Table 2.7 Calorimeter measurement results with sub-optimal PWM control

	First test				Balance test		
	Inlet temp.	Outlet temp.	Input power	Output power	Inlet temp.	Outlet temp.	Input power
	24.9 ^oC	37.0 ^oC	3667W	2640W	24.9 ^oC	37.0 ^oC	1065W
	Time: 7.5 : 8.5				Time: 14.8 : 15.8		
Loss	1027W				1065W		

It is observed from Fig. 2.23 that the working conditions in the machine test and balance test were stable at the end of the tests, as required. The power loss measurement based on the calorimeter was 1065W, and that using input/output method was 1027W. The measurement difference between these two methods is about 3.5% of total system loss measured by calorimeter.

A second set of measurements were taken with the system controlled using a different form of PWM, i.e., the adjustable PWM modulation. Again, the calorimeter achieved equilibrium, as shown by Fig 2.24 (a), (b) and (c). The system loss measured using the calorimeter method was now 1020W, whilst that based on input/output method was 1002W. The variation with time of the loss measurement from input/output method was within ± 2 % of the total loss, as shown in the inset of Fig. 2.24(c).

Whilst the two methods of loss measurement give slightly different results, they both indicate that the second modulation method would give a slight improvement in system loss, 45W from the calorimeter method and 25W using the input/output technique.

The repeatability of the test method is demonstrated by Fig. 2.25, which shows another set of loss measurement results for the same test system as Fig. 2.24 again driven by the adjustable PWM. Table 2.8 gives a summary of the measurement results for the first experiment in Fig.2.24 and the repeated experiment in Fig.2.25. The system loss measured using the calorimeter method was 995W, whilst that with the input/output method was 970W. Again, the loss difference between the two methods is below 4% of the total loss. The total loss measured in this test is 25W lower than in Fig. 2.24, however, it is within the expected level of total error.

Table 2.8 Calorimeter measurement results with adjustable PWM control

		First test				Balance test		
		Inlet temp.	Outlet temp.	Input power	Output power	Inlet temp.	Outlet temp.	Input power
Experiment (Fig 2.24)		24.9 ^oC	36.6 ^oC	3646W	2644W	24.9 ^oC	36.5 ^oC	1020W
Repeated experiment (Fig 2.25)		24.9 ^oC	36.4 ^oC	3622W	2652W	24.9 ^oC	36.4 ^oC	995W
Loss	Fig 2.24	1002W				1020W		
	Fig 2.25	970W				995W		

The flow rate in the calorimeter was maintained constant during all of the above tests, as shown in Fig 2.26.

2.4.7.4 Loss measurement method used in the thesis

Calorimeter based loss measurement method would be expected to be very accurate and is able to measure the true loss in a machine and its drive. However, it is a very time-consuming measurement, a single test being typically 8-12 hours. On the other hand, input/output measurement method is simple, time-efficient, and especially suitable to the case where a large number of measurements need to be taken. The case here of measuring the combined loss of the experimental converter and electrical machine the input/output method would appear have sufficient accuracy.

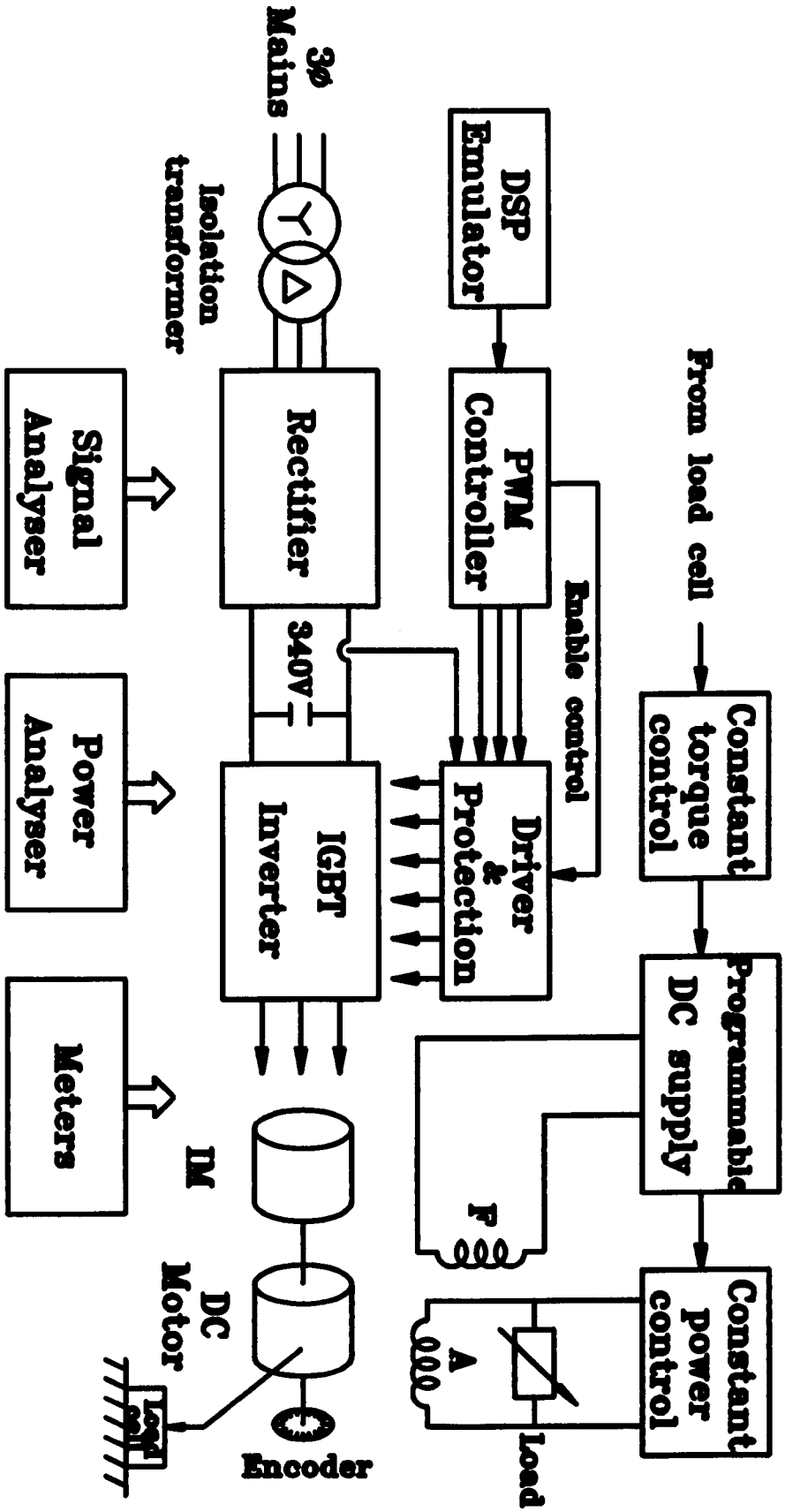

Fig 2.1(a) Schematic of laboratory PWM inverter IM drive system.

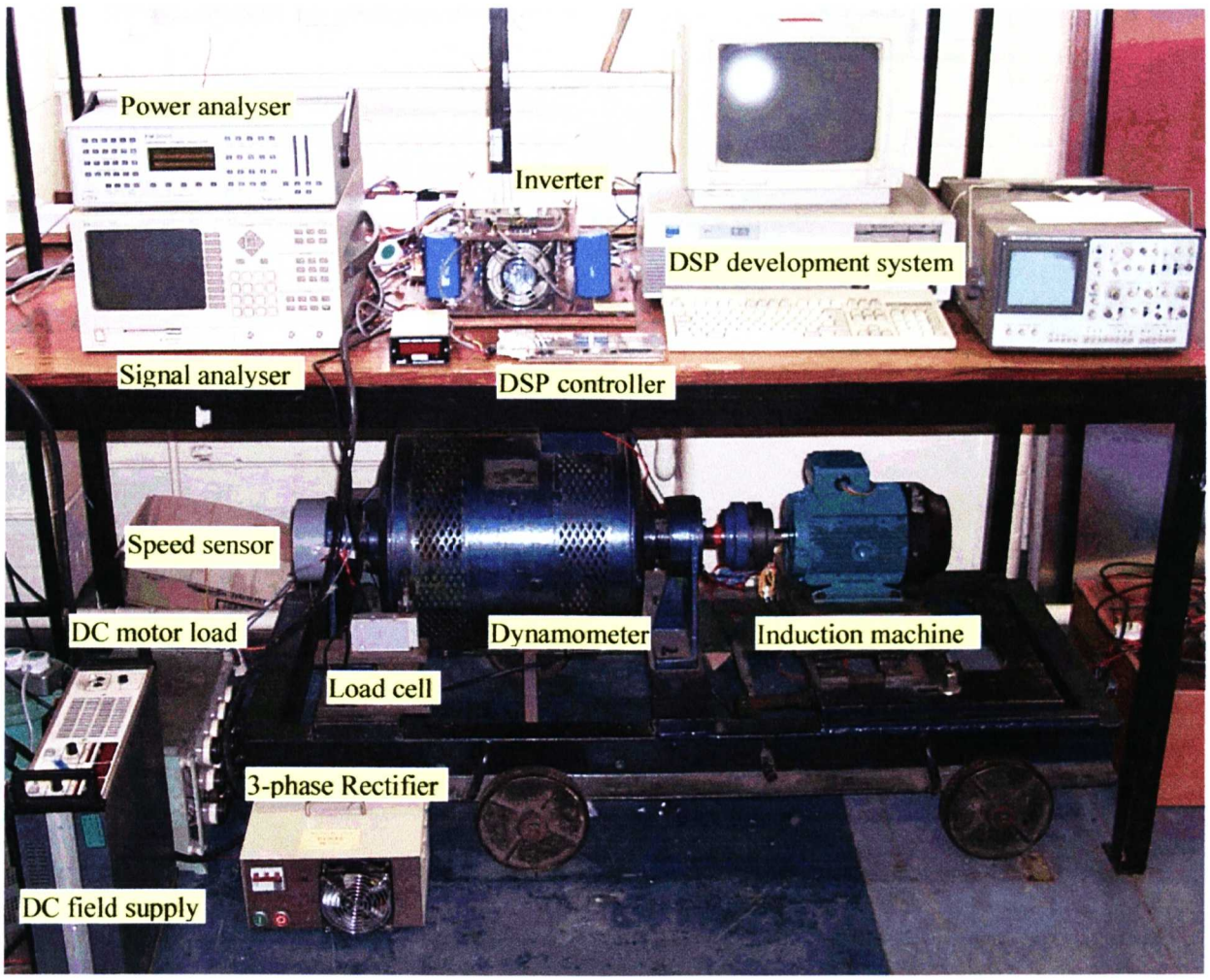

Fig. 2.1 (b). Photograph of the test system.

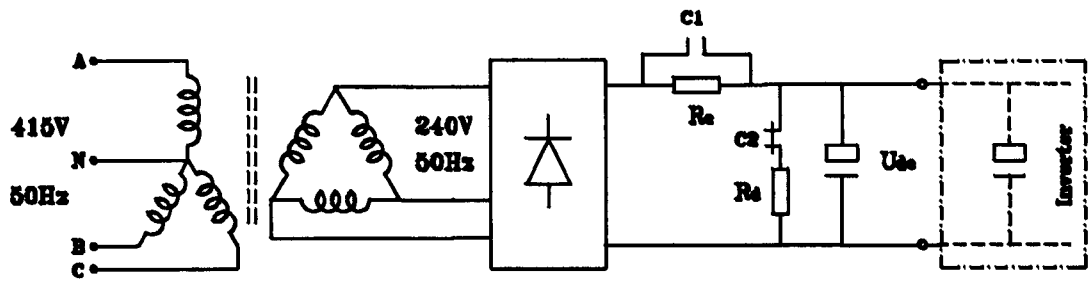

Fig. 2.2 d.c. link power supply.

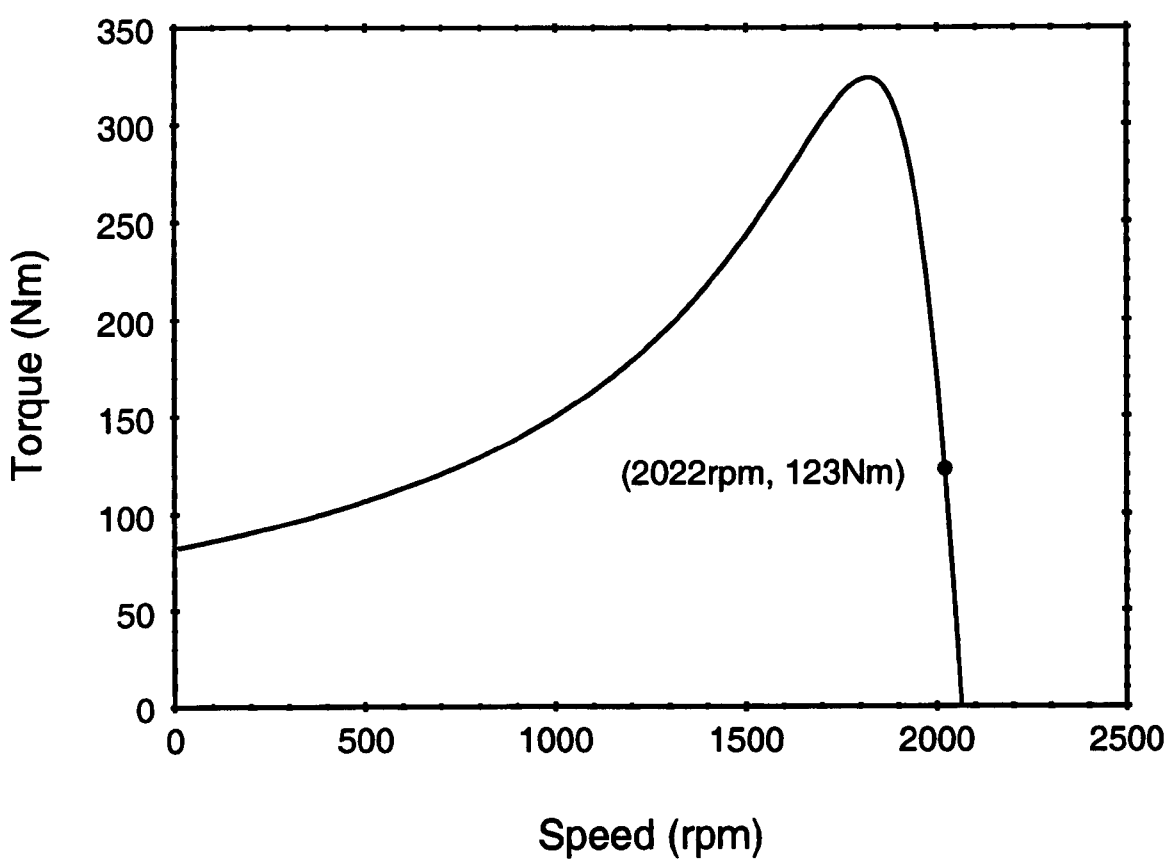

Fig. 2.3 Torque-speed characteristic of the 26kW induction machine at the rated condition.

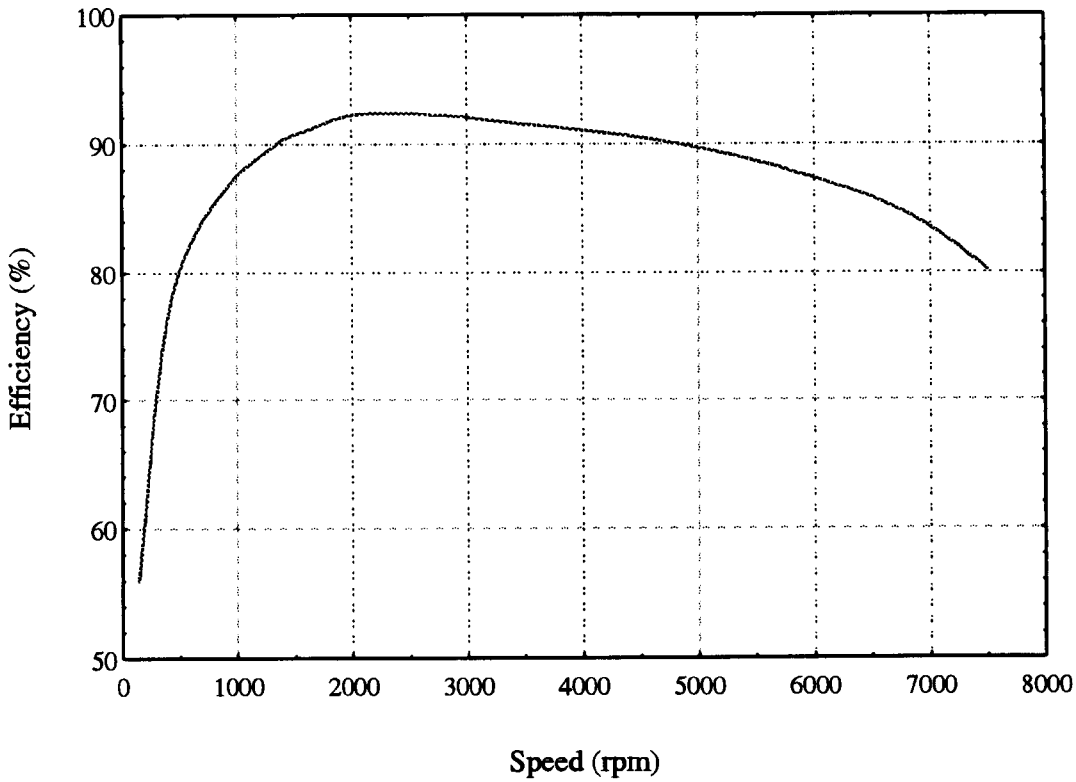

Fig. 2.4 Efficiency characteristic of the 26kW induction machine.

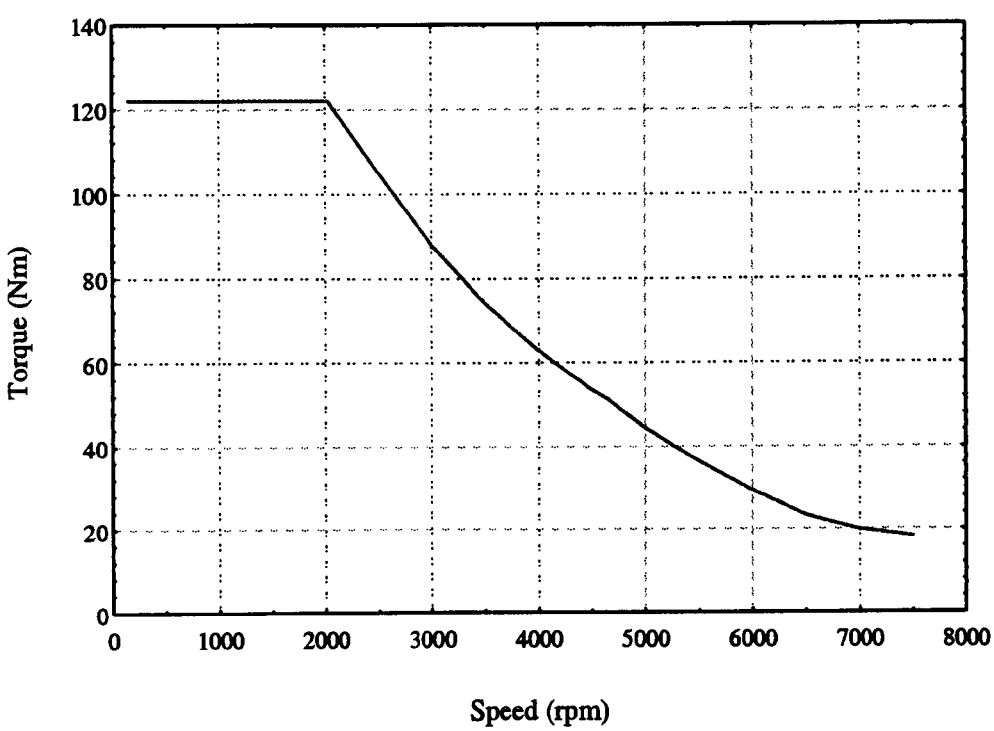

Fig. 2.5 Torque-speed envolope of the 26kW induction machine.

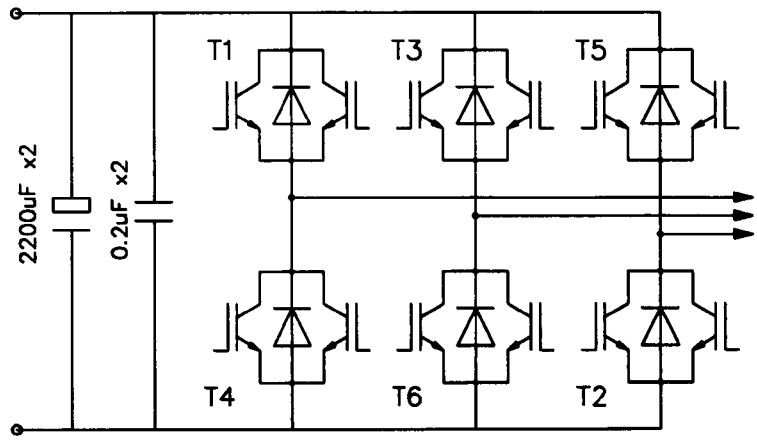

(a)

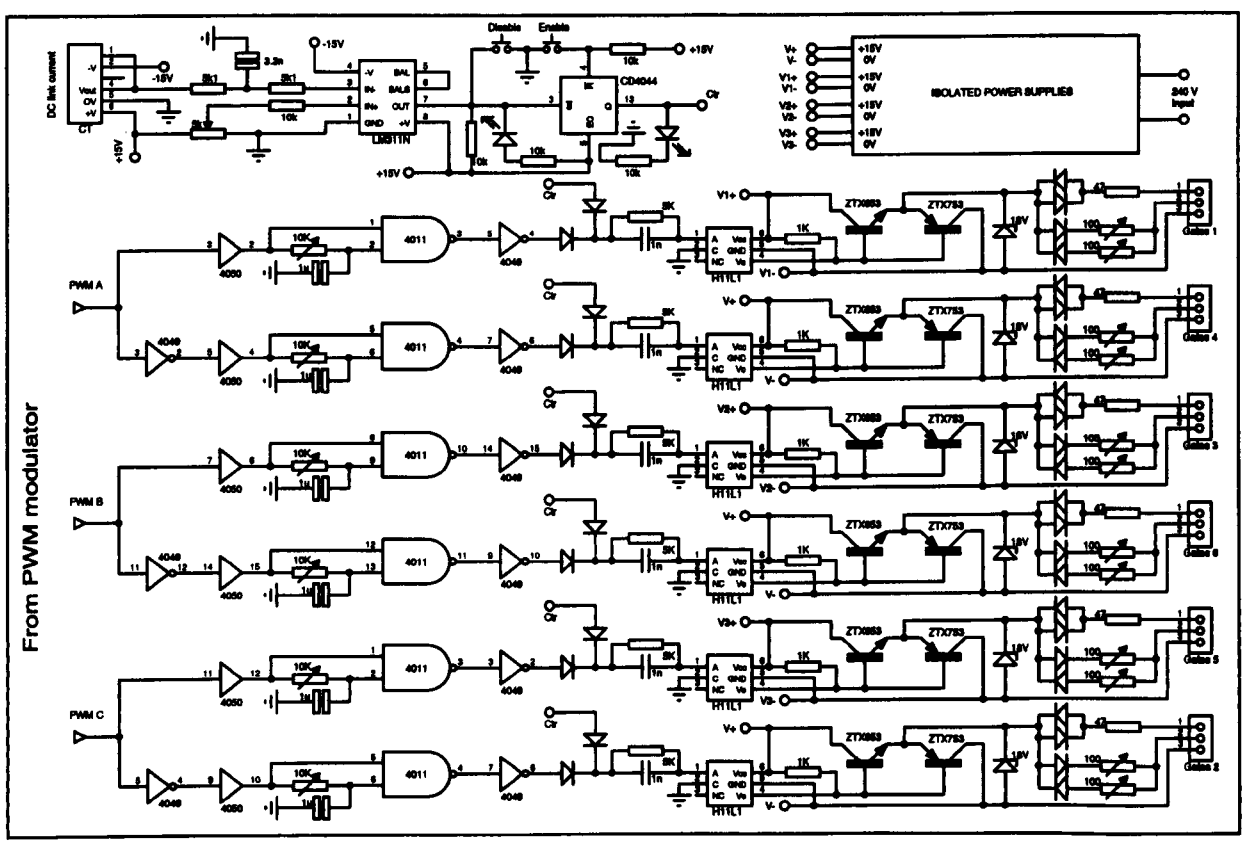

(b)

Fig. 2.6 Schematic diagram of the inverter. (a) inverter main circuit, (b) inverter gate drive circuit.

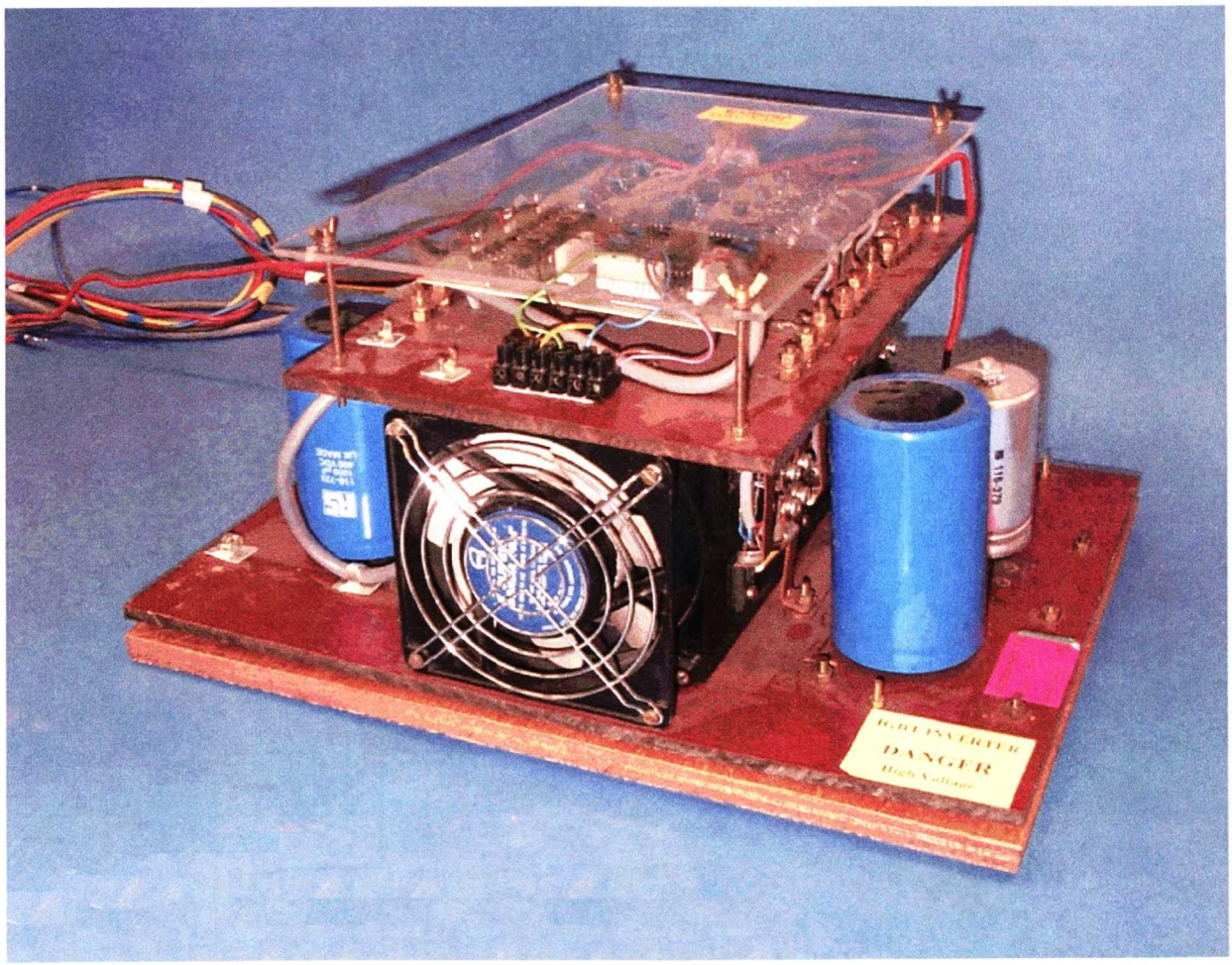

Fig. 2.7 Photograph of the developed three phase IGBT inverter.

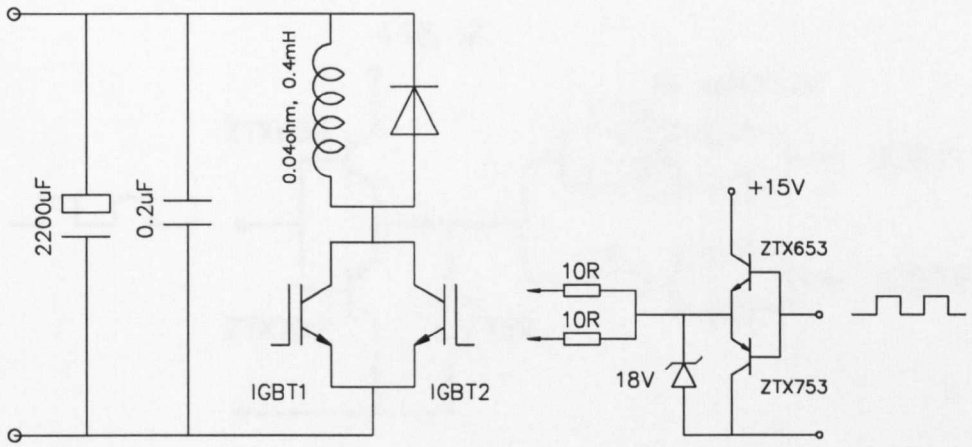

Fig. 2.8 Circuit for IGBT steady state current sharing test.

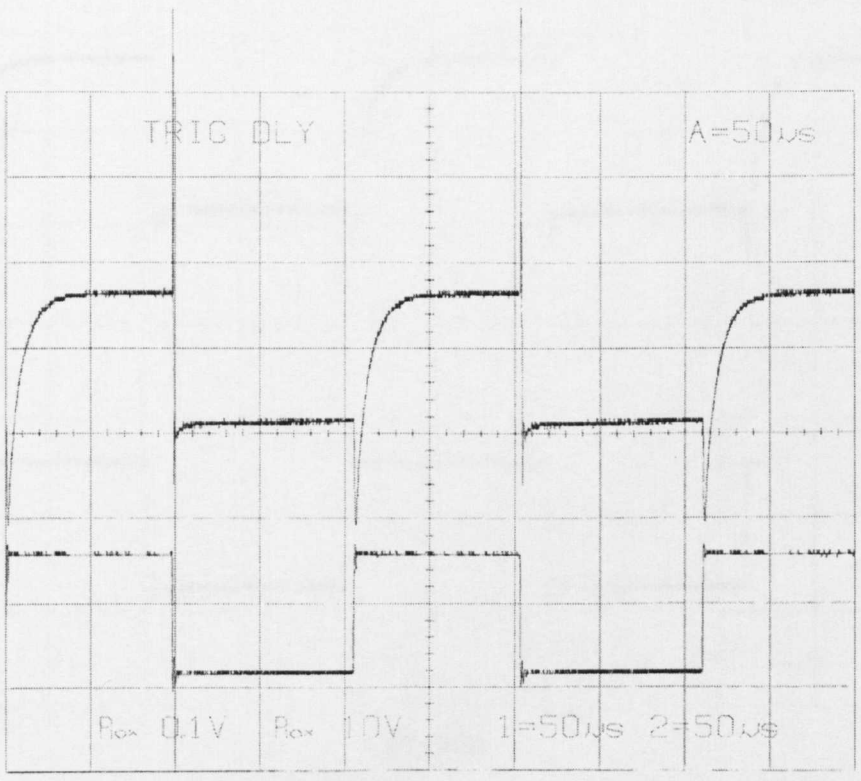

2A/div

10V/div

50µs/div

Fig. 2.9 Steady state current sharing waveform when the total current is 60A.

Top: current difference (2A/div), bottom: gate signal (10V/div).

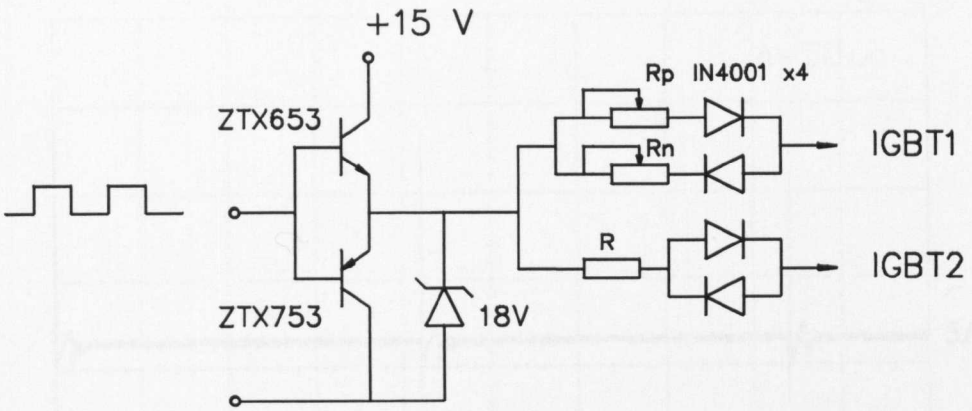

Fig. 2.10 Circuit for IGBT transient current sharing test.

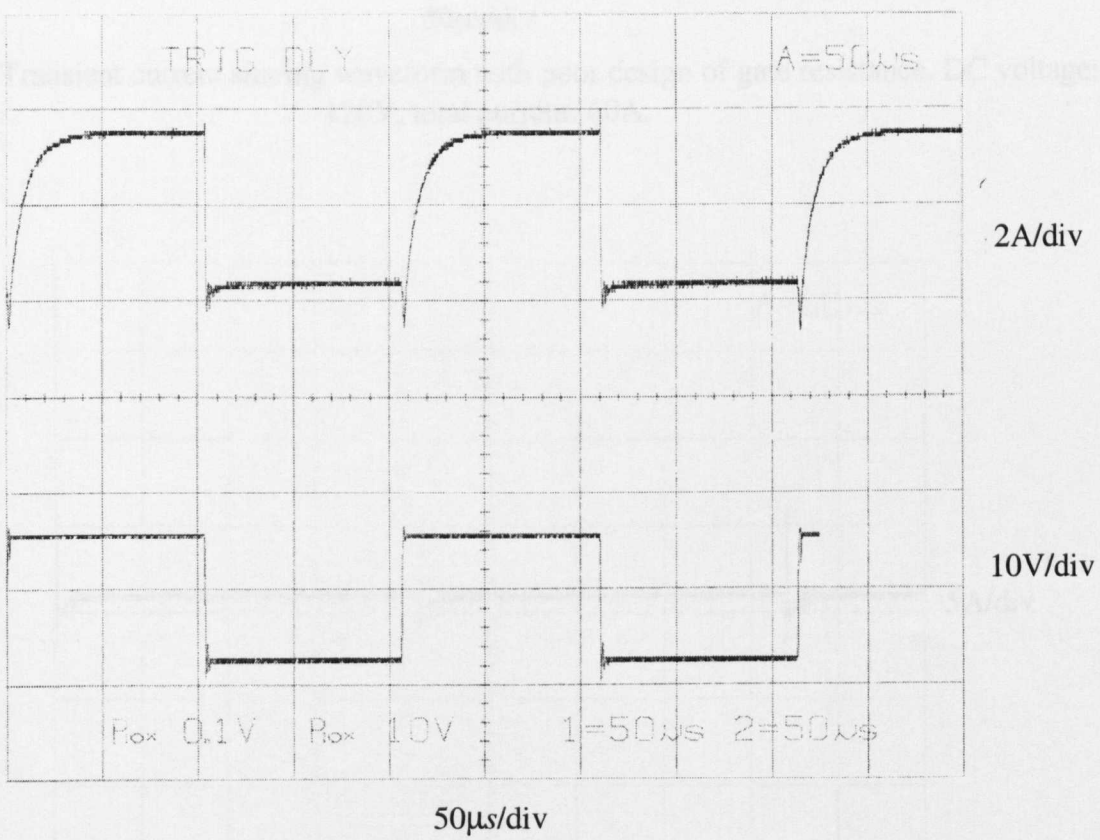

Fig. 2.11 Transient current sharing waveform when the total current is 60A.

Top: current difference (2A/div), bottom: gate signal (10V/div).

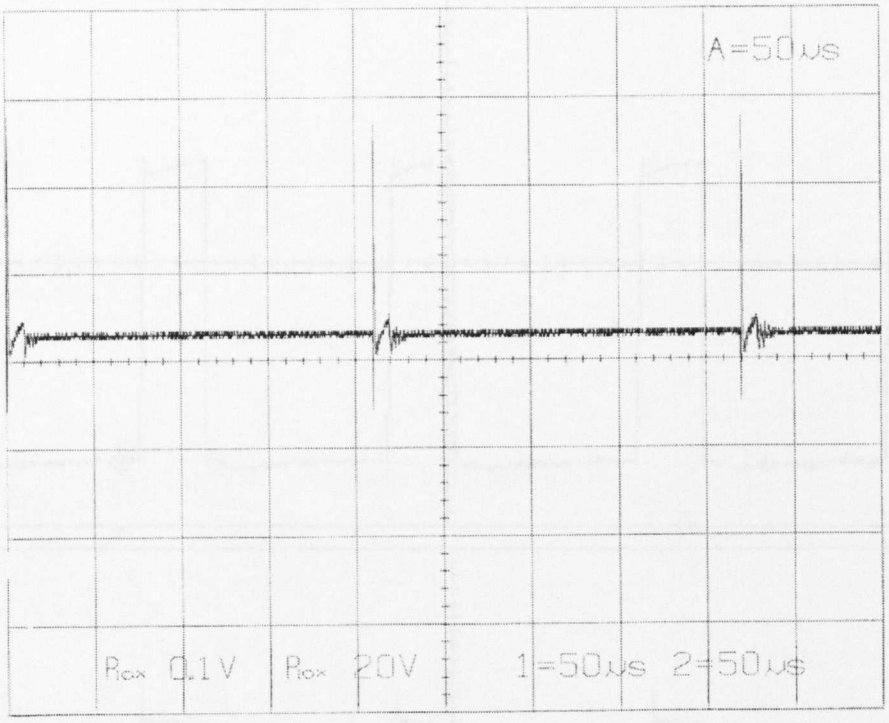

5A/div

50μs/div

Fig. 2.12 Transient current sharing waveform with poor design of gate resistance. DC voltage: 120V, total current: 60A.

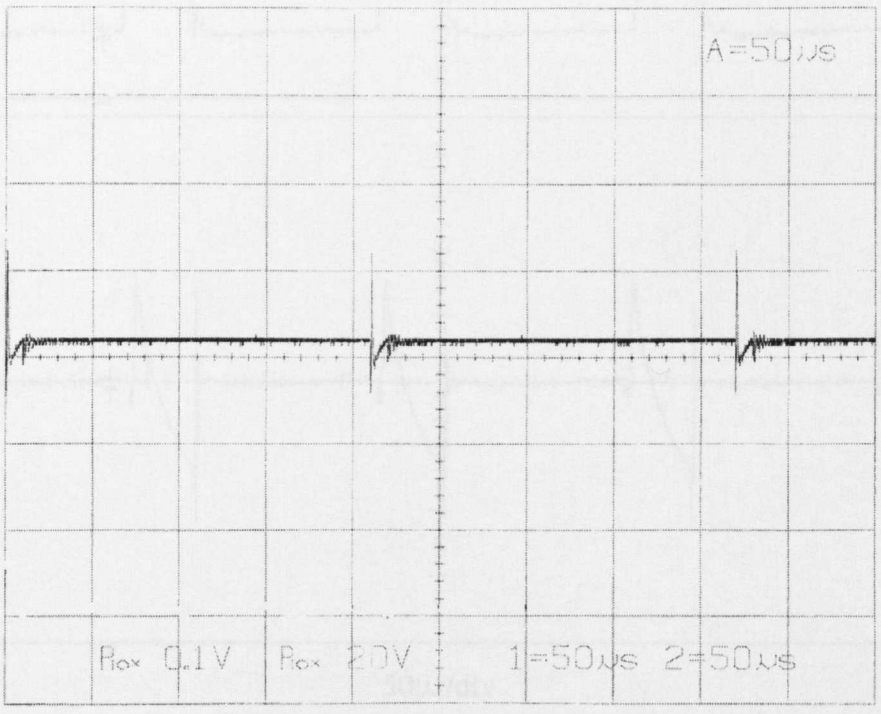

5A/div

50μs/div

Fig. 2.13 Transient current sharing waveform with good design of gate resistance. DC voltage: 120V, total current: 60A.

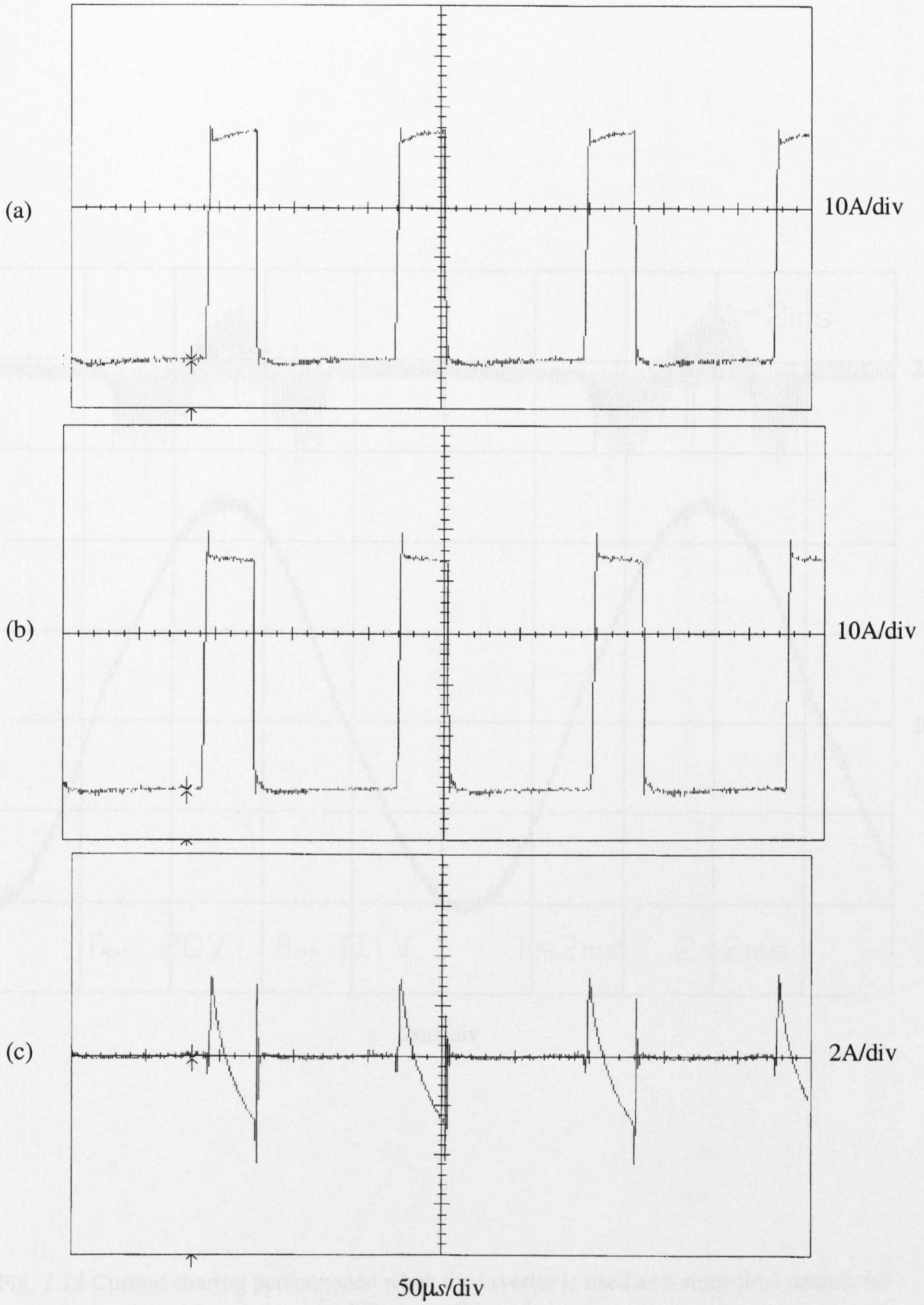

Fig. 2.14 Current sharing performance when the inverter conducting current is DC. (a) conducting current in one device (10A/div), (b) conducting current in another device (10A/div), and (c) current difference (2A/div).

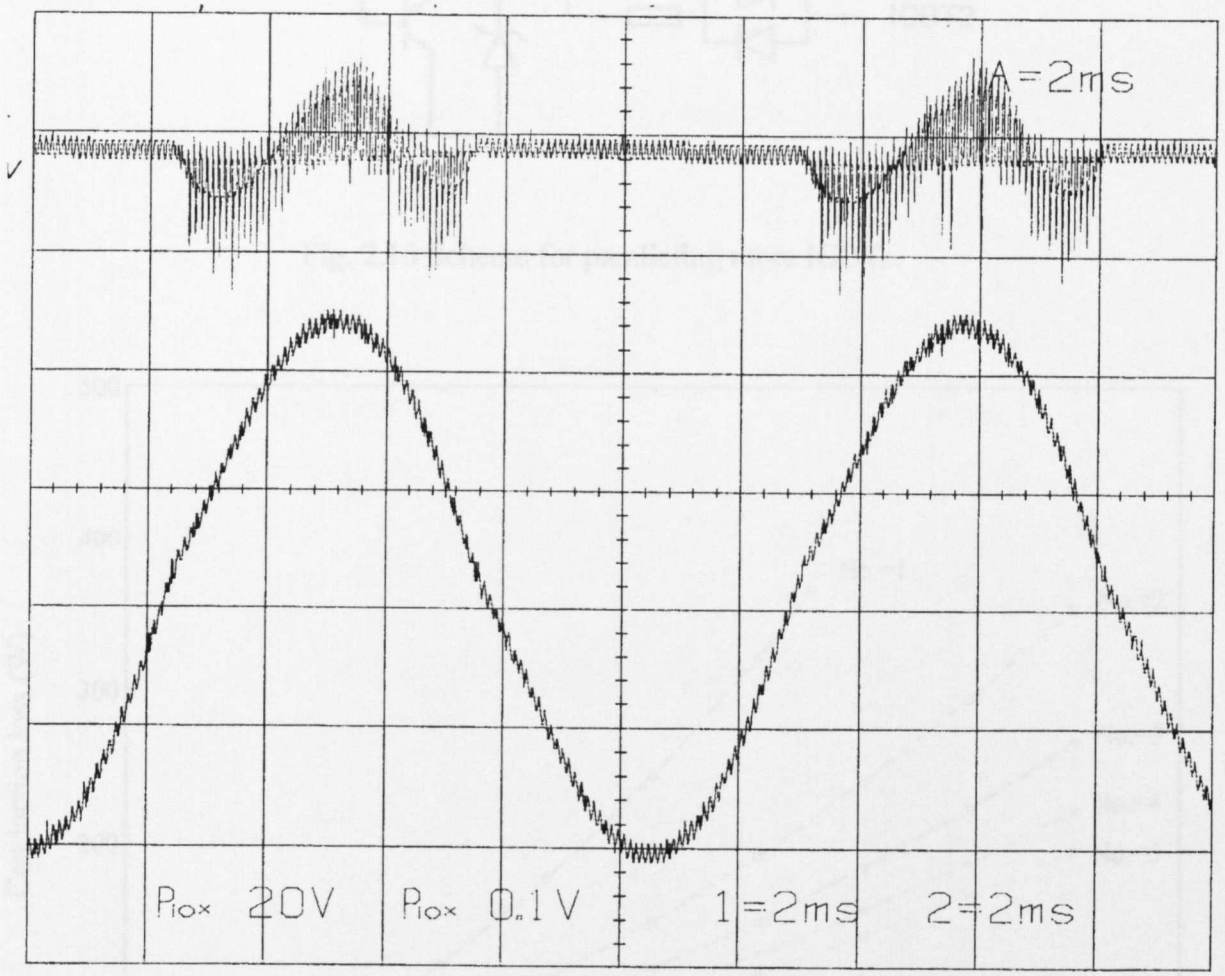

Fig. 2.15 Current sharing performance when the inverter is used as a sinusoidal source. (a) current difference, (b) total current.

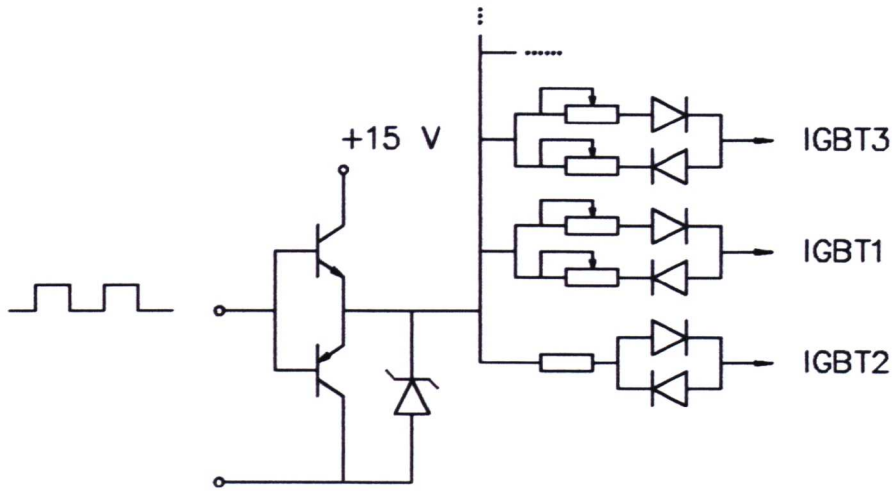

Fig. 2.16 Scheme for paralleling more IGBTs.

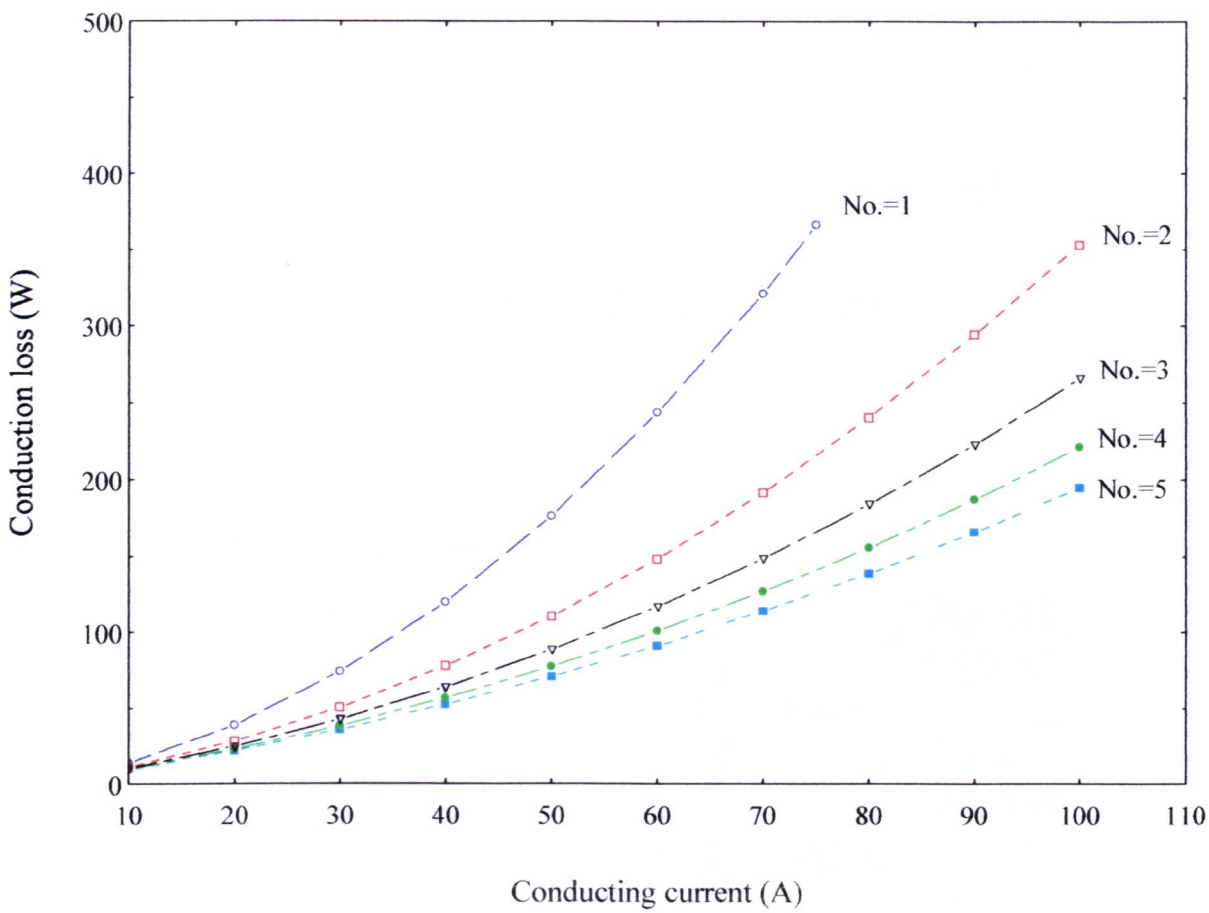

Fig. 2.17 Conduction loss reduction using power component paralleling technique.

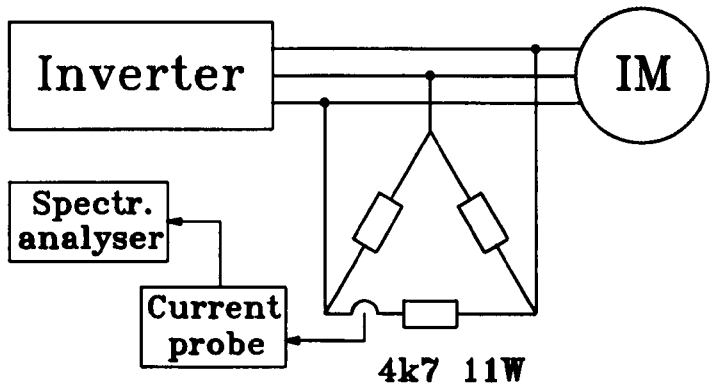

Fig. 2.18 Output line voltage measurement scheme.

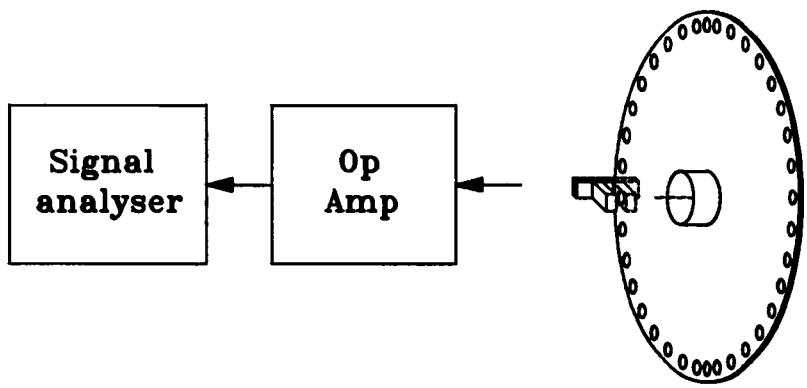

Fig. 2.19 Machine rotating speed measurement.

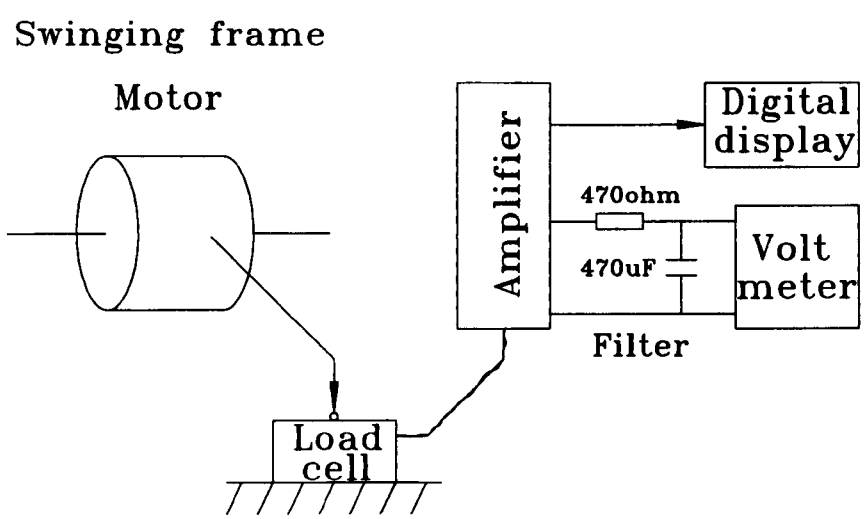

Fig. 2.20 Torque measurement scheme.

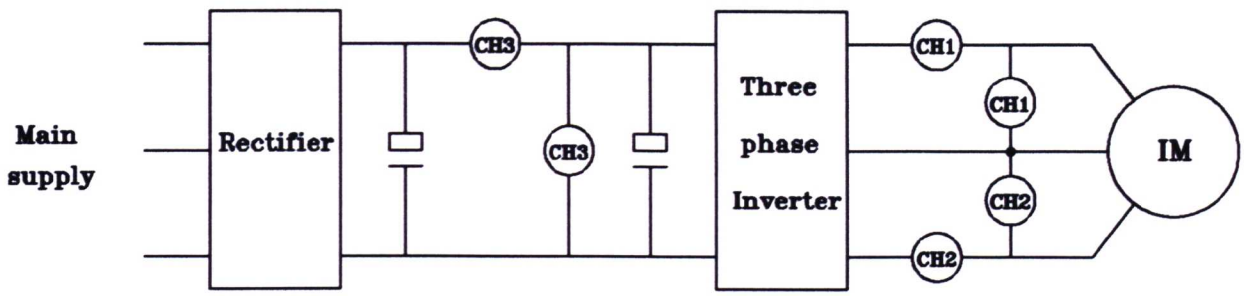

Fig. 2.21 Measurement of inverter input power and machine input power.

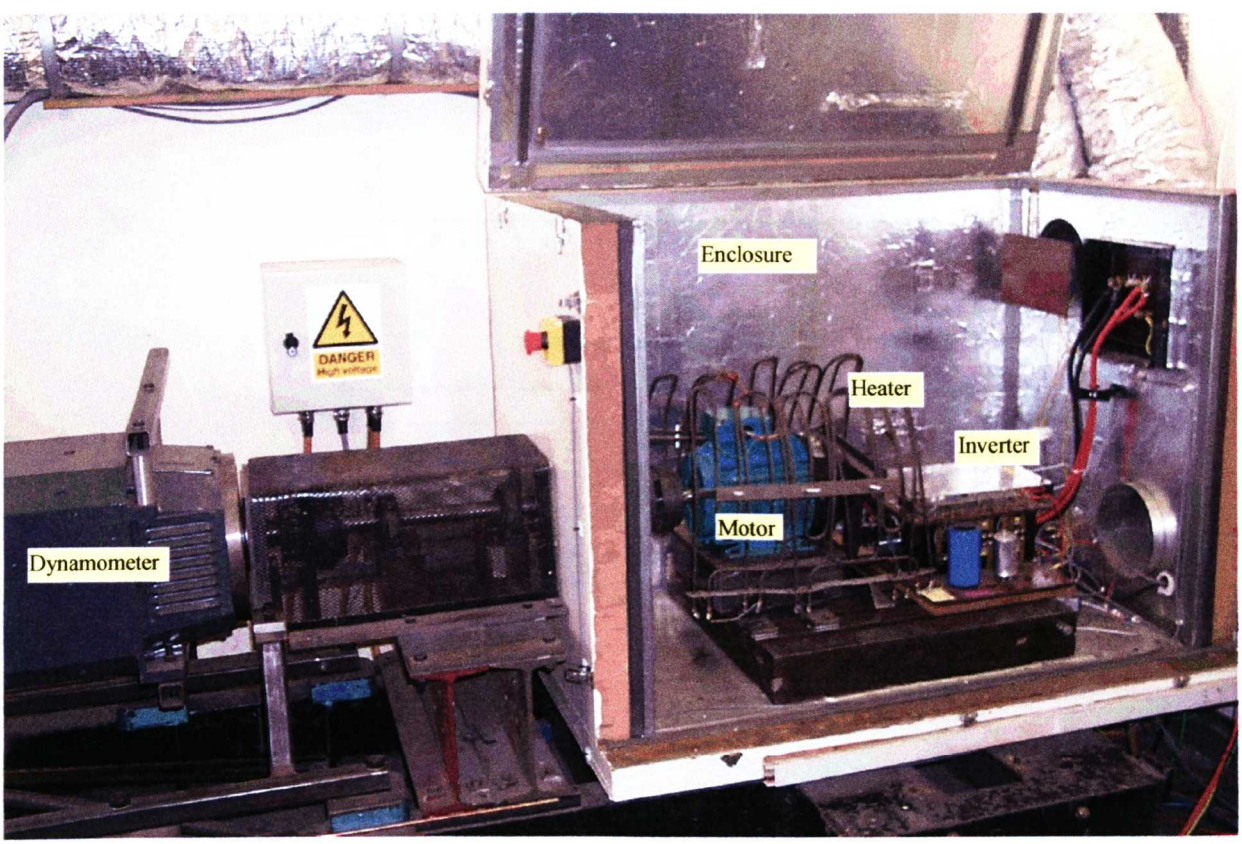

Fig. 2.22 Calorimeter based inverter and machine power loss measurement.

(a)

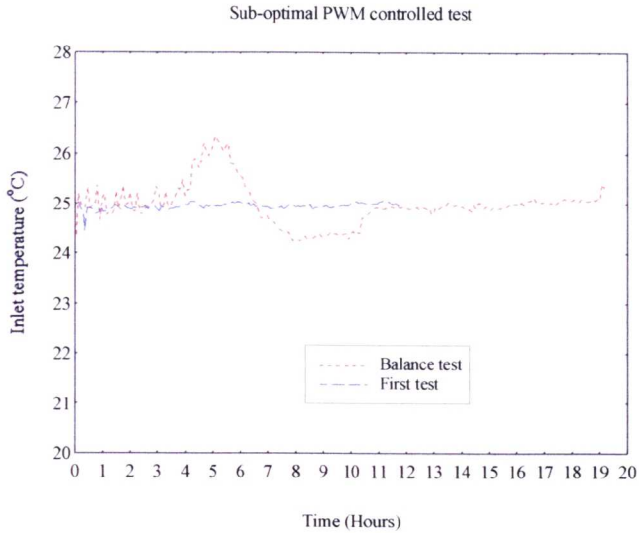

(b)

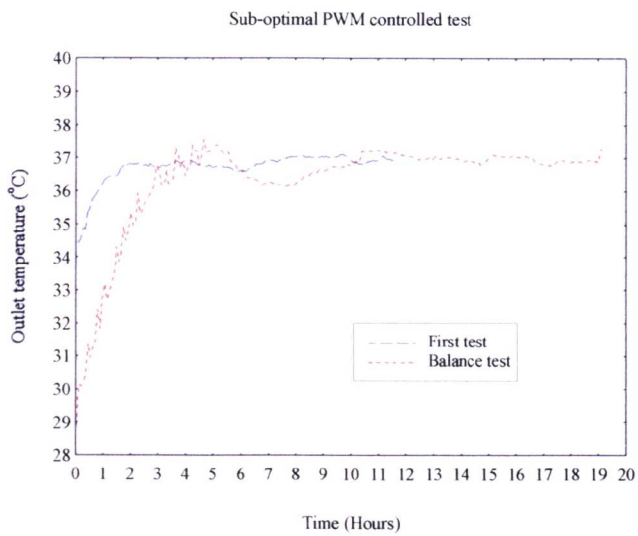

(c)

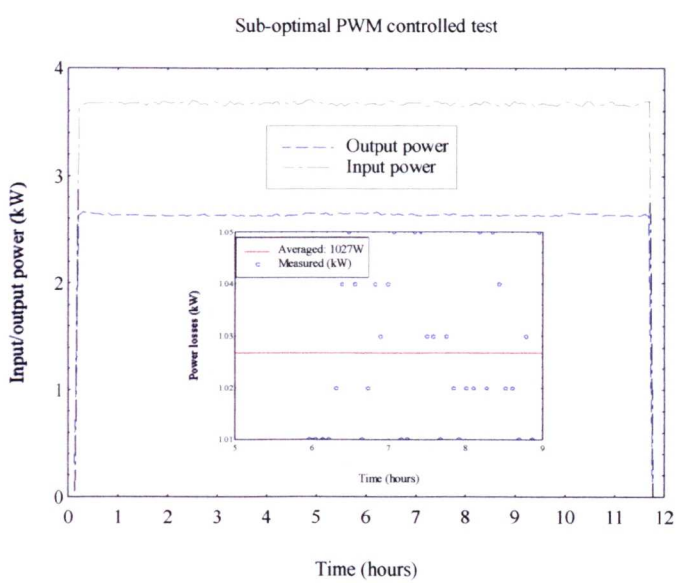

Fig. 2.23 Calorimeter based test results with sub-optimal PWM control. (a) inlet temperatures in the first and balance tests, (b) outlet temperatures in the first and balance tests, (c) input/output powers in the first test.

(a)

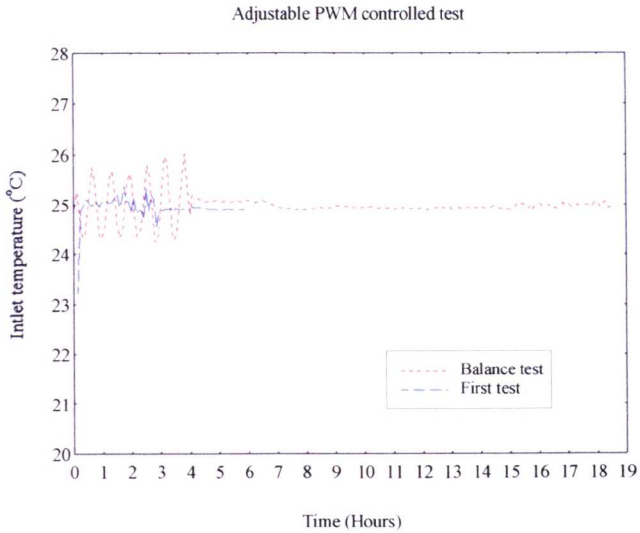

(b)

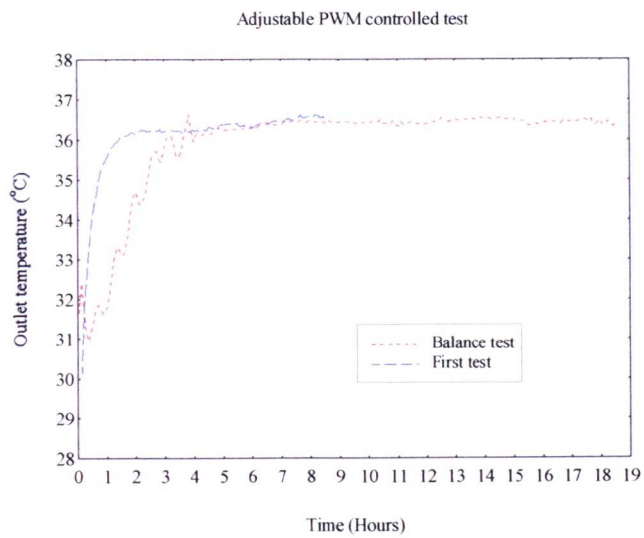

(c)

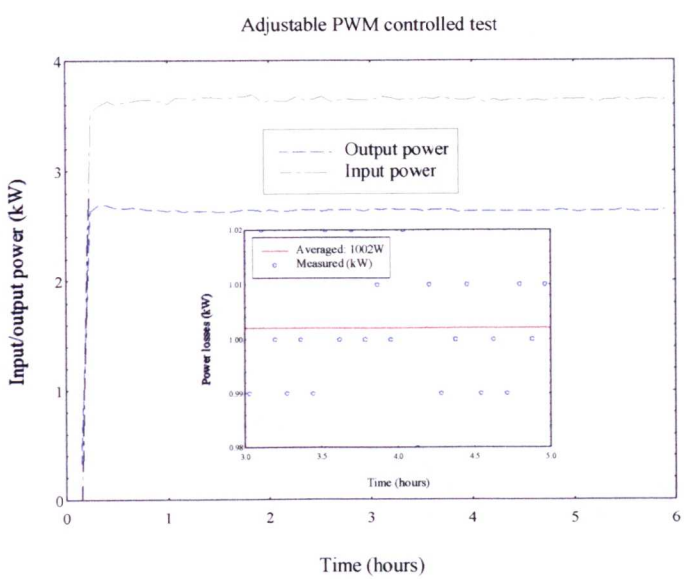

Fig. 2.24 Calorimeter based test results with adjustable PWM control. (a) inlet temperatures in the first and balance tests, (b) outlet temperatures in the first and balance tests, (c) input/output powers in the first test.

(a)

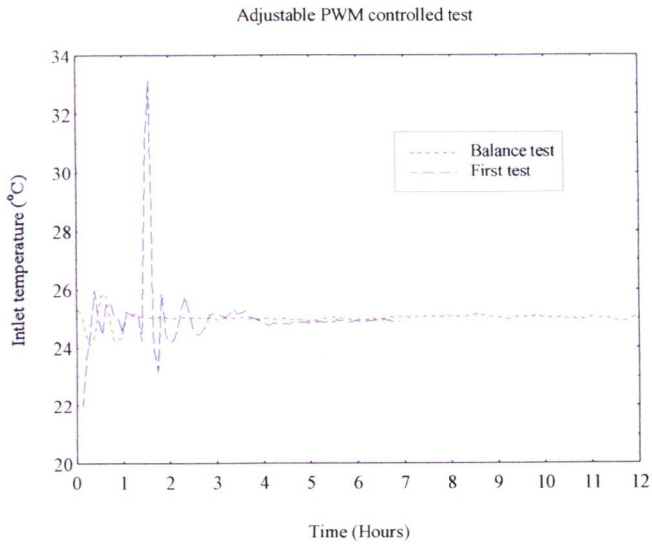

(b)

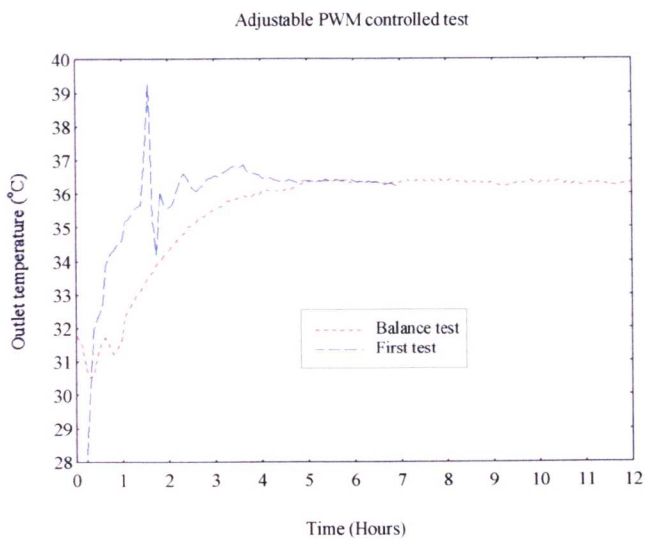

(c)

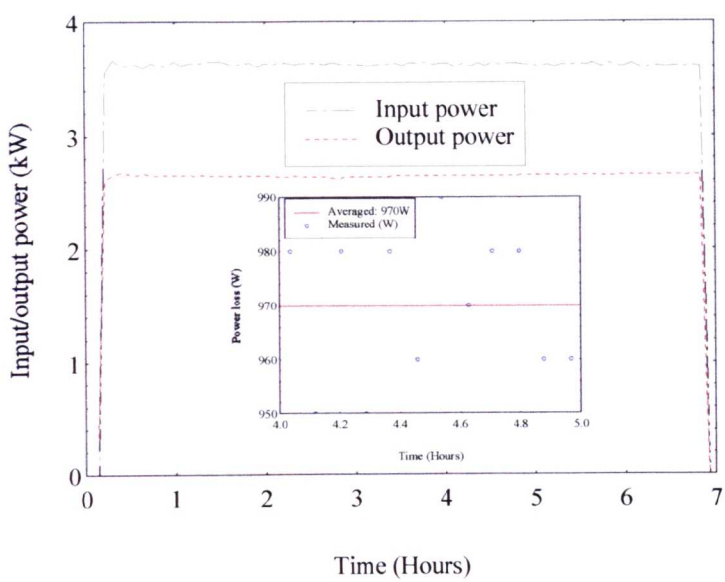

Fig. 2.25 Second calorimeter based test results with adjustable PWM control. (a) inlet temperatures in the first and balance tests, (b) outlet temperatures in the first and balance tests, (c) input/output powers in the first test.

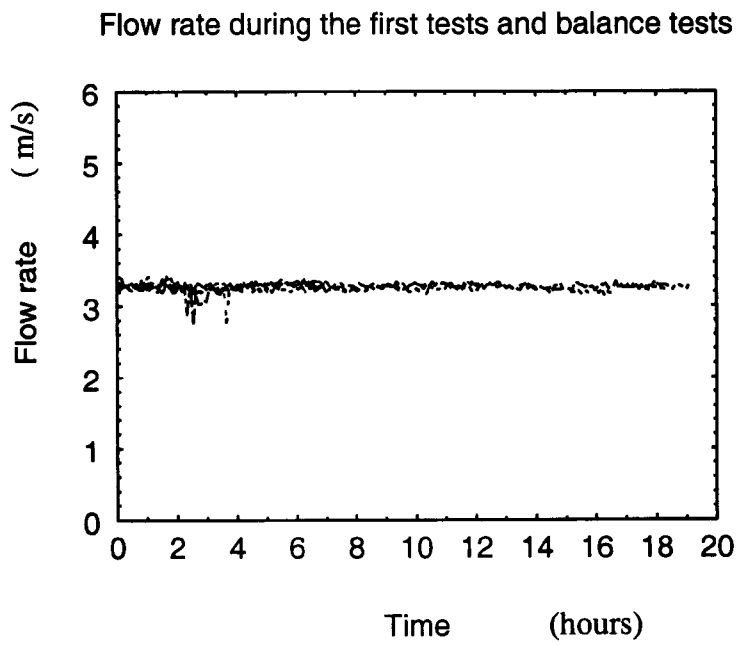

Fig. 2.26 Flow rate in the calorimeter during the tests.

3. Review of Inverter Modulation Strategies and their Digital Implementation

3.1 Introduction

Over the years, a variety of modulation strategies have been proposed for the switching control of inverter drives. The performance criteria commonly used for assessing a particular strategy are the generated waveform quality and the system dynamic response. The waveform quality is usually evaluated by the voltage-based total harmonic distortion (THD), which is a good measure of the additional loss in the electrical machine induced by the harmonics present in the supply. The system dynamic response is often related to the performance of current feedback control system, which in turn depends upon the sampling rate and speed of response of the modulator. Acoustic noise suppression and electromagnetic compatibility (EMC) are also important criteria in the assessment of a particular modulation method.

The chapter undertakes a detailed review of the more promising PWM modulation strategies. The harmonic performance of the various methods are compared together with an assessment of their ease of implementation in a digital system.

3.2 Review of modulation strategies

3.2.1 Feedforward modulation strategies

The basic requirement of all a.c. modulation methods is to generate a variable voltage and variable frequency supply, ideally with a minimum level of distortion. In an analogue implementation, the initial concept is relatively straightforward, i.e. to generate the required switching pattern by comparing a modulating signal (the required output waveform) with a triangular carrier signal. This technique is referred to as natural sampling pulse width modulation (natural sampling PWM). For convenience of digital implementation a regularly sampled version of the original modulating waveform can be used for the comparison, often referred to as regular or uniform sampling PWM [Bowes 1975]. Regular sampling PWM also introduces lower levels of harmonic distortion in the inverter output compared to natural

sampling PWM. Another important feature of the regular sampling method is that in the majority of cases the relationship is linear between the modulation depth and the amplitude of the PWM fundamental output. This provides a simple method of controlling the inverter output voltage. A development of regular sampling modulation is sub-optimal regular PWM, which uses a modulating waveform with an injected third harmonic. By the use of this technique, the harmonic content of regular sampling can be reduced and the output voltage range extended [Bowes 1985, Boys 1985]. With addition of a variable sampling factor, an adjustable PWM method has been proposed, which further reduces the total harmonic distortion, whilst having a capability of suppressing low order harmonics [Mellor 1993].

Along with these on-line calculated PWM processes, off-line optimised PWM schemes have also been established: optimal harmonic elimination PWM [Patel 1973], which eliminates selected harmonics, and optimal harmonic minimisation PWM [Buja 1977], which delivers a minimum harmonic distortion for a given switching frequency. However, the implementation of these optimal methods relies upon storing the off-line calculated results in extensive look-up tables and is only practical in the case of a low number of pulses per fundamental cycle.

An important recent development for the three phase a.c. machine drive waveform generation is the concept of vector space PWM [Holtz 1986, Broeck 1986]. This method uses a rotating space vector representation of the required three phase voltages to decompose the output into three of eight possible inverter switching states, with the durations of the selected states determined using a voltage invariant algorithm. Due to the superior performance of the vector space PWM and its simplicity of implementation, it is finding increasing applications.

Many other feedforward PWM methods have been proposed and can be considered as the modifications towards a particular purpose, for example, the PWM method used in the case where the d.c. link voltage fluctuates [Chen 1995] , the voltage clamped vector space PWM

for reducing inverter switching loss [Handley 1992], and the high voltage suboptimal PWM for a smooth transition from the PWM mode to quasisquare-wave switching [Bowes 1986].

These open-loop feedforward PWM strategies allow direct definition of the switching pattern and thus can be oriented towards a particular requirement, for example the minimum machine harmonic loss or the lowest machine torque ripple. The modulation strategies are generally simple and insensitive to parameter variations, but being essentially open loop, they should be used with an external closed loop current control to improve the system dynamic response. The relative performances of the principal feedforward PWM methods will be discussed in more detail in section 3.3.

3.2.2 Feedback modulation strategies

Feedback PWM strategies fall into categories of methods which allow direct control of machine current, flux or even torque. Feedback methods can be relatively straightforward such as hysteresis control, or be a more complex cascaded structure of a controller and a PWM modulator, and may involve linear or predictive control techniques. In a linear feedback current control scheme the motor currents are directly sensed and compared to reference current demands. The error feedback is processed by a controller (e.g. a conventional PI controller) to provide a modulating signal for a carrier-based PWM modulator. The current control performance is determined by the controller parameters and by the cascaded PWM modulator.

In the basic hysteresis control scheme the motor currents are sensed and compared to the reference current demands using hysteresis comparators. The inverter switches are then driven directly by the comparators' output signals. The motor currents are thus forced to follow the reference within the hysteresis band. Hysteresis controllers are robust and can produce very fast transient responses. However, due to the action of the hysteresis controllers of the three phases, very high switching rates at low modulation depths may occur. Furthermore, the resultant current ripple can exceed the hysteresis band as a result of mutual interaction

between the phases. Improved versions of hysteresis controllers have been proposed [Bose 1990], where the hysteresis band is adapted to the system parameters to maintain the modulation frequency to be nearly constant.

Predictive control methods are generally based on the space vector concept [Le-huy 1994]. The actual motor phase currents are sampled and a corresponding current space vector is calculated. An appropriate voltage space vector that would force the actual current vector to follow a reference vector is then computed using a model of the motor. This voltage vector is then applied to the vector space PWM modulator to generate the switching sequence for the inverter. The control method can provide good steady-state and dynamic performance. However, the computation is complex, and the robustness of the control scheme is poor with regard to the variations in the motor parameters and the d.c. voltage supply.

These three feedback control schemes are indicated in Fig 3.1. In electric vehicle applications, where the dynamic response requirements are moderate, feedforward voltage controlled PWM is preferred since the switching patterns for a given depth of modulation are predefined. Feedforward PWM thus allows a more direct control of the harmonic content of the output current waveform for a given inverter switching frequency. The application of feedback PWM methods to electric vehicle drives lies outside the scope of this thesis.

3.2.3 Other modulation strategies

Alternative modulation strategies to those described have been proposed as means of reducing inverter drive acoustic noise or to control novel inverter formats such as resonant link inverters. In contrast to the standard fixed carrier frequency PWM inverters, the acoustic noise could be reduced by smearing the narrow band or tonal noise into wideband atonal noise of equal energy using the so-called random PWM (RPWM) strategies [Boys 1992, Garcia 1994]. This type of PWM can be categorised into randomised switching frequency RPWM and randomised pulse position RPWM, and even can be optimised in term of "low noise" or

"music" modulated by a melody [Trzynadlowski 1994]. However, these processes tend not to consider the waveform harmonic content and the inverter or motor losses.

Soft switching, resonant d.c. link inverters use a discrete pulse form of modulation, often referred to as Pulse-Density-Modulation (PDM), where the inverter switching events occur only at discrete voltage or current intervals that coincide with the zero-crossings in the resonant circuit [Mertens 1992]. The PDM scheme is illustrated in Fig 3.2. The difference of the voltage demand and the modulator output signal is integrated and fed to a comparator. The comparator output is sampled at the zero-crossing frequency and held for the next sampling period. The output signal is then used as a switching command to directly control the switching state of the respective inverter power semiconductor devices. Three independent modulators can be used to control a three-phase inverter. Since the switching frequency is usually very high for these PWM methods, the harmonic content is generally small and is not of main concern when machine loss is considered.

3.3 Harmonic analyses of feedforward PWM strategies

This section provides analytical expressions for harmonic content of a number of the more common feedforward PWM strategies, including the analogue form, natural PWM, and basic, voltage uncontrollable quasisquare-wave switching. These expressions will be used in Chapter 4 to assess the impact of a particular PWM method on the overall loss in a traction drive.

3.3.1. Natural sampling PWM [Black 1953]

This method of modulation has been used extensively in the past because of its ease of implementation using simple analogue circuits. A typical analogue PWM modulator is shown in Fig 3.3, and is simply composed of a comparator circuit and two signals, a triangular or sawtooth carrier waveform and the modulating signal.

In the double-edged PWM process, a fixed frequency triangular waveform is used as a carrier signal and the demand modulating signal is usually a sinusoidal wave. The comparator

effectively detects the intersections of the carrier wave and the modulating wave, and the resultant output is a periodic, variable width, fixed frequency pulse train. The switching instances of the pulse train are determined by the relative magnitudes, phases and the frequencies of the two waves (Fig 3.4).

For a sinusoidal modulating signal,

$$m(t) = M \sin (\omega t + \delta) \tag{3.1}$$

a general transcendental expression for each successive pulse width is,

$$t_2 - t_1 = \frac{T}{2} [1 + \frac{M}{2} (\sin(\omega t_1 + \delta) + \sin(\omega t_2 + \delta))] \tag{3.2}$$

where T is the carrier cycle (sampling time), ω is the modulating wave frequency, and δ is the phase angle between carrier wave and modulating wave as shown in Fig. 3.4. M is the modulation depth and is defined by,

$$M = \frac{Fundamental\ modulating\ wave\ amplitude}{Carrier\ wave\ amplitude} \tag{3.3}$$

If the modulating wave amplitude is higher than the carrier wave amplitude, the process is called overmodulation. For the basic sinusoidal modulating signal, Eqn. 3.1, overmodulation will occur when $M > 1$.

In a voltage source inverter, the modulation depth can equally be defined as the ratio between the inverter output fundamental voltage peak-peak amplitude and the d.c. link voltage,

$$M = \frac{Output\ fundamental\ voltage\ peak\text{–}to\text{–}peak\ amplitude}{DC\ link\ voltage} \tag{3.4}$$

The natural characteristic of this PWM will enable the process to respond almost instantaneously to demand variations, such as a change in amplitude and frequency of the

modulating wave. This can be seen clearly in the analytical expression for the spectrum distribution of the output PWM pulse train [Black 1953, Mellor 1991],

$$f(t) = M \sin(\omega t + \delta)$$

$$+\sum_{\substack{m=1 \\ m\ odd}}^{\infty} \sum_{\substack{n=-\infty \\ n\ even}}^{\infty} \frac{4 J_n(M m \frac{\pi}{2})}{m \pi} \sin(n\omega t + m\omega_s t + n\delta - \frac{n\pi}{2R} + \frac{m\pi}{2})$$

$$+\sum_{\substack{m=2 \\ m\ even}}^{\infty} \sum_{\substack{n=-\infty \\ n\ odd}}^{\infty} \frac{4 J_n(M m \frac{\pi}{2})}{m \pi} \sin(n\omega t + m\omega_s t + n\delta - \frac{n\pi}{2R} + \frac{m\pi}{2}) \qquad (3.5)$$

where the pulse height has been normalised between ± 1, (or to a base of half the inverter d.c. link voltage), J_n is a Bessel function of the first kind, and ω_s is the carrier (switching) frequency. R is the ratio of the carrier frequency and modulating wave frequency, and is commonly referred to as frequency ratio and can be a rational or nonrational number. However, in high power applications it is common to use a low, fixed integer, frequency ratio. In a three phase converter the choice of a triplen frequency ratio will give further benefit as this automatically suppresses harmonic currents at the carrier frequency and its multiples.

It is observed from Eqn. (3.5) that the fundamental component in the output is identical to the modulating signal. Besides the fundamental component there are harmonics which occur at frequencies centred around multiples of the carrier frequency.

In the particular case where the frequency ratio is an odd integer, only harmonics at odd multiples of the modulating wave fundamental frequency appear in the spectrum. Referring to Eqn. 3.5 the major contribution to the kth harmonic in the spectrum will be formed from two terms such that,

$$m = integer\,(\frac{k}{R}) \text{ and } m \geq 1\ ,\ n = k - mR \tag{3.6}$$

and

$$m = integer\,(\frac{k}{R}) + 1\ ,\ n = k - mR \tag{3.7}$$

Thus, if the kth harmonic is in the range of,

$$pR \leq k < (p+1)R \tag{3.8}$$

where p is a non-negative integer. Then the Eqns. (3.6) and (3.7) are expressed as,

$$m = p\ ,\ n = k - pR \tag{3.9}$$

and

$$m = p + 1\ ,\ n = k - (p+1)R \tag{3.10}$$

The resultant kth harmonic amplitude is calculated from the vector sum of the above two terms, and the effect will be most pronounced when they are in phase, or anti-phase with each other, i.e. when,

$$(k - pR)(\delta - \frac{\pi}{2R}) + \frac{p}{2}\pi = (k - (p+1)R)(\delta - \frac{\pi}{2R}) + \frac{p+1}{2}\pi \tag{3.11}$$

or

$$(k - pR)(\delta - \frac{\pi}{2R}) + \frac{p}{2}\pi + \pi = (k - (p+1)R)(\delta - \frac{\pi}{2R}) + \frac{p+1}{2}\pi \tag{3.12}$$

The above two equations are solved as,

$$\delta = \frac{\pi}{R} \tag{3.13}$$

or

$$\delta = 0 \tag{3.14}$$

With the phase angle defined in Eqn. (3.14), the two terms are always in subtraction, leading to a lower harmonic amplitude. The influence of the modulating wave phase angle to the PWM harmonic distortion has been discussed in detail by Boys and Mellor [Boys 1985, Mellor 1991]. To demonstrate the influence of this phase angle on the harmonic distortion in natural PWM, the variation of total-harmonic-distortion (THD) with the phase angle is shown in Fig. 3.5 for the case of a frequency ratio of 9 and a modulation depth of 0.9. The graph illustrates that a phase angle of 0 corresponds to the lowest THD.

Following the above discussion and applying the optimum phase angle Eqn. (3.14) to Eqn. (3.5), the amplitude of the kth harmonic in the PWM process can be obtained as,

$$|V_k| = \sum_{m=1}^{\infty} \frac{4 J_{mR-k}(\frac{M m\pi}{2})}{m\pi} \tag{3.15}$$

Obviously, for a given modulation depth and a given order of harmonics, the higher the frequency ratio, the lower is the amplitude of the harmonics. This is shown in Fig. 3.6 which plots total harmonic distortion against the modulation depth at various frequency ratio.

For the purpose of comparing the pulse train and the harmonic spectrum of different PWM processes, the example case when the frequency ratio is 9 and the modulation depth is 0.9, will be used throughout the remainder of the chapter. Fig. 3.14(a) gives the pulse pattern for the natural PWM, and Fig. 3.15(a) is its harmonic spectrum distribution at the condition of $R = 9, M = 0.9$.

3.3.2 Regular sampling PWM [Bowes 1975]

In regular sampling PWM, the modulating wave is sampled at regularly spaced intervals, corresponding to the positive and/or the negative peaks of the triangular carrier wave, to produce a sampled modulating wave. Comparison of the sampled modulating wave with the

carrier wave defines the points of intersection used to determine the positions of the resultant pulse edges. If the sampling happens once every carrier cycle, the process is called symmetric regular sampling PWM. Alternatively, if the modulating wave is sampled twice every carrier cycle, so called asymmetric regular sampling PWM is obtained, in which case each edge of the pulse is formed from a different sampled value. Fig 3.7 illustrates the pulse formation of the asymmetric regular sampling process.

The resultant general expression for the pulse width is,

$$t_2 - t_1 = \frac{T}{2}\left[\, 1 + \frac{M}{2}\left(\sin(\omega t_k + \delta) + \sin(\omega t_{k+1} + \delta) \right) \right] \tag{3.16}$$

where the sample points are defined by,

$$t_k = k\frac{T}{2}, \quad with\ k = 0\,,\,1\,,\,2\,,\cdots \tag{3.17}$$

The double-fourier transform method of analysis can also be used to determine the harmonic spectrum of regular sampling PWM. The following expression gives the spectrum distribution for asymmetrical regular sampling PWM,

$$f(t) = \sum_{\substack{n=1 \\ n\ odd}}^{\infty} \frac{4 J_n\left(\frac{M n \pi}{2R}\right)}{\frac{n\pi}{R}} \sin\left(n\omega t + n\delta - \frac{n\pi}{2R}\right)$$

$$+ \sum_{\substack{m=1 \\ m\ odd}}^{\infty} \sum_{\substack{n=-\infty \\ n\ even}}^{\infty} \frac{4 J_n\left(M\left(m + \frac{n}{R}\right)\frac{\pi}{2}\right)}{\left(m + \frac{n}{R}\right)\pi} \sin\left(n\omega t + m\omega_s t + n\delta - \frac{n\pi}{2R} + \frac{m\pi}{2}\right)$$

$$+ \sum_{\substack{m=2 \\ m\ even}}^{\infty} \sum_{\substack{n=-\infty \\ n\ odd}}^{\infty} \frac{4 J_n\left(M\left(m + \frac{n}{R}\right)\frac{\pi}{2}\right)}{\left(m + \frac{n}{R}\right)\pi} \sin\left(n\omega t + m\omega_s t + n\delta - \frac{n\pi}{2R} + \frac{m\pi}{2}\right) \tag{3.18}$$

Besides the combinational terms as in the natural PWM which occur at frequencies centred around the multiples of the carrier frequency, there are forward harmonic terms which occur at odd multiples of the modulating sinusoidal fundamental frequency. The fundamental output is no longer identical to the modulating wave, rather it is composed of a dominant term,

$$V_1 \approx \frac{4 J_1 (\frac{M\pi}{2R})}{\frac{\pi}{R}} \sin (\omega t + \delta - \frac{\pi}{2R}) \tag{3.19}$$

Inspection of this term shows that the amplitude of the fundamental output has a non-linear relationship with the modulation depth, especially when the frequency ratio is low. However, when the frequency ratio is relatively high, this non-linearity is negligible. The regular sampling process also introduces a phase delay in the output fundamental compared to the controlling modulating wave. The frequency ratio dependent fundamental amplitude and phase variation will have an impact on the system steady-state and transient performance during ratio changes, as will be discussed in detail in Chapter 5.

For an odd integer frequency ratio, the major contributions to the kth (an odd order) harmonic in the spectrum are from the following two components in Eqn. (3.18),

$$m = integer (\frac{k}{R}), \; n = k - mR \tag{3.20}$$

and

$$m = integer (\frac{k}{R}) + 1, \; n = k - mR \tag{3.21}$$

Again, the relative effect of these two terms on the harmonic amplitude is dependent on the modulating wave phase angle. An inspection of Eqn. (3.18) shows that when the phase angle is given by,

$$\delta = 0 \tag{3.22}$$

the harmonic magnitude reaches the lowest possible level. In this case, the magnitude of the kth harmonic can be expressed as,

$$|V_k| = \sum_{m=1}^{\infty} \frac{4 J_{mR-k}(\frac{Mk\pi}{2R})}{\frac{k\pi}{R}} - \frac{4 J_k(\frac{Mk\pi}{2R})}{\frac{k\pi}{R}} \qquad (3.23)$$

Since the two dominant terms in the above expression always act to cancel each other regardless of the value of the frequency ratio and the order of the harmonics, the amplitude of the low order harmonics in the regular sampling PWM tend to be lower than in the natural PWM. This can also be shown by comparing Eqn. (3.15) and Eqn. (3.23).

Also, it can be observed from Eqn. (3.23) that with increased frequency ratio, the amplitudes of the harmonics are reduced.

The pulse pattern of the asymmetric regular sampling process is shown in Fig. 3.14(b) at the example frequency ratio of 9 and a modulation depth of 0.9, and its spectrum distribution is given in Fig. 3.15(b).

3.3.3 Sub-optimal regular sampling PWM [Bowes 1985, Boys 1985]

Instead of using a pure sine wave as the modulating signal, as in the natural sampling and regular sampling processes, distorted modulating signals can be used for a balanced three phase drive system which contain a certain amount of "zero" components, such as third and ninth harmonics of the fundamental, etc. Fig 3.8 illustrates such a process where a modulating wave which contains a third harmonic component is applied to regular sampling asymmetrical PWM.

A general form for a modulating signal with an added third harmonic is,

$$m(t) = M [\sin(\omega t + \delta) + \beta \sin 3(\omega t + \delta)] \qquad (3.24)$$

where the parameter β determines the relative level of the third harmonic. It has been shown that the optimal value of β is 25%, since with this value it is possible to achieve a linear voltage control range with depths of modulation ranging from 0 - 1.15 and the waveform harmonic distortion is lower compared to natural PWM and regular sampling PWM. This process is usually called sub-optimal regular PWM [Bowes 1985].

The pulse width in the general case is,

$$t_2 - t_1 = \frac{T}{2}\left[\, 1 + \frac{1}{2}\left(m\left(t_k\right) + m\left(t_{k+1}\right)\right)\right] \tag{3.25}$$

where the sampling points t_k and t_{k+1} are again defined by Eqn. (3.17).

The spectrum distribution of the sub-optimal PWM can be expressed as (see Appendix C for the full derivation),

$$f(t) = \sum_{\substack{n=1 \\ n\ odd}}^{\infty} \sum_{q=-\infty}^{\infty} \frac{4}{\frac{n\pi}{R}} J_{n-3q}\left(\frac{n\pi M}{2R}\right) J_q\left(\frac{n\pi M\beta}{2R}\right) \sin\left(n\omega t + n\delta - \frac{n\pi}{2R}\right)$$

$$+ \sum_{\substack{m=1 \\ m\ odd}}^{\infty} \sum_{\substack{n=-\infty \\ n\ even}}^{\infty} \sum_{q=-\infty}^{\infty} \frac{4}{\left(m + \frac{n}{R}\right)\pi} J_{n-3q}\left(M\left(m + \frac{n}{R}\right)\frac{\pi}{2}\right) J_q\left(M\beta\left(m + \frac{n}{R}\right)\frac{\pi}{2}\right)$$

$$\cdot \sin\left(n\omega t + m\omega_s t + n\delta - \frac{n\pi}{2R} + \frac{m\pi}{2}\right)$$

$$+ \sum_{\substack{m=2 \\ m\ even}}^{\infty} \sum_{\substack{n=-\infty \\ n\ odd}}^{\infty} \sum_{q=-\infty}^{\infty} \frac{4}{\left(m + \frac{n}{R}\right)\pi} J_{n-3q}\left(M\left(m + \frac{n}{R}\right)\frac{\pi}{2}\right) J_q\left(M\beta\left(m + \frac{n}{R}\right)\frac{\pi}{2}\right)$$

$$\cdot \sin\left(n\omega t + m\omega_s t + n\delta - \frac{n\pi}{2R} + \frac{m\pi}{2}\right) \tag{3.26}$$

The fundamental component in the output is therefore,

$$V_1 \approx \sum_{q=-\infty}^{\infty} \frac{4 J_{1-3q}\left(\frac{M\pi}{2R}\right) J_q\left(\frac{M\pi\beta}{2R}\right)}{\frac{\pi}{R}} \sin\left(\omega t + \delta - \frac{\pi}{2R}\right) \qquad (3.27)$$

It can be shown that minimum harmonic distortion in the PWM process will still occur at a phase angle,

$$\delta = 0 \qquad (3.28)$$

With this optimal phase angle, the magnitude of the kth harmonic in the PWM output can be written as,

$$|V_k| = \sum_{m=1}^{\infty} \sum_{q=-\infty}^{\infty} \frac{4 J_{mR-k-3q}\left(\frac{Mk\pi}{2R}\right) J_q\left(\frac{\beta Mk\pi}{2R}\right)}{\frac{k\pi}{R}} - \sum_{q=-\infty}^{\infty} \frac{4 J_{k-3q}\left(\frac{Mk\pi}{2R}\right) J_q\left(\frac{\beta Mk\pi}{2R}\right)}{\frac{k\pi}{R}} \qquad (3.29)$$

The above expression is complex and not easy to visualise. However, it clearly shows that the amplitude of the harmonic is decreased when the frequency ratio is increased. At a frequency ratio of 9, the variation of waveform total harmonic distortion (THD) with the third harmonic factor β is shown in Fig. 3.9. Here $\beta = 0$ represents the asymmetric regular PWM discussed earlier, whereas with $\beta = 0.25$ the process has the lowest harmonic distortion.

Although other triplen harmonics of the supply frequency can be added to the modulating signal, for example, a 9th or 15th harmonic, the benefits are minimal and do not warrant the additional complexity.

The pulse pattern and spectrum distribution of the sub-optimal process at a frequency ratio of 9 and a modulation depth of 0.9 are shown in Fig 3.14(c) and Fig 3.15(c), respectively.

3.3.4 Adjustable regular sampling PWM [Mellor 1991, 1993]

The harmonic distribution of a regular sampling process contains forward harmonic terms as well as combinational harmonics. By manipulating the relative magnitudes of these forward and combinational harmonic terms through a sampling factor, an alternative asymmetric sampling process has been proposed [Mellor 1991]. The process is illustrated in Fig. 3.10. The pulse edges are determined from a transformed version of modulating waveform which may be visualised as a straight line in a sampling interval which lies between a line joining two successive samples (equivalent to a linear interpolation of the natural sampling process) and a line representing the sampled value of the regular sampling process. The transformed waveform, $m_k(t)$, of the original modulating waveform about the sampling instant t_k as given in Eqn. (3.7) is described,

$$m_k(t) = m((1-\varepsilon)(t-t_k)+t_k) \tag{3.30}$$

where ε is referred to as the sampling factor.

When the sampling factor ε is zero the process becomes identical to natural sampling, and alternatively when ε is unity regular sampling is obtained. However, many other sampling processes are possible by varying the sampling factor ε, and particularly values of ε greater than one can lead to lower levels of total harmonic distortion and reduced low order harmonics [Mellor 1993].

With a simple sinusoidal modulating wave, i.e. Eqn. (3.1), the spectrum of the pulse train generated by the adjustable PWM is given by [Mellor 1991],

$$f(t) = \sum_{\substack{n=1 \\ n\ odd}}^{\infty} \frac{4 J_n\left(\frac{M n \varepsilon \pi}{2R}\right)}{\frac{n \varepsilon \pi}{R}} \sin\left(n\omega t + n\delta - \frac{n \varepsilon \pi}{2R}\right)$$

$$+\sum_{\substack{m=1\\ m\,odd}}^{\infty}\sum_{\substack{n=-\infty\\ n\,even}}^{\infty}\frac{4J_n\left(M\left(m+\frac{n\varepsilon}{R}\right)\frac{\pi}{2}\right)}{\left(m+\frac{n\varepsilon}{R}\right)\pi}\sin\left(n\omega t+m\omega_s t+n\delta-\frac{n\varepsilon\pi}{2R}+\frac{m\pi}{2}\right)$$

$$+\sum_{\substack{m=2\\ m\,even}}^{\infty}\sum_{\substack{n=-\infty\\ n\,odd}}^{\infty}\frac{4J_n\left(M\left(m+\frac{n\varepsilon}{R}\right)\frac{\pi}{2}\right)}{\left(m+\frac{n\varepsilon}{R}\right)\pi}\sin\left(n\omega t+m\omega_s t+n\delta-\frac{n\varepsilon\pi}{2R}+\frac{m\pi}{2}\right)$$

(3.31)

The expression corresponds exactly to the natural sampling PWM, Eqn. 3.5, and the asymmetric regular sampling PWM, Eqn. 3.18, when $\varepsilon = 0$ and $\varepsilon = 1$ respectively. In general the spectrum contains both forward and combinational harmonic terms and since the sampling factor ε appears in the arguments of the Bessel functions it will effect the relative magnitudes of these terms.

The phase angle of the modulating wave which results in the minimum harmonic distortion in the PWM process is obtained as,

$$\delta = \frac{\pi}{2R}(\varepsilon - 1) \tag{3.32}$$

and the corresponding magnitude of the kth harmonic of the spectrum for an odd integer frequency ratio R is then,

$$|V_k| = \sum_{m=1}^{\infty}\frac{4J_{mR-k}\left(M\left(m(1-\varepsilon)+\frac{k\varepsilon}{R}\right)\frac{\pi}{2}\right)}{\left(m(1-\varepsilon)+\frac{k\varepsilon}{R}\right)\pi} - \frac{4J_k\left(\frac{Mk\varepsilon\pi}{2R}\right)}{\frac{k\varepsilon\pi}{R}} \tag{3.33}$$

At a given frequency ratio and a modulation depth, any one of the lower order harmonics can be eliminated or suppressed by choosing a value of the sampling factor which results in the complete cancellation of the corresponding forward and combinational terms. This was illustrated by an example [Mellor 1993] where Eqn. (3.33) was solved to eliminate the 13th

harmonic in the PWM process with a frequency ratio of 15. The required sampling factor was found to be largely independent of the modulation depth, and the method would also reduce the magnitude of other low order harmonics. The necessity of extending the sampling factor beyond one was also assessed in the example.

In a similar method to sub-optimal PWM, a third harmonic can also be added to the adjustable sampling process, Eqn. 3.24. In this case, at the appropriate modulating wave phase angle, the magnitude of the kth harmonic in the spectrum is given by [Mellor 1993],

$$|V_k| = \sum_{m=1}^{\infty} \sum_{q=-\infty}^{\infty} \frac{4 J_{mR-k-3q}\left(M\left(m(1-\varepsilon)+\frac{k\varepsilon}{R}\right)\frac{\pi}{2}\right) J_q\left(\beta M\left(m(1-\varepsilon)+\frac{k\varepsilon}{R}\right)\frac{\pi}{2}\right)}{\left(m(1-\varepsilon)+\frac{k\varepsilon}{R}\right)\pi}$$

$$-\sum_{q=-\infty}^{\infty} \frac{4 J_{k-3q}\left(\frac{Mk\varepsilon\pi}{2R}\right) J_q\left(\frac{\beta Mk\varepsilon\pi}{2R}\right)}{\frac{k\varepsilon\pi}{R}} \qquad (3.34)$$

Although it is difficult to visualise this expression, if the amplitude of the fundamental is controlled in the usual way by varying the depth of modulation, then the other parameters (β , ε) can be used to improve the performance of the PWM process, for example, to eliminate two harmonics, or to minimise the total harmonic distortion. Following the investigations by Mellor, useful values for the sampling factor ε and the additional third harmonic factor β may be summarised as follows,

(a) When the frequency ratio is 9, parameters in the range of

$$\begin{cases} 1 < \varepsilon \le 2 \\ 0.25 \le \beta < 0.40 \end{cases} \qquad (3.35)$$

would give a satisfactory modulation process in terms of lower total harmonic distortion and suppression of low-order harmonics. For example, $\varepsilon = 1.8$ and $\beta = 0.39$ would give minimum harmonic distortion.

(b) When the frequency ratio is an odd triplen greater than nine, a sampling factor and a third harmonic factor of

$$\begin{cases} \varepsilon = \dfrac{R-1}{4} \\ \beta = 0 \end{cases} \tag{3.36}$$

will enable the sampling process to minimise the harmonic components below the carrier frequency and still result in a relatively low total harmonic distortion.

The pulse pattern and the spectrum distribution of the adjustable sampling process, with frequency ratio of 9, sampling factor of 1.8, third harmonic factor of 0.39 and modulation depth of 0.9, are shown in Fig 3.14(d) and Fig 3.15(d), respectively.

3.3.5 Optimal harmonic elimination PWM [Patel 1973, Zuckerberger 1986]

In contrast to the previous sampling processes, where the pulse patterns are determined directly on-line from samples of the modulating wave, the optimal harmonic elimination PWM defines the pulse trains by off-line computer calculations, such that a selected objective is reached.

A generalised output waveform $f(\omega t)$ of an inverter is shown in Fig 3.11, where the pulse pattern is assumed to have quarter-wave symmetry.

Assuming there are N pulses per half-cycle, and the N commutation angles in the first quarter cycle $(0, \frac{\pi}{2})$ are $\alpha_1, \alpha_2, \cdots, \alpha_N$. Due to the assumed quarter-wave symmetry of the waveform, the commutation angles in the second quarter cycle $(\frac{\pi}{2}, \pi)$ are then determined as,

$$\alpha_{2N-k+1} = \pi - \alpha_k, \quad \text{for } k = 1, 2, \cdots, N \tag{3.37}$$

and the other commutation angles in the next half cycle can be similarly derived using the half-wave symmetry property. Thus, the pulse pattern is fully defined by the N commutation angles,

$$0 < \alpha_1 < \alpha_2 < \cdots < \alpha_N < \frac{\pi}{2} \tag{3.38}$$

If the Fourier series of the waveform is expressed as,

$$f(\omega t) = \sum_{n=1}^{\infty} a_n \sin(n\omega t) \tag{3.39}$$

then the amplitude of the harmonic component V_n normalised to half the d.c. link can be shown to be [Buja 1977],

$$V_n = r(-1)^N \cdot \frac{4}{n\pi} [\, 1 + 2 \sum_{k=1}^{N} (-1)^k \cos n\alpha_k \,], \quad n \text{ odd} \tag{3.40}$$

where

$$r = \begin{cases} +1, & \text{if } f(\omega t) = 1 \text{ in } \alpha_N < \omega t < \pi/2 \\ -1, & \text{if } f(\omega t) = -1 \text{ in } \alpha_N < \omega t < \pi/2 \end{cases} \tag{3.41}$$

The two values for "r" in the above equation can be regarded being equivalent to shifting the phase of the modulating wave by 180 degrees.

The N commutation angles in the waveform pattern can be viewed as giving N degrees of freedom in controlling the amplitude of the component harmonics, making it possible to eliminate (N-1) of the harmonics and to control the amplitude of the fundamental wave in the range of,

$$0 \le V_1 < \frac{4}{\pi} \tag{3.42}$$

Given a requirement to eliminate selective harmonics in the waveform output, the N equations can be written as,

$$\begin{cases} V_1 = M \\ V_n = 0\,,\ (N-1)\ equations \end{cases} \tag{3.43}$$

which can be solved numerically over the full range of modulation depth, M.

As a three-phase machine usually constitutes a low-pass filter, elimination of low-order harmonics is preferred. For example, if four angles should be determined, the equations will be,

$$\begin{cases} V_1 = M \\ V_5 = V_7 = V_{11} = 0 \end{cases} \tag{3.44}$$

Two solutions are possible to conditions in Eqns. (3.44), depending upon whether the modulation depth, M, is specified as a positive or negative number. Although both will eliminate the lower order harmonics, one will yield a lower total harmonic distortion. Some representative solutions of Eqns. (3.44) are shown in Table 3.1. Note the use of four commutation angles per quarter cycle is equivalent to a switching frequency ratio of 9. The pulse pattern when M=0.9 is shown in Fig 3.14(e), whilst the spectrum distribution is given in Fig 3.15(e).

Table 3.1. Commutation angles in the harmonic elimination PWM. $V_5 = V_7 = V_{11} = 0$

M	0.1	0.2	0.3	0.4	0.5	0.6	0.7	0.8	0.9	1.0	1.1	1.15
α_1	20.77	21.50	22.09	22.69	23.15	23.37	23.12	21.92	19.51	16.83	13.01	11.35
α_2	38.89	37.73	36.67	35.37	33.91	32.21	30.09	27.29	23.95	21.08	17.62	16.25
α_3	60.90	61.85	62.73	63.80	64.96	66.25	67.70	69.35	71.16	72.95	76.69	79.81
α_4	79.46	78.97	78.60	78.24	78.00	77.90	77.95	78.08	78.07	78.04	79.25	81.53

3.3.6 Optimal harmonic minimisation PWM [Buja 1977]

In harmonic minimisation PWM, the commutation angles are pre-calculated to give a pulse pattern so that a minimum total harmonic distortion is reached. Here the standard THD expression below is commonly used, however, other THD formulations have been proposed as being more representative of motor loss.

$$THD = \sqrt{\sum_{n=2}^{\infty} \left(\frac{V_n}{n\, V_1}\right)^2} \tag{3.45}$$

As in the previous case of harmonic elimination PWM, a waveform with quarter-wave symmetry is again assumed. The N commutation angles in a quarter-cycle will be determined to define the fundamental voltage and to minimise the THD.

The THD can be normalised as,

$$THD^* = \sqrt{\sum_{n=2}^{\infty} \left(\frac{V_n^*}{n}\right)^2} \tag{3.46}$$

where the normalised harmonic components are

$$V_n^* = 1 + 2\sum_{k=1}^{N} (-1)^k \cos n\,\alpha_k \tag{3.47}$$

The harmonic distortion minimisation PWM is to solve for α_i ($i = 1, 2, \cdots, N$), so that the THD is minimised with a constraint on the fundamental voltage,

$$V_1 = M = r\,(-1)^N \cdot \frac{4}{\pi} [\, 1 + 2\sum_{k=1}^{N} (-1)^k \cos \alpha_k \,] \tag{3.48}$$

Defining Lagrange's equation of,

$$\sigma = THD^* + \lambda \left[r(-1)^N \left(1 + 2 \sum_{k=1}^{N} (-1)^k \cos \alpha_k \right) - \frac{\pi M}{4} \right] \tag{3.49}$$

the α_i ($i = 1, 2, \cdots, N$) can be found from the set of equations of,

$$\frac{\partial \sigma}{\partial \alpha_i} = 0, i = 1, 2, \cdots, N \tag{3.50}$$

or

$$\sum_{n=2}^{\infty} \left[\frac{4}{n} (-1)^{i+1} \cos n \alpha_i \left(1 + 2 \sum_{k=1}^{N} (-1)^k \cos n \alpha_k \right) \right] + 2 r (-1)^N \lambda (-1)^{i+1} \sin \alpha_i = 0 \tag{3.51}$$

The above equations can be solved numerically, and one set of the solutions is shown in Table 3.2.

Table 3.2. Commutation angles in THD minimisation PWM. Four angles.

M	0.1	0.2	0.3	0.4	0.5	0.6	0.7	0.8	0.9	1.0	1.1	1.15
α_1	60.78	61.55	62.34	63.19	64.09	65.03	66.08	5.76	6.61	7.46	8.25	8.56
α_2	75.41	74.65	74.06	73.72	73.39	73.12	72.97	69.13	70.94	73.25	76.58	79.02
α_3	79.69	76.79	77.24	77.91	78.55	79.21	79.92	76.38	76.53	77.18	78.85	80.47
α_4	89.47	88.93	88.38	87.87	87.36	86.87	86.42	86.56	87.35	88.14	88.91	89.29

The pulse pattern and the spectrum distribution for M=0.9 are shown respectively in Fig 3.14(f) and Fig 3.15(f).

3.3.7 Vector space PWM [Holtz 1986, Broeck 1986]

As opposed to using individual three phase voltages to define the pulse patterns, a rotating stator voltage vector $\vec{V}$ is used to represent the entire three phase supply. The three phase voltage vectors $\vec{V_a}$, $\vec{V_b}$ and $\vec{V_c}$ can be derived from this vector using,

$$\vec{V} = \vec{V_a} + \vec{V_b} + \vec{V_c} \tag{3.52}$$

The corresponding flux linkage vector in the machine can be expressed as,

$$\vec{\psi} = \int \vec{V} dt \tag{3.53}$$

The principle of vector space PWM is to construct the machine rotating voltage vector from the three phase voltages so that the required magnitude of rotating field (flux linkage) or the voltage-time integral is maintained. In a three phase a.c. machine, the three voltages are balanced, and the resultant machine voltage vector is a circular. Because of this, vector space PWM has also been referred to as circular-locus PWM [Murai 1987].

At any given instant of time, the machine three phase voltage vectors are determined by the on/off status of the switches of the inverter. If each of the phase leg voltages of the inverter is defined in such a manner that when the top switch is on it is normalised as 1, and when the bottom switch is on it is 0, and if the three phase voltages are used to form a voltage vector (V_a , V_b , V_c), then the rotating voltage vector can be considered as constructed by eight possible voltage vectors, i.e., $\vec{V_0}$ (000), $\vec{V_1}$ (001), $\vec{V_2}$ (010), $\vec{V_3}$ (011), $\vec{V_4}$ (100), $\vec{V_5}$ (101), $\vec{V_6}$ (110) and $\vec{V_7}$ (111). The vectors $\vec{V_0}$ and $\vec{V_7}$ represent the states when the inverter three phase legs are switched simultaneously to the d.c. link negative rail and the positive rail, respectively. Since they don't contribute to the rotating voltage vector, and are usually named zero vectors. Conversely, the vectors $\vec{V_1} \rightarrow \vec{V_6}$ are often referred to as non-zero vectors. A representative inverter and its switching voltage vectors are shown in Fig 3.12(a) and (b), respectively.

Following the above discussion, the inverter switching voltage vectors can be used to construct the machine rotating voltage vector. In a given sampling period, for the purpose of limiting the switching times usually only two adjacent non-zero vectors are used. If the

voltage-time integral invariant rule is applied, the following equation can be used to describe the construction of the rotating vector,

$$\vec{V} = d_x \vec{V_x} + d_y \vec{V_y} + d_z \vec{V_z} \tag{3.54}$$

where $\vec{V_x}$ and $\vec{V_y}$ are two of the six non-zero vectors, and d_x and d_y are the required duty ratios of these two vectors in the sampling period. To fill the sampling period, a zero vector $\vec{V_z}$ (either $\vec{V_0}$ *or* $\vec{V_7}$) is also used with a duty ratio d_z, as noted in Eqn. (3.54).

If the desired rotating machine voltage vector is defined as,

$$\vec{V} = M_v e^{j\alpha} = M_v e^{j(\omega t + \delta)} \tag{3.55}$$

then the duty ratios of the adjacent non-zero vectors and the zero vector can be solved as,

$$\begin{cases} d_x = \dfrac{\sqrt{3}}{2} M \sin(60^o - \alpha) \\ d_y = \dfrac{\sqrt{3}}{2} M \sin\alpha \\ d_z = 1 - d_x - d_y \end{cases} \tag{3.56}$$

where δ is the initial angle of the rotating voltage vector, which is equivalent to the modulating wave phase angle referred to earlier. M is the modulation depth and is related with the amplitude of the rotating voltage vector, M_v, by,

$$M = \frac{4}{3} M_v \tag{3.57}$$

$M_v = \dfrac{\sqrt{3}}{2}$ *or* $M = \dfrac{2}{\sqrt{3}}$ corresponds to the largest circle inside the hexagon bounded by the six non-zero vectors. Thus, a maximum modulation depth of 1.15 is achievable.

The full spectrum distribution for the vector space PWM can also be obtained using a double Fourier transformation. However, the analysis is complex and the results of published analyses [Boys 1990] will be used here.

The dominant component in the fundamental output of the vector space PWM can be approximated as,

$$V_1 \approx \frac{4 J_1 (\frac{M \pi}{2R})}{\frac{\pi}{R}} (1 + \frac{M^2}{21.3 R^2}) \sin (\omega t + \delta - \frac{\pi}{2R}) \qquad (3.58)$$

It is observed that similar to the regular sampling process, the amplitude of the fundamental voltage has a non-linear relationship with the PWM modulation depth, especially when the frequency ratio is low. However, when the frequency ratio is relatively high, this non-linearity is negligible. There is also a phase shift between the PWM output fundamental and the modulating signal.

As with other forms of PWM, the phase angle also plays an important role in determining the harmonic content in the vector space PWM. Inspection of the published expression [Boys 1990] shows that the phase angle which gives the PWM a minimum harmonic distortion is again,

$$\delta = 0 \qquad (3.59)$$

Another important parameter in vector space PWM is the duty ratio of the choice of zero vectors. The apportioning of the total null voltage vector time between $\vec{V0}$ and $\vec{V7}$ essentially influences the level of common mode triplen harmonic components present in the PWM waveform and thus gives some control on harmonic distortion. It has been shown by simulation (Fig. 3.13) that an equal division of the zero vector time between $\vec{V0}$ and $\vec{V7}$ in a cycle will give a low level of THD. If the total zero vector time is set at the beginning or alternatively at the end of each cycle, then two types of voltage-clamped vector space PWM

methods are obtained, 120^o bus clamped vector space PWM and 60^o bus clamped vector space PWM, respectively [Handley 1992]. It has been claimed that the voltage-clamped vector space PWM features fewer number of switching events in a fundamental period and thus less switching loss in an inverter. However, it presents more harmonic distortion in the inverter output [Casanellas 1995], even when compared with normal vector space PWM at an equivalent switching frequency.

The pulse pattern and its spectrum distribution of vector space modulation with a frequency ratio of 9, a modulation depth of 0.9 and an equal division of the two zero vectors, are shown respectively in Fig 3.14(g) and Fig 3.15(g).

3.3.8 Quasisquare wave switching

At extreme values of modulation (overmodulation) the PWM output will tend towards a 180^o square wave pulse train. This strategy is usually called quasisquare wave switching or alternatively six-step switching, since the load phase to neutral voltage waveform is composed of six steps.

In the square wave switching scheme each switch of the inverter-leg conducts for the maximum one-half cycle (180^o) of the desired output frequency, and therefore it will give the highest fundamental frequency voltage component, equivalent to an overmodulation of,

$$M = \frac{4}{\pi} = 1.27 \tag{3.60}$$

This mode of operation is often used in the machine field weakening operation region beyond the base speed, where it may be desirable to maintain the inverter output at its maximum.

Another advantage of the square wave operation is that each inverter switch has minimum number of changes of state, i.e. only twice per fundamental cycle, which is important at very high power levels when the solid-state switches generally have slower turn-on and turn-off

speeds. A serious disadvantage of square wave switching is that the inverter is not capable of regulating the output voltage magnitude. Therefore the d.c. input voltage to the inverter must be adjusted in order to control the magnitude of the inverter output voltage.

The pulse pattern for quasi-square wave and the spectrum distribution are shown in Fig 3.14(h) and Fig 3.15(h), respectively.

3.4 Digital implementation of PWM strategies

Digital implementation of PWM is preferred to its analogue counterpart because of its flexibility, reliability and low cost. Also it has a superior harmonic performance and a capability of minimising harmonic distortion. In this section, the development of a digital PWM modulator based on a digital signal processor (DSP) and a field programmable gate array (FPGA) is described. The system has been designed to have a flexible pulse formation strategy in order that the modulator can easily accommodate the various PWM strategies described earlier. The detailed implementation of the various PWM methods will be given. Finally, both the modulator performance and the implementation strategy are experimentally validated.

3.4.1 Digital PWM modulator topologies

Hardware-based digital PWM modulators such as those using EPROMs are inflexible and highly complex, and have largely been superseded by software-based modulators. Currently there are many hardware formats that have been proposed to digitally implement feedforward PWM, of which the most common ones are,

(a) Single-counter implementation

(b) Two-counter implementation

(c) Three-counter implementation

(d) Four-counter implementation

Of these the four-counter topology is simplest in design and is more versatile of being able to implement almost all the PWM strategies, as will be discussed later. In addition the computation overhead is the least. It will be shown that using advanced circuit integration techniques, a minimal system can be obtained for the four-counter implementation, and thus the resulted cost increase is negligible compared to the other methods.

Four-counter implementation

In a modulation process, the fundamental cycle can be divided into a series of sub-cycles (e.g. the carrier cycles in a carrier-based PWM process) and corresponding to each sub-cycle there will be a pulse for each of the three phases (some of which could be null pulses). Dividing each sub-cycle into two halves such that all the rising edges of the three phases sit in the first half period and the falling edges in the second half period, then three counters can be used to define the three-phase pulses edges in each half sub-cycle, whilst the fourth counter is employed to control the timing of the whole process. The principle is illustrated in Fig 3.16, and may be explained as follows. At the start of each sub-cycle three counters are loaded with constants t_{a1} , t_{b1} and t_{c1} that correspond to the timings of the prepulse times for the three phases, whilst the number loaded into the fourth counter represents the first half sub-cycle period T_1. On completion of each phase timing period, the appropriate phase output is set via a logic circuit. When the fourth counter is counted down to zero, the three phase counters are reloaded with constants t_{a2} , t_{b2} and t_{c2} corresponding to the remaining pulse width times, and the fourth counter is again loaded with a constant equivalent to the second sub-cycle period T_2. On completion of each pulse period, the appropriate phase output is reset logically and the cycle is repeated.

3.4.2 A digital PWM modulator

In line with the current trend of digital system integration to minimise component count to reduce cost and increase reliability, the customised digital PWM modulator was developed based on two integrated circuits, a FPGA (Field Programmable Gate Array) and a DSP (Digital Signal Processor).

The structure of the digital PWM modulator is shown in Fig 3.17(a). The DSP is the Texas Instrument TMS320E15 which is in the form of a single chip microprocessor with an on-board 4K program EPROM [Appendix D]. The customised chip FPGA is the Texas Instrument TPC1020A and has been configured mainly as a quadruple 12-bit counter [Appendix D]. The schematic of the internal structure of the programmed FPGA is shown in Fig 3.17(b). The counters in FPGA operate from a fixed 2.5 MHz counter clock which gave a resolution of approximately 0.01 degrees for the pulse edges at a 50 Hz fundamental frequency and 0.1 degrees for a 500 Hz output. In each switching cycle, the four counter values are calculated in the DSP and transferred to the inputs of the corresponding counters through 12-bit latches. The counter 0 free runs and when its count reaches zero all four counters are automatically reloaded with the precalculated values. This "count down to zero" signal is also used as an interrupt to control the software. The "count down to zero" signals of other counters are used to form the phase PWM output pulses via negative edge toggled flip-flops. The modulator circuit has been designed to be capable of generating PWM at inverter switching frequencies of up to 6 kHz, a value typically used in high power traction drives.

Although the four-counter implementation scheme is ideally suited to regular sampling PWM, it can be adapted to cater for unequally spaced pulse formations, such as those of off-line optimal PWM techniques, by arranging for the hardware to have a facility of generating a null count, i.e. sending a zero to any counter that will result in no change in the pulse output.

The modulator hardware and software allow on-line programming of the PWM parameters. These include,

PWM mode selection

Output frequency adjustment

Depth of modulation

Frequency ratio setting

Phase angle adjustment

Third harmonic factor adjustment (for sub-optimal and adjustable PWM methods)

Zero vector ratio adjustment (for vector space PWM)

Sampling factor adjustment (for adjustable regular PWM)

Pulse width limit setting

Interlocks to prevent sudden parameter variation

The counter clock frequency can be varied up to 10MHz to extend the maximum fundamental and switching frequencies.

3.4.3 Implementation of PWM strategies

As described earlier, to generate the PWM pulse pattern only two properly defined times are required for one pulse in one phase. In the four-counter scheme the pulse is sub-divided into two periods set by the first counter, and the other counters are then used to count the intervals to the pulse leading edges and then the falling edges. In this section the details of the implementation of the various PWM methods will be discussed.

3.4.3.1 Implementation of natural sampling PWM

An exact form of natural sampling PWM would be difficult to be realised digitally due to the transcendental form of relationship which governs the pulse widths. However, the process may be approximated by linearly interpolating the modulating curve over each half carrier cycle [Mellor 1992], as shown in Fig 3.18. The pulse width in this case is determined by,

$$t_1 = \frac{1 - S_1}{2 + (S_2 - S_1)} \frac{T}{2} \tag{3.61}$$

$$t_2 = \frac{1 + S_2}{2 + (S_2 - S_3)} \frac{T}{2} \tag{3.62}$$

where S_1 , S_2 and S_3 are the values of the modulating wave sampled every half carrier cycle.

Since the linear interpolated natural PWM can be considered as a special case of the adjustable PWM, its detailed implementation is the same as adjustable PWM and is described later in the relevant section.

3.4.3.2 Implementation of regular sampling processes

The inherent sampling and the simplicity of regular sampling PWM as described in Eqn. (3.16) enable it to be readily implemented in microprocessor-based control systems.

Both the symmetrical and the asymmetrical regular sampling PWM methods can be considered as special cases of the sub-optimal PWM. The first counter is loaded with a constant equal to half of the carrier cycle,

$$T_1 = T_2 = \frac{1}{2f_s} \tag{3.63}$$

Taking phase A as an example, the values loaded into phase counters to define the rising and falling edges of the three phase pulses are then calculated from,

$$t_1 = \frac{T}{4}(1 + S_1) \tag{3.64}$$

$$t_2 = \frac{T}{4}(1 - S_2) \tag{3.65}$$

where

$$S_1 = M(\sin(\omega t_k + \delta) + \beta \sin 3(\omega t_k + \delta)) \tag{3.66}$$

$$S_2 = M(\sin\omega(t_k + \delta + T/2) + \beta \sin 3\omega(t_k + \delta + T/2)) \tag{3.67}$$

and t_k is defined in Eqn. (3.17).

A digital representation of the required three phase modulating signal is precalculated and stored in a look-up table, such as,

DATA $\sin 3\omega t$, $\sin \omega t$, $\sin (\omega t + 2\pi/3)$, $\sin (\omega t + 4\pi/3)$

The detailed implementation of the regular sampling process is shown by the flowchart in Fig 3.19.

If the third harmonic factor is set to zero, the process will be identical to asymmetric regular sampling PWM. If the second sampled value S_2, is replaced by the first sampled value S_1 in Eqn. (3.65), then symmetric regular sampling PWM is obtained.

3.4.3.3 Implementation of adjustable sampling process

Similar to natural sampling, the pulse edges are not easily derived directly from the intersections of the triangular waveform and the transformed modulating waveform. Instead the transformed waveform is approximated by a line interpolated between two points derived from the samples of the modulating waveform.

$$m_k(t) = m(t_k) \tag{3.68}$$

$$m_k(t_{k+1}) = m\left(t_k + (1-\varepsilon)\frac{T}{2}\right) \tag{3.69}$$

The first sample point, Eqn. (3.68), is identical to that used in regular sampling, i.e. Eqn. (3.66). The other is obtained from later (for $\varepsilon < 1$) or previous ($\varepsilon > 1$) samples of the modulating waveform. The transformed sampled values are calculated from regular sampled modulating wave data, using,

$$S_2' = S_{2-N} + (N-\varepsilon)(S_{2-N} - S_{1-N}) \tag{3.70}$$

$$S_3' = S_{3-N} + (N-\varepsilon)(S_{3-N} - S_{2-N}) \tag{3.71}$$

where

$$N = Integer\ (\varepsilon) \tag{3.72}$$

$$S_r = m\,(t_{k-1+r}),\ \ with\ r = 1, 2, 1-N, 2-N, \text{and } 3-N \tag{3.73}$$

Applying linear interpolation between (t_k, S_1) and (t_{k+1}, S_2'), (t_{k+1}, S_2) and (t_{k+2}, S_3') the pulse edges will be determined by the time intervals,

$$t_1 = \frac{1 - S_1}{2 + (S_{2-N} - S_1) - (N - \varepsilon)(S_{2-N} - S_{1-N})} \frac{T}{2} \tag{3.74}$$

$$t_2 = \frac{1 + S_2}{2 + (S_2 - S_{3-N}) - (N - \varepsilon)(S_{3-N} - S_{2-N})} \frac{T}{2} \tag{3.75}$$

However, the above two equations can be simplified if the range of the sampling factor ε is restricted, for example,

(a) When the frequency ratio is 9, ε would normally be between 1.0 and 2.0, Eqn. (3.35). The pulse edges are then determined from,

$$t_1 = \frac{1 - S_1}{2 - (1 - \varepsilon)(S_1 - S_0)} \frac{T}{2} \tag{3.76}$$

$$t_2 = \frac{1 + S_2}{2 - (1 - \varepsilon)(S_2 - S_1)} \frac{T}{2} \tag{3.77}$$

(b) When the frequency ratio is an odd triplen and over nine, the parameter ε is set to $\frac{R-1}{4}$, Eqn. (3.36), and the pulse timings then become,

$$t_1 = \frac{1 - S_1}{2 - (S_1 - S_{2-N})} \frac{T}{2} \tag{3.78}$$

$$t_2 = \frac{1 + S_2}{2 - (S_{3-N} - S_2)} \frac{T}{2} \tag{3.79}$$

The Eqns. (3.76) and (3.77), or the Eqns. (3.78) and (3.79), can be generalised as,

$$\begin{cases} t_1 = \dfrac{a_1}{1 - x_1} \\ t_2 = \dfrac{a_2}{1 - x_2} \end{cases} \tag{3.80}$$

where

$$a_1 = \frac{T}{4}\,(\,1 + S_1\,) \tag{3.81}$$

$$a_2 = \frac{T}{4}\,(\,1 + S_2\,) \tag{3.82}$$

$$x_1 = \begin{cases} (1 - \varepsilon)\,(\,S_1 - S_0\,)/2\,, & \text{for } R = 9 \\ (\,S_{2-N} - S_1\,)/2\,, & \text{for } R = 15\,,\,21\,,\,27\,,\cdots \end{cases} \tag{3.83}$$

$$x_2 = \begin{cases} (1 - \varepsilon)\,(\,S_1 - S_2\,)/2\,, & \text{for } R = 9 \\ (\,S_2 - S_{3-N}\,)/2\,, & \text{for } R = 15\,,\,21\,,\,27\,,\cdots \end{cases} \tag{3.84}$$

$$S_r = M\,(\,\sin\,(\omega(t + \frac{T}{2}\,r) + \delta\,) + \beta \sin 3(\omega(t + \frac{T}{2}\,r) + \delta\,))\,,\ \textit{with}\ r = 0,\,1,\,2,\,2\text{–}N,\,3\text{–}N \tag{3.85}$$

Since

$$\begin{aligned} |\,x_1\,| &< 1 \\ |\,x_2\,| &< 1 \end{aligned} \tag{3.86}$$

the times of the pulse edges can be evaluated from the numerical series,

$$\begin{cases} t_1 = a_1 + x_1\,(a_1 + x_1\,(a_1 + \cdots\,))) \\ t_2 = a_2 + x_2\,(a_2 + x_2\,(a_2 + \cdots\,))) \end{cases} \tag{3.87}$$

In the real-time calculations the above expression is truncated when it reaches the required accuracy, i.e. when the frequency ratio is 9, only the first three terms of the series need to be evaluated, and for frequency ratios above 9, the first nine terms of the series are evaluated.

The remaining implementation of adjustable PWM is identical to regular sampling PWM.

3.4.3.4 Implementation of vector space PWM

To implement the vector space PWM, the three phase pulse trains in the vector space should be transformed to the three phase domain. From Eqn. (3.56) it is noticed that in one cycle zero vectors ($\vec{V_0}$ and/or $\vec{V_7}$) should be inserted to fill the sampling interval left by the two non-zero vectors. If both $\vec{V_0}$ and $\vec{V_7}$ are used, it is essential that $\vec{V_0}$ and $\vec{V_7}$ are placed at the beginning and the end of one cycle, to ensure transition from one state to the next by switching only one leg. The cycle with transition from $\vec{V_0} - \cdots - \vec{V_7}$ coincides with rising edges of the three phase pulses, and the cycle with transition from $\vec{V_7} - \cdots - \vec{V_0}$ coincides with falling edges of the three phase pulses.

The vector space is divided into six 60^o-wide sectors by the six non-zero vectors, and each sector is sub-divided into Ns segments representing individual switching intervals. The inverter state is changed three times within each segment with each change of state requiring only one switching event across the three phases. Therefore the number of pulses P of the switching signal in a given phase of the inverter, per cycle of the output frequency, is $P = 3\,N_S$. An example with $N_S = 1$ is shown in Fig 3.21.

Due to the sextant symmetry, only the range of $0^o - 60^o$ is required when calculating the state duty ratios of d_x, d_y and d_z, or the time intervals of T_1, T_2 and T_0,

$$T_1 = \frac{T_s}{2} \cdot \frac{\sqrt{3}}{2} M \sin(60^o - \alpha) \tag{3.88}$$

$$T_2 = \frac{T_s}{2} \cdot \frac{\sqrt{3}}{2} M \sin\alpha \tag{3.89}$$

$$T_0 = \frac{T_s}{2} - T_1 - T_2 \tag{3.90}$$

where

$$0 \le \alpha = \omega t + \delta < 60^o \tag{3.91}$$

The other five vector space sectors can be mapped to the base sector ($\theta^o = 0 - 60^o$) by

$$\theta = N * \theta^o \quad (N = 1, 2, 3, 4, 5) \tag{3.92}$$

If it is assumed that the portion of zero vector time T_{01}, which is,

$$T_{01} = z \cdot (\frac{T_s}{2} - T_1 - T_2), \quad z = 0 - 1 \tag{3.93}$$

is assigned to the first zero vector in a cycle, and that the assignment of T_1 and T_2 to the two non-zero vectors in a cycle is in an anti-clockwise direction, i.e.,

$$\rightarrow \vec{V4} \rightarrow \vec{V6} \rightarrow \vec{V2} \rightarrow \vec{V3} \rightarrow \vec{V1} \rightarrow \vec{V5} \rightarrow$$

then, for the pulse rising edges in the base sector, the voltage vector state starts from $\vec{V0}$ (T_{01}) and ends at $\vec{V7}$, with the intermediate states being $\vec{V4}$ (T_1) and $\vec{V6}$ (T_2). Considering the desired feature of a transition from one state to the next should involve only one switching event the best sequence is,

$$\vec{V0} \rightarrow \vec{V4} \rightarrow \vec{V6} \rightarrow \vec{V7}$$

i.e., switching A-B-C.

Therefore, the three time intervals T_{01}, $T_{01} + T_1$ and $T_{01} + T_1 + T_2$ should be assigned to phases A, B and C, respectively.

Similarly, for the pulse falling edges, the vector states start at $\vec{V7}$ (T_{01}) and ends at $\vec{V0}$, with intermediate vectors $\vec{V4}$ (T_1) and $\vec{V6}$ (T_2). The sequence of states is thus,

$$\vec{V7} \rightarrow \vec{V6} \rightarrow \vec{V4} \rightarrow \vec{V0}$$

i.e., switching C-B-A.

Therefore, the time intervals of $T_{01}+T_1+T_2$, $T_{01}+T_2$ and T_{01} are assigned to phase A, B and C, respectively.

Extending this methodology to the other sectors, and defining,

$$\begin{cases} U = T_{01} \\ V_1 = T_{01} + T_1 \\ V_2 = T_{01} + T_2 \\ W = T_{01} + T_1 + T_2 \end{cases} \tag{3.94}$$

a mapping between the times and the phases is obtained, as in Table 3.3.

If the values of U, V_1, V_2 and W are arranged in a memory space as in Table 3.4, and the table is updated each cycle, then the timings of rising and falling edges for each phase correspond to the following table addresses,

$$\begin{cases} T_{1a} = (ADDR + N) \\ T_{2a} = (ADDR + 3 + N) \end{cases} \tag{3.95}$$

$$\begin{cases} T_{1b} = (ADDR + 4 + N) \\ T_{2b} = (ADDR + 1 + N) \end{cases} \tag{3.96}$$

$$\begin{cases} T_{1c} = (ADDR + 2 + N) \\ T_{2c} = (ADDR + 5 + N) \end{cases} \tag{3.97}$$

where N is the sector sequence number,

$$\text{N} = 0, 1, 2, 3, 4, 5 \tag{3.98}$$

and T_{a1}, T_{a2}, T_{b1}, T_{b2}, T_{c1}, and T_{c2} are defined as in Fig 3.22.

Similar to the implementation of regular sampling process, the vector space PWM is controlled by continuously loading the first counter (counter 0) with a period representing half the carrier cycle. The three other counter values are determined using the procedure,

(a) create a counter constants table in the processor memory space, and,

(b) assign the constants to individual counters, according to the location of the vectors.

Table 3.3. Assignment of time intervals to three phases

Sectors	Edges	Transitions	A	B	C
Base sector	Rising	$\vec{V0} - \vec{V4} - \vec{V6} - \vec{V7}$	U	V_1	W
$0 - 60^o$	Falling	$\vec{V7} - \vec{V6} - \vec{V4} - \vec{V0}$	W	V_2	U
First sector	Rising	$\vec{V0} - \vec{V2} - \vec{V6} - \vec{V7}$	V_2	U	W
$60^o - 120^o$	Falling	$\vec{V7} - \vec{V6} - \vec{V2} - \vec{V0}$	V_1	W	U
Second sector	Rising	$\vec{V0} - \vec{V2} - \vec{V3} - \vec{V7}$	W	U	V_1
$120^o - 180^o$	Falling	$\vec{V7} - \vec{V3} - \vec{V2} - \vec{V0}$	U	W	V_2
Third sector	Rising	$\vec{V0} - \vec{V1} - \vec{V3} - \vec{V7}$	W	V_2	U
$180^o - 240^o$	Falling	$\vec{V7} - \vec{V3} - \vec{V1} - \vec{V0}$	U	V_1	W
Fourth sector	Rising	$\vec{V0} - \vec{V1} - \vec{V5} - \vec{V7}$	V_1	W	U
$240^o - 300^o$	Falling	$\vec{V7} - \vec{V5} - \vec{V1} - \vec{V0}$	V_2	U	W
Fifth sector	Rising	$\vec{V0} - \vec{V4} - \vec{V5} - \vec{V7}$	U	W	V_2
$300^o - 360^o$	Falling	$\vec{V7} - \vec{V5} - \vec{V4} - \vec{V0}$	W	U	V_1

The vector space PWM only requires samples of the sine wave over a 60^0 interval, and the corresponding data table is arranged as,

DATA $\sin(\pi/3 - \omega t)$, $\sin \omega t$

The detailed program flowchart is given in Fig 3.23.

Table 3.4. A data table for pulse edges determination.

ADDR	
	U
	V_2
	W
	W
	V_1
	U
	U
	V_2
	W
	W
	V_1
	U

An alternative implementation method which avoids the use of a look-up table will be discussed later in Chapter 5.

3.4.3.5 Implementation of optimal PWM processes

The pulse patterns of the optimal PWM methods are generally unequally spaced. However, the four counter structure of the PWM modulator can still be used to generate the required pulse train. First by defining a group of irregularly spaced trigger points a relationship is established between the pulse pattern and the pulse interval counter (counter 0). The intervals between the required three-phase pulse edges and the nearest trigger points are then used as the counter constants of the three phase counters. If a change in output is not required, i.e. the phase counter value is greater than the corresponding interval counter value, a phase counter will be loaded with zero.

The counter settings that would be used to generate the pulse patterns with a 50 Hz fundamental with a counter clock of 2.5 MHz are given in Table 3.5 and Table 3.6, respectively for optimal harmonic elimination PWM and optimal harmonic minimisation PWM. Here it is seen that the optimal pulse pattern can be realised by varying the interval

count t_o and using zero counts in the edge timings. The flowchart for the implementation is shown in Fig. 3.24.

Table 3.5. Optimal harmonic elimination PWM. Counter constants for the case of M=0.9

Trigger	t_0	t_a	t_b	t_c	Trigger	t_0	t_a	t_b	t_c
14.615	7.115	4.895	3.455	0	194.615	7.115	4.895	3.455	0
21.73	16.54	2.22	0	14.32	201.73	16.54	2.22	0	14.32
38.27	7.115	0	3.66	2.22	218.27	7.115	0	3.66	2.22
45.385	29.23	25.775	3.455	14.615	225.385	29.23	25.775	3.455	14.615
74.615	7.115	3.455	0	4.895	254.615	7.115	3.455	0	4.895
81.73	16.54	0	14.32	2.22	261.73	16.54	0	14.32	2.22
98.27	7.115	3.66	2.22	0	278.27	7.115	3.66	2.22	0
105.384	29.23	3.455	14.615	0	285.385	29.23	3.455	14.615	25.775
134.615	7.115	0	4.895	3.455	314.615	7.115	0	4.895	3.455
141.73	16.54	14.32	2.22	0	321.73	16.54	14.32	2.22	0
158.27	7.115	2.22	0	3.66	338.27	7.115	2.22	0	3.66
165.285	29.23	14.615	25.775	3.455	345.385	29.23	14.615	25.775	3.455

Table 3.6. Optimal harmonic minimisation PWM. Counter constants for M=0.9.

Trigger	t_0	t_a	t_b	t_c	Trigger	t_o	t_a	t_b	t_c
3.305	10.43	3.305	7.635	0	183.305	10.43	3305	7.635	0
13.735	8.205	0	2.795	0	193.735	8.205	0	2.795	0
21.94	8.06	0	5.41	0	201.94	8.06	0	5.41	0
30	8.06	0	2.65	0	210	8.06	0	2.65	0
38.06	8.205	0	5.41	0	218.06	8.205	0	5.41	0
46.265	10.43	0	2.795	7.125	226.265	10.43	0	2.795	7.125
56.695	6.61	0	0	3.305	236.695	6.61	0	0	3.305
63.305	10.43	7.635	0	3.305	243.305	10.43	7.635	0	3.305
73.735	8.205	2.795	0	0	253.735	8.205	2.795	0	0
81.94	8.06	5.41	0	0	261.94	8.06	5.41	0	0
90	8.06	2.65	0	0	270	8.06	2.65	0	0
98.06	8.205	5.41	0	0	278.06	8.205	5.41	0	0
106.265	10.43	2.795	7.125	0	286.265	10.43	2.795	7.125	0
116.695	6.61	0	3.305	0	296.695	6.61	0	3.305	0
123.305	10.43	0	3.305	7.635	303.305	10.43	0	3.305	7.635
133.735	8.205	0	0	2.795	313.735	8.205	0	0	2.795
141.94	8.06	0	0	5.41	321.94	8.06	0	0	5.41
150	8.06	0	0	2.65	330	8.06	0	0	2.65
158.06	8.205	0	0	5.41	338.06	8.205	0	0	5.41
166.265	10.43	7.125	0	2.795	346.265	10.43	7.125	0	2.795
176.695	6.61	3.305	0	0	356.695	6.61	3.305	0	0

Note: in Table 3.5 and 3.6 the data are in degrees.

3.4.3.6 Implementation of quasi-square wave switching

The implementation of quasi-square wave switching is trivial, and relates to the flowchart shown in Fig. 3.25.

3.4.4 Performance of the modulator on a practical inverter drive

The four-counter structure provides a simple and computational efficient method of implementing PWM. However, the practical realisation of a modulator may introduce spectral errors because of the limitations of the fixed-point arithmetic and finite word length in the digital system, and due to switching delays in an inverter and its gate drivers.

3.4.4.1 Digital implementation effects

The DSP TMS320E15 is a fixed-point processor that uses a fixed word length of 16 bits to represent variables and coefficients and has a 32 bits arithmetic core. The finite word-length errors are introduced as a result of truncation during calculations, and round-off errors in fixed coefficients (coefficient quantisation). For example, the 12-bit counter in the PWM modulator gives an accuracy of 1 in 4096 or an error of 0.02%.

To eliminate the effects of overflow and minimise truncation errors during the intermediate and final calculation states, appropriate scaling factors must be developed so that the full dynamic range of variables and coefficients are catered for, and the equations must be modified to ensure minimal rounding errors. For example, in order to obtain the correct frequency ratio the 12 bits data was read and multiplied by the sample time held in memory. The result was then divided by 4096 to reduce its size so that it could be used in further calculations. As integer arithmetic was used the sine values stored in the look up table were multiplied by 1024 and taken to the nearest integer values. The scaling factors of 1024 and 4096 were used to ease the problematic division by employing the multiple right shift in the DSP instruction set.

Comparisons of the spectrum distributions of the digital modulator output and the idealised modulator performance are given in Fig 3.26(a) and (b), Fig 3.27(a) and (b), and Fig 3.28(a) and (b), respectively for regular sampling PWM, adjustable PWM and optimal harmonic elimination PWM. It is observed that the effects of digital quantisation are negligible.

3.4.4.2. Spectral limitations introduced by a practical inverter

The finite switching times of the power semiconductors in a practical inverter will also potentially introduce spectral errors. A dead zone is usually required between the switching signals of the upper and lower devices in a phase leg to prevent simultaneous conduction, and pulses with very narrow widths are normally eliminated or dropped. Also, the effect of conduction voltage drops across the switches and freewheel diodes will lead to a non uniform pulse amplitude. The spectral errors can be generalised into four phenomena, as indicated in Fig 3.29,

(a) rising spectral errors occurring at the leading edges of the PWM signal;

(b) falling spectral errors occurring at the trailing edges of the PWM signal;

(c) commutation timing errors occurring at the trailing and leading edges of PWM waveform;

(d) amplitude distortion errors due to variation of the pulse amplitude caused by device conduction voltages and as a result of the finite smoothing capability of the d.c. link filter capacitance.

Various techniques, including time domain impulse train [Theocharis 1990] and Fourier series representation[Pitel 1981], have been used to analyse these effects. The results broadly show that the spectral errors are linearly dependent on the rising, falling and commutation time intervals.

3.4.4.3 Experimental investigation of spectral errors

The practical performance of the digital modulator was evaluated on the experimental inverter motor drive system, and the spectra and the THD of the modulator output switching signals

and the inverter output voltages were measured using the HP-35660A Dynamic Signal Analyser. The results are compared against the calculated THD for the idealised waveform in Table 3.7 for various PWM strategies.

From these tests it is concluded that the digital implementation of PWM has negligible effect on THD, whilst a small increase in the THD is observed on the inverter output. However since at most the increase in THD is in the order of 3%, the spectral errors introduced by the inverter can be ignored.

Table 3.7. Comparison of simulated and tested THD figures. Modulation depth is 90%.

PWM method		Calculated	Modulator signal	Inverter output voltage	
				No-load	60% load
Symmetric regular PWM	Ratio=9	5.40	5.44	5.46	5.49
	R=15	3.21	-	3.25	3.27
	R=45	0.94	-	0.98	0.99
Sub-optimal PWM	R=9	4.65	4.68	4.72	4.76
	R=15	2.74	-	2.78	2.79
	R=45	0.68	-	0.73	0.73
Adjustable PWM	R=9	4.12	4.14	4.16	4.19
Harmonic elimination PWM	R=9	4.87	4.90	4.95	4.99

An example of the measured spectra when the sub-optimal PWM was applied to the drive system with motor operated at 60% of full load is shown in Fig. 3.30. Comparisons of practically obtained results with the ideal distribution in Fig 3.30(a) indicate a clear similarity in the spectra. An investigation of the spectral errors in the inverter phase voltage, as shown in Fig 3.30(e), show a 50 Hz component which is introduced by the mains derived d.c. link supply, and harmonic contents caused by mechanical eccentricity of the induction motor rotor, which occur at the frequencies of,

$$fh = (1 \pm \frac{1-s}{p}) f1 \qquad (3.99)$$

where s is the machine speed slip, p is the machine pole pairs and f_1 is the supply frequency. The motor phase current spectrum distribution is also shown in Fig 3.30(f).

Finally, various PWM strategies were applied to the inverter fed induction machine drive at the operating condition used in preceding sections, i.e. a frequency ratio of 9 and a modulation depth of 0.9. The measured machine phase voltage and current waveforms are shown in Fig 3. 31.

3.4.5 Comparison of the digital implementation of the various PWM strategies

Generally, the digital implementation of a PWM strategy is not a problem with today's development in digital signal processing. However, a PWM method, which is easy to implement, has a fast execution time and uses minimal processor memory space, is always preferred. The realisation of a full optimal PWM modulator is cumbersome because of the need to access a large memory which contains tabulated pulse patterns for the full range of modulation depths and frequency ratios. In view of this and the complex nature of generating the waveforms, the optimal PWM methods, i.e. optimal harmonic elimination and optimal harmonic minimisation, are rarely used. The implementation of the regular sampling and the vector space method is by comparison much simpler. The computational overhead needed to perform these algorithms on TMS320E15 DSP are summarised in Table 3.8. The vector space method has the fastest execution time and as a result would be preferred to the sub-optimal technique, as they have the similar performance. The adjustable regular process uses a more complex algorithm to calculate the pulse edges, which is reflected in its execution time twice that of vector space PWM. However, it does have a lower harmonic distortion which is beneficial at low switching frequencies where execution time is not critical.

Table 3.8 Comparison of TMS320E15 implementation of PWM strategies

PWM methods	Number of cycles	Execution time	Max. switching frequency
Sub-optimal PWM	267	53.4 μs	9.36 kHz
Vector space PWM	245	49.0 μs	10.20 kHz
Adjustable PWM	533	106.6 μs	4.69 kHz

(a)

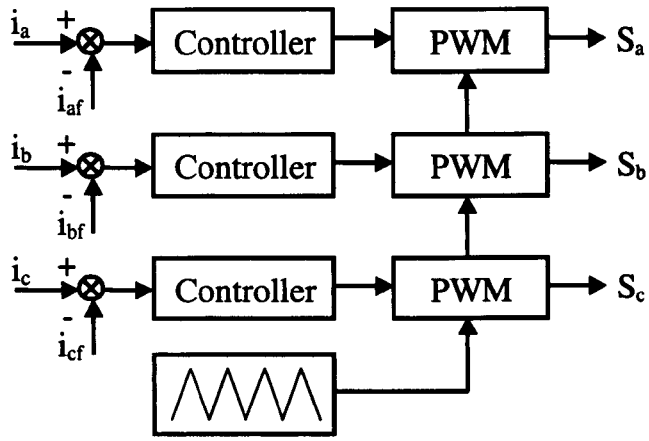

(b)

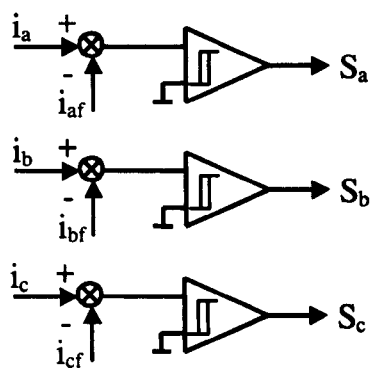

(c)

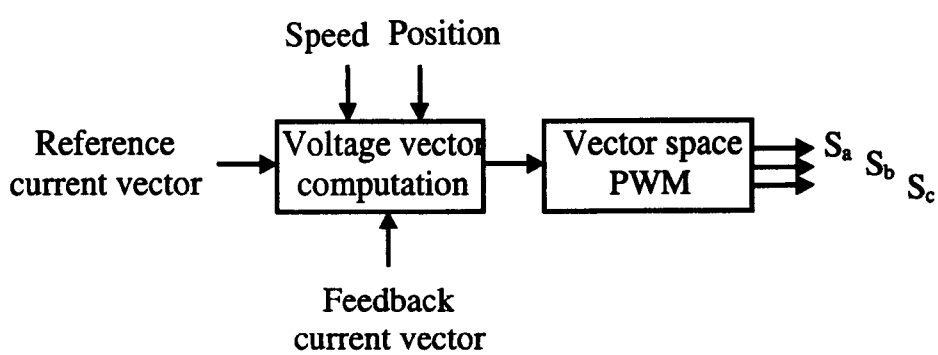

Fig. 3.1 Feedback current control PWM strategies.

(a) Linear control. (b) Hysteresis control. (c) Predictive control.

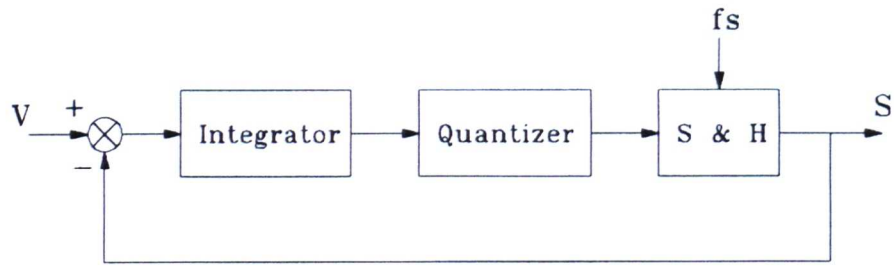

Fig. 3.2 Pulse density modulator.

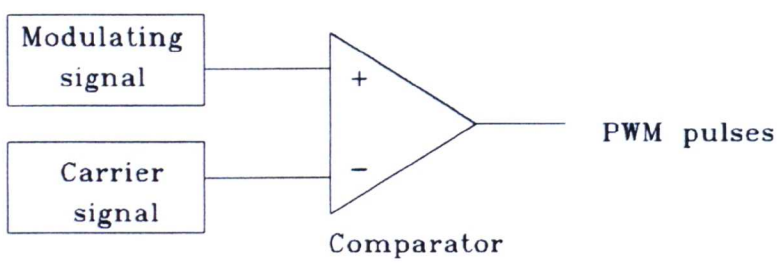

Fig. 3.3 Analogue implementation of natural PWM

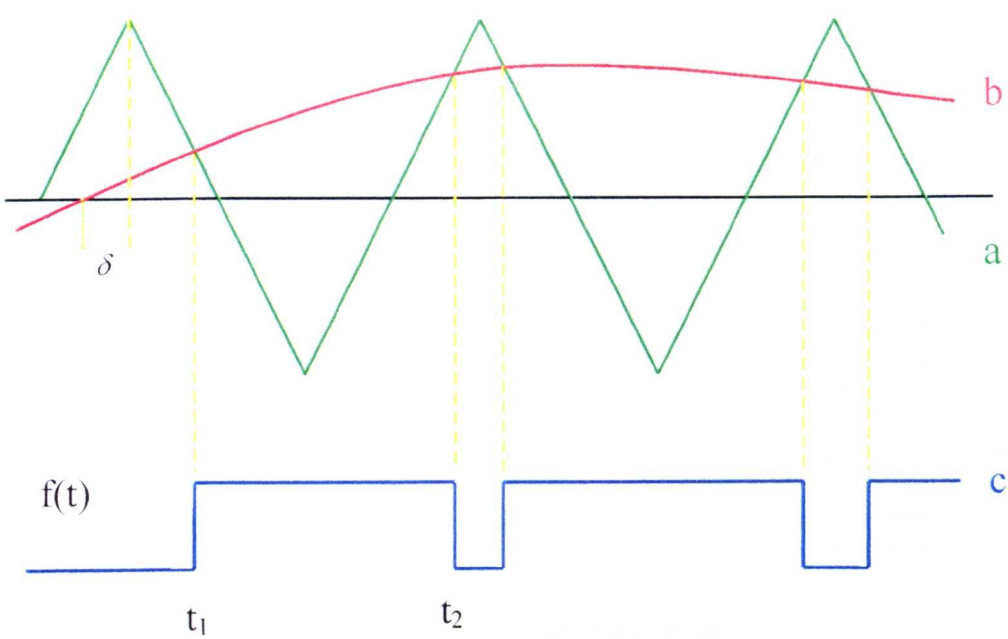

Fig. 3.4 Pulse formation of natural PWM. a - carrier signal, b - modulating signal, c - PWM pulse train.

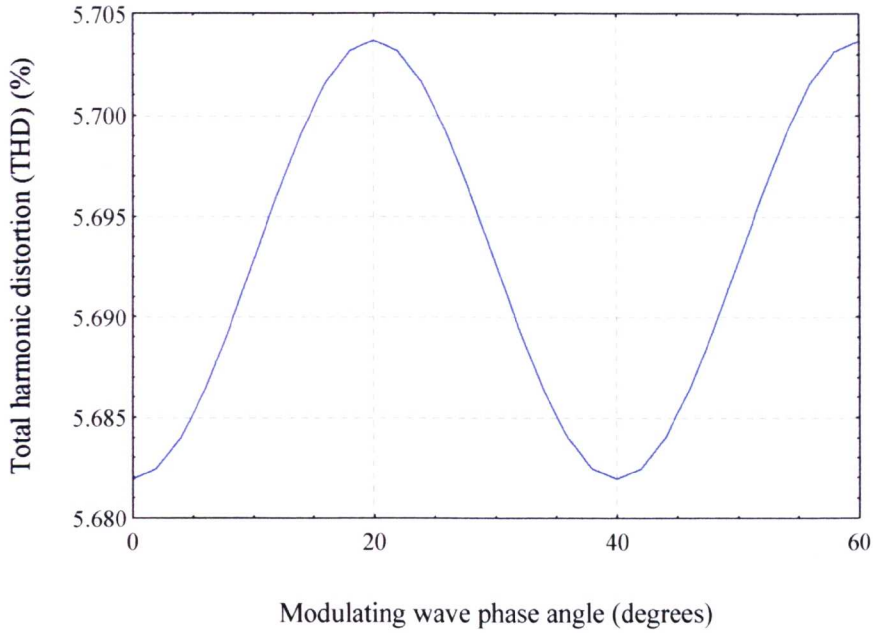

Fig. 3.5. Variation of total harmonic distortion with modulating wave phase angle for natural PWM, the frequency ratio is 9, and the modulation depth is 0.9.

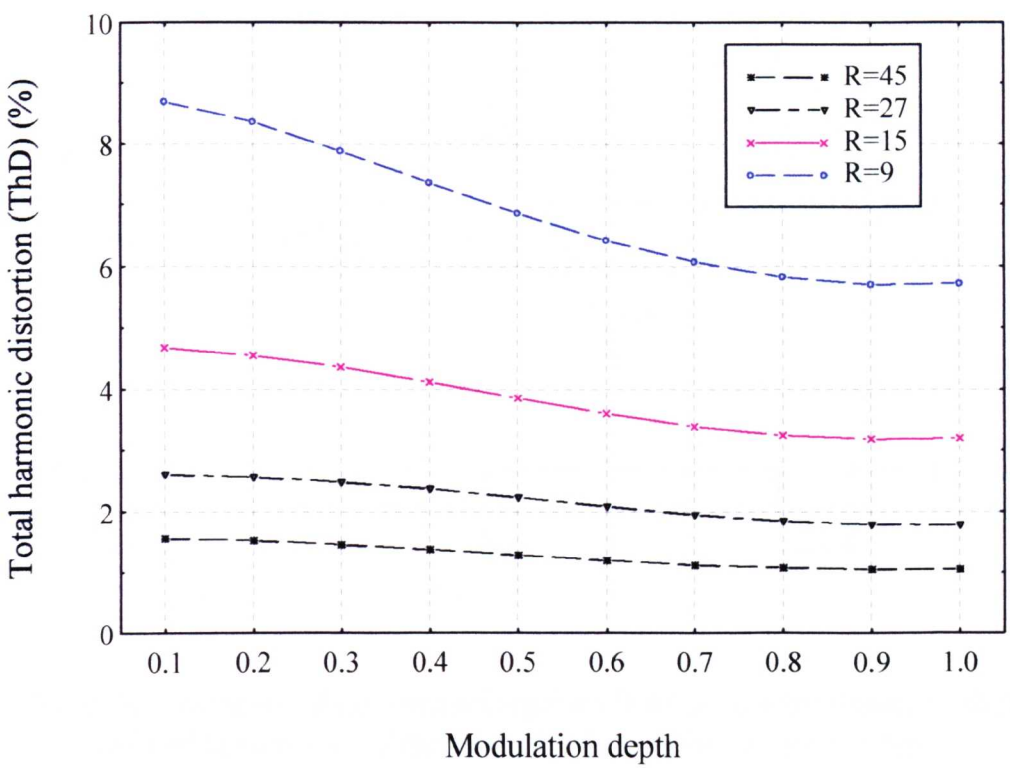

Fig. 3.6. Variation of total harmonic distortion with modulation depth at various frequency ratios for natural PWM.

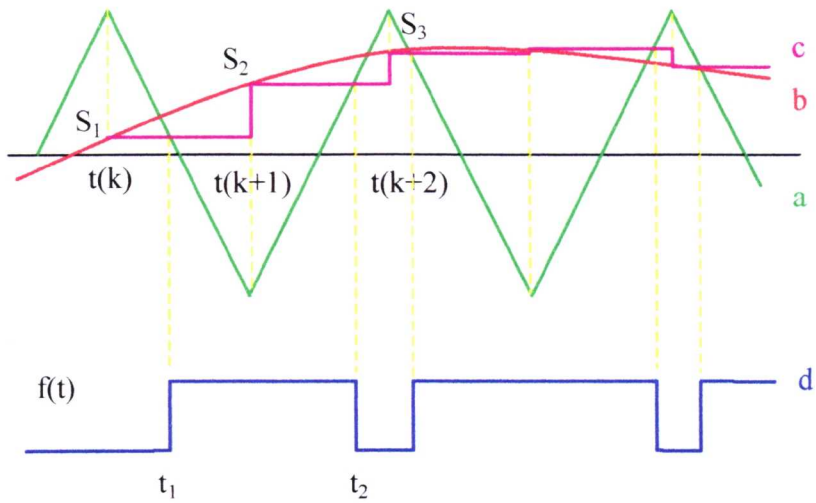

Fig. 3.7 Pulse formation of regular sampling PWM. a - carrier signal, b - modulating signal, c - sampled modulating signal, d - pulse train.

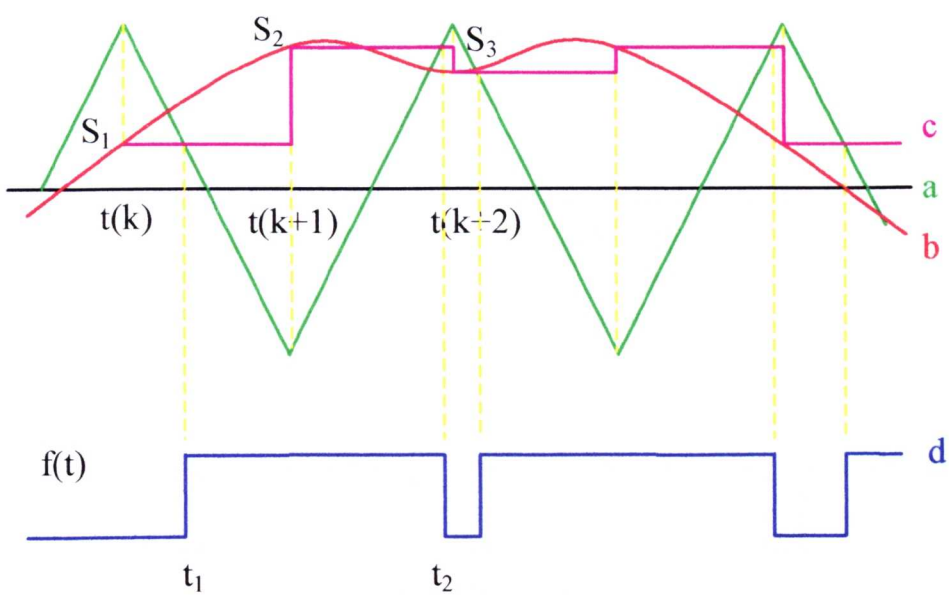

Fig. 3.8 Pulse formation of sub-optimal regular PWM. a - carrier signal, b - distorted modulating signal, c - sampled modulating signal, d - pulse train.

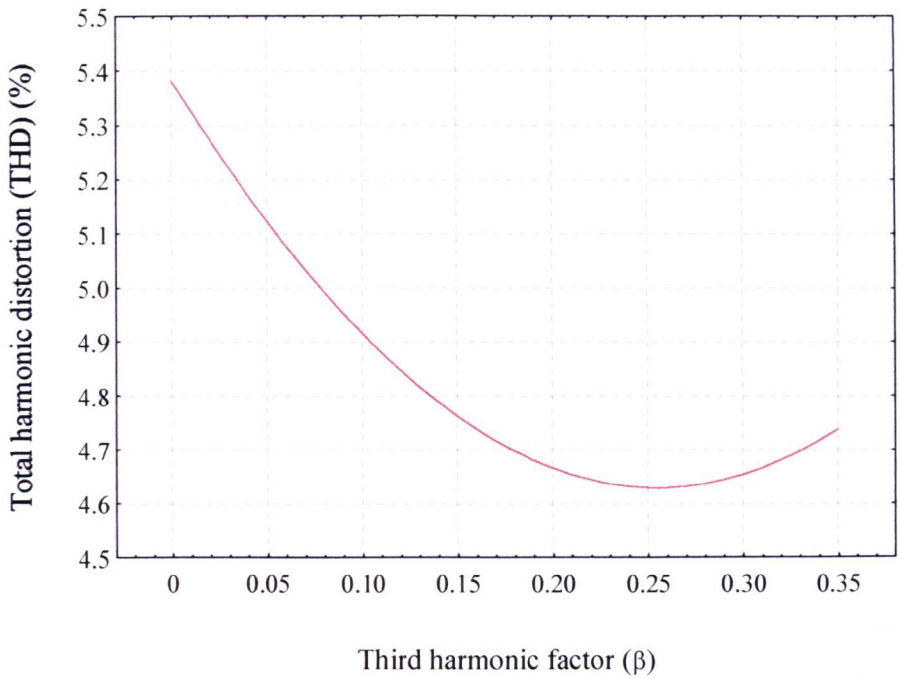

Fig. 3.9. Variation of total harmonic distortion with third harmonic factor for sub-optimal PWM. The frequency ratio is 9, and the modulation depth is 0.9.

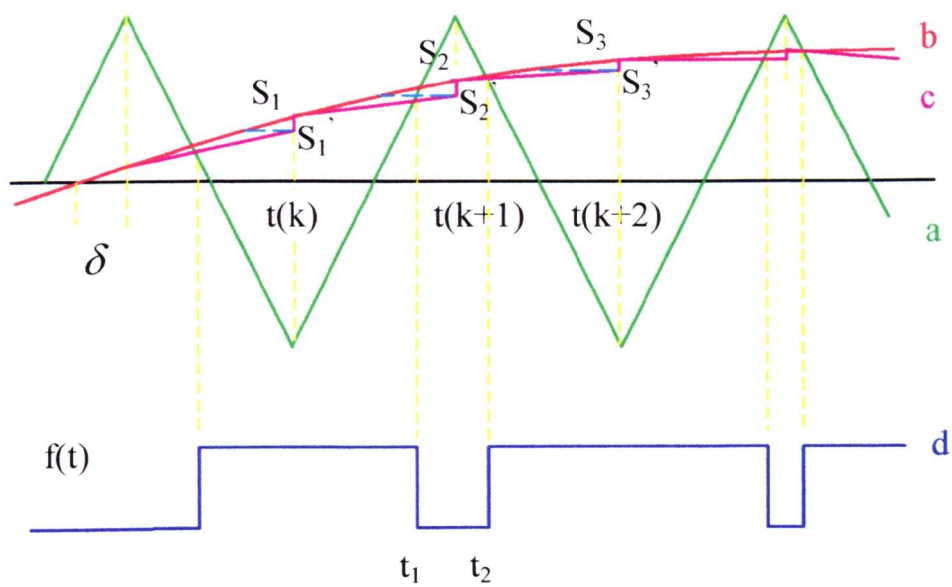

Fig. 3.10 Pulse formation of adjustable regular sampling PWM. a - carrier signal, b - modulating signal, c - transformed modulating signal, d - pulse train

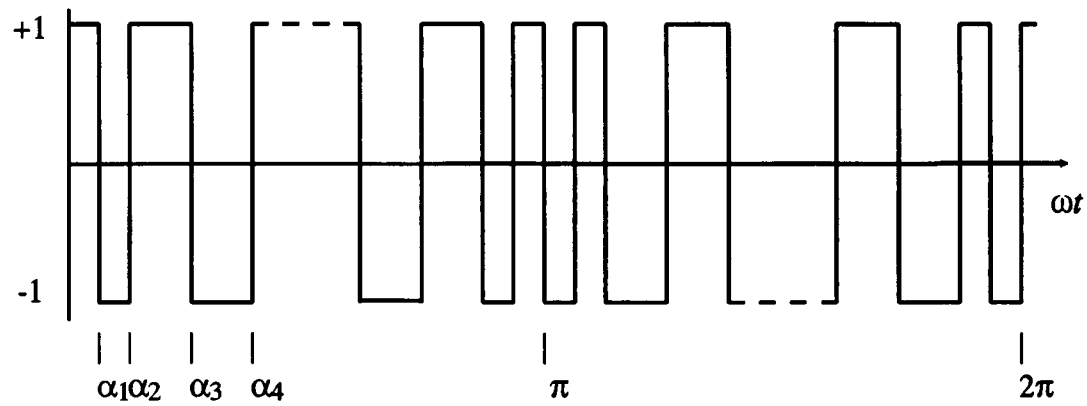

Fig. 3.11 Generalised inverter output waveform with quarter-wave symmetry.

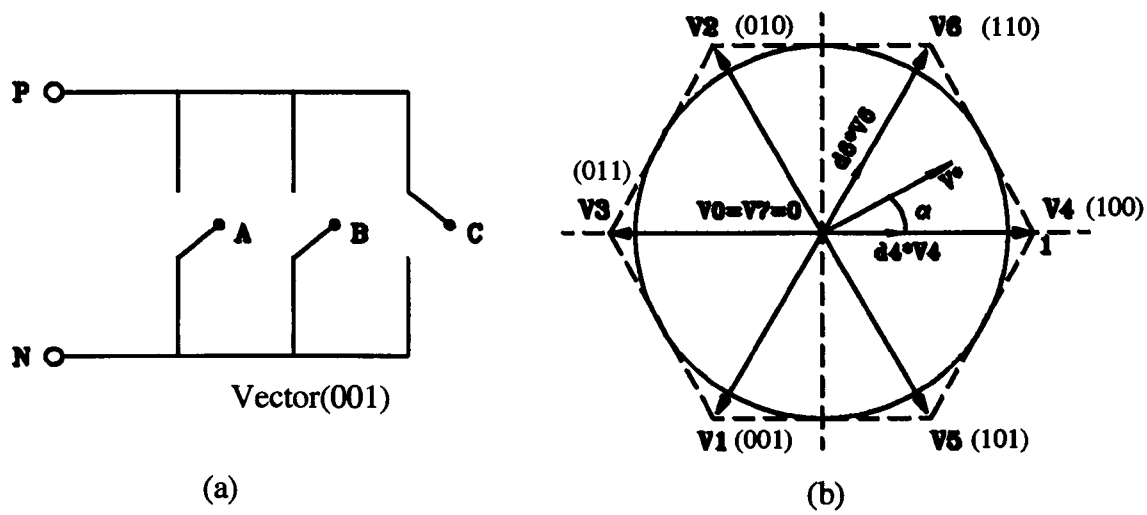

Fig. 3.12 The representative leg voltages and voltage vectors in a three phase inverter.

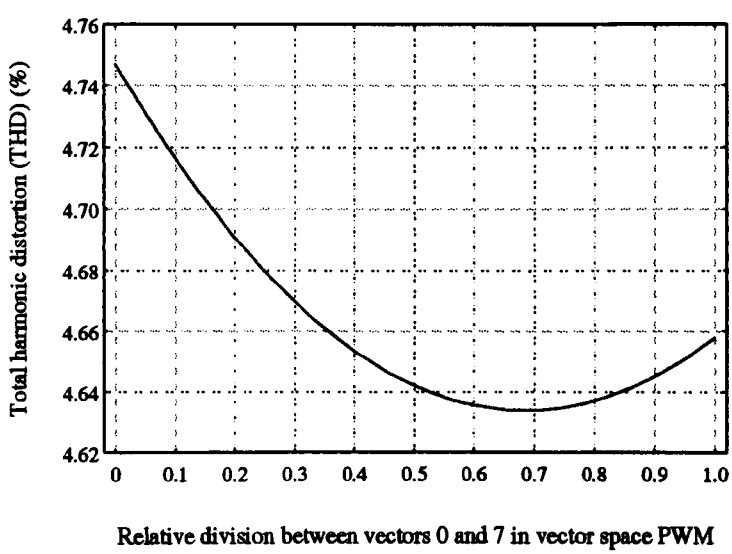

Fig. 3.13. Variation of total harmonic distortion with disposition of zero vectors in vector space PWM.

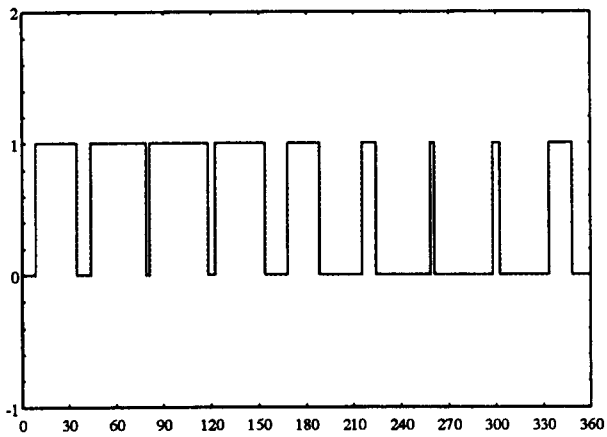

(a) Linear interpolated natural PWM

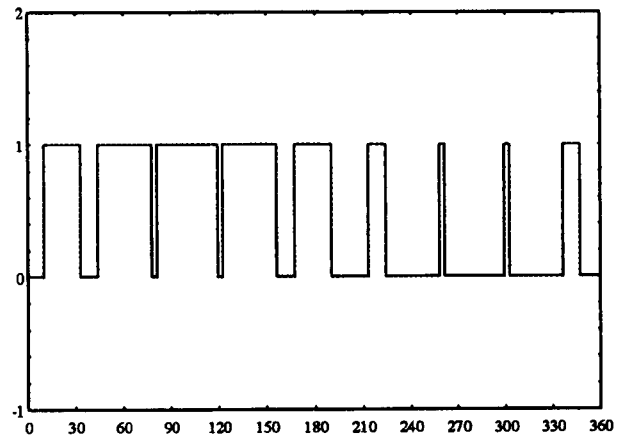

(b) Symmetric regular sampling PWM

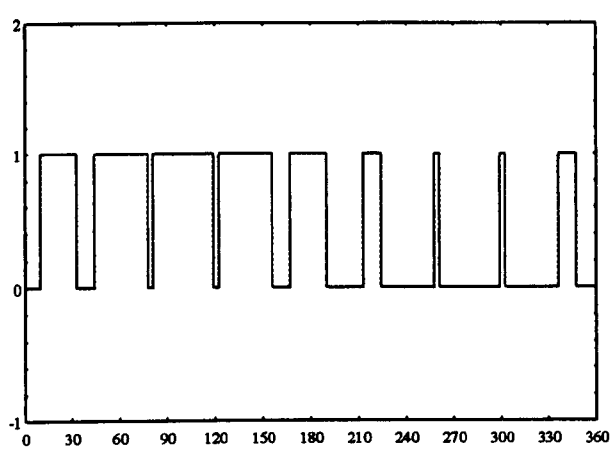

(c) Sub-optimal PWM

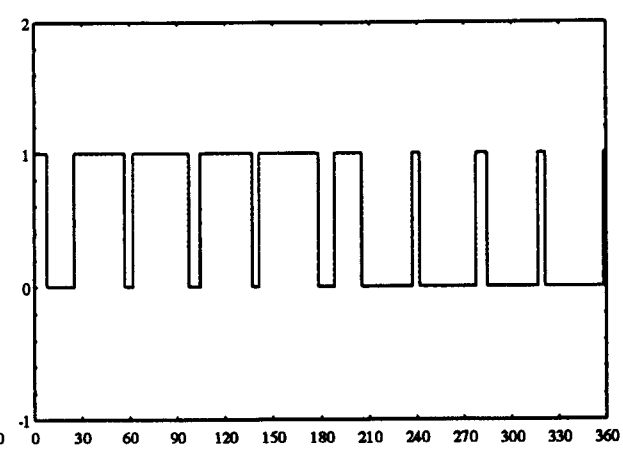

(d) Adjustable sampling PWM

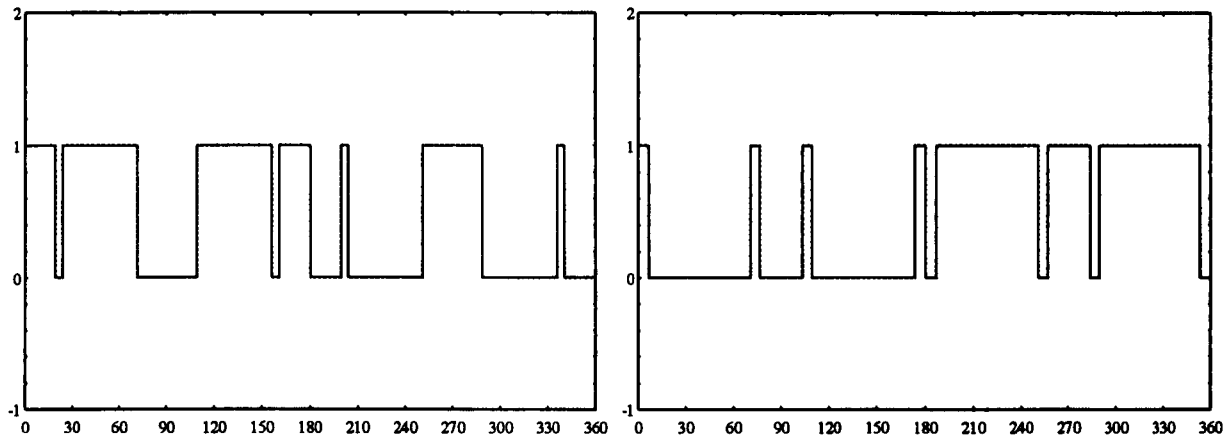

(e) Optimal harmonic elimination PWM

(f) Optimal harmonic minimisation PWM

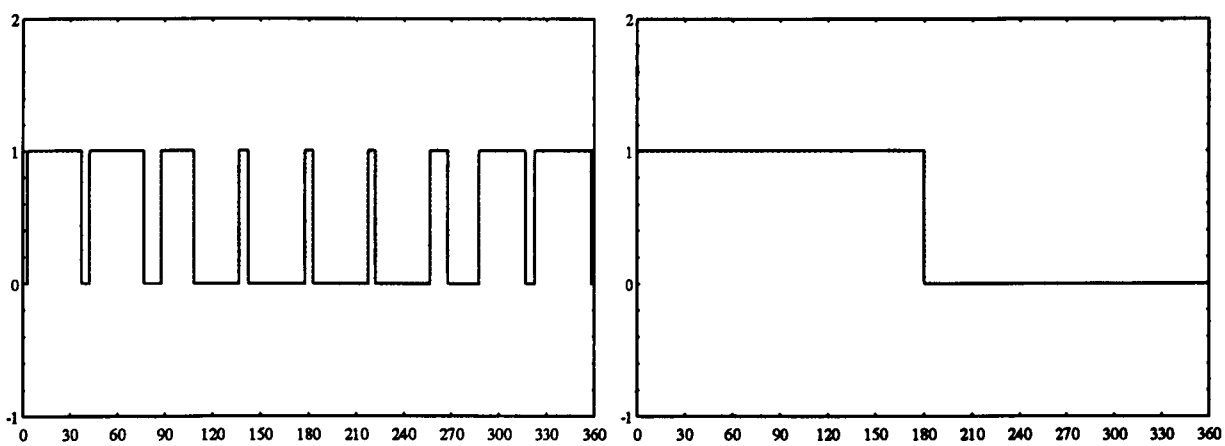

(g) Vector space PWM

(h) Quasi-square wave switching.

Fig. 3.14. Pulse patterns of various PWM strategies.

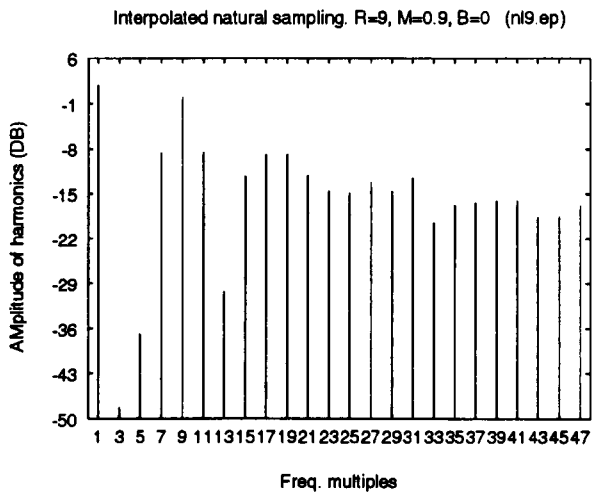

(a) Linear interpolated natural PWM

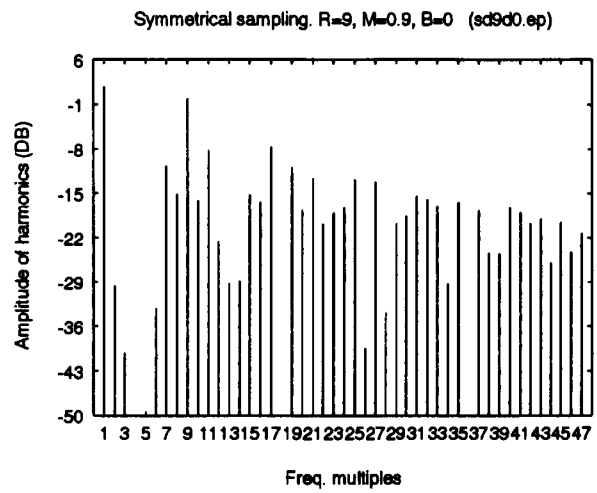

(b) Symmetric regular sampling PWM

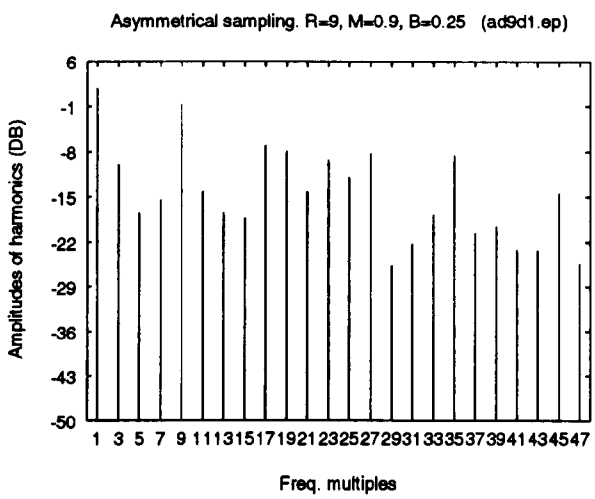

(c) Sub-optimal PWM

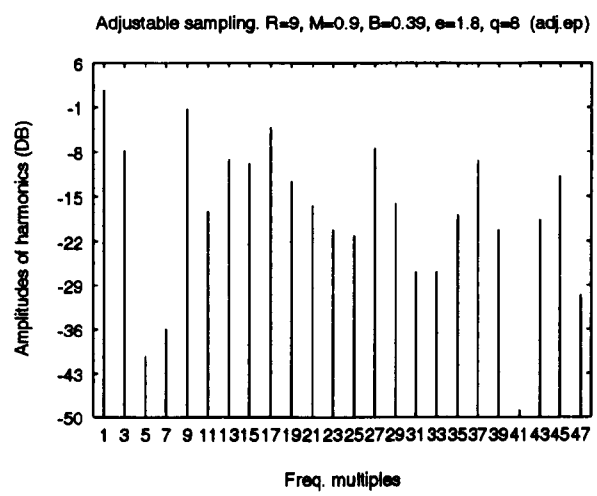

(d) Adjustable sampling PWM

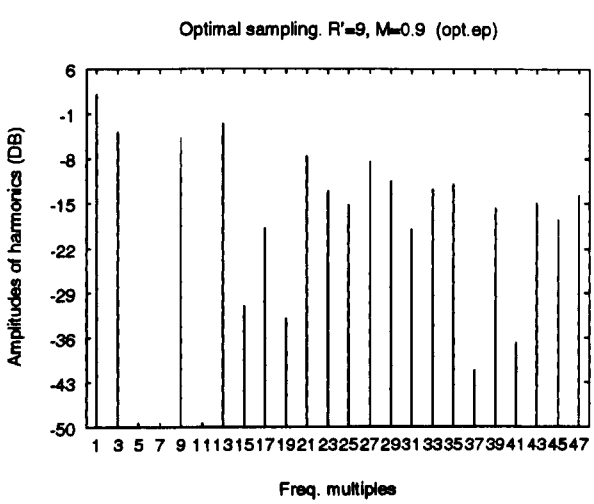

(e) Optimal harmonic elimination PWM

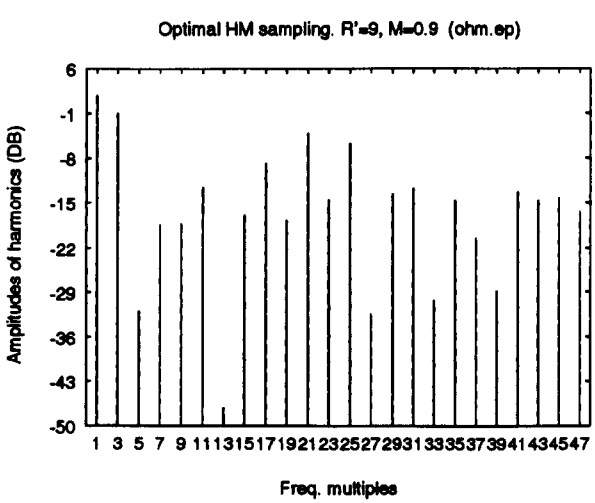

(f) Optimal harmonic minimisation PWM

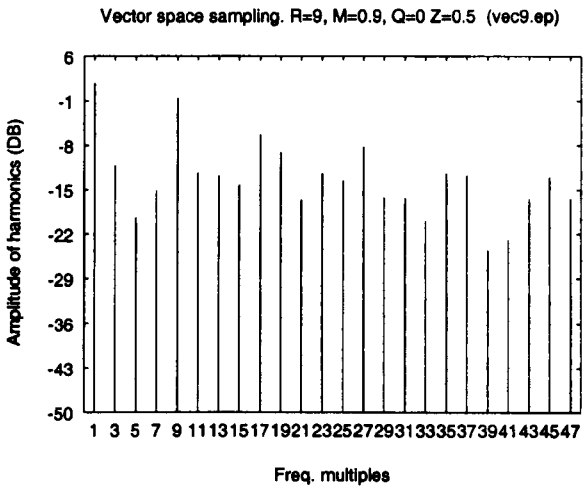

(g) Vector space PWM

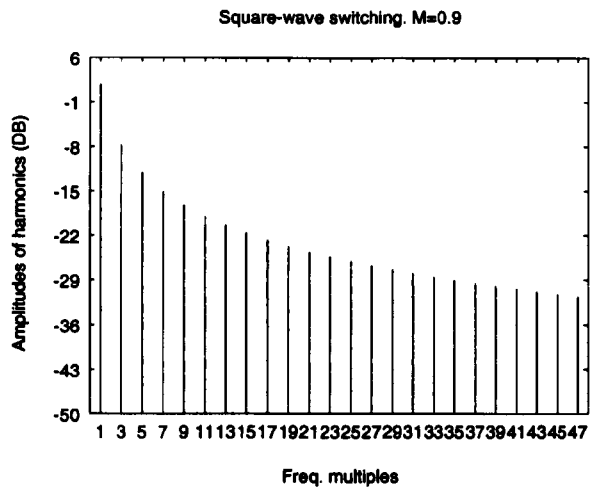

(h) Quasi-square wave switching.

Fig. 3.15. Spectrum distributions of various PWM pulse patterns.

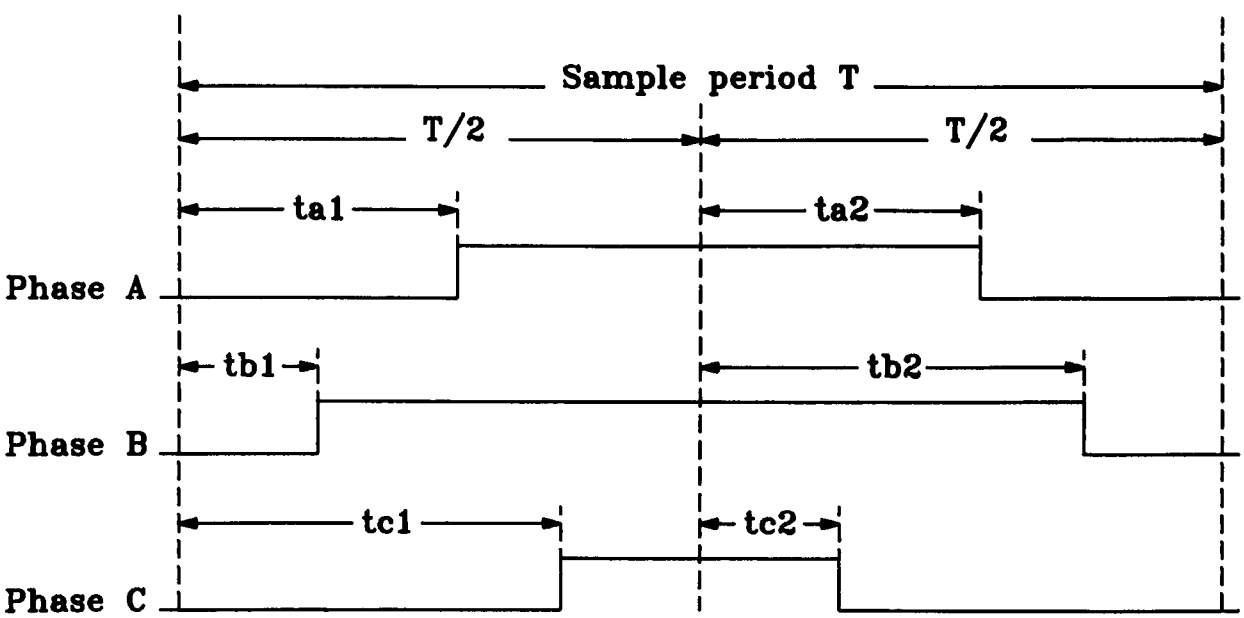

Fig. 3.16. Four-counter digital PWM implementation scheme.

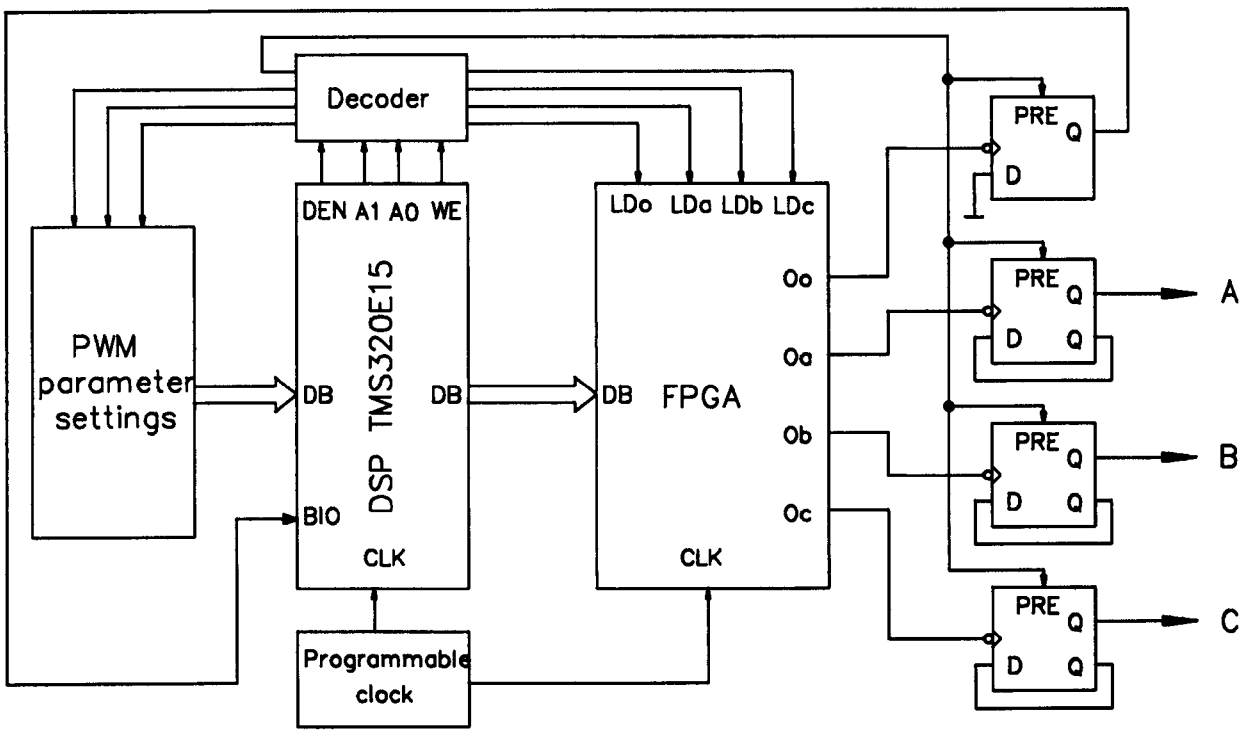

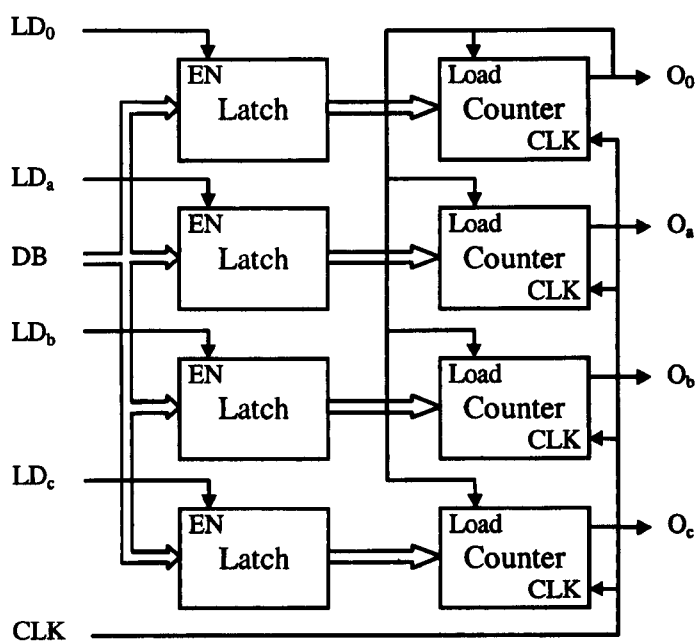

Fig. 3.17 The digital three phase PWM modulator. (a) Diagram of the modulator. (b) Schematic of the internal structure of the programmed FPGA.

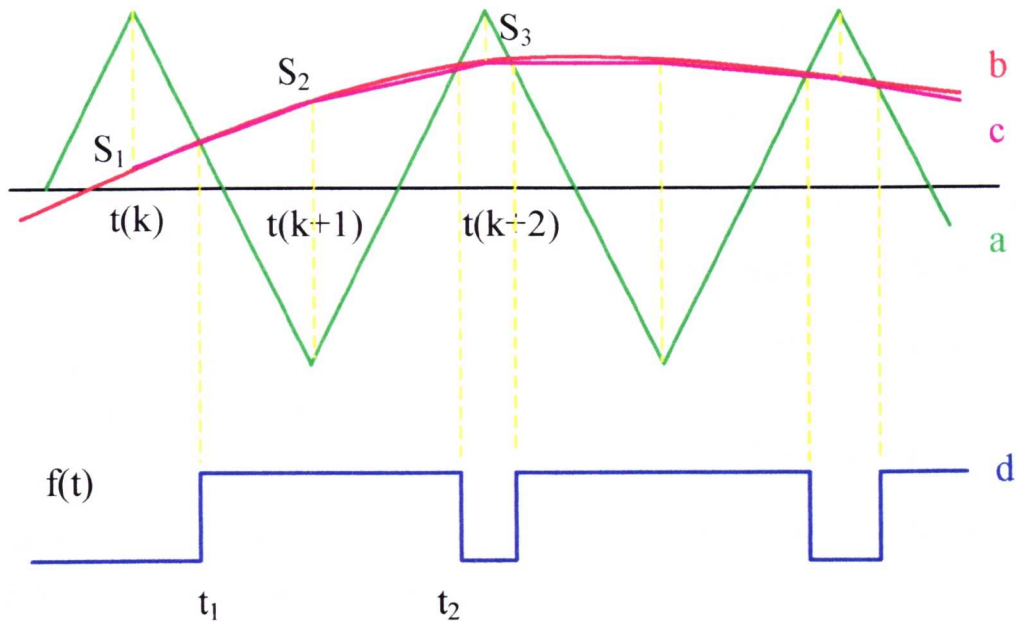

Fig. 3.18. Pulse formation of linear interpolated natural PWM. a - carrier signal, b - modulating signal, c - linear interpolated modulating signal, d - pulse train.

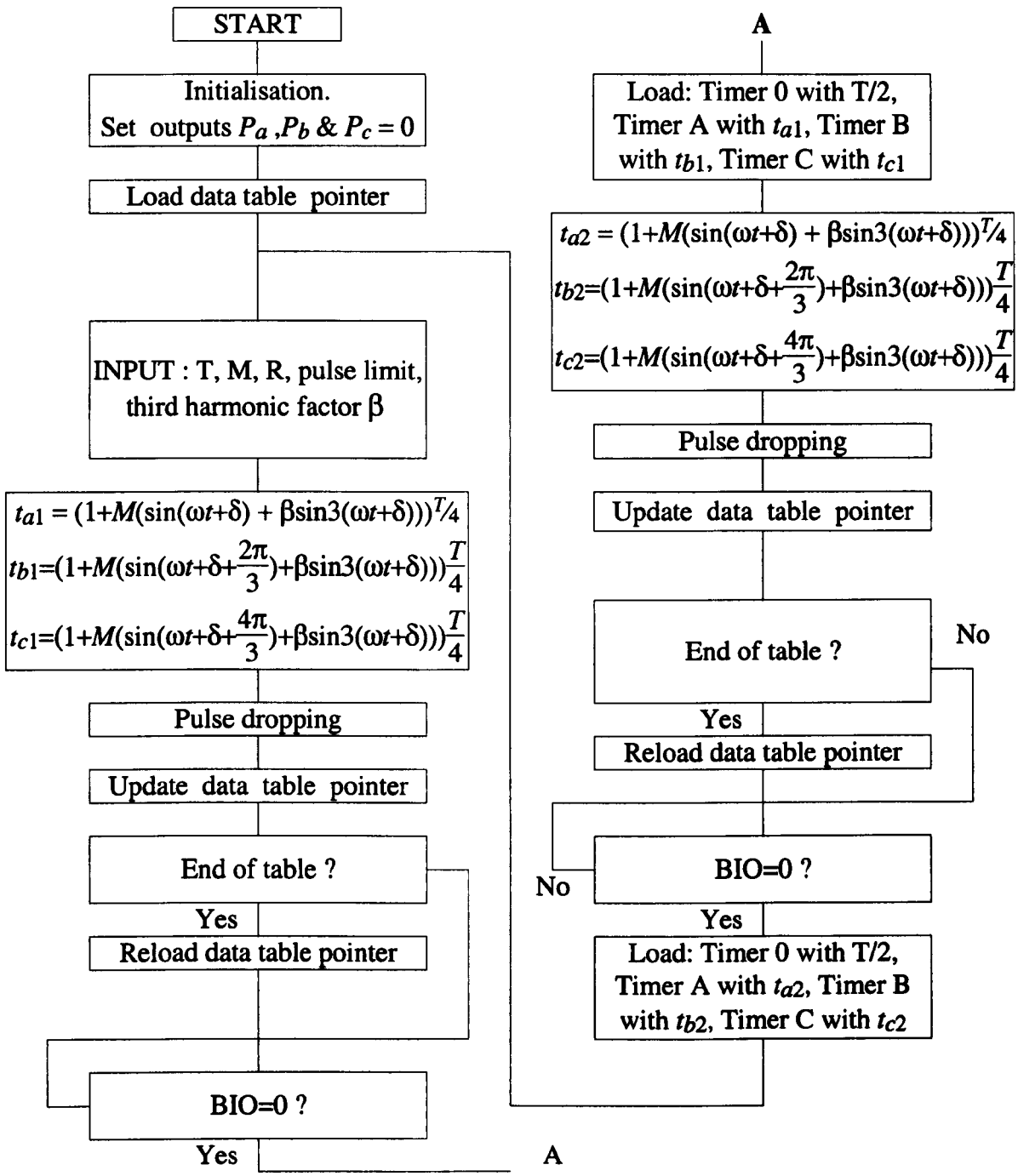

Fig. 3.19 Implementation of regular sampling PWM.

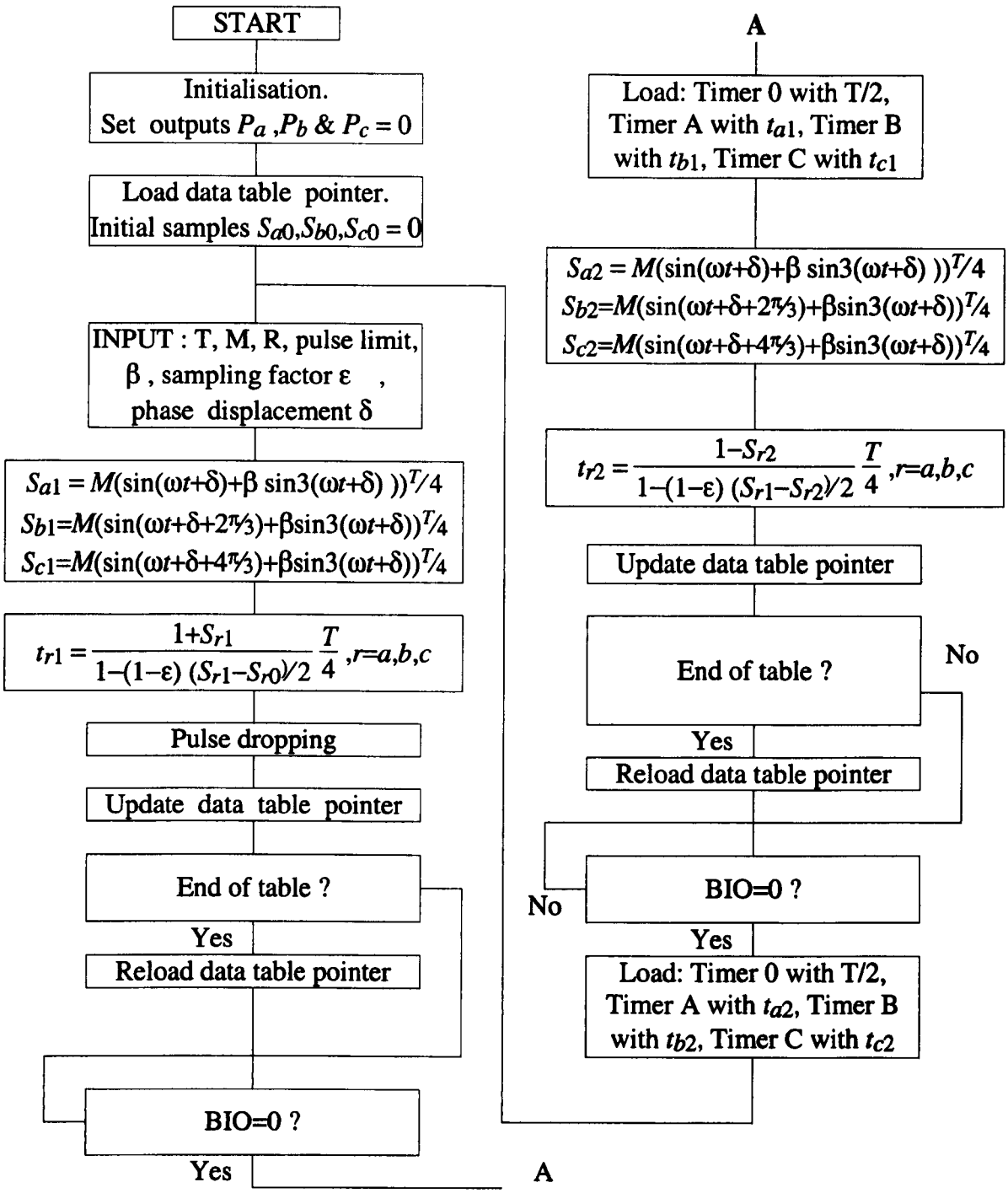

Fig. 3.20. Implementation of adjustable PWM.

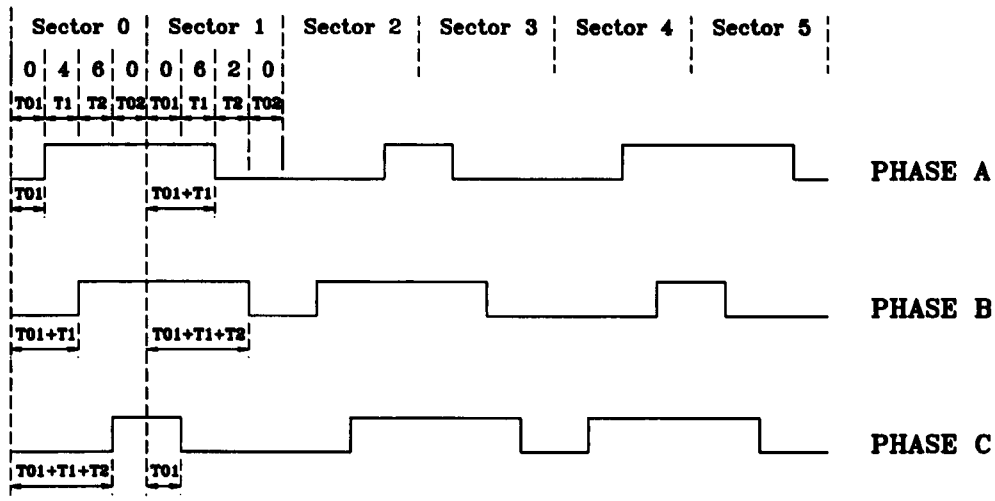

Fig. 3.21. Three phase vector space PWM pulse patterns, showing states for the case of one segment in one sector.

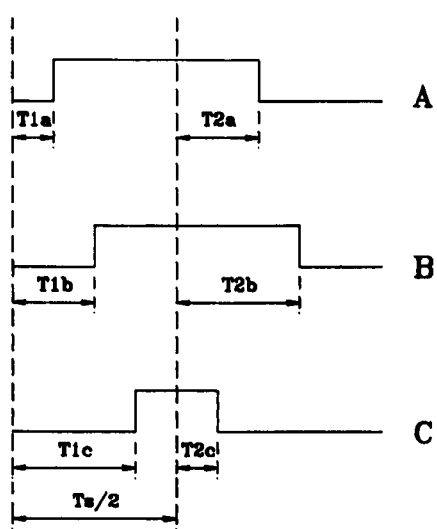

Fig. 3.22. Definition of timing intervals of three phase vector space PWM.

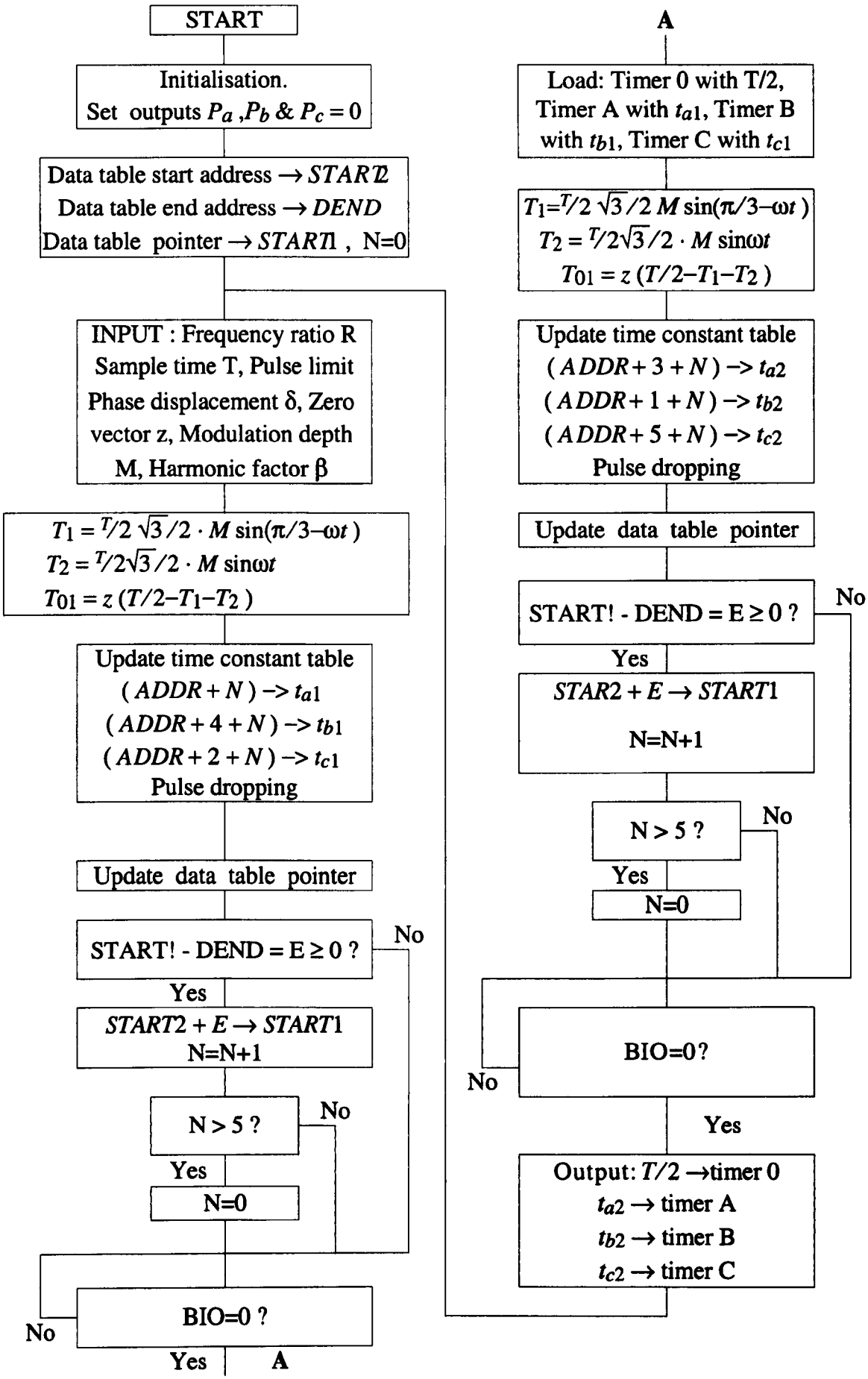

Fig. 3.23. Implementation of vector space PWM.

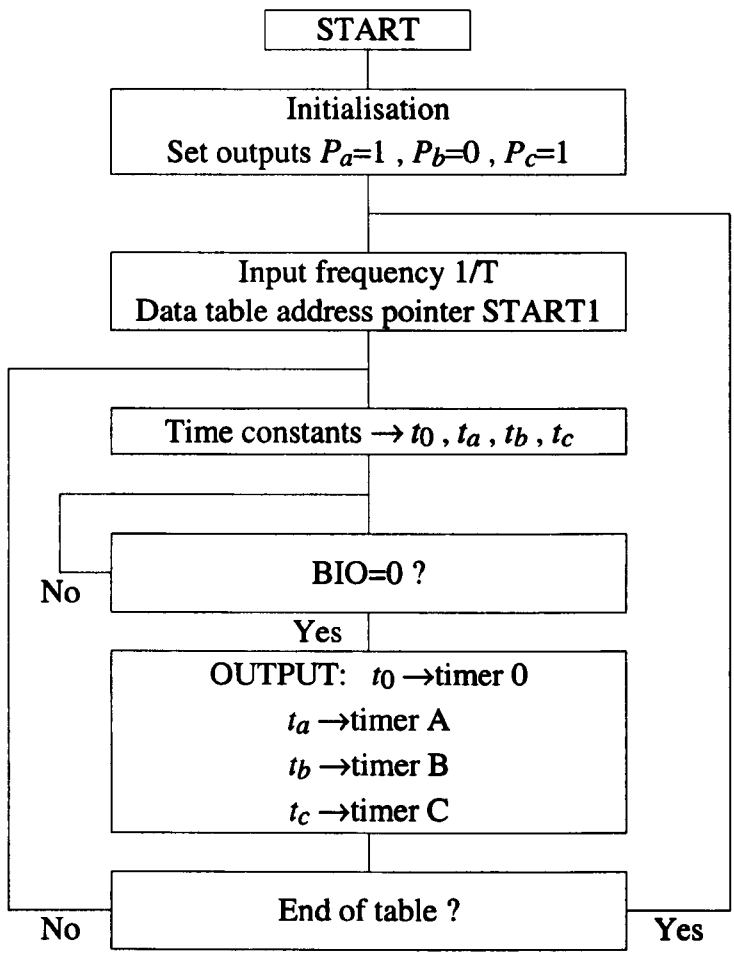

Fig. 3.24. Implementation of optimal harmonic elimination PWM and optimal harmonic minimisation PWM.

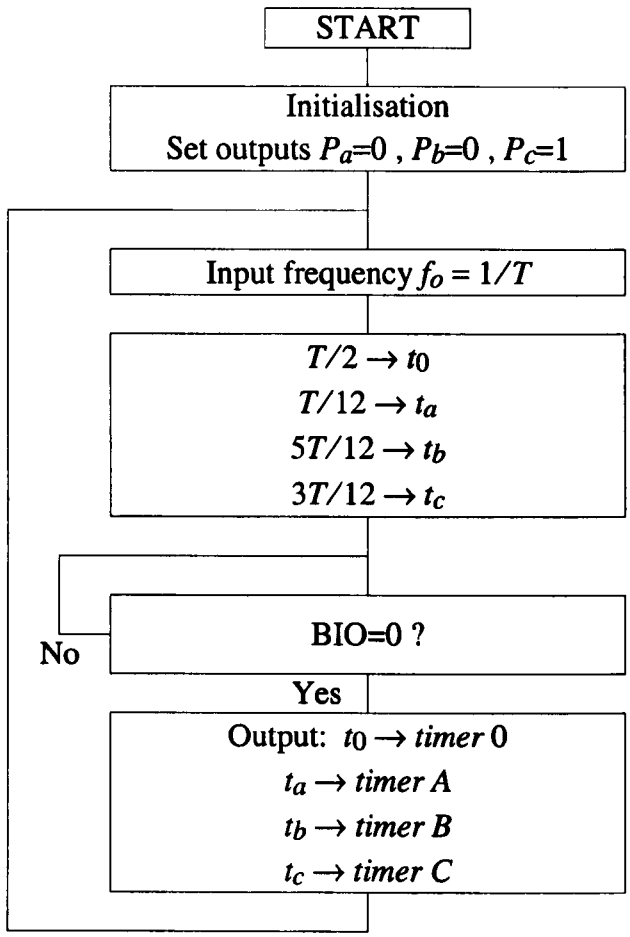

Fig. 3.25 Implementation of quasi-square wave switching scheme.

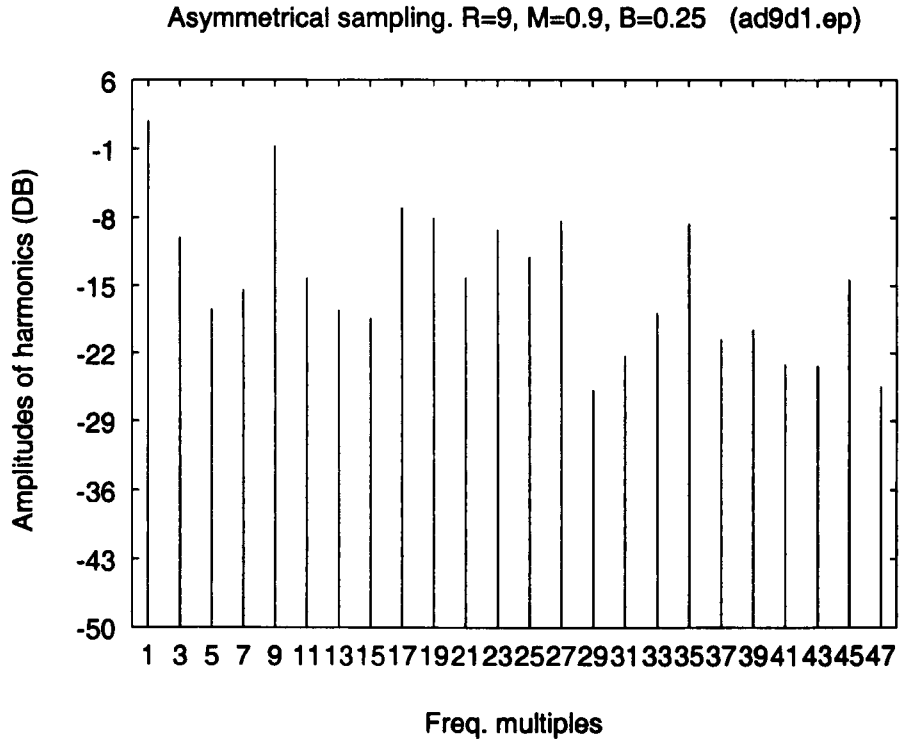

(a) Idealised spectrum distribution.

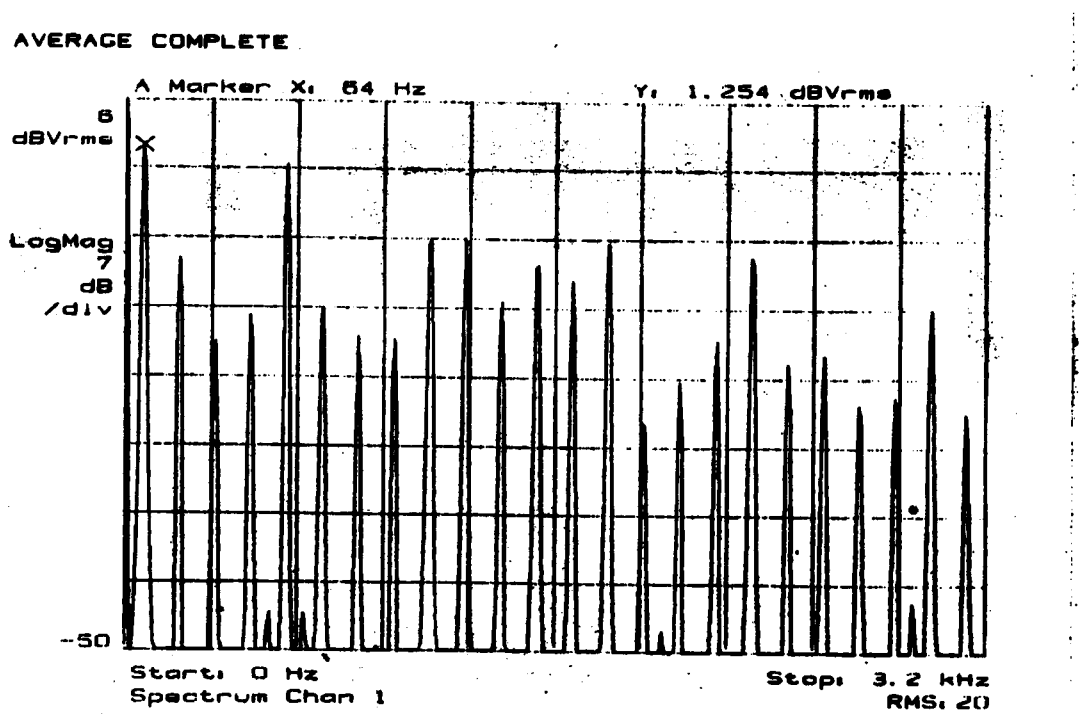

(b) Practical spectrum distribution.

Fig. 3.26 Comparison of ideal and measured spectrum distributions for regular sampling PWM.

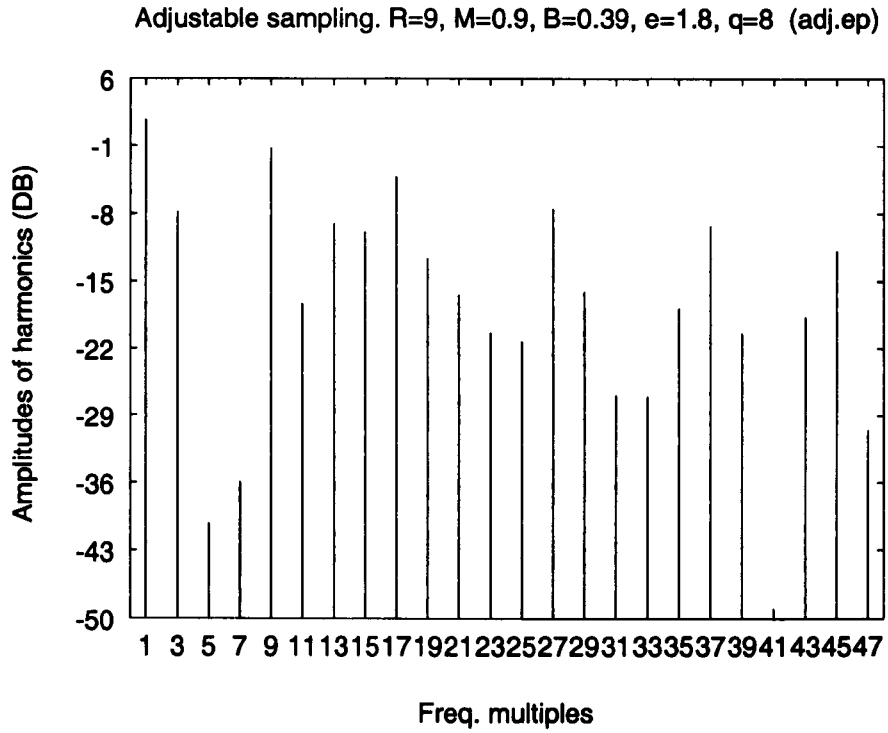

(a) Idealised spectrum distribution.

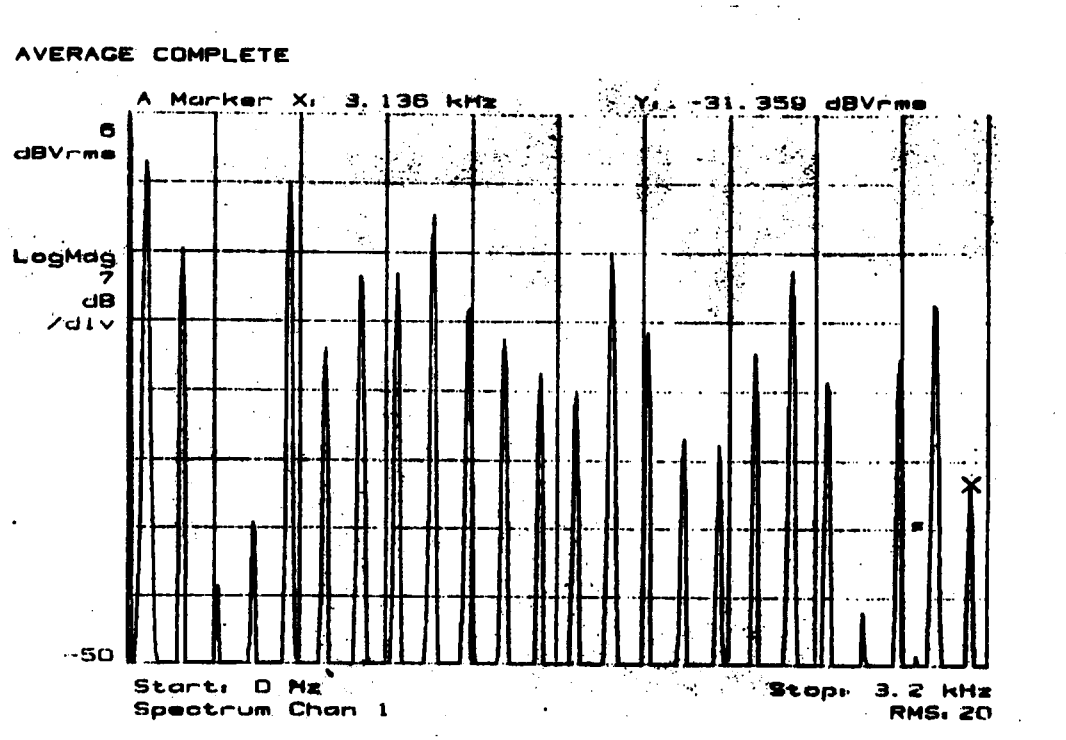

(b) Practical spectrum distribution.

Fig. 3.27 Comparison of ideal and measured spectrum distributions for adjustable sampling PWM.

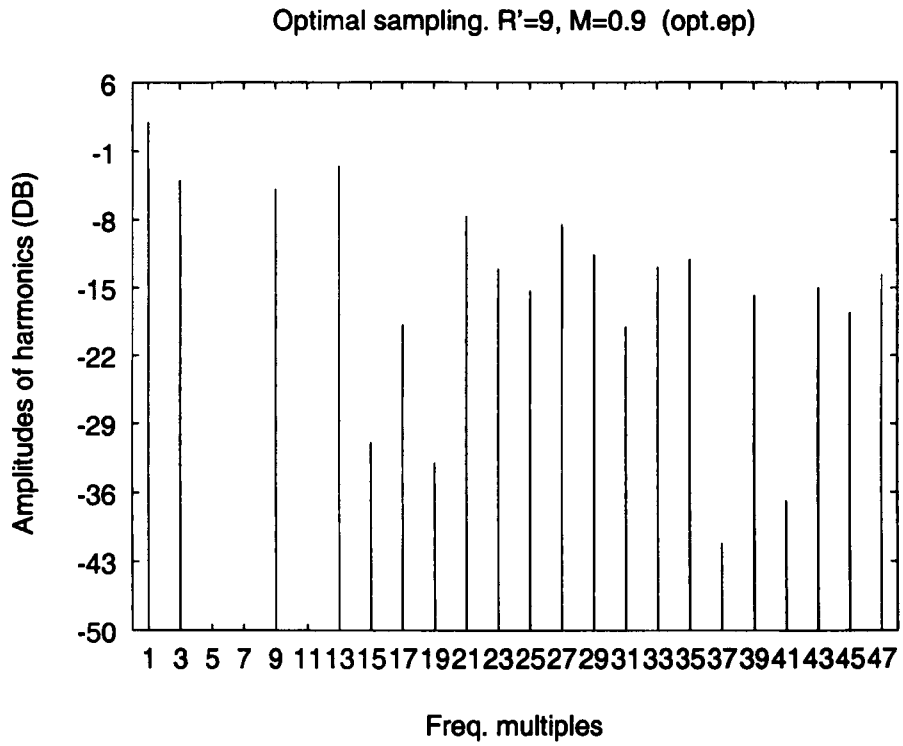

(a) Idealised spectrum distribution.

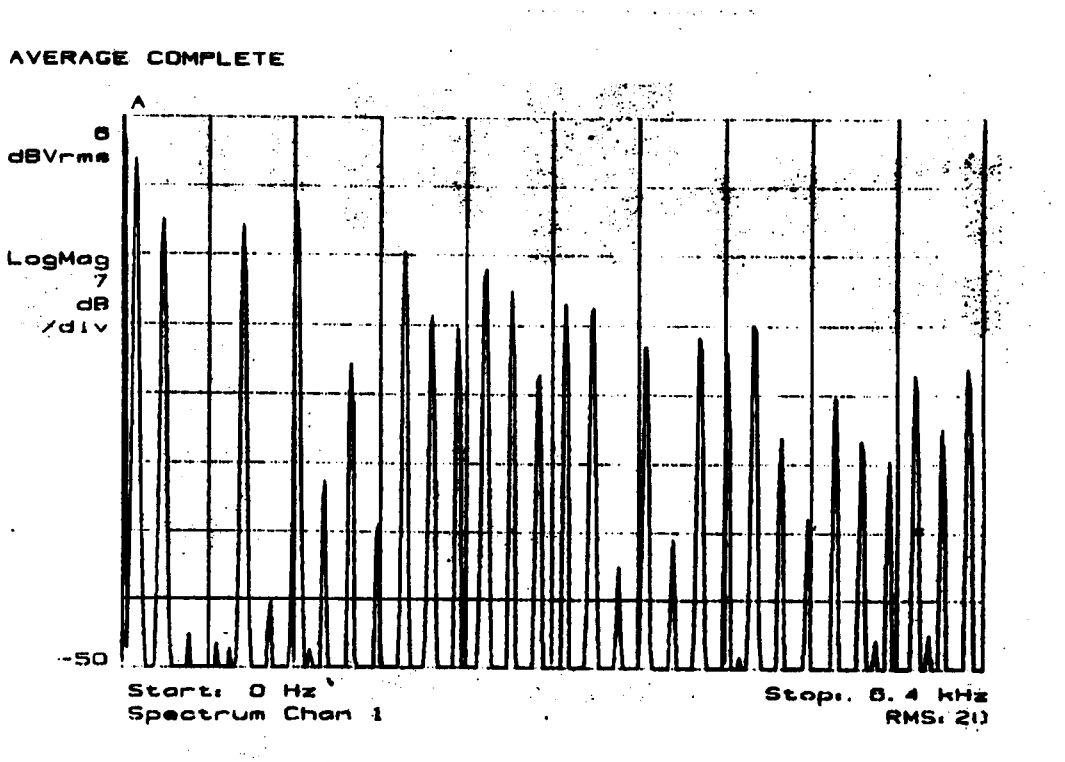

(b) Practical spectrum distribution.

Fig. 3.28 Comparison of ideal and measured spectrum distributions for optimal harmonic elimination PWM.

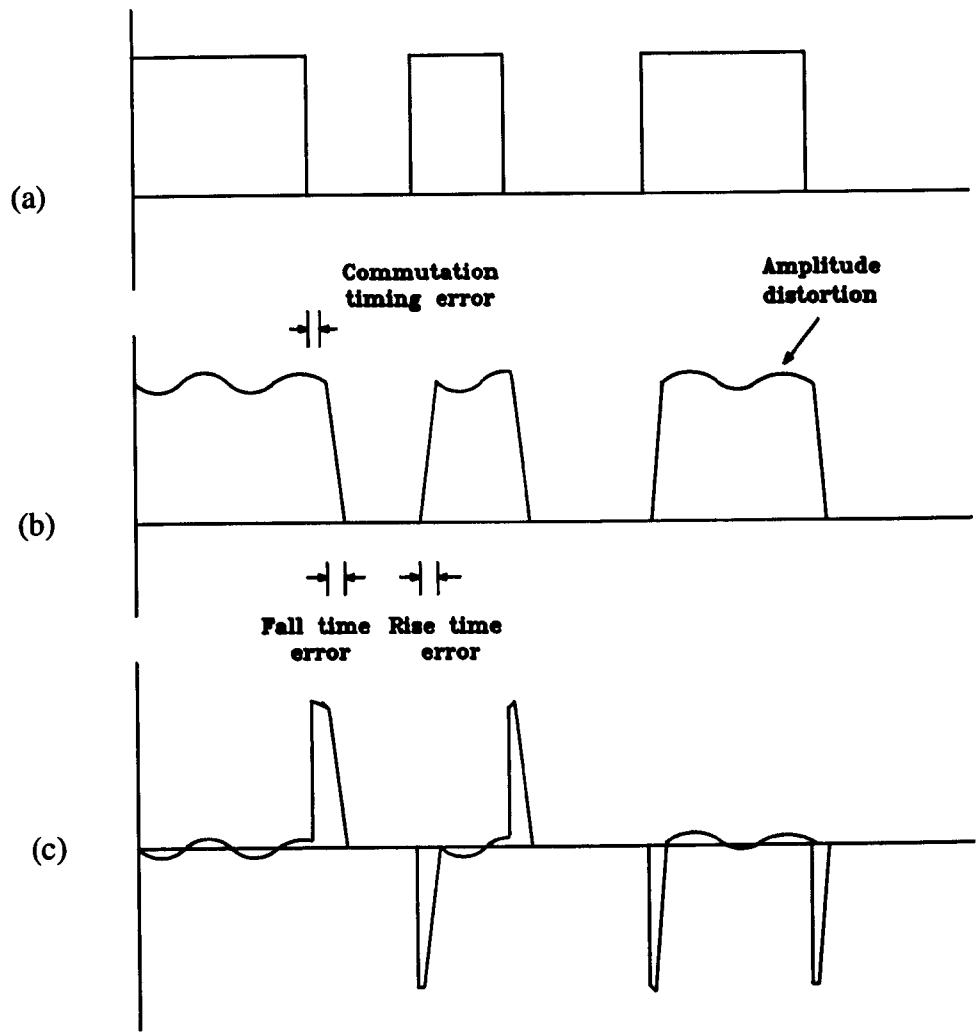

Fig. 3.29 Spectral error mechanisms in an inverter drive.

(a) idealised, (b) actual, and (c) error.

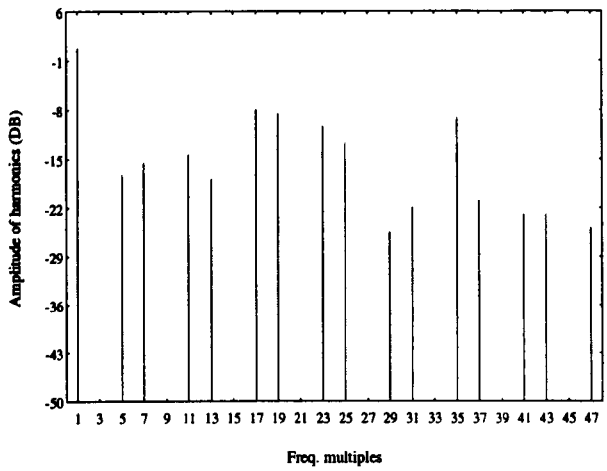

(a) Ideal spectrum.

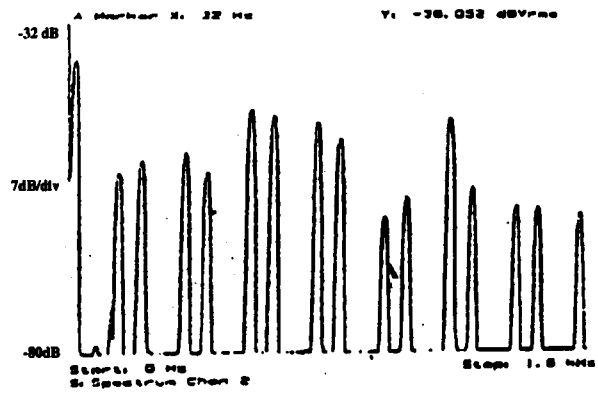

(d) Inverter output.
(0 - 1.6 kHz frequency span)

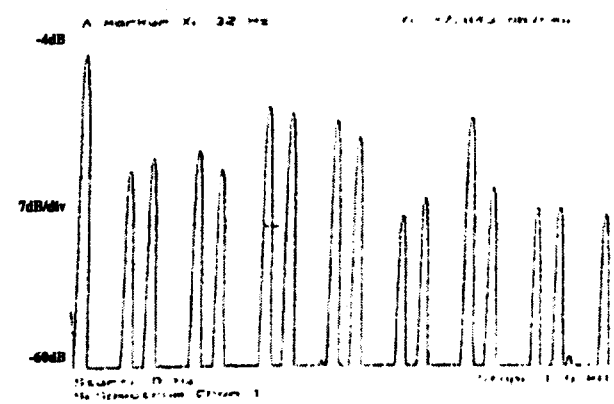

(b) Modulator output across two phases.
(0 - 1.6 kHz frequency span)

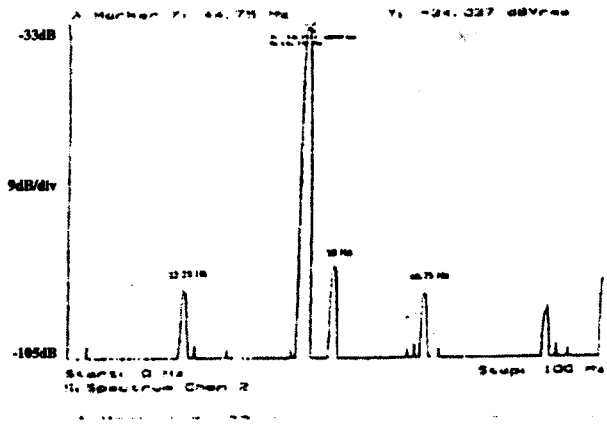

(e) Detailed view of the inverter output.
(0 - 100 Hz frequency span)

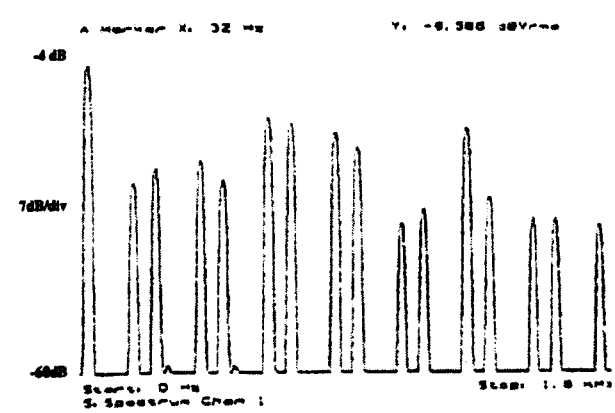

(c) Gate drive output.
(0 - 1.6 kHz frequency span)

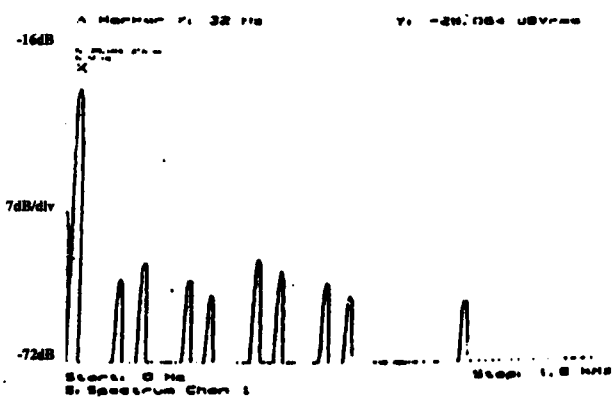

(f) Machine phase current.
(0 - 1.6 kHz frequency span)

Fig. 3.30. Signal spectrum distribution in the sub-optimal PWM controlled induction machine drive.

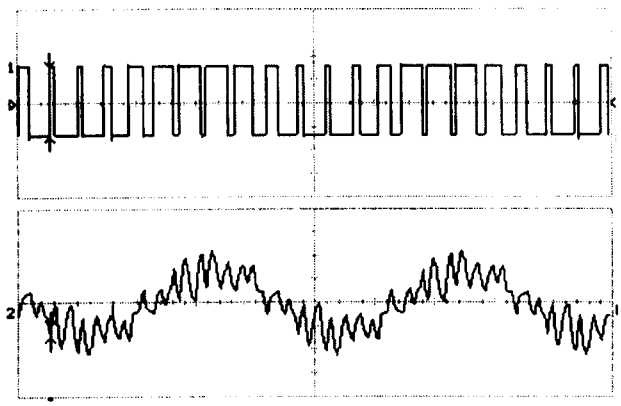

(a) Linear interpolated natural PWM.

(current: 2A/div, time: 20ms/div)

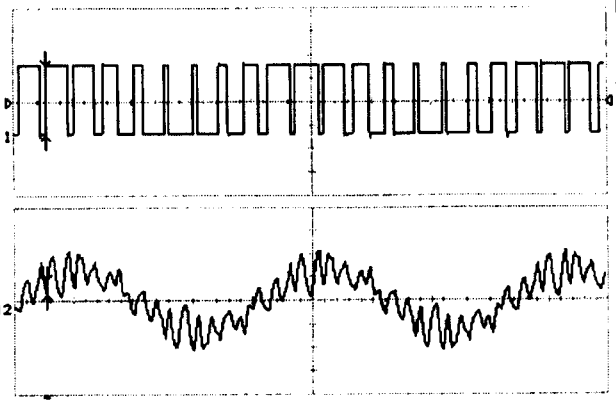

(b) Symmetric regular sampling PWM.

(current: 2A/div, time: 20ms/div)

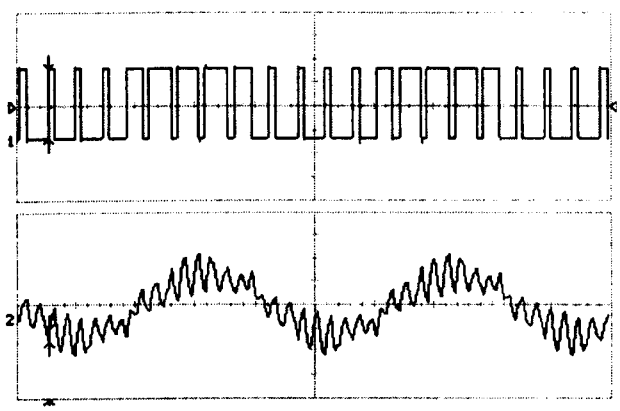

(c) Sub-optimal PWM.

(current: 2A/div, time: 20ms/div)

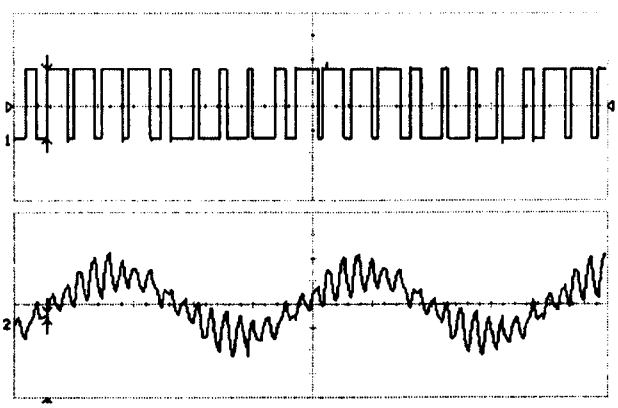

(d) Adjustable sampling PWM.

(current: 2A/div, time: 20ms/div)

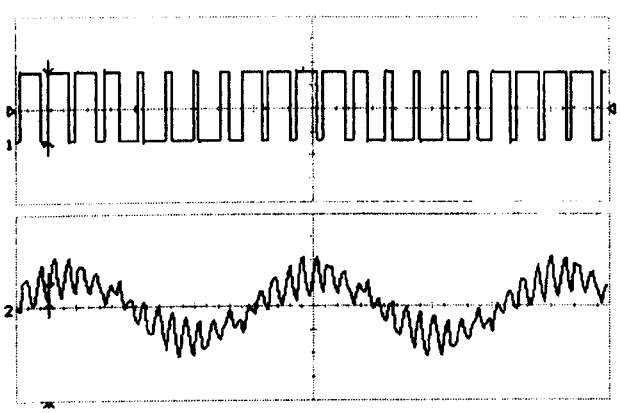

(e) Vector space PWM.

(current: 2A/div, time: 20ms/div)

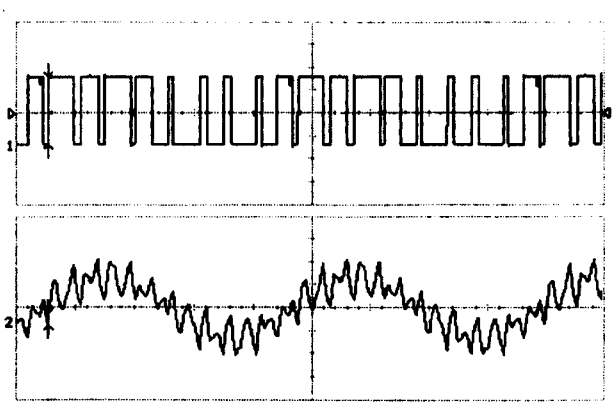

(f) Optimal harmonic elimination PWM.

(current: 2A/div, time: 20ms/div)

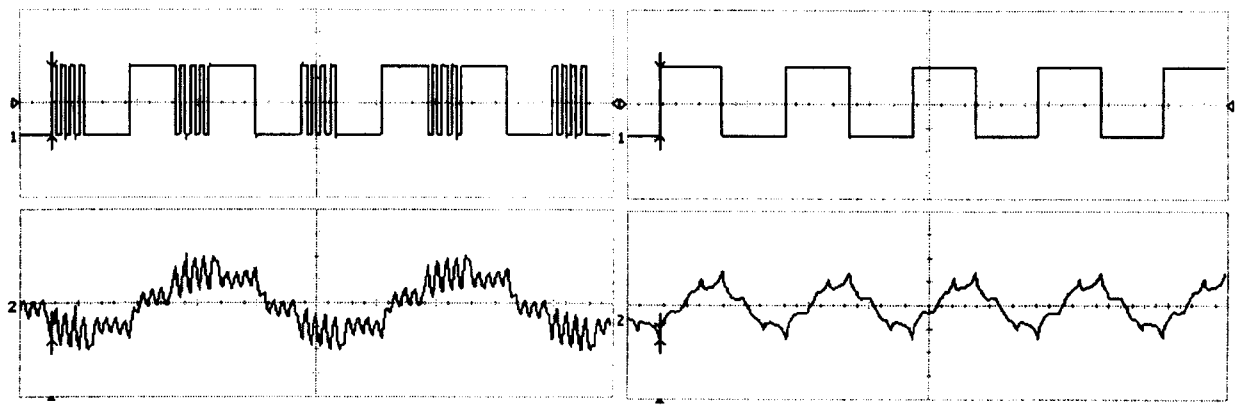

(g) Optimal harmonic minimisation PWM.

(current: 2A/div, time: 20ms/div)

(h) Quasi-square wave switching.

(current: 2A/div, time: 50ms/div)

Fig. 3.31 Measured line voltage and machine current waveforms with various PWM strategies.

4. Assessment of Loss in Induction Machine Drive under different PWM Strategies

4.1 Introduction

To achieve variable speed operation of a cage induction machine, a method of power conversion is necessary to provide the machine with a variable voltage and variable frequency supply. For reason of efficiency, this power conversion is only practical through the application of power semiconductors operated in the switch mode. However, the power converter will be an extra source of loss, and the switching operation of the converter will introduce voltage and current harmonics onto the motor supply, which in turn will cause additional machine harmonic losses, torque ripple and increased acoustic noise. In this chapter, the effect of a PWM inverter on the induction machine drive system will be analysed, and the impact under different PWM strategies on the drive system loss quantified.

Initially, the basic electrical relationships in the PWM inverter induction machine drive system will be defined. Fig 4.1 shows a schematic of the basic drive system and illustrates the nomenclature.

The PWM modulating signal is defined as

$$m(t) = M \sin(\omega t + \delta) \tag{4.1}$$

where M is the depth of modulation, and δ is the phase angle of the modulation signal, as defined in Chapter 3.

The inverter output phase fundamental voltage is therefore,

$$v_{AO}(t) = \frac{V_d}{2} M \sin(\omega t + \delta - \theta) \tag{4.2}$$

where V_d is the supply d.c. link voltage, and θ accounts for any phase shift introduced by the modulation process. Inherent in the above expression is an assumption that the modulator is switching at a sufficiently high frequency such that the fundamental is a linear function of the modulation depth.

It follows that the inverter line fundamental voltage is,

$$v_{AB}(t) = \frac{V_d}{2}\sqrt{3}\,M \sin(\omega t + \delta - \theta + \frac{\pi}{6}) \tag{4.3}$$

and the motor phase current for a Δ connected machine is,

$$i_a(t) = I_m \sin(\omega t + \delta - \theta + \frac{\pi}{6} - \varphi) \tag{4.4}$$

where I_m is the motor peak fundamental phase current, and φ is the fundamental power factor angle.

The correspond motor line current is,

$$i_A(t) = \sqrt{3}\, I_m \sin(\omega t + \delta - \theta - \varphi) \tag{4.5}$$

In the calculation of inverter loss, the inverter output voltage v_{AO} and current i_A will be used. Similarly, the machine fundamental power losses are determined from the machine phase voltage v_{AB}, phase current i_a and power factor angle φ.

4.2 Voltage control

The magnitude of output fundamental voltage generated by the inverter is controlled by the PWM modulation depth. Ideally a linear relationship between the fundamental output and the modulation depth is desired and the linear range of fundamental voltages should also be maximised for a given inverter d.c. link voltage.

4.2.1 Linearity of voltage control

When the ratio of switching to fundamental frequency is sufficiently high, i.e. above 9, the relationship between the modulation depth and the inverter output fundamental voltage can be considered to be linear, regardless of the PWM method used. However, for frequency ratios below 9, the relationship is no longer linear, although linearisation is possible by adjusting the modulating wave phase angle or by software compensation. The dependency of the voltage control linearity upon the frequency ratio has already been analysed in Chapter 3. Fig 4.2 shows a comparison of the voltage control properties of various PWM methods at frequency ratio of 9, where for each method the phase angle has been set for the lowest possible harmonic distortion. It can be observed that all the methods exhibit a near linear control characteristic, with vector space PWM and sub-optimal PWM being indistinguishable from the ideal characteristic of optimal method.

4.2.2 Range of linear voltage control

The effective voltage control ranges without overmodulation of various PWM methods are given in Table 4.1. The quasi-square wave switching realises the highest possible output voltage, but the output amplitude cannot be adjusted. With adjustable PWM, vector space PWM and sub-optimal PWM, the peak output voltage can theoretically be extended by 15% above that of the d.c. link voltage.

Table 4.1 Voltage control ranges of various PWM methods without overmodulation

PWM	Natural	Regular	sub-optim.	Vector space	Adjust.	Opt. elimi.	Opt. min.	six-step
Range	0-1.0	0-1.0	0-1.15	0-1.15	0-1.15	< 1.27	< 1.27	1.273

4.3 Harmonic distortion

4.3.1 Analysis of harmonic distortion

The loss in an electrical machine is highly dependent on the purity of its supply and an inverter driven motor will inevitably have a poorer efficiency compared with operation on an ideal supply. The detailed analysis of supply induced harmonic loss in electrical machines is complex, however reasonable results can be obtained by separating the effects of the individual harmonics and applying superposition. Based on this approach a number of harmonic loss models have been proposed of varying sophistication and accuracy. However, it has been shown that, simply in terms of assessing whether one PWM waveform will result in lower or higher harmonic losses than another, the exactness of the model is not very critical [Murphy 1983].

A common performance criteria used in the assessment of three phase inverter waveform quality is the voltage based THD (total harmonic distortion) figure calculated from,

$$THD = \sqrt{\sum_{\substack{n=2 \\ n \neq triplen}}^{\infty} \left(\frac{V_n}{n\,V_1}\right)^2} \tag{4.6}$$

where V_1 is the fundamental voltage and V_n are the nth harmonic voltages. The voltage THD will give a measure of the magnitude of the harmonic currents drawn by the machine. If it is assumed that the harmonic impedance of the machine is dominated by the winding effective inductance L, i.e. the combined rotor and stator leakage inductance in an induction machine, then the harmonic rms current is given by,

$$I_{hrms} = \frac{V_1}{\sqrt{2}\,\omega\,L} \times THD \tag{4.7}$$

where $V_1/\omega L$ is a constant at a fixed machine supply frequency.

The effectiveness of using THD to indicate the level of machine harmonic loss will be validated later against experimental measurements.

4.3.2 Harmonic performance of PWM strategies

Fig 4.3 compares the total harmonic distortion (THD) of different PWM strategies in the case of a waveform with frequency ratio of 9, and over the full range of modulation depths for each particular strategy.

By definition the optimal harmonic minimisation method gives the lowest level of harmonic distortion. The discontinuity in the optimal curve is a result of the multivalued nature of the optimisation problem and it is necessary to include sudden changes in the pulse pattern to maintain the lowest level of THD. Such non-linearities make this optimal PWM highly complex to implement. Although the optimal harmonic elimination method can eliminate several lower order harmonics which may be beneficial to reduce the machine torque ripple and low frequency acoustic noise, it has a higher harmonic distortion and also features the same complexity of implementation as the optimal harmonic minimisation method. The original analogue circuit based natural sampling PWM gives the highest harmonic distortion followed by the simple asymmetrical regular sampling process. Sub-optimal sampling which uses a distorted modulating waveform and vector space modulation have very similar performance. The adjustable technique has a THD approaching that of the optimal harmonic minimisation method and has the best performance of all the regular sampling methods. At higher number of pulses per cycle similar results are obtained, however the benefit of using the adjustable process compared with vector space PWM is less pronounced, as shown in Fig. 4.4 where a frequency ratio of 15 is applied.

4.4 Loss model of a voltage source PWM controlled inverter

4.4.1 Determination of power losses in an inverter

The power loss in a power semiconductor switching device can be separated into three components:

a) Switching losses, comprising of turn-on losses and turn-off losses.
b) On-state losses (conduction losses).
c) Off-state losses.

The leakage currents in high power devices during the off-state are several orders of magnitude smaller than the rated current. As a consequence the off state losses are usually considered negligible.

Switching losses occur during the transition from the off to on state and the on to off state, refereed to as turn-on and turn-off losses respectively. Integrating the product of current and voltage over the switching interval yields expressions for energy dissipation, thus:

$$W_{on} = \int_{t_{on}} i(t)\, v(t)\, dt \tag{4.8}$$

$$W_{off} = \int_{t_{off}} i(t)\, v(t)\, dt \tag{4.9}$$

Conduction losses are formed from the product of the on-state voltage of the transistor and the collector current during the time the device is conducting,

$$W_{cond.} = \int_{conduction\ period} V_{CE(sat)}\, I_c \cdot dt \tag{4.10}$$

The magnitudes of the switching and conduction losses are clearly influenced by the type of circuit in which the power semiconductors are used, the operation mode and modulation technique, the operating frequency, and the conduction and switching characteristics of a particular device. The switching characteristics are generally specified in manufacturers' data

sheets for only a particular operational condition, normally close to the maximum specified device rating, and are highly dependent upon the external power circuit, the detailed design of the gate or base drive circuit and the operational temperature. Because of these uncertainties, the manufacturers' data sheets only give a rough estimation of the switching loss [Casanellas 1994] and the switching losses coefficients are best determined experimentally under conditions representative of their final application. A test methodology will be proposed for this purpose, which has been employed to predict the power losses in the experimental three phase full bridge voltage source inverter described in Chapter 2.

4.4.1.1 Formulation of conduction power loss model

When the PWM switching control of the inverter has a relatively low number of pulses per fundamental cycle, the losses can be found by using time domain simulation to find the instantaneous values of device voltage and current between each switching event and summing the effects. However, this is not practical at higher carrier frequencies because of the large amount of calculations required, and rather the formulation of a general expression is preferred.

At high carrier frequencies relative to the fundamental frequencies the performances of the various PWM methods become very similar, and the pulse pattern may be expressed in terms of a generalised conduction period in a carrier cycle, expressed as,

$$t_2 - t_1 = \frac{T}{2}\left(1 + M\sin(\omega t + \delta)\right) \tag{4.11}$$

where $M\sin(\omega t + \delta)$ represents the modulating signal. For clarity the modulation signal phase angle, δ, will be assumed to be zero in the following analysis.

Consider an individual inverter leg connected to an inductive load, Fig 4.5. The load current i_L may be assumed to be sinusoidal if the inductance of the load compared to the carrier frequency is sufficiently large such that current ripple can be neglected,

$$i_L = I_m \sin(\omega t - \varphi) \tag{4.12}$$

where φ is the inductive load power factor angle.

During the positive half cycle of the load current $0 < \omega t < \pi$, power devices T_1 and D_2 are on, and during the negative wave cycle $\pi < \omega t < 2\pi$ symmetric operation occurs with T_2 and D_1 conducting. Thus, only the positive cycle of the current waveform needs to be considered as the losses in the negative cycle will be identical, but dissipated in different devices.

Let the fundamental load voltage be depicted as,

$$u = V_1 \sin \omega t \tag{4.13}$$

and correspondingly the modulating signal is

$$M \sin \omega t \tag{4.14}$$

Here the phase shift due to modulation is neglected because of the assumption of relatively high switching frequency.

At high carrier frequencies the duration (T) of the carrier cycle can be donated by $\Delta(\omega t)$, thus using Eqn. (4.11),

$$T_{on} = \frac{1}{2} \Delta(\omega t)(1 + M \sin \omega t) \tag{4.15}$$

The off-time of the transistor (or the on-time of the recovery diode) in one carrier cycle is then,

$$T_{off} = \frac{1}{2} \Delta(\omega t)(1 - M \sin \omega t) \tag{4.16}$$

The conduction voltage drop across a saturated power semiconductor junction may be written as a constant component plus a component that depends linearly upon conducting current,

$$V_T = V_{To} + K_T\, i \tag{4.17}$$

Similarly the conduction voltage drop for fast recovery diode is given by,

$$V_D = V_{Do} + K_D\, i \tag{4.18}$$

The conduction power loss in the power semiconductor switch is therefore,

$$P_T = \frac{1}{\pi}\int_0^{\pi} V_T\, i\, T_{on} \tag{4.19}$$

and the conduction power loss in the diode is,

$$P_D = \frac{1}{\pi}\int_0^{\pi} V_D\, i\, T_{off} \tag{4.20}$$

Combining Eqn. (4.19) and Eqns. (4.12), (4.14), (4.15), in limit as $\Delta(\omega t) \rightarrow d(\omega t)$ the conduction loss for the power semiconductor switch is thus,

$$\begin{aligned} P_T &= \frac{1}{\pi}\int_0^{\pi} (V_{To} + K_T I_m \sin (\omega t - \varphi)) I_m \sin (\omega t - \varphi) \cdot \frac{1}{2} (1 + M \sin \omega t)\, d (\omega t) \\ &= \frac{V_{To} I_m}{\pi} [1 + \frac{\pi}{4} M \cos \varphi] + \frac{K_T I_m^2}{\pi} [\frac{\pi}{4} + \frac{2}{3} M \cos \varphi] \end{aligned} \tag{4.21}$$

and similarly the expression for the diode conduction loss is

$$\begin{aligned} P_D &= \frac{1}{\pi}\int_0^{\pi} (V_{Do} + K_D I_m \sin (\omega t - \varphi)) I_m \sin (\omega t - \varphi) \cdot \frac{1}{2} (1 - M \sin \omega t)\, d (\omega t) \\ &= \frac{V_{Do} I_m}{\pi} [1 - \frac{\pi}{4} M \cos \varphi] + \frac{K_D I_m^2}{\pi} [\frac{\pi}{4} - \frac{2}{3} M \cos \varphi] \end{aligned} \tag{4.22}$$

The above expressions are in agreement with those published in [Mesha 1989], which were derived using a more complicated analysis that included the use of Bessel functions.

4.4.1.2 Formulation of switching power loss model

Compared to conduction power losses, the analysis of switching power losses is more difficult because of the dependency of device switching times upon the external circuit parameters. As a result switching losses and their relationship with d.c. link voltage and load current are best measured under representative circuit operational conditions.

Formulation of switching power loss in a power device and diode pair

Switching losses are highly dependent upon circuit operation, the most arduous condition occurring when as a result of modulation it is necessary to force commutate the freewheel diode. For example Fig 4.6 illustrates the current flow interchanges between the upper power switch T_1 and the lower diode D_2 when there is a positive current flow out of the inverter pole. When T_1 is turned-on, it force commutates diode D_2 leading to a high reverse recovery current in the device and an instantaneous condition when the full d.c. voltage is supported across the diode and transistor.

(a) Switching power loss in an IGBT power semiconductor switch

In general the switching loss can be expressed as the sum of turn-on and turn-off losses,

$$P_{Tsw} = P_{on} + P_{off} = f_s \, (W_{on} + W_{off}) \tag{4.23}$$

where f_s is the switching frequency, W_{on} is the turn-on energy dissipation in a single switching event and W_{off} is the turn-off energy dissipation in a single switching event.

Fig 4.7a illustrates the idealised turn-on voltage and current waveforms of an IGBT. The turn-on energy loss occurs mainly during the turn-on rise time period t_{on1}, since the loss over the turn-on delay time is negligible as a result of the relatively small collector current, hence,

$$W_{on1} = \int v(t)\, i(t)\, dt = \frac{I_c\, V_d\, t_{on1}}{k_{on}} \tag{4.24}$$

The IGBT turn-off can be separated into the three events illustrated in Fig 4.7b, and each has an associated loss, thus,

$$W_{off} = W_{offd} + W_{off1} + W_{off2} \tag{4.25}$$

where, W_{offd} is the power dissipation during turn-off delay time t_{offd},

$$W_{offd} = V_{CE(sat)}\, I_c\, t_{offd} \tag{4.26}$$

W_{off1} is the power dissipation during the fall time t_{off1},

$$W_{off1} = \frac{I_c\, V_d\, t_{off1}}{k_{off}} \tag{4.27}$$

and W_{off2} is the power dissipation during tail current fall period t_{off2},

$$W_{off2} = \frac{I_{CT}\, V_d\, t_{off2}}{2} \tag{4.28}$$

In the above equations,

V_d off-state voltage applied to IGBT, or the d.c. link voltage

I_c collector current

k_{on} turn-on coefficient

k_{off} turn-off coefficient

I_{CT} tail current

The coefficients k_{on} and k_{off} are determined from the waveform of collector current and collector-emitter voltage during switching, and can be considered as constant for particular set of power components and circuit arrangement.

The switching times of IGBT's are related to the gate-emitter voltage and the collector current waveform. The turn-on time will be reduced for a high gate drive voltage, and the turn-off time, as the major switching times in an IGBT, will be enlarged with an increased conducting current [Chokhawala 1995]. However, without loss of generality, it will be assumed that for a

fixed gate drive voltage only the fall time t_{off1} changes with collector current I_c. The total switching power loss in one power semiconductor switch is then,

$$P_{Tsw} = f_s \left(k_1 \, t_{off1} \, I_c \, V_d + k_2 \, I_c + k_3 \, V_d \right) \tag{4.29}$$

(b) Switching power loss in a diode

The switching losses in a diode can be derived in a similar way. However, compared to an IGBT, switching times in a diode are much shorter and can be treated as constants when the switching losses are calculated. Therefore, the switching losses in a diode can be expressed as,

$$P_{Dsw} = f_s \left[k_4 \, I_c \, V_d + k_5 \, I_c \right] \tag{4.30}$$

where coefficients k_4 and k_5 are constants.

(c) Switching loss in a power semiconductor switch and diode pair

By combining of Eqns. (4.29) and (4.30), an expression for switching loss in a power semiconductor switch and diode pair can be obtained as follows,

$$P_{sw} = f_s \left[I_c \, V_d \left(k_1 \, t_{off1} + k_4 \right) + \left(k_2 + k_5 \right) I_c + k_3 \, V_d \right] \tag{4.31}$$

or

$$P_{sw} = \left(\alpha_1 \, I_c + \alpha_2 \right) f_s \, I_c \, V_d + \alpha_3 \, f_s \, I_c + \alpha_4 \, f_s \, V_d \tag{4.32}$$

where

$$k_1 \, t_{off1} + k_4 = \alpha_1 \, I_c + \alpha_2 \tag{4.33}$$

$$k_2 + k_5 = \alpha_3 \tag{4.34}$$

$$k_3 = \alpha_4 \tag{4.35}$$

Here the four coefficients α_1, α_2, α_3 and α_4 are determined experimentally.

It is clear from Eqn. (4.32) that the switching power loss is related to load current, d.c. supply voltage and switching frequency. It has a quadratic relationship with load current, a linear relationship with d.c. link voltage and a linear relationship with switching frequency. These relationships will be verified experimentally.

Switching loss during sinusoidal PWM operation

Since under sinusoidal operation the waveforms are symmetrical over positive and negative cycles, only the positive half cycle of the load current will be considered. The discussion is still based on the assumption that the carrier frequency is high relative to the modulating frequency.

Assuming a sinusoidal load current, Eqn. (4.12), the switching power loss can be obtained by integrating the switching energy dissipation over the half fundamental cycle,

$$P_{swPWM} = \frac{1}{\pi}\int_{-\varphi}^{\pi-\varphi} P_{sw}\, d(\omega t)$$

$$= f_s \left[\frac{1}{2}\alpha_1 V_d I_m^2 + \frac{2}{\pi}(\alpha_2 V_d + \alpha_3) I_m + \alpha_4 V_d \right] \qquad (4.36)$$

4.4.1.3 Formulation of inverter total loss model

By summing Eqn. (4.21) for power semiconductor switch conduction loss, with Eqn. (4.22) for diode conduction loss and Eqn. (4.36) for switching loss, an expression for the total losses dissipated in one power semiconductor switch and one diode pair when operating under sinusoidal PWM mode is obtained,

$$P_{PWM} = \frac{V_{T_o} I_m}{\pi}\left(1 + \frac{\pi}{4} M\cos\varphi\right) + \frac{K_T I_m^2}{\pi}\left(\frac{\pi}{4} + \frac{2}{3} M\cos\varphi\right)$$

$$+ \frac{V_{D_o} I_m}{\pi}\left(1 - \frac{\pi}{4} M\cos\varphi\right) + \frac{K_D I_m^2}{\pi}\left(\frac{\pi}{4} - \frac{2}{3} M\cos\varphi\right)$$

$$+ f_s \left[\frac{1}{2} \alpha_1 V_d I_m^2 + \frac{2}{\pi} (\alpha_2 V_d + \alpha_3) I_m + \alpha_4 V_d \right] \quad (4.37)$$

4.4.1.4 Experimental determination of inverter loss coefficients

Principle of switching loss measurement

(a) Power losses in the inverter tests

The breakdown of losses in an inverter system when supplying a fixed inductive load is illustrated in Fig 4.8. Power balance across the system yields,

$$P_{IN} = P_C + P_{INV} + P_{R_L} \quad (4.38)$$

where

P_{IN} Input power from the d.c. supply.

P_C Capacitor bank power loss. This is assumed to be negligible.

P_{R_L} Load resistance loss.

P_{INV} Inverter loss, which is comprised of conduction loss P_{cond} and switching loss P_{sw},

$$P_{INV} = P_{cond} + P_{sw} \quad (4.39)$$

Since device conduction loss has a direct relationship with current it would be advantageous to determine the conduction loss from tests performed at a constant d.c. load current. The conduction loss can thus be expressed as,

$$P_{cond} = I_c V_T \lambda + I_c V_D (1 - \lambda) \quad (4.40)$$

where

I_c Collector current

V_T IGBT conduction voltage drop

V_D Diode conduction voltage drop

λ Duty cycle

The conduction voltage drop across an IGBT is the sum of two components: the P-N junction voltage and the voltage drop across the driving MOSFET. Thus, the conduction voltage drop across an IGBT never goes below the junction threshold. The voltage drop across the driving MOSFET, on the other hand, has the characteristic of a typical low voltage MOSFET, i.e. has an approximately linear relationship with conducting current. The conduction voltage drop and its relationship with the conducting current for a particular device is best obtained through experimental measurements due to the sensitivity of the IGBT conduction voltage drop to the gate control voltage level. In the experimental inverter, a pair of paralleled IXSH40N60 IGBTs were used, and their conduction voltage followed the relationship,

$$V_T = 1.20 + 0.039\, I_c \tag{4.41}$$

The conduction voltage drop of the freewheel diode was measured to be approximately constant,

$$V_D = 0.90 \tag{4.42}$$

The resistance losses in the load were calculated using,

$$P_{R_L} = I_L^2\, R_L \tag{4.43}$$

The resistance of the load inductor, R_L, was characterised over a range of temperature, $T\,(^oC)$, and was found to be,

$$R_L = (\,33.8 + 0.166\, T\,)/1000\ \ (\,Ohm\,) \tag{4.44}$$

Thus, the switching loss in the inverter can be separated by a simple calculation,

$$P_{sw} = P_{IN} - P_{cond} - P_{R_L} \tag{4.45}$$

(b) Inverter switching loss measurement scheme

The inverter switching power loss is dependent on three parameters: d.c. link supply voltage, load current and switching frequency. To investigate the individual relationships between the switching loss and these parameters the measurement scheme shown in Fig 4.9 was adopted.

In this test an H-bridge was employed with the four power semiconductors switched in pairs, T_1 T_2 and T_3 T_4 , i.e. T_1 and T_2 are on whilst T_3 and T_4 off, or vice versa. The switching pulses were obtained by comparing a d.c. signal with a bipolar triangular signal, which was calibrated such that when the reference demand is zero the duty cycle was exactly 50%.

Since the resistance of the load inductor used was very small (0.04Ω), only a small variation of duty cycle around 50% is required to obtain the rated d.c. load current. At the duty cycle of 50% the peak current ripple can be calculated from,

$$\Delta I = \frac{V_d}{2 f_s L} \tag{4.46}$$

where f_s is the switching frequency, and L is the load inductance.

In the tests, the switching loss of a semiconductor switch and diode pair can then be separated by subtracting the conduction loss and copper loss in the load inductor from the total input power,

$$P_{sw} = \frac{1}{2}\left(P_{IN} - 2P_{cond} - P_{R_L} \right) \tag{4.47}$$

where

$$P_{IN} = V_d I_d \tag{4.48}$$

$$P_{cond} = I_L V_T \lambda + I_L V_D \lambda \quad , \lambda = 0.5 \tag{4.49}$$

$$P_R = R_L I_L^2 + \frac{1}{12} R_L (\Delta I)^2 \tag{4.50}$$

Inverter loss measurement results

Using the experimental inverter described in Chapter 2 it is possible to derive three H-bridges, viz., $T_1T_3T_4T_6$, $T_1T_5T_4T_2$ and $T_3T_5T_6T_2$. The losses in each H-bridge were measured with,

(A) A variable load current I_L, and fixed d.c. supply voltage and switching frequency.
(B) A variable d.c. supply voltage V_d, and fixed load current and switching frequency.
(C) A variable switching frequency f_s, and fixed d.c. supply voltage and load current.

The test results are given in Appendix E, and are summarised in Fig. 4.10, Fig. 4.11 and Fig.4.12, which plot the inverter loss P_{INV} against load current I_L (equal to the IGBT conducting current I_c), d.c. link supply voltage V_d, and switching frequency f_s, respectively.

Analysis of inverter loss test results

Using curve fitting techniques, the following relationships were obtained from the tests,

(a) Relationship between inverter loss and load current,

$$P_{INV} = 0.0617 I_L^2 + 2.19\, I_L + 3.95$$

$$\text{with } V_d = 60\ V,\ f_s = 10\ kHz$$

$$V_{T_o} = 1.20,\ K_T = 0.039,\ V_{D_o} = 0.90 \qquad (4.51)$$

(b) Relationship between inverter loss and d.c. supply voltage,

$$P_{INV} = 0.61\, V_d + 186$$

$$\text{with } I_L = 45\ A,\ f_s = 10\ kHz \qquad (4.52)$$

(c) Relationship between inverter loss and switching frequency,

$$P_{INV} = 3.96 f_s + 177$$

$$\text{with } I_L = 45A,\ V_d = 60\ V \qquad (4.53)$$

The results indicate the expected relationships, i.e. the inverter loss has a quadratic relationship with load current, a linear relationship with d.c. supply voltage and a linear relationship with switching frequency.

Determination of coefficients in switching power loss expression

Since during the tests, the total inverter loss is given by,

$$P_{INV} = 2 \cdot P_{cond} + 2 \cdot P_{sw}$$

$$= 2\, I_c\, V_T\, \lambda + 2\, I_c\, V_D\, (1-\lambda) + 2\, (\alpha_1\, I_c + \alpha_2)\, f_s\, I_c\, V_d + 2\, \alpha_3\, f_s\, I_c + 2\, \alpha_4 f_s\, V_d \tag{4.54}$$

where the operating duty of the switches is approximately 50%, i.e.,

$$\lambda = 0.5 \tag{4.55}$$

Here the conducting current I_c is equal to the load current I_L, and V_T and V_D are given by Eqns. (4.41) and (4.42), respectively.

Comparing to Eqns. (4.51), (4.52) and (4.53) yields the following set of simultaneous equations,

$$\begin{cases} V_{T_o} + V_{D_o} + 20\, \alpha_3 + 1200\, \alpha_2 = 2.19 \\ 1200\, \alpha_4 = 3.95 \\ 900\, (\, 45\, \alpha_1 + \alpha_2\,) + 20\, \alpha_4 = 0.61 \\ 5400\, (\, 45 \alpha_1 + \alpha_2\,) + 90\, \alpha_3 + 120\, \alpha_4 = 3.96 \end{cases} \tag{4.56}$$

which were solved to give,

$$\begin{cases} \alpha_1 = 1.3 \times 10^{-5} \\ \alpha_2 = 2.0 \times 10^{-5} \\ \alpha_3 = 3.3 \times 10^{-3} \\ \alpha_4 = 3.3 \times 10^{-3} \end{cases} \tag{4.57}$$

The experimentally derived expression for the switching power loss of two paralleled IGBTs and a diode is therefore,

$$P_{sw} = (1.3\times10^{-5} I_c + 2.0\times10^{-5}) f_s I_c V_d + 3.3\times10^{-3} f_s I_c + 3.3\times10^{-3} f_s V_d \quad (4.58)$$

Although the experimental data in Fig. 4.12 only extends down to switching frequencies of 4kHz, considering the good linearity of the data relationship, it is believed that the model is applicable to the case where the switching frequency is below 1kHz. The validation of the model can be further illustrated in Fig. 4.13 by the good agreement between the predicted and measured inverter losses when driving the 3kW induction machine at the rated flux and 15Nm (75% of full load), with the inverter switching frequency varying in the range of 100Hz and 3kHz.

4.4.1.5 Experimental validation of sinusoidal PWM inverter loss model

The experimental inverter configured as an H-bridge was also used to validate the sinusoidal PWM loss model given in Eqn. (4.37). The inverter was switched using natural sampling sinusoidal PWM at an output frequency $f_o = 100\ Hz$ and a switching frequency $f_s = 10\ kHz$. The load was the air-cored inductor used earlier. To verify the effectiveness of the loss model over a wide operating conditions, the inverter output voltage, inverter output current and the d.c. link voltage were all varied during the tests. The inverter losses were obtained from the tests by subtracting the measured temperature compensated load resistive loss from the measured total inverter input power, i.e.

$$P_{INV} = P_{IN} - P_{R_L} \quad (4.59)$$

$$P_{IN} = V_d I_d \quad (4.60)$$

$$P_{R_L} = R_L I_m^2/2 \quad (4.61)$$

For each tested inverter operation state the inverter loss was also predicted using the derived model of Eqn. (4.37) and the parameters given in Eqns. (4.41), (4.42) and (4.57). The

measured and predicted values of inverter loss are summarised in Table 4.5, and indicate a good agreement between the developed loss model and the measurement.

Table 4.5. Measured and predicted losses in inverter under PWM control during H bridge tests

M	0.35	0.43	0.55	0.62	0.74	0.81	0.48	0.66	0.86
V_d (V)	20	20	20	20	20	20	30	30	30
I_d (A)	1.56	2.64	4.35	5.70	8.00	9.80	4.75	9.30	16.6
I_m (A)	15.5	22.5	30.8	36.4	44.4	49.7	42.0	63.0	85.4
T_{R_L} (^oC)	21	21	22	23	24	26	29	29	28
R_L ($m\Omega$)	37.3	37.3	37.4	37.6	37.8	38.1	38.6	38.6	38.4
P_{IN} (W)	31.2	52.8	87.0	114.0	160.0	196.0	142.5	279.0	498.0
P_{R_L} (W)	4.5	9.4	17.7	24.9	37.2	47.0	34.0	76.6	140.0
P_{INV} (W)	26.7	43.4	69.3	89.1	122.8	149.0	108.5	202.4	358.0
$P_{INV(PWM)}$ (W)	28.6	44.6	66.9	83.9	117.4	131.0	104.5	190.4	309.6
M	0.22	0.43	0.54	0.70	0.40	0.29	0.22	0.19	
V_d (V)	40	40	40	40	60	73.1	106.2	121.6	
I_d (A)	0.97	5.00	8.00	13.90	6.00	3.90	2.70	2.50	
I_m (A)	18.2	51.8	68.6	92.4	72.8	60	60	60	
T_{R_L} (^oC)	28	28	30	32	33	24	25	27	
R_L ($m\Omega$)	38.4	38.4	38.8	39.1	39.3	37.8	38.0	38.3	
P_{IN} (W)	38.8	200.0	320.0	556.0	360.0	285.1	286.7	304.0	
P_{R_L} (W)	6.4	51.5	91.3	166.9	104.1	68.0	68.4	68.9	
P_{INV} (W)	32.4	148.5	228.7	389.1	255.9	217.1	218.3	235.1	
$P_{INV(PWM)}$ (W)	36.7	144.9	222.1	359.4	256.9	196.2	213.6	221.8	

Note: P_{INV} (W) is the measured power loss and $P_{INV(PWM)}$ (W) is the predicted power loss in the PWM inverter.

4.4.2 Comparison of the proposed inverter switching loss model with an alternative published model

Following a similar procedure to that used to model the conduction losses for an IGBT inverter, an alternative inverter switching loss model has been proposed by Casanellas, using parameters from the manufacturer data sheets [Casanellas 1995]. This switching loss model is

summarised in terms of three expressions, Eqns. (4.63) - (4.65), representing turn-on loss, turn-off loss and recovery loss respectively, i.e.,

$$P_{sw} = P_{swon} + P_{swoff} + P_{rr} \tag{4.62}$$

where

$$P_{swon} = \frac{V_d\, t_{rn}\, I_c^2\, f_s}{8\, I_{cn}} \tag{4.63}$$

$$P_{swoff} = V_d\, I_c\, t_{fn}\, f_s\, (\frac{1}{3\pi} + \frac{1}{24}\frac{I_c}{I_{cn}}) \tag{4.64}$$

$$P_{rr} = f_s\, V_d\, [\, (\, 0.28 + \frac{0.38}{\pi}\frac{I_c}{I_{cn}} + 0.015\, (\frac{I_c}{I_{cn}})^2\,)\, Q_{rr} + (\frac{0.8}{\pi} + 0.05\frac{I_c}{I_{cn}})\, I_c\, t_{rrn}\,] \tag{4.65}$$

V_d - inverter dc link voltage (V)

I_c - collector current (A)

I_{cn} - rated collector current (A)

f_s - switching frequency (Hz)

t_{rn} - rated rise time (ns)

t_{fn} - rated fall time (ns)

t_{rrn} - rated recovery time (ns)

Q_{rrn} - rated recovery charge (nc)

The relevant parameters taken from the manufacturers' data sheet are listed in Table. 4.6 for the IGBTs and diode used in the experimental inverter (IXSH40N60 and DSE12X61-60C).

Table 4.6 Inverter parameters for switching loss modelling

t_{rn}	t_{fn}	t_{rrn}	Q_{rrn}	I_{cn}
200 ns	300 ns	35 ns	140 nc	150 A

Since the experimental inverter utilised two IGBTs in parallel as one switch, the value of I_{cn} is twice the rated current of a single IGBT.

Table 4.7 compares the measured inverter switching losses with the proposed model in this thesis and the published model by Casanellas. It is observed that the proposed model gives better matches to the measurements than the published model.

Table 4.7 Inverter switching losses calculated with two different models.

Operating conditions	Measurements	Proposed method	Casanellas' method
$V_d = 60V, f_s = 10kHz, I_c = 45A$	41W	40 W	28 W
$V_d = 60V, f_s = 18kHz, I_c = 45A$	82W	70 W	52 W
$V_d = 117V, f_s = 10kHz, I_c = 45A$	83 W	74 W	57 W

4.4.3 Influence of PWM strategies on inverter loss

The influence of a particular PWM strategy on the overall inverter loss was also investigated using the developed device switching and conduction loss models. For the purpose of this study, the operation of the 26kW electric vehicle induction machine at the rated torque and variable speed was considered. Although the fundamental current conducting through the inverter will be the same for all PWM strategies, the different pulse patterns of the various PWM methods may impose different conduction and switching losses in the inverter. An interative technique was employed to estimate the loss from the individual PWM pulse patterns. Since the pulse patterns all have half-wave symmetry, for any turn-on instant there will be a turn-off instant having the same output voltage value but with opposite polarity. This is the same for output current. Thus, to calculate the switching loss, only the turn-on instants or only the turn-off instants need to be considered, and the previously derived IGBT and diode pair, single pulse (one turn-on and -off) switching loss model can be used. The IGBT and diode conduction losses were calculated based on the current magnitude and direction during each pulse.

Fig 4.14 show the simulated inverter losses when the driven induction machine is operating at rated torque (122Nm) over a speed range from 0 to the rated value (2022rpm), and the inverter switching frequency ratio maintained at 9. It is observed that the inverter loss is only marginally influenced by modulation methods and supports conclusions from other workers [Murphy 1983]. The effectiveness of the inverter loss model derived based on the assumption of relatively high frequency ratio is also illustrated in Fig. 4.14.

4.5 Inverter driven induction machine harmonic power losses

The analysis and prediction of harmonic losses in induction machines when operating with periodic nonsinusoidal supply voltages have received much attention over the years. Usually, it is assumed that each harmonic present in the supply waveform may be treated separately and the effects added using the principle of superposition. Accordingly, the supply voltage waveform is expressed as a Fourier series, and the effect of each harmonic component is calculated by applying that harmonic voltage to the induction machine equivalent circuit, in which reactance components and slip are scaled for frequency. Based on this approach, Klingshirn and Jordan [Klingshirn 1968] have presented some general expressions for describing machine harmonic losses, and found that, for some input waveforms of high harmonic content, the harmonic losses may be as high as the losses contributed by the fundamental voltage and current. Chalmers and Sarkar [Chalmers 1968] have published a detailed breakdown of the harmonic losses in induction machines. This theoretical and experimental investigation concluded that the increase in core loss due to time harmonic main fluxes is negligible, and the core loss due to space harmonic fluxes is also small, but the end-leakage and skew-leakage fluxes may produce an appreciable core loss at the harmonic frequencies. Although this work is a very useful guide to machine design, it is not easily translated into a method for quantifying the machine harmonic loss. Williamson and Cann [Williamson 1984] detailed each component in the equivalent circuit, and proposed an iron-loss resistance model to account for harmonic eddy-current loss and hysteresis loss. However, with the suspect accuracy of determining this component even with a pure

sinusoidal supply, the calculation of iron losses with a nonsinusoidal voltage is somewhat obscure. Without using the equivalent circuit, Buck et. al. [Buck 1984] proposed a method of estimating the additional harmonic loss based on the machine nominal loss at the rated condition. At each harmonic frequency, the stator, rotor and iron losses are estimated separately. From knowledge of the voltage spectrum of the supply, the total harmonic loss is then obtained by summing the loss contributions of the separate harmonics. Skin effects and leakage effects were included in the model using factors based on empirical data, the machine power rating and the machine geometry. The semi-empirical machine loss model developed by Buck considered harmonics between about 100Hz and 20,000Hz, and has been verified by experiments on a range of machines of power rating from 1 to 1000 kW. The work also included a comparison with previously published measured machine harmonic losses of [Klingshirn 1968] and [Chalmers 1968], giving added validity to the model.

In this thesis, no attempt is intended to look into the detail of each harmonic loss component in an induction machine, rather the simple but reliable machine loss modelling methodology, as presented by Buck, is employed to investigate the machine losses under PWM control. The effectiveness of the model for the application in the thesis will also be validated by comparing the measured and predicted machine harmonic losses.

4.5.1 Induction machine harmonic loss model

For an unskewed induction machine, the supply induced harmonic losses in the machine include components of,

(a) Stator harmonic copper loss
(b) Rotor harmonic copper loss
(c) Harmonic iron loss

Due to the skin effect, the rotor and stator resistances will increase with harmonic frequencies, whilst the leakage inductances will decrease with harmonic frequencies. These variations can be expressed with respect to their d.c. or normal values as respectively [Buck 1979, 1984],

$$R_s(f_n)/R_{s,dc} = 1 + C_s H_s^4 f_n^2 \tag{4.66}$$

$$R_r(f_n)/R_{r,dc} = 1 + C_r H_r f_n^{0.5} \tag{4.67}$$

$$L_l(f_n)/L_{l,nom} = \begin{cases} 2 f_n^{-0.16}, & \text{for } f_n \geq 100Hz \\ 1, & \text{for } f_n < 100Hz \end{cases} \tag{4.68}$$

where

f_n is the harmonic frequency, n>1.

H_s is the stator slot depth in cm.

H_r is the rotor conductor height in cm.

C_s and C_r are coefficients dependent upon the motor power rating. For the 3kW induction machine, $C_s = 0.63 \times 10^{-8}$ and $C_r = 0.025$; for the 26kW traction machine, $C_s = 0.63 \times 10^{-8}$ and $C_r = 0.05$ [Buck 1984].

At harmonic frequencies the machine speed slip is nearly unity, the magnetising current component can generally be neglected and the harmonic current magnitude is primarily determined by the leakage reactance, which dominates over the stator and rotor resistances. Thus, the rms value of the nth harmonic phase current can be obtained as,

$$I_n = \sqrt{\frac{3}{2}} \cdot \frac{V_n}{n X} \tag{4.69}$$

where V_n is the amplitude of the nth harmonic in the inverter output phase voltage, and X is the machine leakage reactance at the harmonic frequency and is found from the machine normal leakage reactance X_{nom} at the rated frequency f_e, using,

$$X = \frac{f_1}{f_e} X_{nom}\, \sigma \tag{4.70}$$

where σ is a factor which accounts for the machine leakage inductance variation with frequency, Eqn. (4.68),

$$\sigma = \begin{cases} 2 f_n^{-0.16}, & \text{for } f_n \geq 100Hz \\ 1, & \text{for } f_n < 100Hz \end{cases} \tag{4.71}$$

This expression was found approximately independent of motor power rating [Buck 1984].

4.5.1.1. Stator harmonic copper loss

Since each harmonic current is assumed independent of all of the others, a series of independent equivalent circuits, one for each harmonic, can be used for the calculation of harmonic copper loss.

The stator copper loss at the nth harmonic frequency in one phase is obtained using Eqn. (4.66) as,

$$P_s(f_n) = (1 + C_s H_s^4 f_n^2) R_{s,dc} I_n^2 \tag{4.72}$$

Applying superposition, the total stator harmonic copper loss is thus,

$$P_{sT} = 3 \sum_{n=2}^{\infty} (1 + C_s H_s^4 f_n^2) R_{s,dc} I_n^2 \tag{4.73}$$

4.5.1.2 Rotor harmonic copper loss

Similarly, the total rotor harmonic resistive loss can be expressed using Eqn. (4.67) as,

$$P_{rT} = 3 \sum_{n=2}^{\infty} (1 + C_r H_r f_n^{0.5}) R_{r,dc} I_n^2 \tag{4.74}$$

4.5.1.3 Harmonic iron loss

Machine harmonic iron losses are significantly influenced by the method of machine construction and the magnetic materials used, and as a result are very difficult to predict accurately. The harmonic iron loss in an unskewed induction machine can be considered to be composed of,

(a) Core losses due to harmonic main fluxes. The stator core loss (hysteresis loss and eddy current loss) is a function of the flux density in the stator core and at constant fundamental voltage and frequency, is approximately constant [Chalmers 1968]. The rotor core loss is a function of flux density and speed, and is virtually negligible at rated speed. Although the presence of harmonic currents will act to increase the peak flux density, and thus increase the core loss. However, this increase in loss has been found to be only a small fraction of the total core loss, and can be neglected in the total loss evaluation [Klingshirn 1968].

(b) Loss due to end-leakage fluxes. These losses occur in the end regions of both the stator and the rotor and are a function of the harmonic frequency. It has been found that end-leakage loss is the dominant component of the stray load loss at the harmonic frequencies, whereas other stray load losses are sufficiently small to be neglected [Chalmers 1968]. It has been also suggested that the total stray load loss at nth harmonic is proportional to [Buck 1984],

$$I_n^2 f_n^{1.18} \tag{4.75}$$

Thus, the harmonic iron loss at the nth harmonic could be expressed as,

$$P_I(f_n) = C_i f_n^{1.18} i_n^2 P_{i,nom} \tag{4.76}$$

where

$$i_n = \frac{I_n}{I_1} \tag{4.77}$$

I_1 is the stator fundamental phase current in rms, $P_{i,nom}$ is the normal iron loss when the machine is supplied from a pure sinusoidal source, and C_i is a machine specific loss coefficient. For the 3kW induction machine, $C_i = 2.5 \times 10^{-3}$, and for the 26kW machine, $C_i = 8.8 \times 10^{-4}$.

The machine total harmonic iron loss is therefore,

$$P_{iT} = \sum_{n=2}^{\infty} C_i f_n^{1.18} i_n^2 P_{i,nom} \qquad (4.78)$$

4.5.1.4. Experimental validation of induction machine harmonic loss model

When an induction machine is operated at a particular speed and load point, the application of different PWM methods will yield different drive system total loss, and if the modulation frequency, fundamental frequency and voltage are fixed the system loss difference will indicate the variation in machine harmonic loss only. Here, the experimental 3kW induction machine has been used to evaluate the machine harmonic loss model. The relevant geometrical and electrical parameters of the machine are listed in Table 4.8, and the system operation conditions are given in Table. 4.9.

Initially, the machine was driven by the vector space PWM and operated at the rated flux and at a constant torque of 15Nm (75% of full load). The harmonic content in the machine supply was varied by adjusting the frequency ratio in the vector space PWM. The detailed experiment results are given in Appendix F, and the measured and predicted machine harmonic losses are shown in Fig. 4.15, which indicate a good agreement for modulation depth above 0.6. At lower modulation depths the model tends to underestimate the machine harmonic loss with a maximum error of 80W.

Also, Fig. 4.16 shows the measured and modelled difference in system loss when sub-optimal PWM and the adjustable PWM were applied to the 3kW inverter fed induction machine drive. The predictions and the experimental results show a fairly good agreement and indicate a trend of increased harmonic loss difference with modulation depth. However, a relatively large error of about 20W between prediction and measurement occurs below a modulation depth of 0.6, as shown in Fig.4.16. Considering the relative small difference in loss compared to the total machine harmonic loss for either method, the error is within the experimental accuracy of the measurements.

Table. 4.8 Geometrical and electrical parameters of experimental 3kW induction machine for harmonic loss calculations

Stator slot depth	H_S	15.5	mm
Rotor conductor height	H_r	15.0	mm
Stator d.c. resistance	$R_{s,dc}$	1.96	Ω
Rotor d.c. resistance	$R_{r,dc}$	1.74	Ω
Nominal leakage reactance @50Hz	X_{nom}	4.93	Ω
Machine fund. current @ 75% load	I_1	4.88	A
Machine nominal iron loss @50Hz	$P_{I,nom}$	350	W
Stator loss coefficient	C_s	6.3×10^{-9}	
Rotor loss coefficient	C_r	5×10^{-2}	
Iron loss coefficient	C_i	2.5×10^{-3}	

Table. 4.9 3kW machine operation conditions for machine harmonic loss evaluation

d.c. link voltage	340	V
Machine load	15 (75% FL)	Nm
PWM frequency ratio	9	
PWM modulation depth	0.1 - 1.1	

4.5.2. Assessment of influence of PWM strategies on induction machine harmonic losses in a traction drive

Again for the purpose of this analysis, the 26kW induction machine was assumed to be controlled under the constant flux mode and was operating at rated torque with the speed varying from 0 to the rated value. The machine additional losses, viz., stator harmonic copper loss, rotor harmonic copper loss and machine harmonic iron loss, were calculated for various PWM strategies. Here, for the purpose of comparing machine harmonic losses between different PWM methods, a fixed frequency ratio of 9 was used. Further investigations of machine harmonic loss with variable frequency ratio will be undertaken in section 4.7. The relevant geometrical and electrical parameters for the 26kW induction machine are given in

Table 4.10. The simulated results are shown in Fig 4.17, where (a) shows the variation of stator harmonic copper loss with the machine supply voltage (modulation depth) and different PWM methods, (b) the rotor harmonic copper loss, (c) the machine harmonic iron loss, and (d) the machine total harmonic loss. It is observed that the optimal harmonic minimisation method induces the lowest harmonic loss in the machine, as would be expected. Adjustable PWM gives the lowest machine harmonic loss amongst the on-line PWM strategies, especially when the modulation depth is relatively high. Vector space PWM and sub-optimal PWM result in almost identical machine harmonic loss, whilst natural sampling PWM gives the poorest performance. Though the optimal harmonic elimination PWM has the capability of eliminating low order harmonics, it introduces a relatively high machine harmonic loss over most of the operating voltage range.

Table 4.10. Geometrical and electrical parameters of the 26kW induction machine for harmonic loss calculations

Stator slot depth	H_s	22.69	mm
Rotor conductor height	H_r	13.44	mm
Stator dc resistance	$R_{s,dc}$	0.0528	Ω
Rotor dc resistance	$R_{r,dc}$	0.0531	Ω
Nominal leakage reactance @103.2Hz	X_{nom}	0.4453	Ω
Machine rated frequency	f^*	103.2	Hz
Machine rated current	I_1	75	A
Machine nominal iron loss @103.2Hz	$P_{I,nom}$	1215	W
Stator loss coefficient	C_s	6.3×10^{-9}	
Rotor loss coefficient	C_r	2.5×10^{-2}	
Iron loss coefficient	C_i	8×10^{-4}	

It is also interesting to note that the calculated machine harmonic loss trends follow the THD figure fairly well, which demonstrates the effectiveness of using a simple THD term to assess the harmonic loss performance with different PWM strategies.

4.6. Complete induction machine drive system additional losses

The additional losses in an inverter drive system are the sum of the harmonic losses in the induction machine, and the conduction and switching losses in the inverter.

4.6.1 Simulation of influence of PWM strategies on induction machine drive system additional losses

Although the various PWM strategies have a marginal influence on the inverter loss, the difference in machine harmonic loss can be a significant proportion of total system additional loss, particularly when the frequency ratio is relatively low, e.g. 9, as discussed earlier. Fig 4.18 show the simulated system additional losses for the 26kW induction machine traction drive, when controlled in constant flux mode and operated at rated torque and variable speed. The inverter loss and machine harmonic loss are also shown in Fig 4.18 (a) and (b), respectively.

Due to the dominant effect of machine harmonic loss, the system additional loss variation with different PWM methods follows a similar trend to the machine harmonic loss variations, i.e. the optimal harmonic minimisation method yields the lowest system loss, whilst the adjustable PWM, the vector space PWM and sub-optimal PWM present low system loss.

4.6.2. Experimental assessment of influence of PWM strategies on induction machine drive system additional losses

The 3kW laboratory induction machine drive system was also used to investigate the influence of PWM strategies on the total system additional loss. Provided that the induction machine is operated at the same speed, the same load and the same level of fundamental current, the only variation of total system losses would be those introduced by the inverter and those caused by the harmonic effects. Therefore, an evaluation of the system additional loss can be made based on the measurement of the total system loss.

The total system loss was obtained from the difference of input and output power measurements. As has been discussed in Chapter 2 that such a loss measurement scheme has an accuracy of approximately 4% of the total loss, and when applied to the 3kW experimental system the accumulated errors for the loss measurement will be in the order of ± 10 Watts. The fundamental voltage and frequency were set using a constant V/f relationship and at each frequency the same depth of modulation was used to give equal fundamental current. The tests were performed at fundamental frequencies over the range of 10Hz to 46Hz, and a fixed load of 15 Nm (75% rated torque). The modulation frequency ratio was fixed at 9. The test results are shown in Fig 4.19. To highlight the trend of system loss variations, a straight line has been curve fitted against each set of the data. The obtained results follow the same trend as the THD of the idealised waveforms given in Fig 4.3. This again suggests that the voltage based THD figure of the loss performance of different modulation strategies is a valid indicator of the machine harmonic loss.

4.7 Influence of frequency ratio on machine harmonic loss and inverter switching loss

As the inverter switching frequency is increased, the quality of the supply to the induction machine will improve with a corresponding reduction in machine harmonic loss. However, the inverter switching loss will increase proportionally. Thus, when the drive system additional losses are considered, there will be an optimal balance between the increased inverter loss and the reduced machine harmonic loss.

To investigate the influence of the switching frequency on the machine harmonic loss and inverter switching loss, a series of computer simulations were undertaken on the 26kW induction traction motor fed from the IGBT inverter. Here, the vector space PWM was used and the machine was controlled at rated flux and rated current, with the inverter switching frequency ratio being varied over the range from 9 to 63. Fig 4.20 shows the modelled machine harmonic loss and inverter switching loss, as function of the machine speed and the frequency ratio. As would be expected, at increased speeds and output powers the value of

frequency ratio which corresponds to the maximum overall efficiency reduces, and at high speeds minimal losses are achieved at low frequency ratio. The value of inverter switching frequency which gives minimum system loss is also given in Fig. 4.21. Here the optimal inverter switching frequency varies within a band and demonstrates that adopting a gear changing scheme would be an effective method of realising the switching frequency control. However, as will be discussed later in Chapter 7, the gear changing scheme is not so suitable for electric traction applications, where the machine load varies along with the machine speed.

It is believed that the optimal switching to fundamental frequency ratio that gives maximum efficiency will be similar for different PWM strategies, since the performance of the various PWM methods are very similar for frequency ratios above 15. However, the optimal frequency ratio will clearly depend upon the characteristics of the different power semiconductors used in the inverter design. Power devices with lower conduction voltage drop and longer switching times (for example, a standard IGBT, BJT and MCT) will lower the optimal frequency ratio, whilst devices with higher conduction voltage drop and shorter switching times (for example, MOSFET and ultrafast IGBT) will give a higher optimal frequency ratio.

4.8 Torque ripple effects

4.8.1. Determination of inverter drive induction machine torque ripple

Torque ripple will occur in inverter fed machine drives, especially if supply waveform to the machine contains high level of low-order harmonic components. The level of torque ripple can be estimated by considering the fundamental flux and the harmonic currents. This is particularly true in the case of a cage-rotor induction machine, where the 5th and 7th harmonics due to the fundamental air-gap flux distribution are normally small. The back-emf in phase A can be written as,

$$e_a = E_1 \sin \omega t \tag{4.79}$$

and the harmonic series for the current in phase A supply from the inverter is,

$$i_a = I_1 \sin(\omega t - \varphi) + I_5 \sin 5(\omega t - \varphi_5) + I_7 \sin 7(\omega t - \varphi_7)$$
$$+ I_{11} \sin 11(\omega t - \varphi_{11}) + I_{13} \sin 13(\omega t - \varphi_{13}) + \cdots \tag{4.80}$$

and does not contain any triplen harmonics.

The product $e_a\, i_a$ contains an average component and even-order harmonics:

$$e_a\, i_a = P_o + P_2 \cos 2(\omega t - \varphi_2) + P_4 \cos 4(\omega t - \varphi_4)$$
$$+ \frac{1}{2} E_1 \left(I_7 \cos(6\omega t - 7\varphi_7) - I_5 \cos(6\omega t - 5\varphi_5) \right) + \cdots \tag{4.81}$$

The total instantaneous torque can thus be obtained by summing of the torque produced by phases A, B and C,

$$T_{em} = \frac{1}{\omega_m} \left(e_a\, i_a + e_b\, i_b + e_c\, i_c \right) \tag{4.82}$$

where ω_m is the mechanical rotating frequency of the rotor, e_b and e_c are the back-emfs of phase B and C respectively, and i_b and i_c are the corresponding phase currents.

Because of the supply balance across the three phases, the resultant torque will only contain an average component and harmonics orders with multiples of six. For example, a sixth harmonic torque ripple will be given by,

$$T_{em,6} = \frac{3}{2\,\omega_m} E_1 \left(I_7 \cos(6\omega t - 7\varphi_7) - I_5 \cos(6\omega t - 5\varphi_5) \right) \tag{4.83}$$

Other orders of torque ripple, such as 12th and 18th, can be obtained similarly.

4.8.2. Comparison of torque ripple induced by different PWM strategies

A torque ripple factor may be defined for the purpose of comparing the various PWM strategies,

$$\sigma_{T,n} = \sqrt{A^2 + B^2 - 2\,A\,B\cos(\alpha-\beta)} \tag{4.84}$$

where

$$A = V_{6n+1}/(6n+1) \tag{4.85}$$

$$B = V_{6n-1}/(6n-1) \tag{4.86}$$

$$\alpha = (6n+1)\,\varphi_{6n+1} \tag{4.87}$$

$$\beta = (6n-1)\,\varphi_{6n-1} \tag{4.88}$$

n=1,2 and 3 correspond to the torque ripple of order 6th, 12th and 18th, respectively.

The calculated torque ripple factors for various PWM strategies are shown in Fig. 4.22 for a frequency ratio of 9. The optimal harmonic elimination method cancels the 5th, 7th and 11th harmonics, and thus eliminates the 6th harmonic torque component. However, the resultant 12th harmonic is the highest among the PWM methods. The adjustable PWM method similarly acts to suppress 6th harmonic torque ripple, however, it gives much lower 12th harmonic torque ripple. The sub-optimal and vector space PWM methods again have an almost identical behaviour. Although the optimal harmonic minimisation method gives the lowest total harmonic distortion, it causes a high low order torque ripple. The 18th harmonic torque ripple for all PWM methods are similar.

4.8.3. Evaluations of torque ripple by experiment

The direct measurement of machine torque ripple requires the use of an inline torque transducer which is costly and difficult to set up. An estimation of torque ripple may be

obtained however from measurement of the inverter d.c. link current harmonics provided that the switching frequrency is relatively low, as described in Chapter 2. This method has been employed here to evaluate the torque ripple caused by the different PWM strategies at a relatively low switching frequency of about 170Hz. Fig 4.23 gives the inverter d.c. link current spectral distribution when sub-optimal PWM was applied, whilst Fig 4.24, Fig. 4.25 and Fig. 4.26 are the results with adjustable PWM, optimal harmonic elimination method, and optimal harmonic minimisation method, respectively. It is observed that the optimal harmonic elimination method has a very low 6th harmonic current component of d.c. link current, whilst the adjustable PWM has a lower 6th harmonic component than the sub-optimal PWM. Other observations are in agreement with the conclusions in the earlier simulations, for example, the optimal harmonic minimisation method results in a high sixth-order harmonic in the d.c. link current.

4.9 Acoustic noise effects

The presence of harmonic currents will also lead to increased acoustic noise in the driven machine. It has been recognised that most of the acoustic noise associated with a PWM driven induction machine is caused by the interaction of harmonic currents with the machine flux (predominately the fundamental), and the worst case may occur when one of the frequencies of the electromagnetically excited forces equals a natural frequency of either the machine or its surrounding environment. However, the noise problem can be reduced in several different ways, following considerations of audibleness, loudness and human ear noise annoyance. The magnetic noise can be forced into superaudible range by increasing the switching frequency above 16 kHz. However, this method is only effective in machines with small output capacity, since for large output power machine it may not be feasible because of the excessive inverter switching loss. Secondly, the magnetic noise loudness level can be reduced by proper selection of the switching frequency and by improvement of the inverter output waveform quality. The purpose of the former approach is to avoid the resonances of the machine [Belmans 1987], and the latter can be achieved by addition of an inverter output filter or by

suitable PWM design to suppress the undesirable harmonic frequencies which interact with the machine natural resonance frequencies [Garcia 1994]. Finally, instead of using the fixed frequency switching, the switching frequency can be changed at random to spread the energy over a wide bandwidth, since narrow band or tonal acoustic noise is subjectively more annoying to humans than broadband atonal noise of equal energy [Boys 1992].

Although different PWM methods lead to different levels of harmonic current distortion, during the laboratory experiments no obvious differences in acoustic noise were observed. In a high power electric vehicle drive, the acoustic noise may be of less concern compared to efficiency. Furthermore, since there may be efficiency benefits in operating the induction machine with reduced excitation field, particularly at light load, it will additionally reduce the acoustic noise during cruising and normal urban driving.

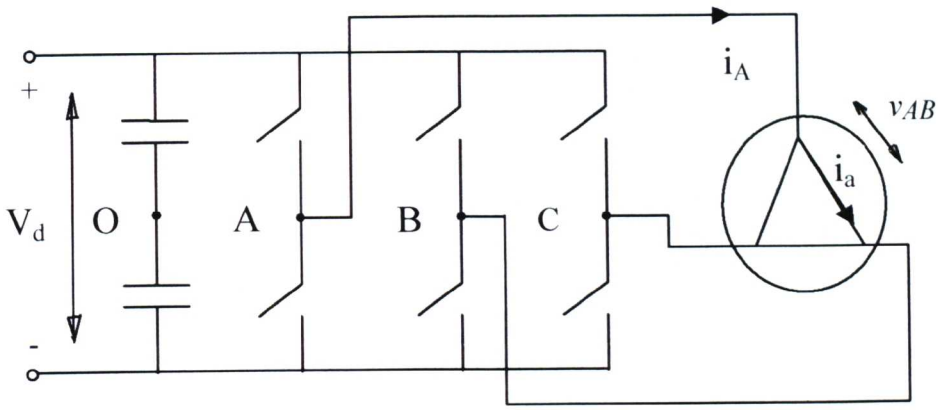

Fig. 4.1 Schematic of PWM inverter induction machine drive system.

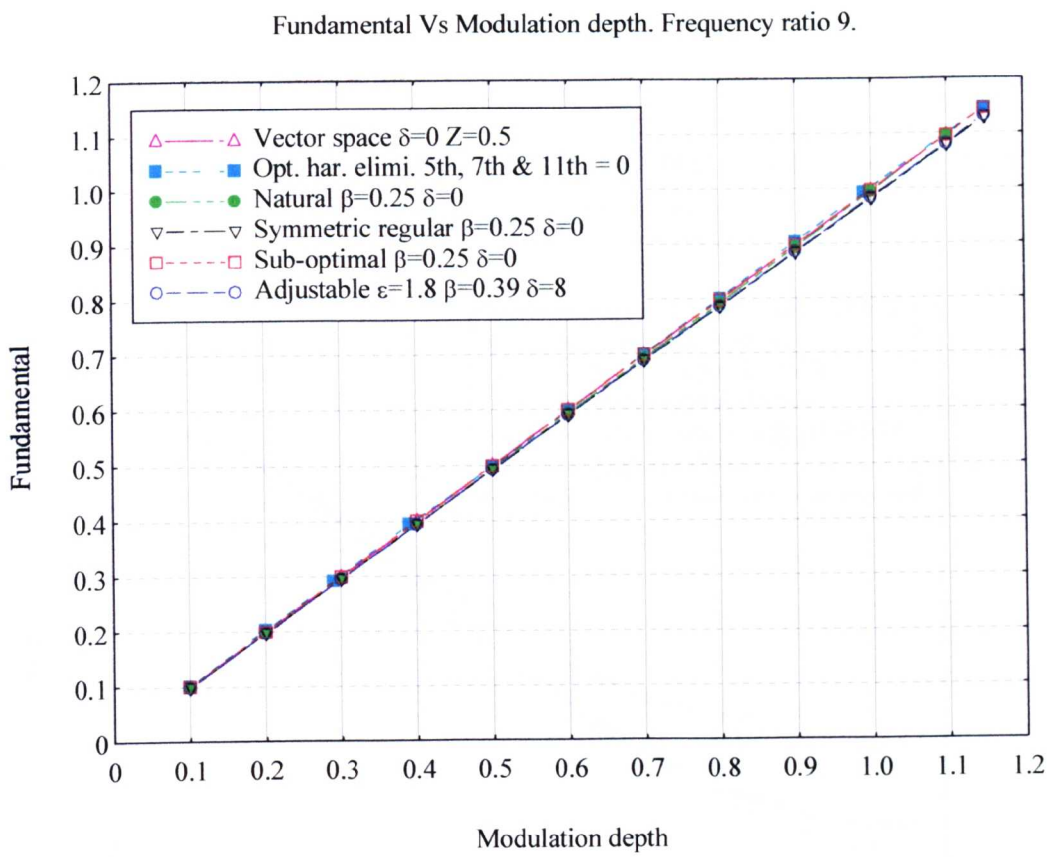

Fig 4.2 Linearity of voltage control of various PWM methods at frequency ratio of 9.

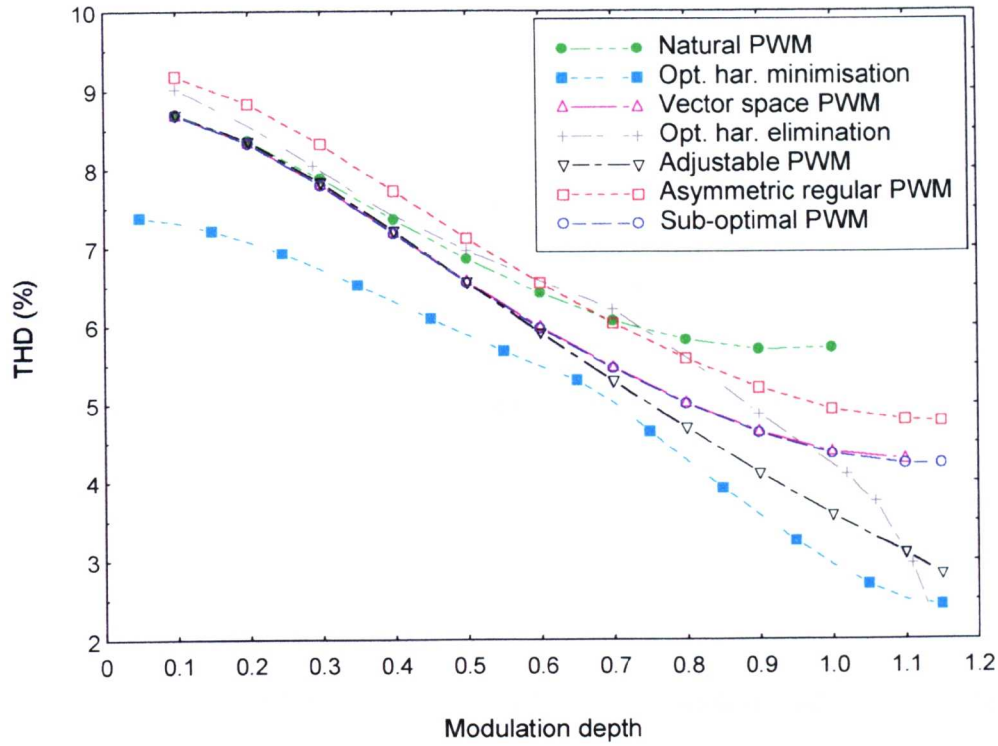

Fig 4.3 Total harmonic distortion (THD) of different PWM strategies against modulation depth. The frequency ratio is 9.

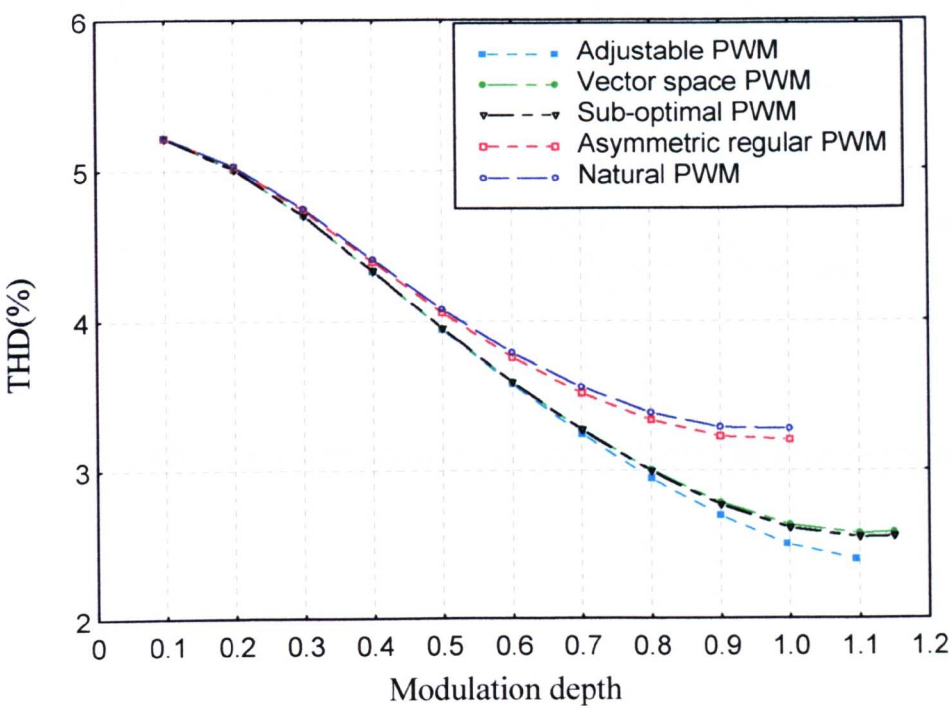

Fig 4.4 Total harmonic distortion (THD) of different PWM strategies against modulation depth. The frequency ratio is 15.

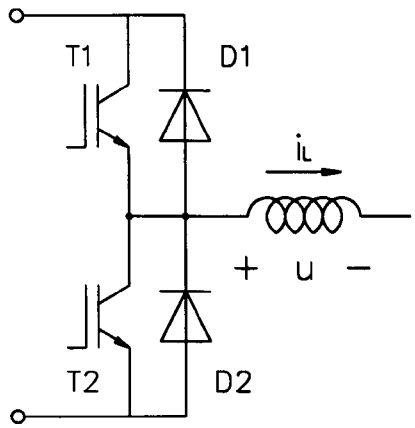

Fig 4.5 Inverter leg with an inductive load for conduction loss formulation.

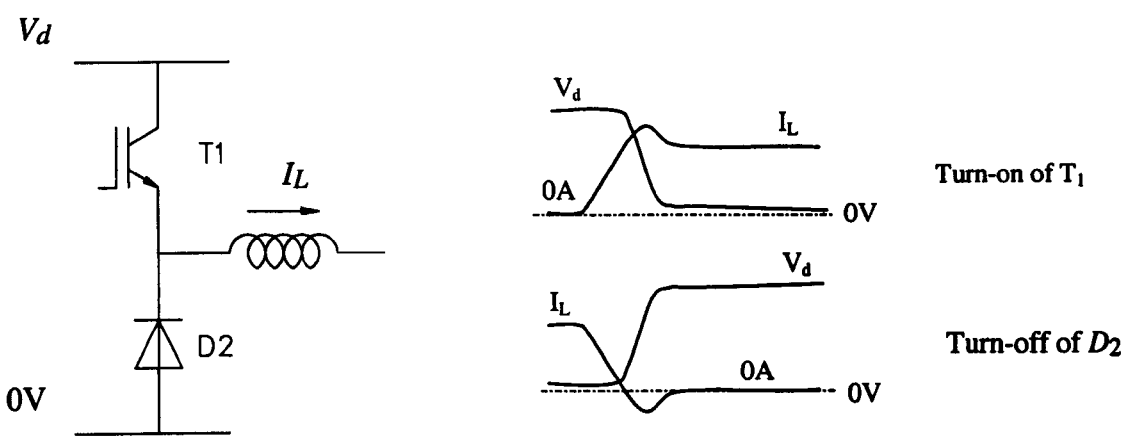

Fig 4.6 Force commutation of inverter pole with an inductive load.

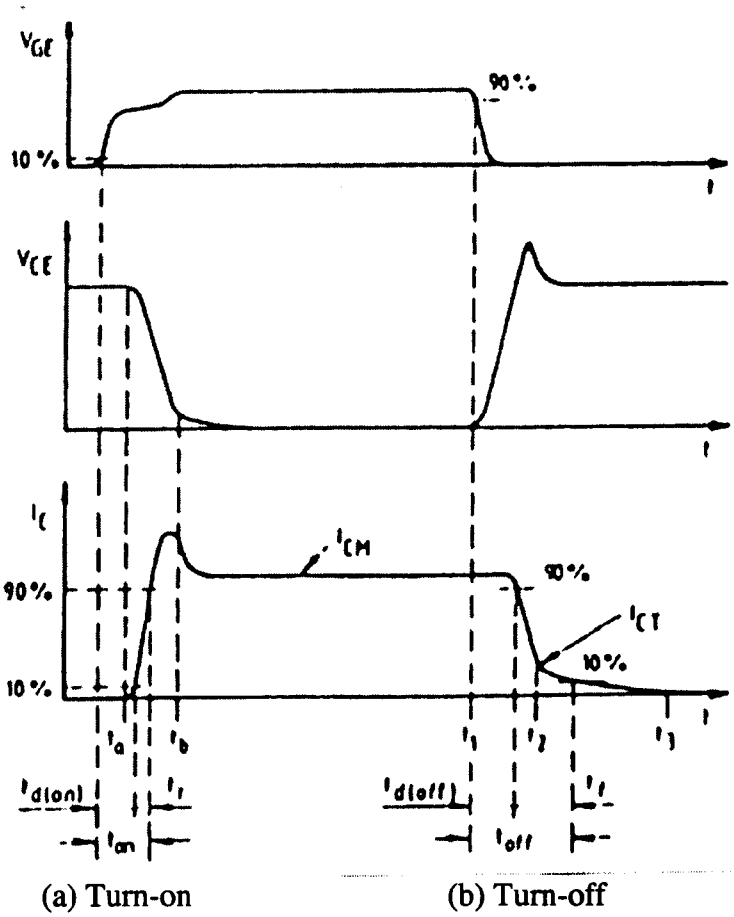

(a) Turn-on (b) Turn-off

Fig. 4.7 Switching characteristics of an IGBT device.

(© SEMIKRON)

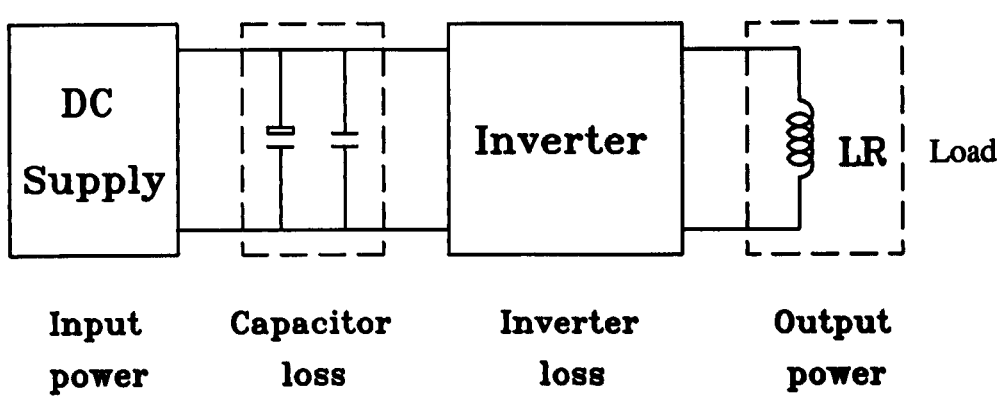

Fig 4.8 Separation of power loss in an inverter under test.

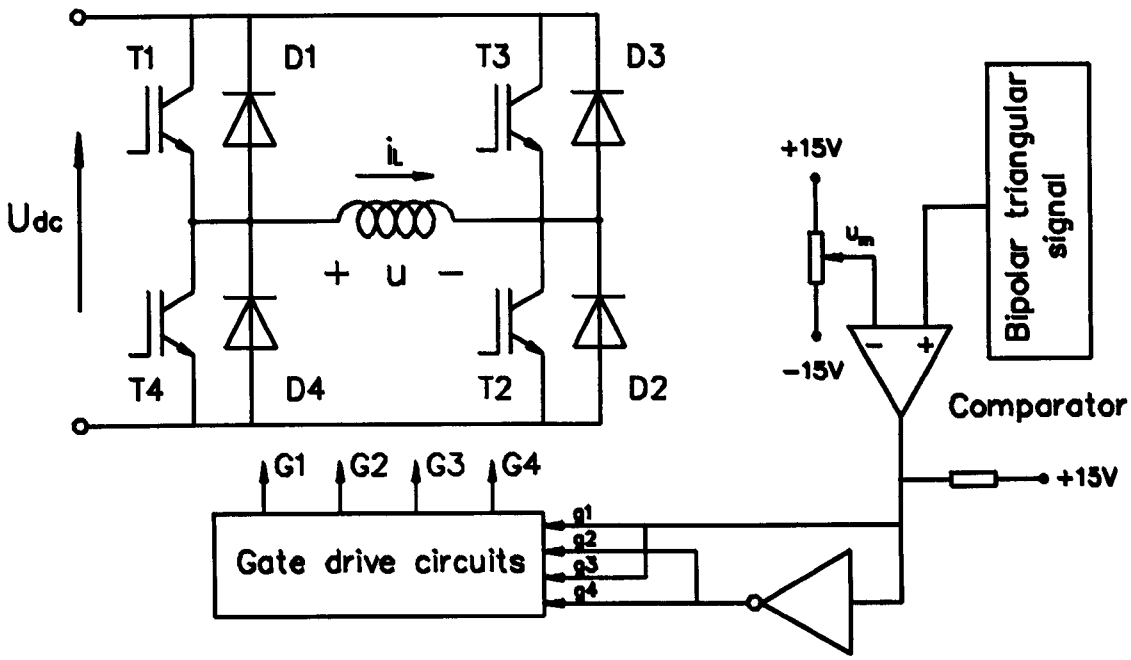

Fig 4.9 Test circuit for inverter switching loss measurement.

H-bridge inverter. DC supply 60V, switching frequency 10kHz.

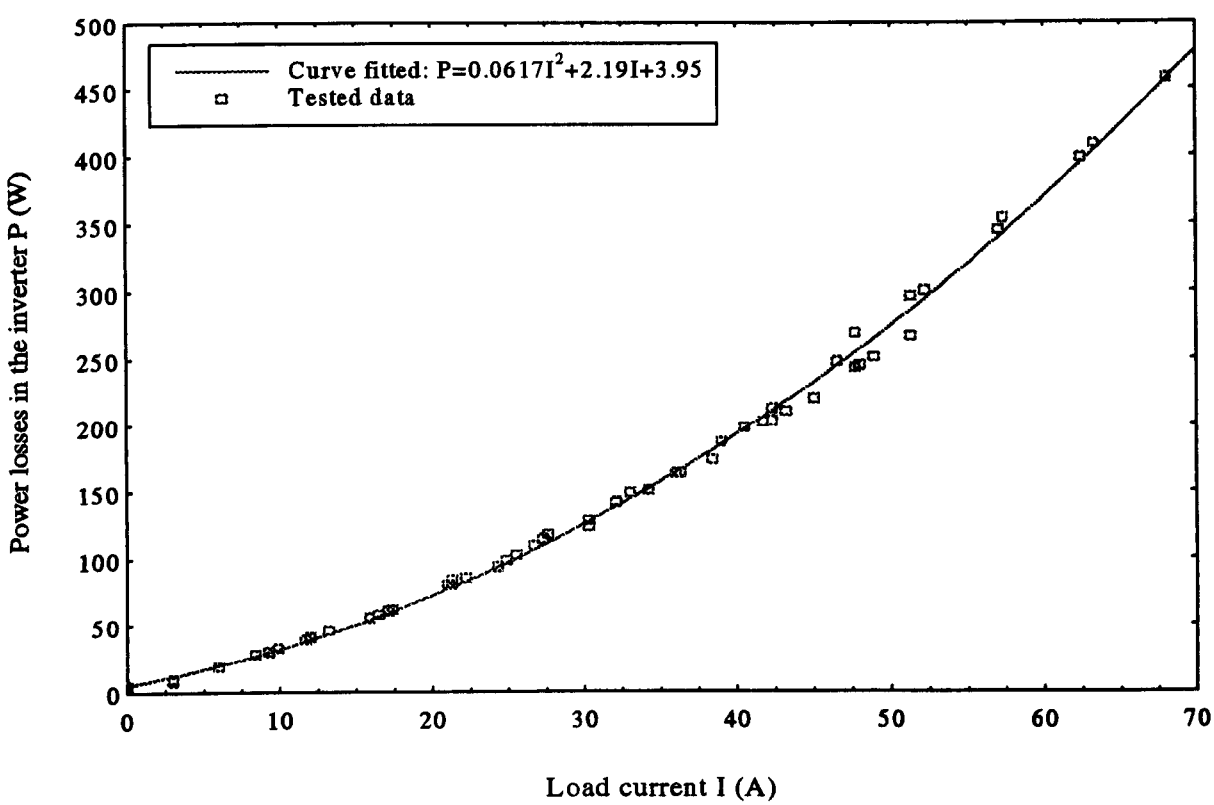

Fig 4.10 Measured H-bridge power loss as a function of load current.

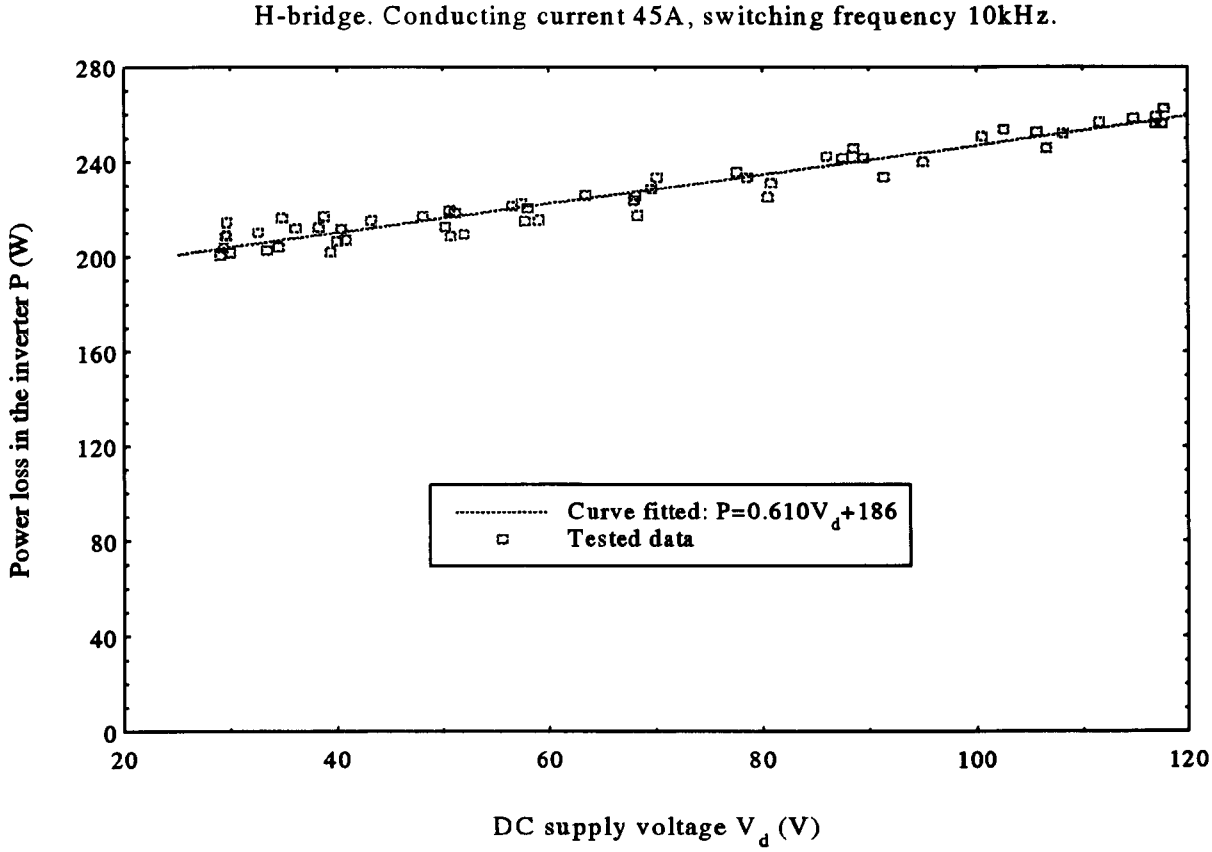

Fig 4.11 Measured H-bridge power loss as a function of d.c. supply voltage.

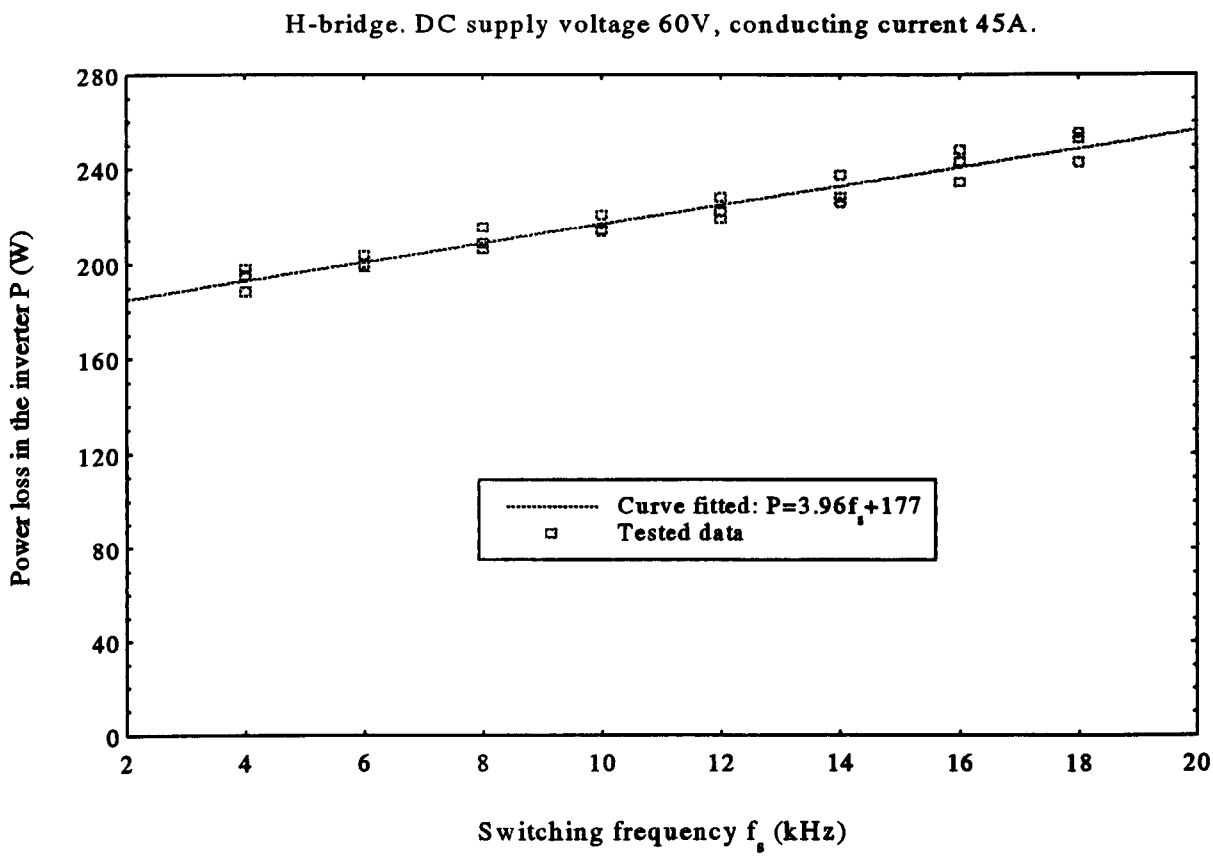

Fig 4.12 Measured H-bridge power loss as a function of switching frequency.

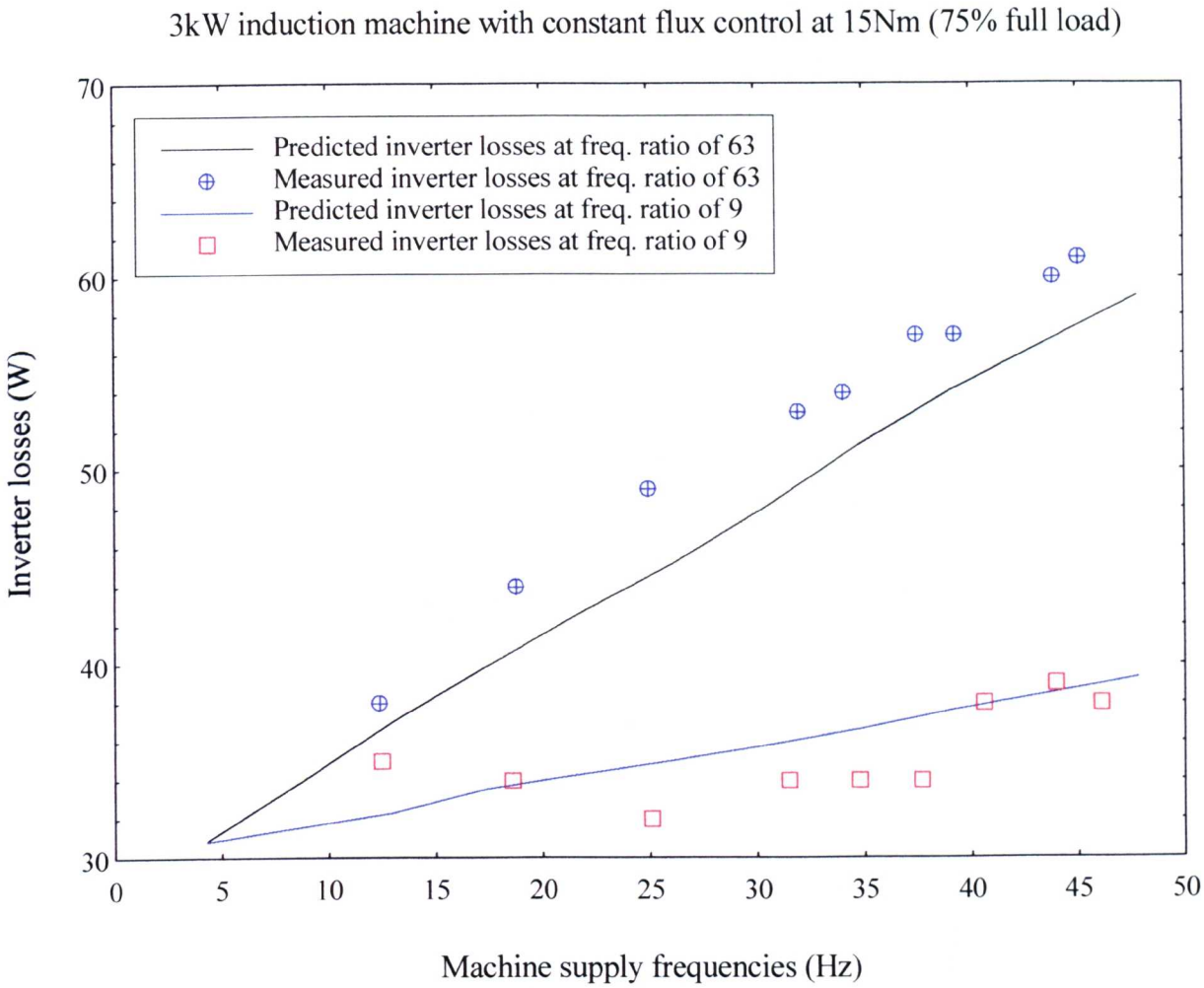

Fig. 4.13. Predicted and measured inverter losses when driving a 3kW induction machine at the rated flux and 15Nm (75% of full load), with the inverter switching frequency varying from 100Hz to 3kHz.

(a)

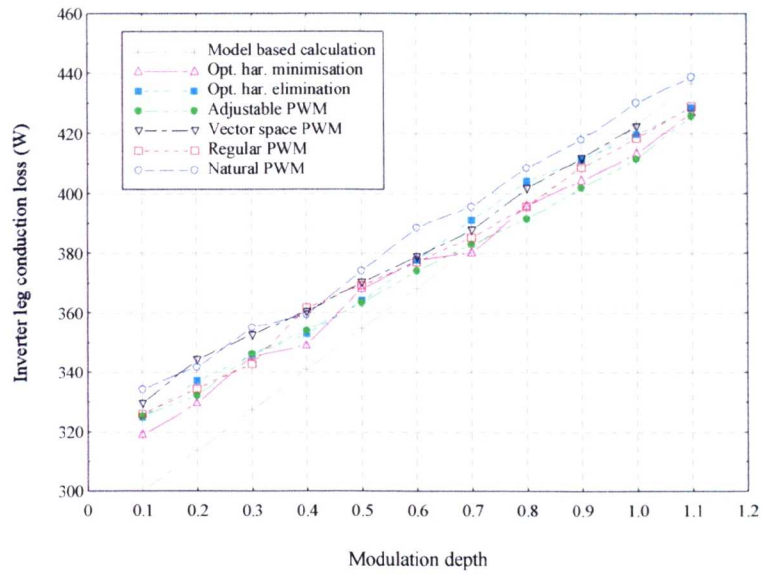

(b)

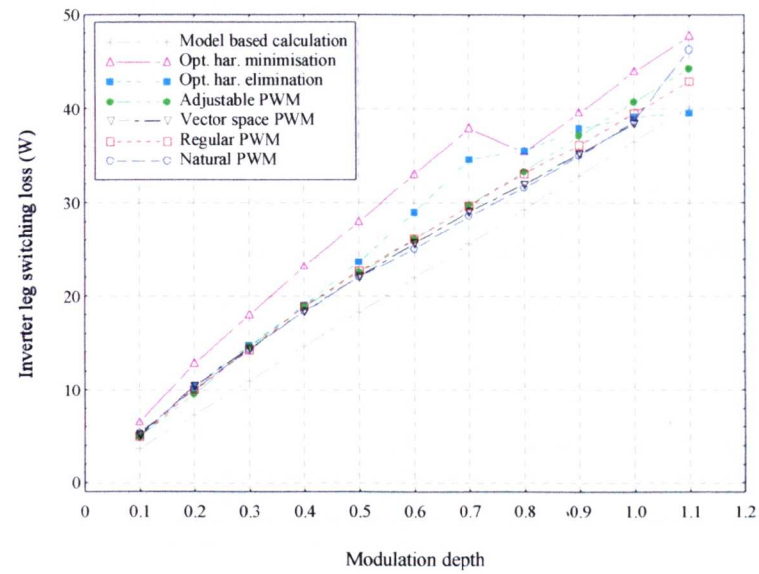

(c)

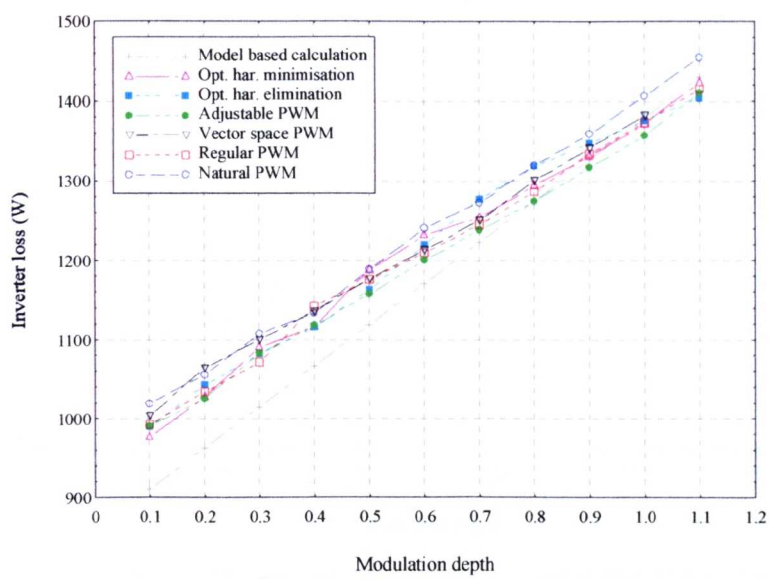

Fig 4.14 Estimated inverter power losses with different PWM strategies. 26 kW induction machine, operating at the rated torque with the speed varying from 10% to the rated speed. Inverter frequency ratio is 9. (a) conduction loss, (b) switching loss, and (c) total loss.

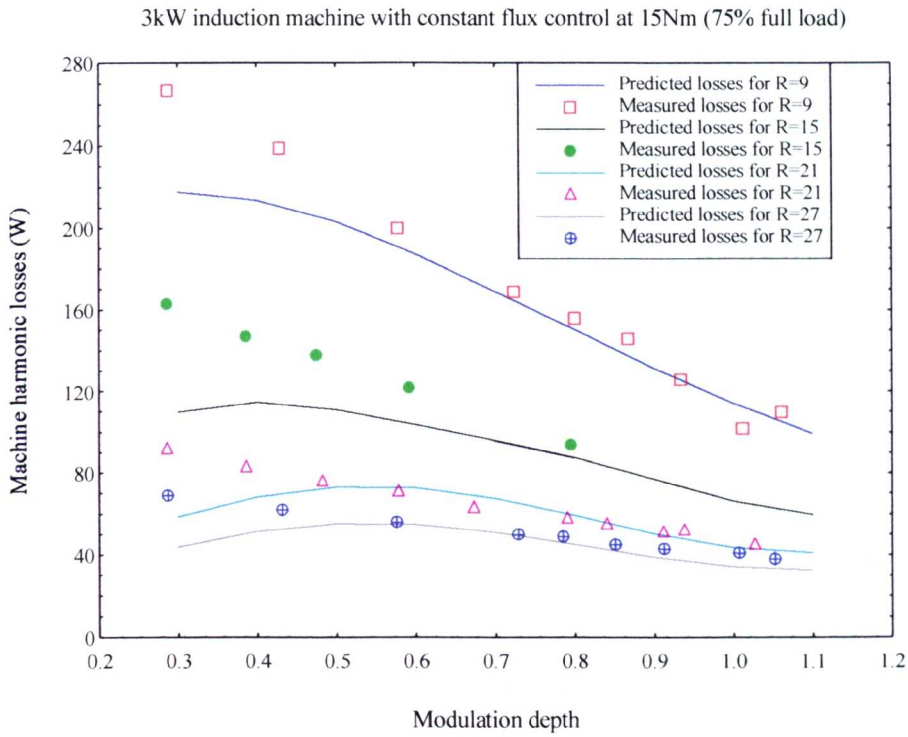

Fig. 4.15. Predicted and measured harmonic losses of a 3kW induction machine driven by vector space PWM with variable frequency ratios. The machine was operated at the rated flux and 15Nm (75% of full load).

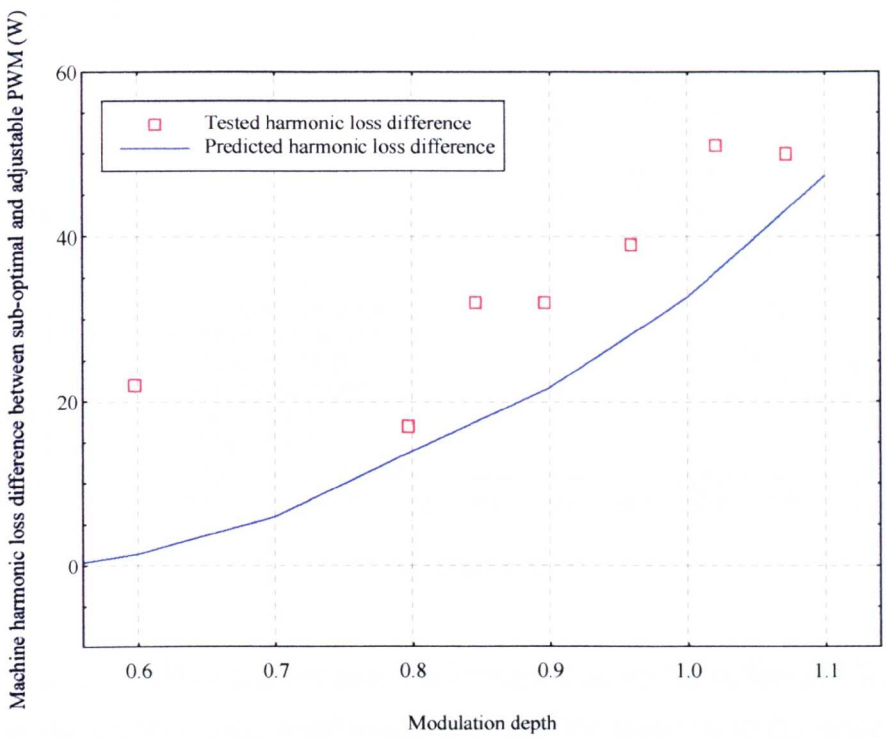

Fig 4.16 Predicted and measured harmonic loss difference for the 3kW experimental induction machine drive, when controlled with sub-optimal PWM and adjustable PWM. The machine is operating at 75% full load and the PWM frequency ratio is 9.

(a)

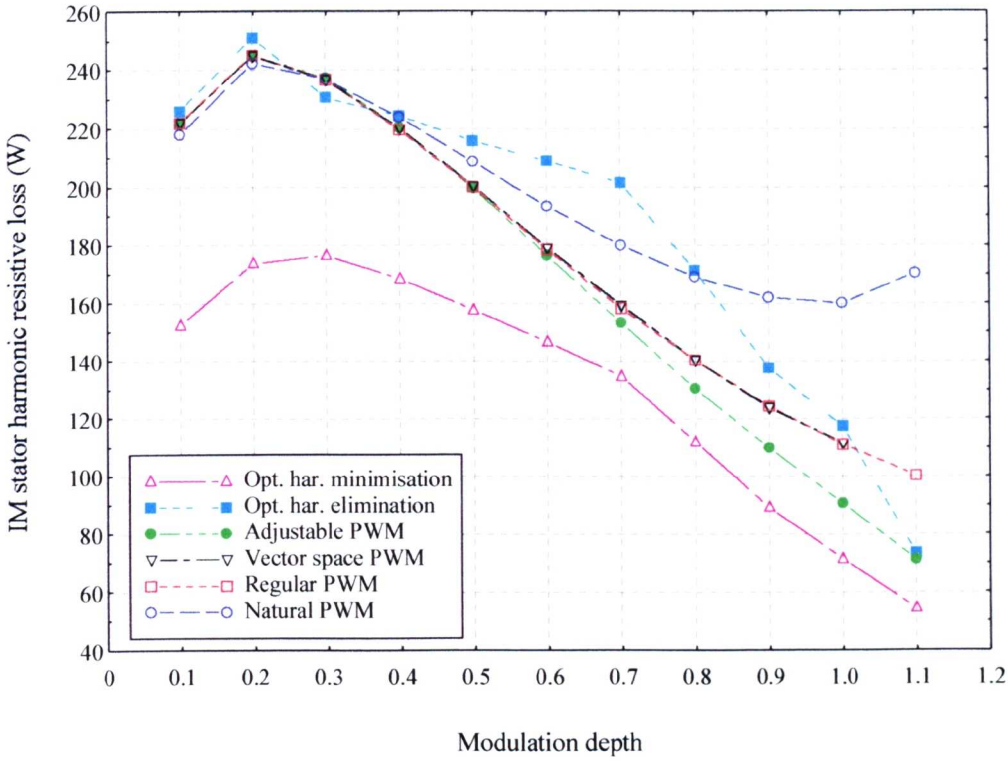

(b)

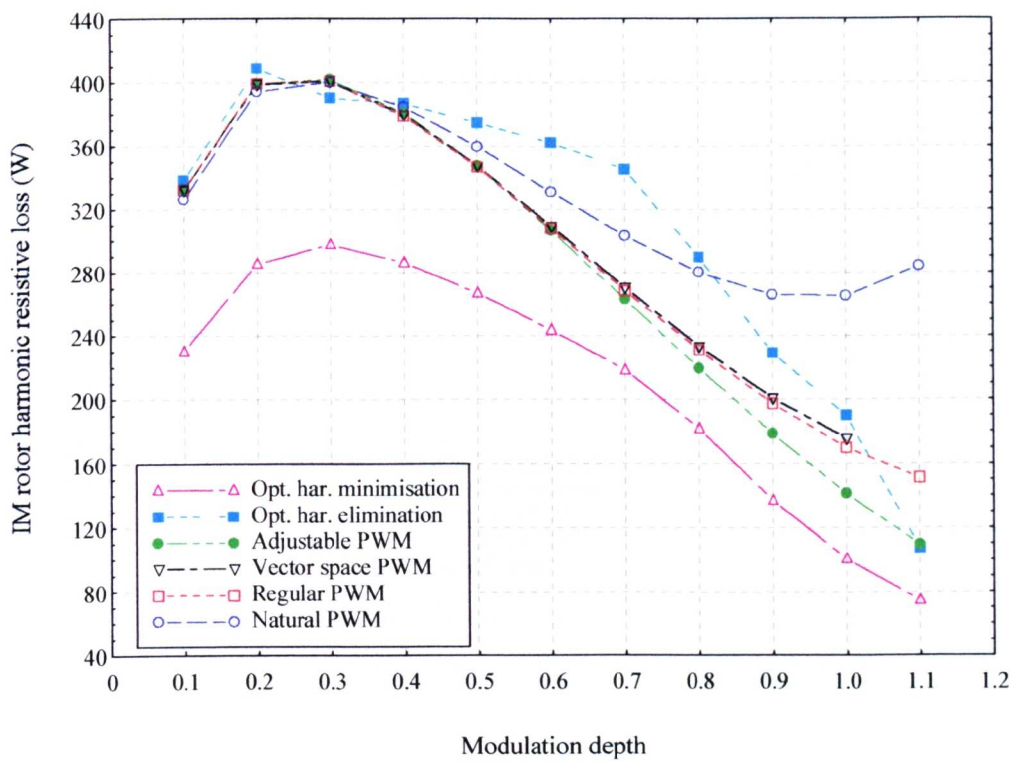

Fig 4.17 Calculated 26 kW induction machine harmonic losses for different PWM strategies. The machine is operating at the rated torque and variable speed up to the rated. The PWM frequency ratio is 9. (a) Machine stator harmonic copper loss against modulation depth (machine supply voltage). (b) Machine rotor harmonic resistive loss against modulation depth.

(c)

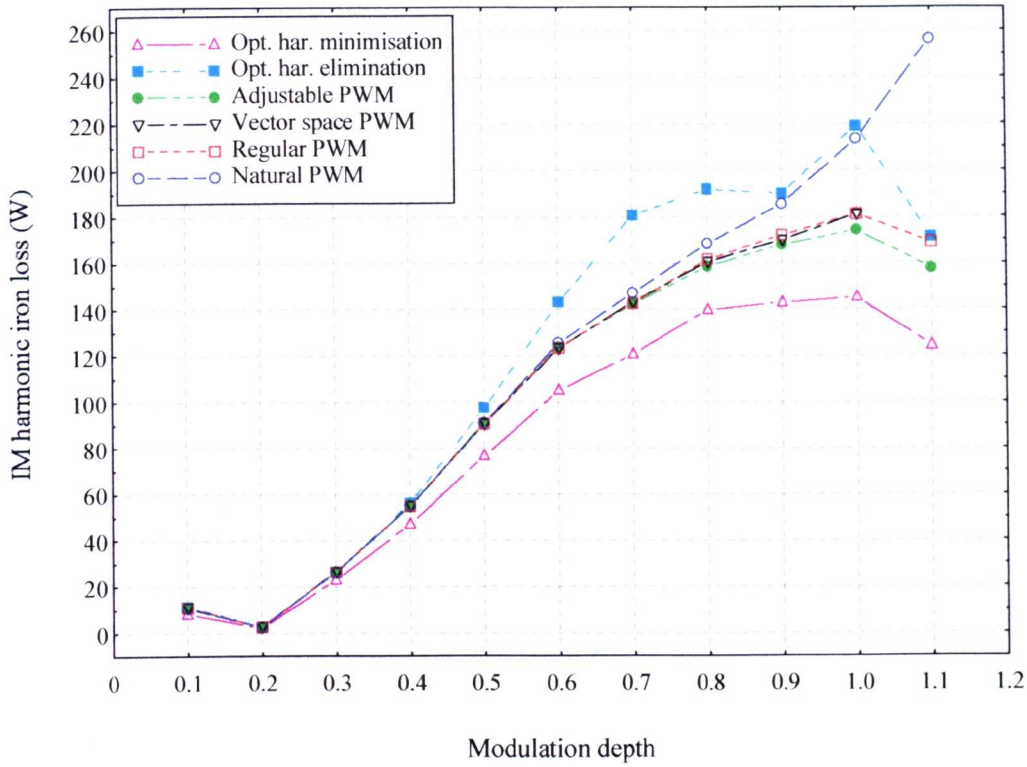

(d)

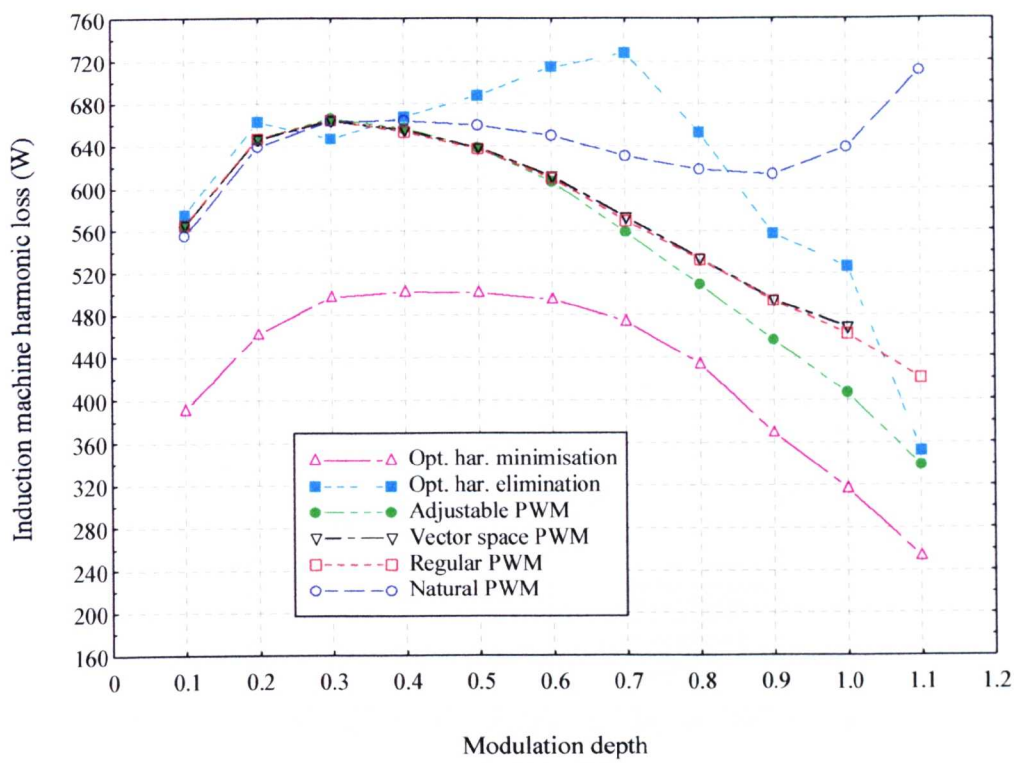

Fig 4.17 Calculated 26 kW induction machine harmonic losses for different PWM strategies. The machine is operating at the rated torque and variable speed up to the rated. The PWM frequency ratio is 9. (c) Machine harmonic iron loss against modulation depth. (d) Machine total harmonic loss against modulation depth.

(a)

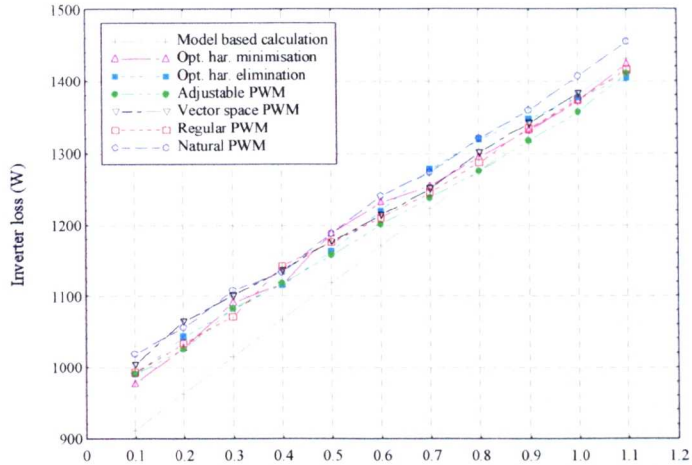

(b)

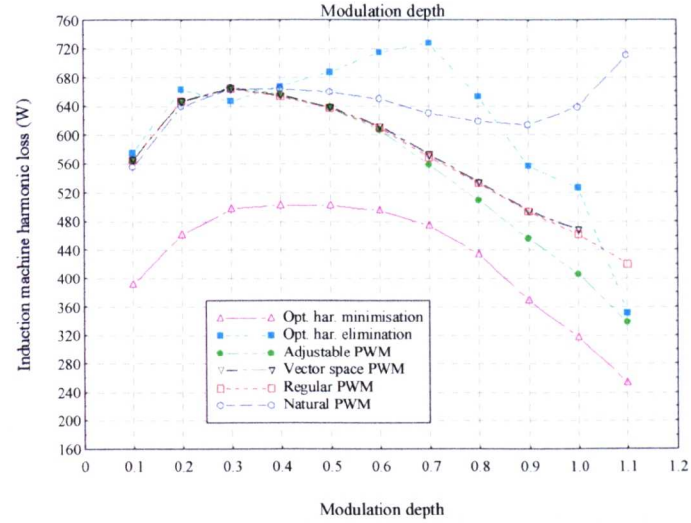

(c)

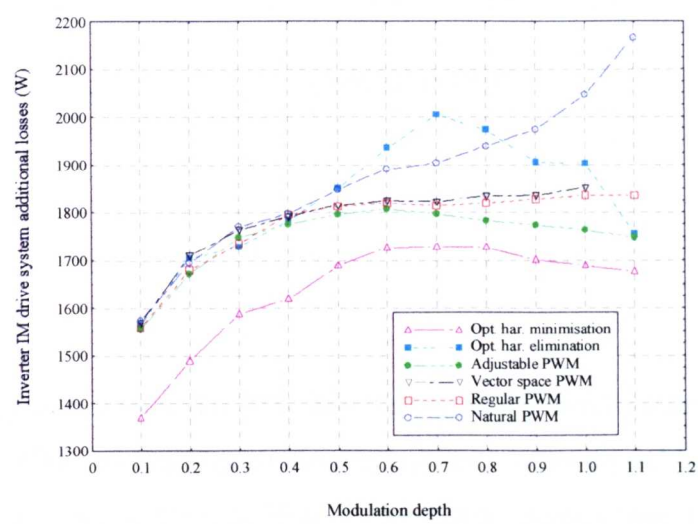

Fig 4.18 Calculated 26 kW drive system additional losses for different PWM strategies. The machine is operating at the rated torque and variable speed. The PWM frequency ratio is 9. (a) Inverter loss. (b) Machine harmonic loss. (c) Drive system additional loss.

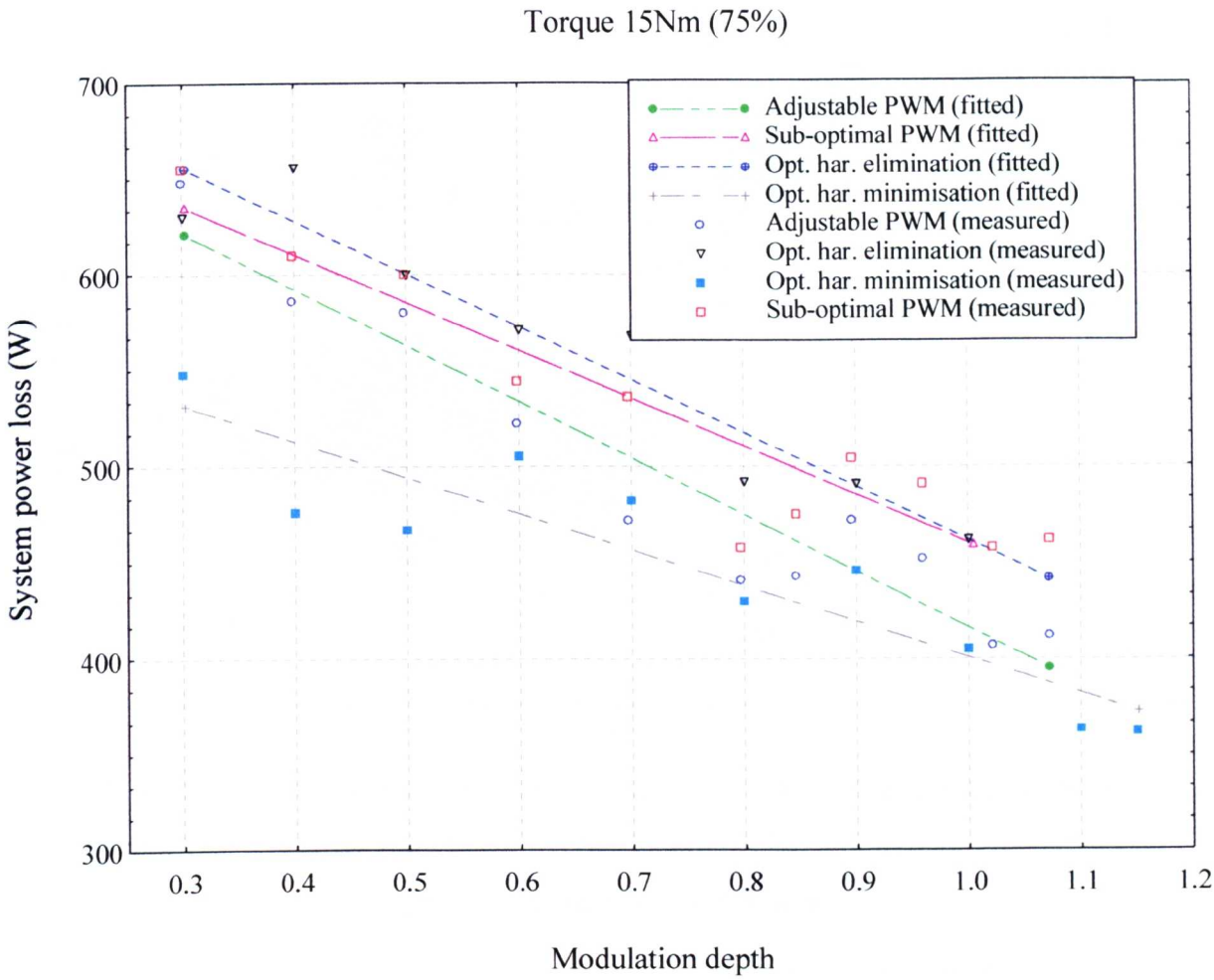

Fig 4.19 Measured system losses in a 3kW inverter induction machine drive, with sub optimal PWM, adjustable PWM , optimal harmonic minimisation and optimal harmonic elimination methods. The machine is operating at 75% full load at frequency over 10 Hz to 46 Hz. The PWM frequency ratio is 9.

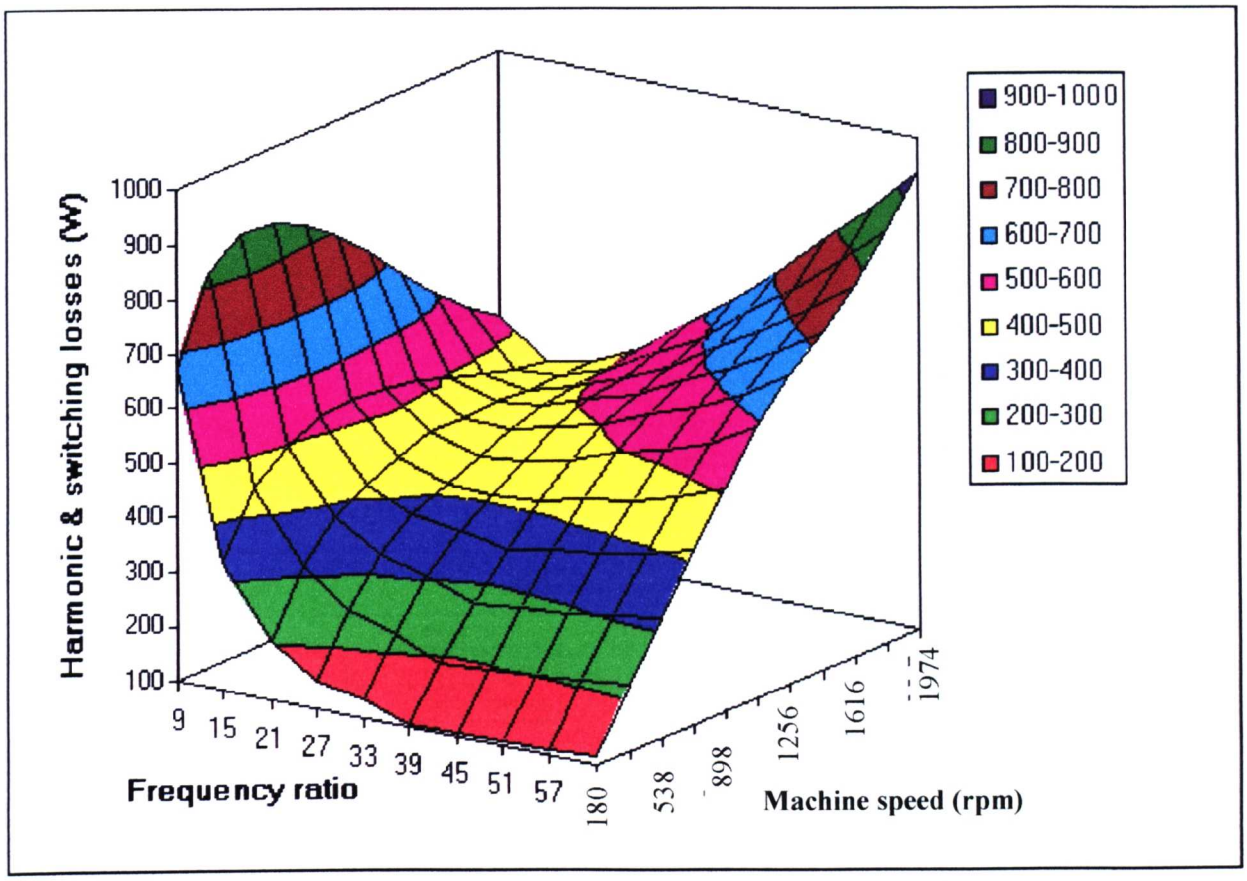

Fig 4.20 Variation of system harmonic loss and inverter loss as a function of supply frequency and frequency ratio in an inverter-fed 26kW induction motor traction drive, operating at rated flux and torque.

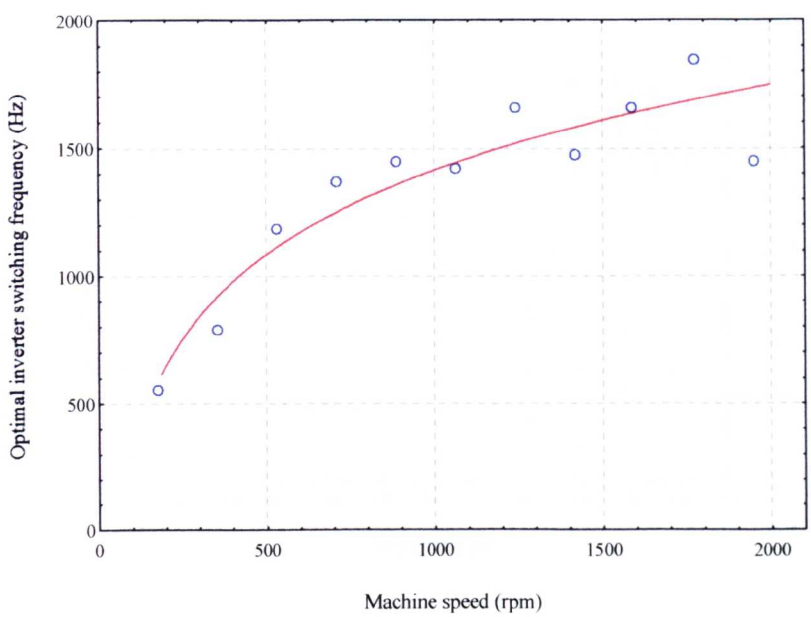

Fig. 4.21. Optimal switching frequency for the 26kw induction machine drive at the rated load and rated flux.

(a)

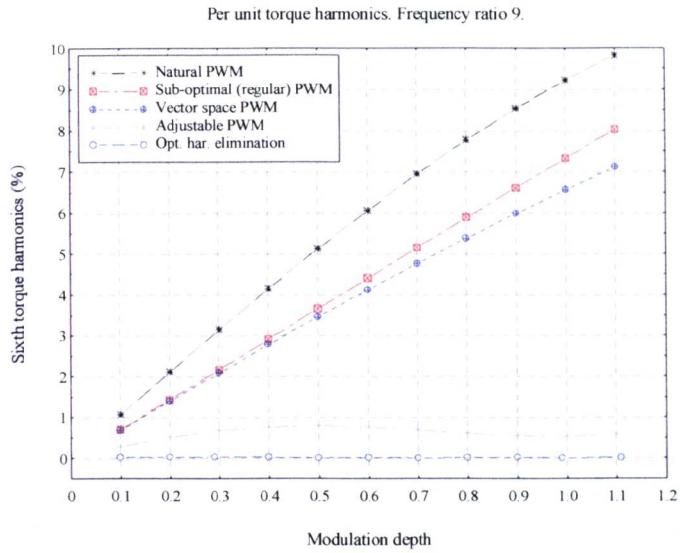

(b)

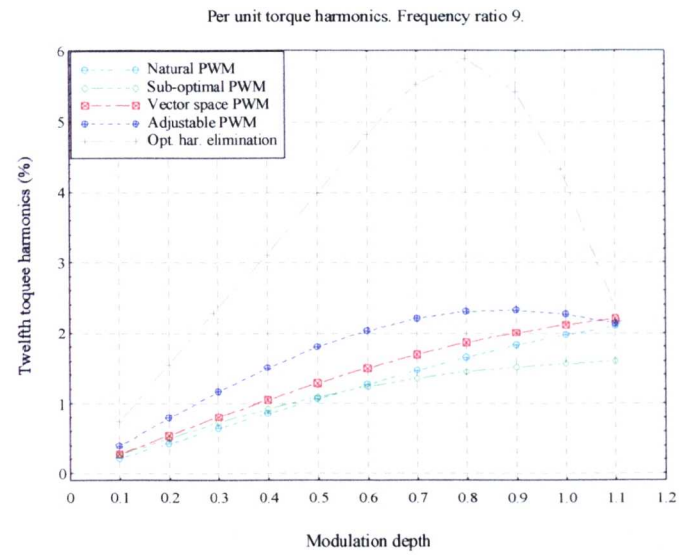

(c)

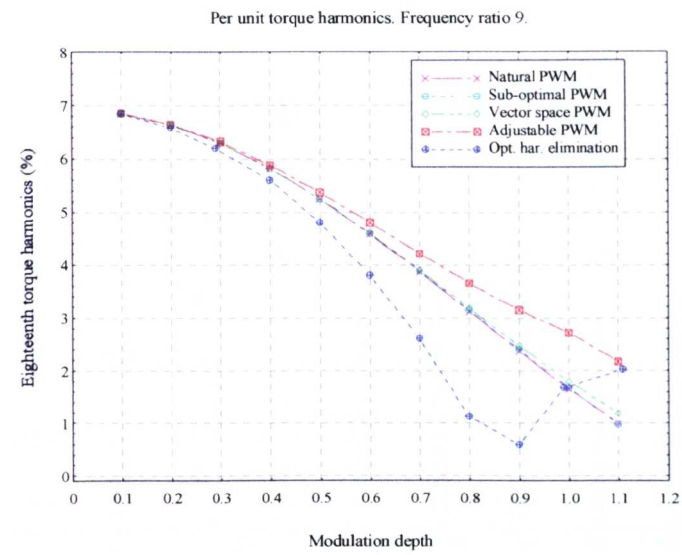

Fig 4.22 Calculated torque ripple factor for different PWM strategies. The frequency ratio is 9. (a) 6th harmonic torque ripple, (b) 12th harmonic torque ripple, and (c) 18th harmonic torque ripple.

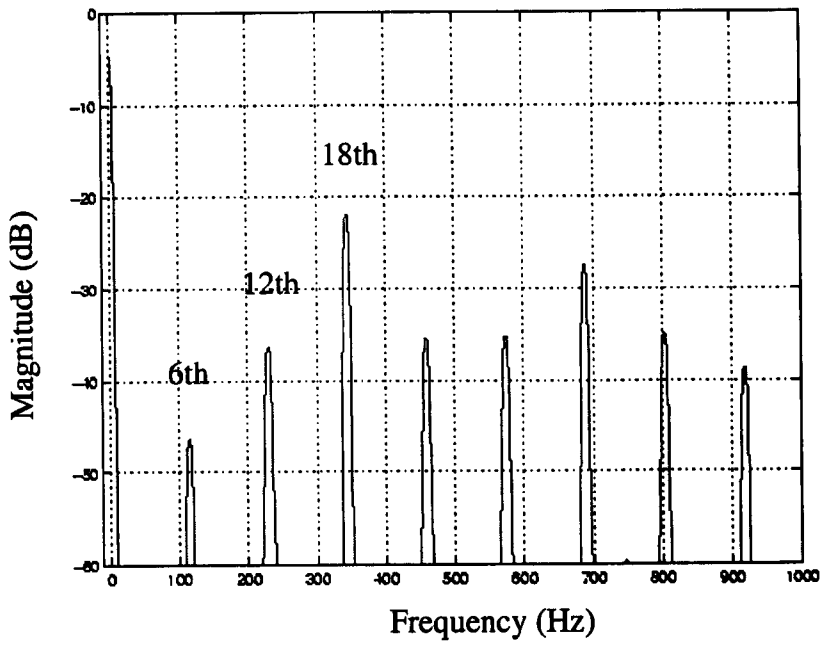

Fig. 4.23. Inverter d.c. link current spectrum for sub-optimal PWM.

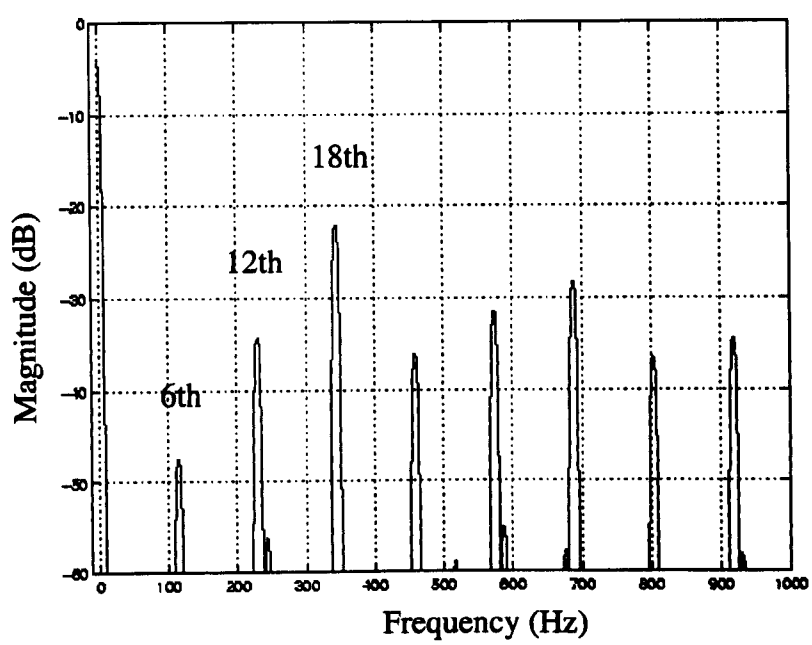

Fig. 4.24. Inverter d.c. link current spectrum for adjustable sampling PWM.

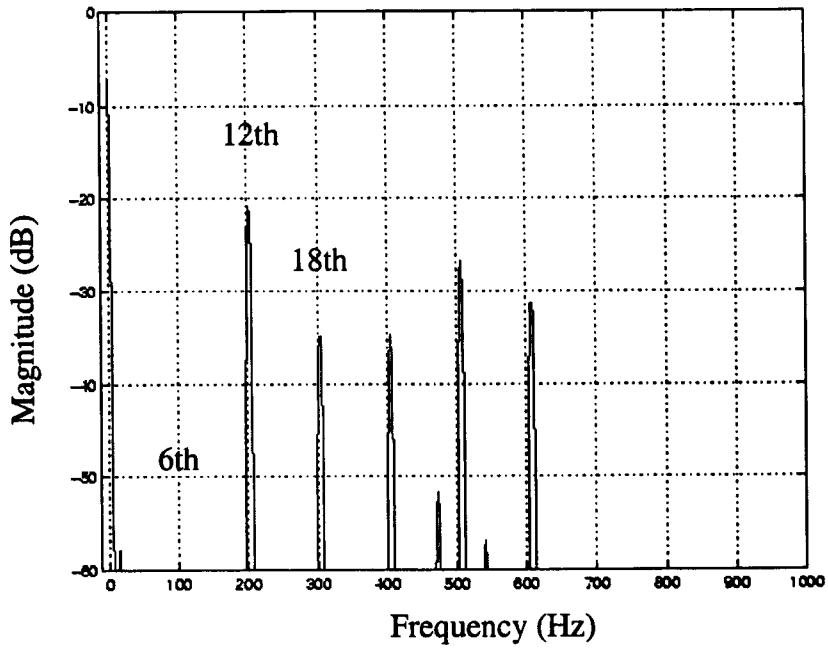

Fig. 4.25 Inverter d.c. link current spectrum for optimal harmonic elimination PWM.

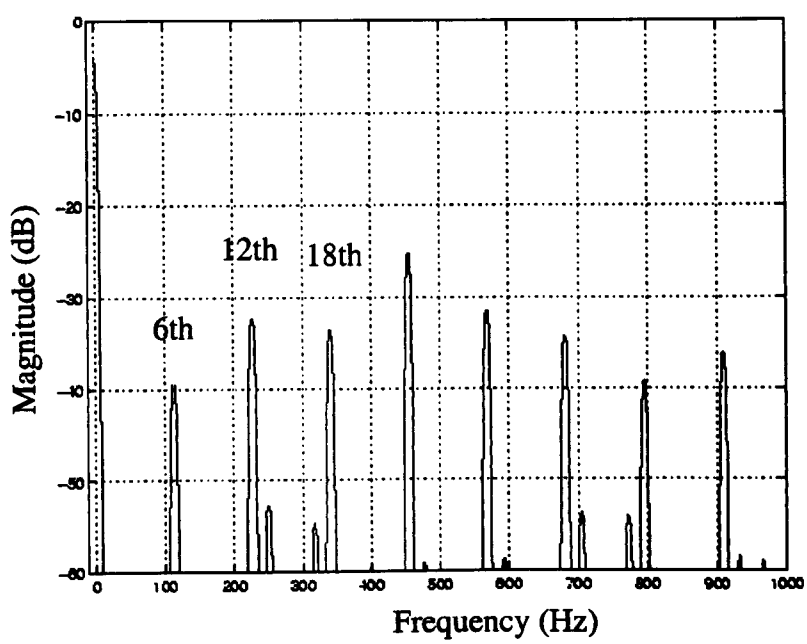

Fig. 4.26 Inverter d.c. link current spectrum for optimal harmonic minimisation PWM.

5. Novel Implementation of a Vector Space Gear Changing Modulator with Good Steady State and Transient Performances

5.1 Introduction

It has been shown previously that apart from natural PWM, the relationship between the PWM output fundamental amplitude and the modulation depth can be non-linear at low frequency ratios, and the modulation process introduces a phase delay in the PWM output fundamental. Further, the extent of the non-linearity and phase delay will vary with frequency ratio. In this chapter, a control method will be proposed which enables a smooth transition during changes in frequency ratios, whilst tuning the PWM process to maintain the lowest possible harmonic distortion. The method is based on vector space PWM, as it has been singled out from other PWM methods as being the easiest to implement whilst having a good performance. An advanced digital implementation strategy will also be proposed for vector space PWM, which can more easily accomodate on-line variations of the modulation parameters.

5.2 Implications of frequency ratio changes on the modulator performance

Although increasing the ratio of the PWM switching frequency to the fundamental frequency can reduce the level of current harmonics in the machine supply, and thereby reduce the machine harmonic losses, ultimately the ratio is limited by the maximum switching frequency capability of the power semiconductor devices and a consideration of the overall system efficiency. An established solution for variable-speed operation is to use a scheme in which the frequency ratio is continuously changed among a group of triplen odd integers, a higher ratio being used at low speed with the ratio being decreased towards unity as the speed and the power increase. This is usually implemented in terms of a frequency ratio gear changing scheme in a variable speed drive (Fig 5.1). However, in implementing the ratio changing scheme care must be taken to ensure that during ratio transitions the amplitude and phase angle of the fundamental voltage remains unchanged so as to prevent sudden changes in current or machine torque.

Each of the PWM strategies discussed in Chapter 3 can be considered as being generated by a common sinusoidal modulating signal, with a fundamental component defined as,

$$m(t)=M \sin (\omega t + \delta) \tag{5.1}$$

The phase angle, δ, gives a reference for the position of the modulating wave with respect to the carrier wave, as shown in Fig. 3.4, or similarly defines its initial position in the space vector frame of reference, as shown in Fig. 3.12.

The fundamental component of the PWM output voltage can be written as,

$$v_1(t) = V_1 \sin (\omega t + \delta - \theta) \tag{5.2}$$

where the amplitude V_1 and phase shift θ can be found using the double Fourier series analysis, as given in Chapter 3. In the case of asymmetric regular sampling PWM, the amplitude of the fundamental output is mainly determined by,

$$V_1 = \frac{4 J_1 (\frac{M\pi}{2R})}{\frac{\pi}{R}} \tag{5.3}$$

and the phase shift is expressed as,

$$\theta = \frac{\pi}{2R} \tag{5.4}$$

It is observed that the phase shift, θ, between the output fundamental voltage and the modulating signal, varies with the frequency ratio. Also the output voltage amplitude is potentially a non-linear function of the modulation depth, M.

If, for each frequency ratio, the phase angle, δ, of the modulating wave was defined as being equal to θ, i.e. $\frac{\pi}{2R}$, the phase shift of the fundamental is independent of frequency ratio R. However, this value of δ will not give minimum possible harmonic distortion. For example,

assuming an odd integer frequency ratio, the 5th harmonic component in the output is principally made up of the following terms, Eqn. (3.18), with other terms having much lower amplitudes,

$$J_5\left(\frac{5M\pi}{2R}\right)\sin\left(5\omega t+5\delta-\frac{5\pi}{2R}\right)+J_{5-R}\left(\frac{5M\pi}{2R}\right)\sin\left(5\omega t+5\delta-\frac{5\pi}{2R}+\pi-R\delta\right) \tag{5.5}$$

At a value of δ equal to zero the two terms destructively interfere, and therefore give minimum harmonic distortion. If the phase of the modulating wave was set as $\delta=\frac{\pi}{R}$, then the two terms would constructively interfere and lead to maximum harmonic distortion. The condition of no phase variation in the fundamental during frequency ratio transitions, i.e. $\delta=\frac{\pi}{2R}$ lies between these two extremes. This effect is illustrated in Fig 5.2, which shows the variation in THD with modulating wave phase angle in the case of sub-optimal regular sampling PWM with a frequency ratio of 3.

Other modulation processes behave in a similar manner, i.e. the value of the modulating wave phase angle which results in smooth ratio transitions differs from that which gives minimum harmonic distortion. In the case of vector space PWM, when the frequency ratio is equal to or greater than 9, a modulating wave phase angle of zero will result in minimum harmonic distortion in the output, with the fundamental being directly proportional to the depth of modulation; whilst at a ratio of 3, the minimum harmonic distortion is achieved at an angle of 30^o, where the voltage control is highly non-linear. If these angles are not adjusted prior to a frequency ratio transition, sudden variations in the output voltage will occur, particularly when the ratio is relatively low (Fig 5.3).

5.3 Modulator performance control algorithm

By performance control, it is meant that a PWM process is monitored so that it has a lowest possible harmonic distortion in its output during steady state, and its fundamental output keeps invariant during the frequency ratio transition.

During the frequency ratio transition periods, the harmonic distortion and the system efficiency are not of great significance if the change occurs over a relatively short time, and can be compromised to achieve a smooth transition. Thus, the PWM strategy which gives a minimum harmonic distortion and that which yields a smooth transition over ratio changes can effectively be decoupled due to the different time spans, and a two-degree-of-freedom controller can be designed based on the control variables of modulation depth M and modulating wave phase angle δ. The control is accomplished in two steps,

(i) the transient control during frequency ratio transitions, when the sudden change of modulating wave phase angle and the necessary voltage amplitude compensation are involved at the instant of ratio change, and

(ii) the transition from transient state to steady-state, in which the phase angle for the transient control is gradually adjusted to the value required for minimum harmonic distortion.

In the remaining subsections a transient control algorithm for vector space PWM modulation will be described.

5.3.1 Vector space steady-state performance control algorithm

$$\begin{aligned} &When\ R \geq 9 \begin{cases} \delta = 0 \\ M = V_1 \end{cases} \\ &When\ R = 3 \begin{cases} \delta = 30^o \\ M = 0.8928\ (V_1 + 0.0226\ ) \end{cases} \end{aligned} \tag{5.6}$$

where the modulation depth for the case of R=3 is derived to compensate the non-linearity in the PWM process.

This algorithm ensures that the output voltage is a linear function of the modulation depth and the modulation process operates with minimum harmonic distortion.

5.3.2 Vector space ratio transition control algorithm

$$\begin{cases} M=V_1\ ,\ or\ M=0.8928\ (V_1+0.0226)\ when\ R=3 \\ \delta_2=\delta_2-\dfrac{\pi\ (R_2-R_1\ )}{2R_1R_2} \end{cases} \tag{5.7}$$

where R_1 and R_2 are, respectively, the frequency ratios before and after the ratio transition, and δ_1 and δ_2 are the corresponding modulating wave phase angles required for steady-state operation.

When the ratios are higher than 3, a new modulating wave phase angle is fixed over the ratio transition to ensure there is no change in the phase of the fundamental. In the case of a frequency ratio of 3, additional voltage amplitude compensation is employed to ensure no voltage amplitude change. Due to the dependency of the voltage amplitude on the phase angle, the transition from the transient state to the steady-state should be avoided at the frequency ratio of 3, rather the transition is accomplished at frequency ratio of 9. This can be explained by the following examples:

(a) Transition from 3 to 9

At the instant of ratio transition, set $M=V_1$ and $\delta=10^o$ so that the fundamental voltage remains unchanged; then, move δ gradually from 10^o to 0^o for the transition from transient state to steady-state at the frequency ratio of 9.

(b) Transition from 9 to 3

Before ratio transition, move δ gradually from 0^o to10^o at the frequency ratio of 9; then, set $\delta = 30^0$ and $M = 0.8928\ (V_1 + 0.0226)$ at the ratio transition to keep the fundamental voltage unchanged.

5.3.3 Special case with transition between PWM and quasi-square wave control

The main features of quasi-square wave operation are that the fundamental voltage amplitude and the waveform shape are fixed. Thus, a transition between the PWM control mode and the quasi-square wave control mode can be considered to be related not to phase angle variation as above, but the change of voltage amplitude. Usually, the transition from PWM mode to quasi-square wave mode is achieved by forcing the PWM into overmodulation and introducing pulse drop. Alternatively, the voltage control non-linearity at ratio 3 can be employed by adjusting the modulating wave phase angle so that the switching instant moves to a position where, for a given minimum pulse width, the fundamental is a maximum.

5.4 Experimental validation of controller performance

The above proposed control algorithm has been applied to the 3kW DSP-controlled induction motor drive, and the observed machine currents were used to verify the controller performance.

At high values of frequency ratio, the variation of voltage during the transition due to the voltage amplitude control and the phase shift was very small, and the current overshoot was observed to be negligible. Fig 5.4 shows the current waveforms for a ratio transition of 21 to 15, with and without the ratio transient control being applied, and in these cases the transition is unnoticeable.

At low frequency ratios such as 9 and 3, significant current overshoot and torque variation may occur during the transitions between ratios. This is shown by the measured current waveform in Fig 5.5(a). However, when the phase angle was controlled in the manner described above, the current overshoot was greatly reduced, Fig 5.5(b), and a further improvement can be achieved by the addition of voltage amplitude control, i.e. full ratio transient control, as shown in Fig 5.5(c).

The effectiveness of using the voltage non-linear control characteristics for the transition between the PWM mode, with a ratio of 3, and the quasi-square wave output control is shown in Fig 5.6.

The test results also confirm that phase changes in the harmonic components of the output voltage during the transitions have negligible influence on the transient performance of a modulation process, and that the control design methodology, which considers the fundamental component only is adequate. Moreover, due to the fast switching of modern semiconductors, the inverter dead time has a negligible influence on the voltage variation.

5.5 An advanced digital implementation strategy for vector space PWM

A strategy for implementing vector space PWM has been developed, in which both the system control variables of supply voltage, supply frequency and switching frequency, and the performance control variable of modulating wave phase angle, can be adjusted on-line. On consideration of the possible wide variation of the frequency ratio, the usual way of using a look-up table is not realistic. In the following, an alternative digital implementation strategy is described.

5.5.1 Pulse width calculations

The pulse width timings for the vector space algorithm are determined using,

$$\begin{cases} T_1 = \dfrac{T_s}{2} M \dfrac{\sqrt{3}}{2} \sin(\pi/3 - \alpha) \\ T_2 = \dfrac{T_s}{2} M \dfrac{\sqrt{3}}{2} \sin\alpha \qquad , \alpha = 0 \rightarrow \dfrac{\pi}{3} \\ T_0 = z\,(\dfrac{T_s}{2} - t_x - t_y) \end{cases} \tag{5.8}$$

Substituting,

$$h = \alpha - \pi/6 \tag{5.9}$$

and the varaible h varies between $-\pi/6 \rightarrow \pi/6$, then Eqn. (5.8) becomes,

$$\begin{cases} T_1 = \dfrac{T_s}{2} \dfrac{\sqrt{3}}{2} M \sin(\pi/6 - h) \\ T_2 = \dfrac{T_s}{2} \dfrac{\sqrt{3}}{2} M \sin(\pi/6 + h) \\ T_0 = z\,(\dfrac{T_s}{2} - t_x - t_y) \end{cases} \tag{5.10}$$

The sine functions in Eqn. (5.10) are expanded using a Taylor series with the fourth order and higher components in the series neglected, i.e.,

$$\left| \frac{h^4}{4!} \sin(\pi/6) \right| < 0.0016 < \sin(0.1^o) \tag{5.11}$$

then

$$\sin(\pi/6 + h) \approx \frac{1}{2} + \frac{\sqrt{3}}{2} h - \frac{1}{4} h^2 - \frac{\sqrt{3}}{12} h^3 \tag{5.12}$$

$$\sin(\pi/6 - h) \approx \frac{1}{2} - \frac{\sqrt{3}}{2} h - \frac{1}{4} h^2 + \frac{\sqrt{3}}{12} h^3 \tag{5.13}$$

thus,

$$\begin{cases} T_1 = \dfrac{T_s}{2} M\,(\dfrac{\sqrt{3}}{4} - \dfrac{3}{4} h - \dfrac{\sqrt{3}}{8} h^2 + \dfrac{1}{8} h^3) \\ T_2 = \dfrac{T_s}{2} M\,(\dfrac{\sqrt{3}}{4} + \dfrac{3}{4} h - \dfrac{\sqrt{3}}{8} h^2 - \dfrac{1}{8} h^3) \\ T_0 = z\,(\dfrac{T_s}{2} - t_x - t_y) \end{cases} \tag{5.14}$$

The above equations can be implemented relatively easily within a DSP.

5.5.2 On-line adjustment of voltage, frequency, frequency ratio and phase angle

The inverter output is controlled by the modulating wave amplitude and frequency. For the system efficiency, the inverter switching frequency, or switching to fundamental frequency ratio, is also varied, which in practice is accomplished by the adjustment of the angle step. Some examples are given in Table 5.1.

Table. 5.1 Adjustment of frequency ratio by angle step.

Ratio R	3	9	15	21	27	33	39	45	51	57	63
Step $\Delta\theta$	60^o	20	12	8.57	6.67	5.45	4.62	4	3.53	3.16	2.86

On consideration of the system steady state and transient performance (minimum harmonic distortion in steady state and least current overshoot during ratio transition), the modulating wave phase angle δ should be adjusted as well. The vector angle is then,

$$\alpha = \delta + \Delta\theta \tag{5.15}$$

In the previous PWM implementation, the process is controlled by $T_S/2$ (half of switching cycle). However, in a variable speed drive, the fundamental cycle (or frequency) is specified, and the PWM control parameter $T_S/2$ is varied with frequency ratio R. If it is supposed that the fundamental cycle is represented by T_O (the real fundamental time is $6T_O$), the cycle for PWM control will be,

$$\frac{T_S}{2} = \frac{T_O}{2k+1} \tag{5.16}$$

where $k = 0, 1, 2, \cdots$, respectively for $R = 3, 9, 15, \cdots$

The flowchart for the implementation of this strategy is shown in Fig. 5.7.

This vector space PWM modulator has been successfully used for the constant torque control and the constant power control tests in Chapter 6 for the investigation of machine loss minimisation control strategies.

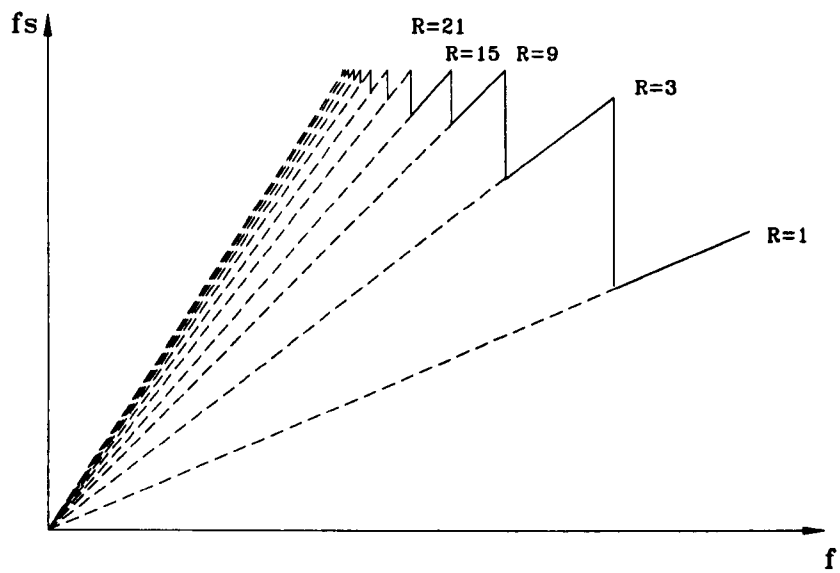

Fig. 5.1. A frequency ratio gear changing scheme.

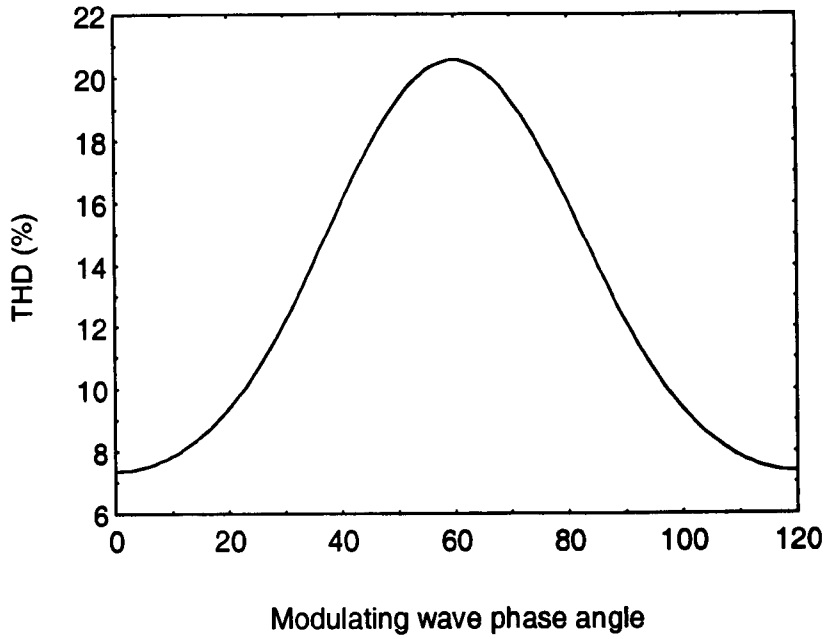

Fig 5.2 Variation of harmonic distortion against phase angle for sub-optimal PWM with frequency ratio of 3.

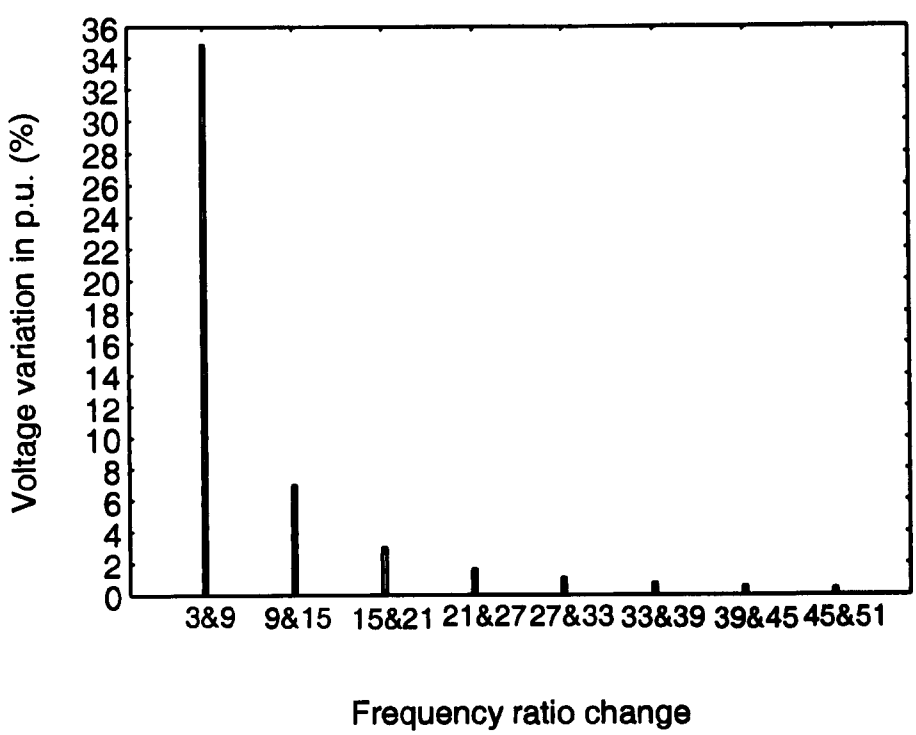

Fig 5.3 Maximum p.u. voltage variations on frequency ratio transitions.

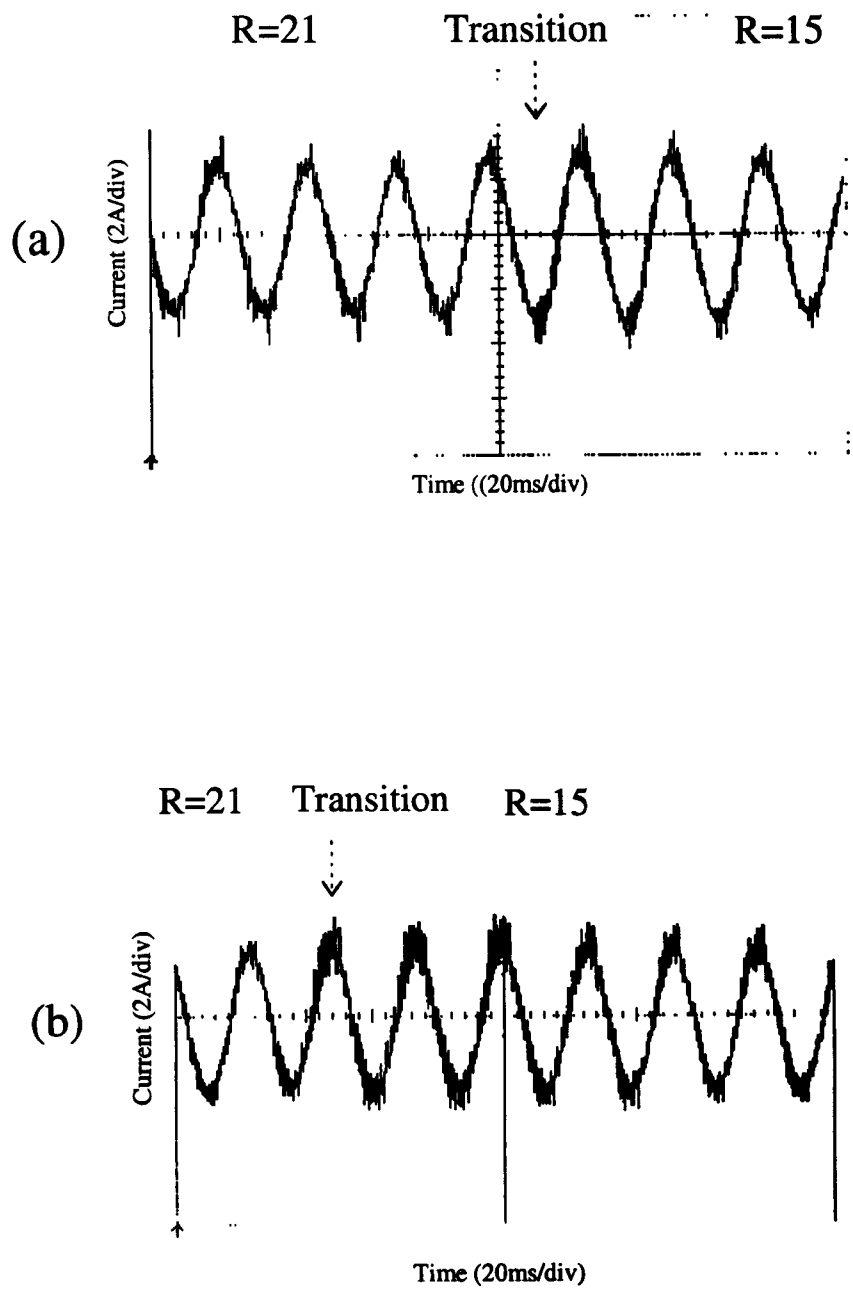

Fig 5.4 Machine current waveforms for the ratio transition from 21 to 15. (a) Without transient control, (b) with transient control.

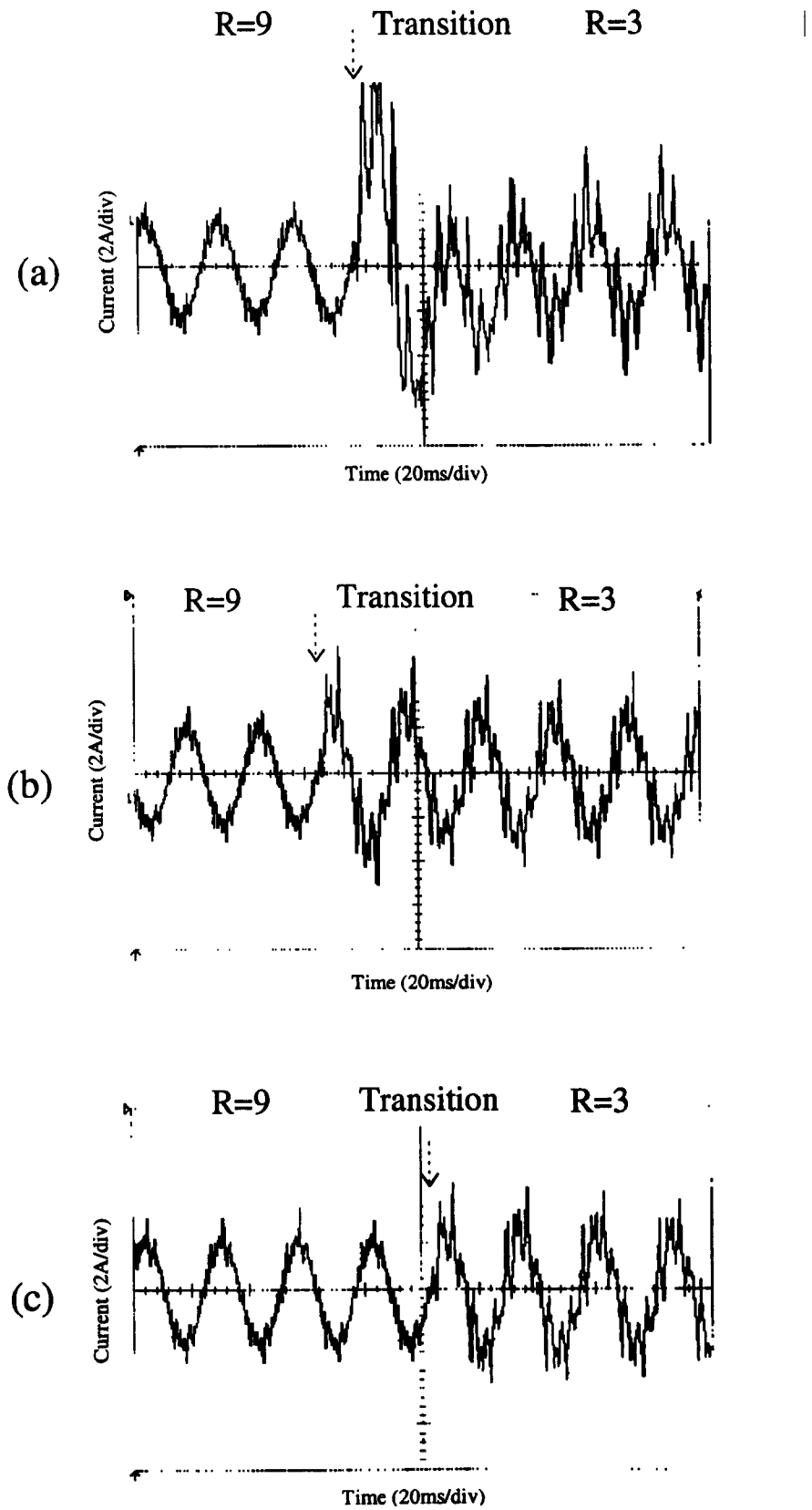

Fig 5.5 Machine current waveforms for the ratio transition from 9 to 3. (a) Without transient control, (b) with phase angle control only, (c) with full phase angle and voltage amplitude control.

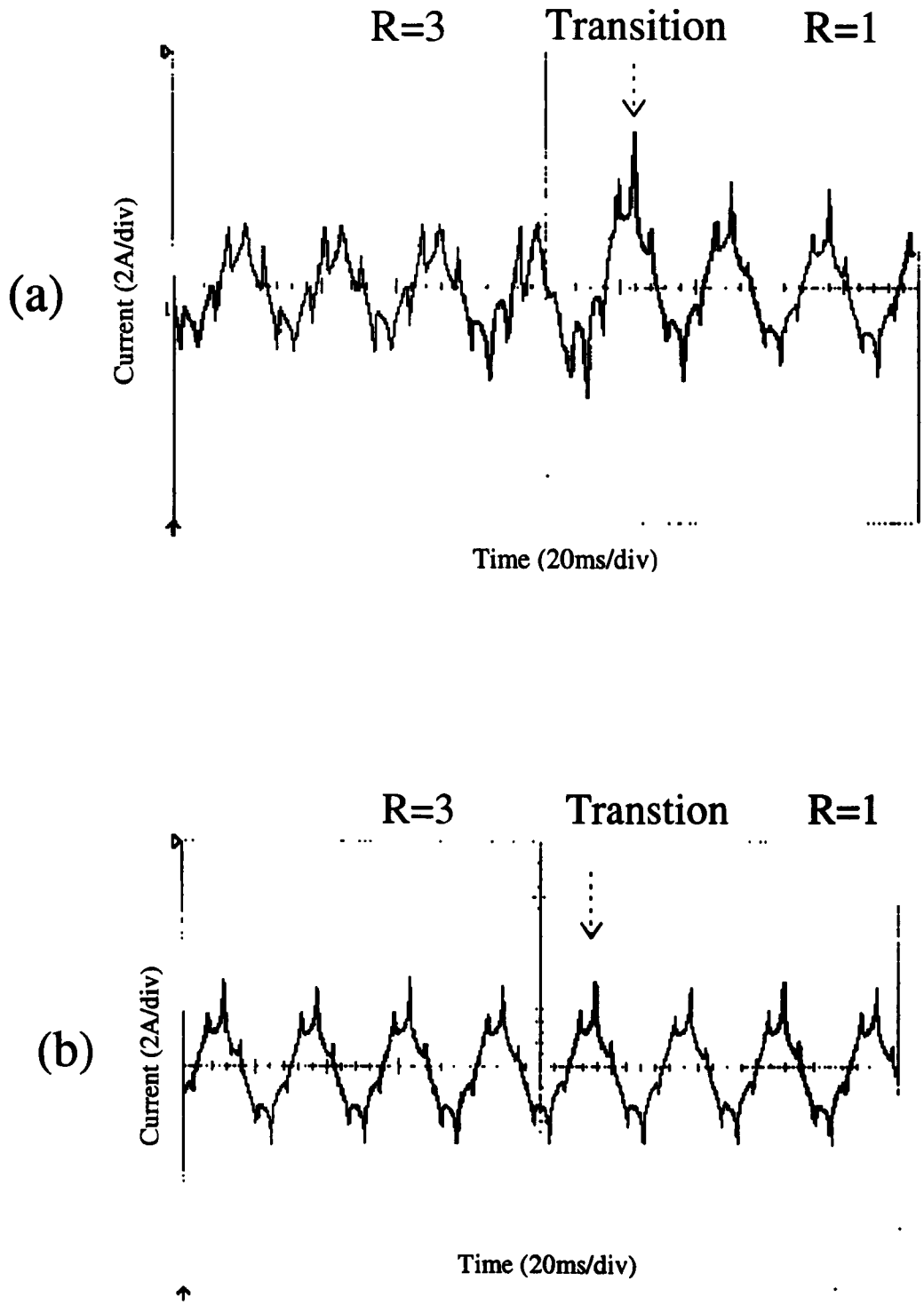

Fig 5.6 Machine current waveforms for the control mode transition from PWM to quasi-square wave switching. (a) Without transient control, (b) with transient control.

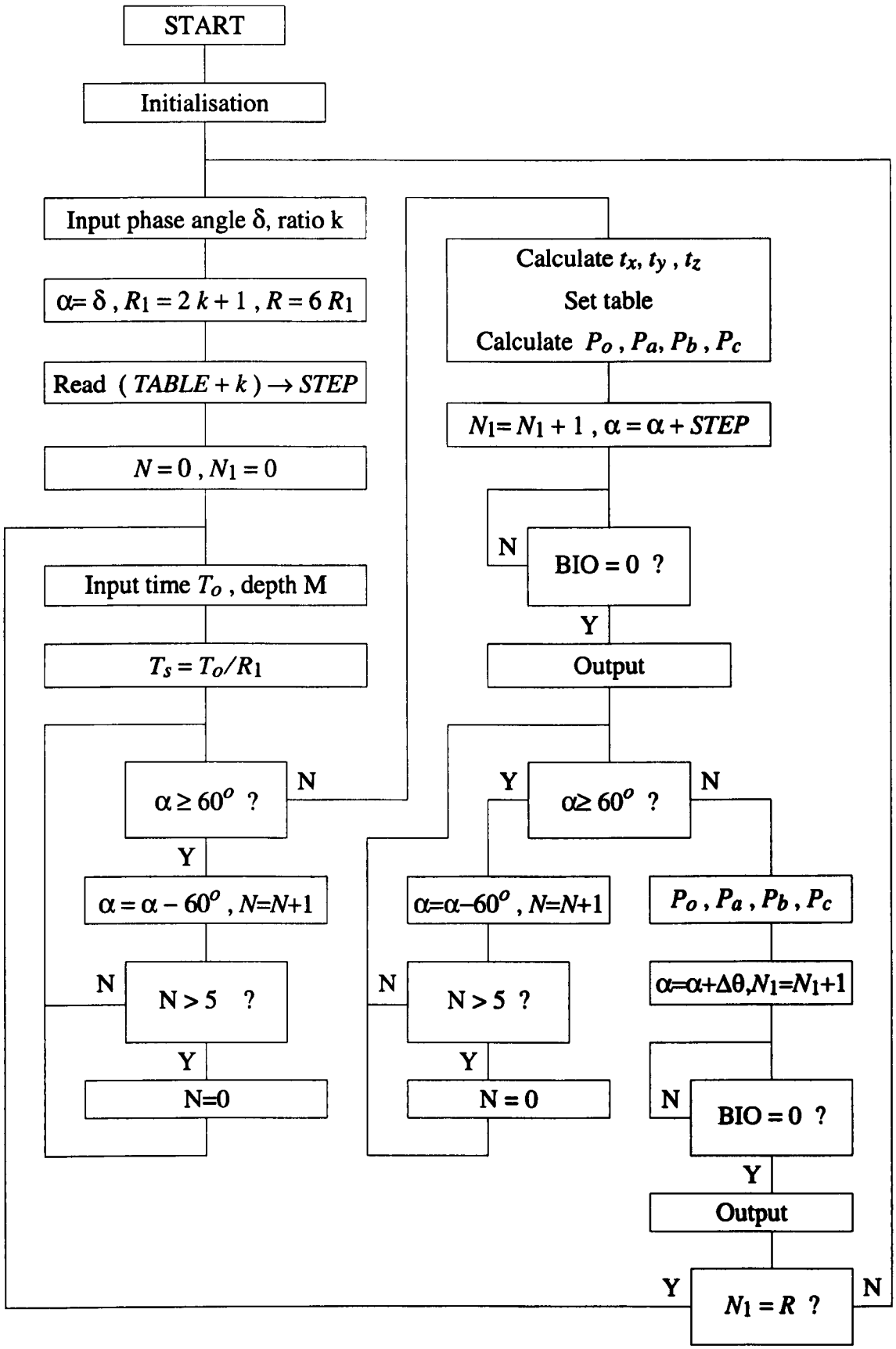

Fig. 5.7 Program flowchart for vector space PWM implementation

6. Maximum Efficiency Control of Induction Machine Traction Drive

6.1 Introduction

The realisable working envelop of an electric vehicle traction motor can be defined by a constant torque region, a constant power region and a high speed region, and the machine may be required to operate anywhere within this envelop. In the case of a traction drive comprising of an induction machine and a variable voltage and variable frequency PWM inverter, the drive system efficiency at a given machine operating point will be determined by the fundamental voltage and frequency of the supply to the induction machine, the PWM modulation strategy used and the switching rate of power semiconductors. In this chapter a minimum loss control strategy will be developed based on these three control parameters, i.e. machine voltage, machine frequency and inverter switching frequency, for a vector space modulated drive.

Initially, the relative influences of these three parameters on the system efficiency were quantified from a series of tests on the 3kW experimental drive.

6.2 Influence of inverter switching frequency on system efficiency

The variation of system additional loss, i.e., the induction machine harmonic loss and the inverter loss, with inverter switching frequency was investigated experimentally on the 3kW prototype drive system. The machine was controlled over a range of speeds under vector space modulation in such a way that its air-gap flux, load torque, and fundamental stator current magnitude remained constant. At each operating point, the inverter input power, the machine input total power, the machine input fundamental power and the machine output power were measured using a high bandwidth power analyser. These measurements are then used to deduce the inverter power loss and the machine harmonic loss.

6.2.1 Constant torque control

The 3kW dynamometer test facility as described in Chapter 2 was adopted to provide a closed loop control of the machine output torque. The torque control system is shown in Fig 6.1, where the torque is measured using the load cell, and the obtained signal is filtered, amplified and used as the torque feedback. The torque control was accomplished by adjustment of the field winding supply of the d.c. dynamometer. Although an external PID torque controller could have been designed for this purpose, it was more convenient to use the external voltage sensing function of the d.c. field power supply and allowed the the torque command to be set using the front panel of the d.c. supply. It was found that this control technique was effective in maintaining the specified machine torque over a wide speed range.

The adopted experiment procedure was as follows,

(i) Set a torque level using the field power supply front panel;
(ii) Set a PWM frequency ratio on the DSP modulator;
(iii) Set minimum required machine supply frequency, and adjust the PWM modulation depth until the machine stator fundamental current reached the prespecified value which would enable the machine to work at the rated air-gap flux. At steady state, the drive system input power, the machine total input power and fundamental input power, and other relevant data were measured;
(iv) Increase the machine supply frequency by a small increment, and adjust the modulation depth so that the same specified machine stator fundamental current was observed.
(v) Repeat step (iv) until the machine supply voltage could not be increased further to give machine the required air-gap flux;
(vi) Change the frequency ratio, and repeat the steps of (iii) - (v);

6.2.2 Experimental results with constant torque control

The test machine torque was maintained at 15Nm (75% of full load) and operated over a wide speed range, and with different inverter switching frequencies. The test results are given in

Appendix F. The effectiveness of the torque and flux control methods are clearly shown by plotting the machine input current figure, Fig 6.2, which is constant over the entire speed range. The measured machine harmonic loss, the inverter loss and the total additional loss with the frequency ratio are shown respectively in Fig 6.3 (a), (b) and (c). The results are also plotted in Fig 6.4(a), (b), (c) and (d), where the machine harmonic losses and inverter losses are compared at different frequency ratios. At relatively low frequency ratios, the machine harmonic loss dominates the total drive system additional losses, whereas at high switching frequencies the inverter loss becomes the major component of the system additional loss, as detailed in the inset of Fig. 6.3. The results indicate however, that there is an optimal frequency ratio at which the machine harmonic loss and the inverter loss become equal, and this represents the point of minimal additional loss in the drive.

6.3 Influence of voltage, frequency and switching frequency on system efficiency

In the following, the influences of the three control variables, viz. machine supply voltage and frequency, and inverter switching frequency, on the system efficiency are investigated experimentally, while the machine is working at a given operating point.

6.3.1 Constant power control

The 3kW test dynamometer was configured such that the induction machine would be loaded at a constant output power and operate at a fixed specified point. The system input power was monitored whilst adjusting machine supply voltage, machine supply frequency, and the inverter switching frequency, so that a minimum input power to the system was achieved.

Since the machine output power was somewhat difficult to be obtained directly, the dynamometer output DC voltage was used instead to control the induction machine output power indirectly. The principle can be explained as follows,

The induction machine output power,

$$P_{out} = T_m \omega_m / \eta_d = U_L^2 / (\eta_d R_L) \quad (6.1)$$

η_d is the dynamometer efficiency to account for the friction and windage loss, and dynamometer copper and iron loss, and can be considered to be constant at a particular working point. U_L is the dynamometer output voltage and R_L is the load resistance. If the resistor's temperature variation is assumed to be negligible during a particular test, a constant voltage across the resistor would give a constant machine output power.

The test system is shown in Fig 6.5 and the experimental test procedure was as follows,

(i) Set a power level using the d.c. machine field power supply front panel;
(ii) Set a frequency ratio on the DSP modulator;
(iii) Set a possible minimum machine supply frequency, and then adjust the PWM modulation depth to obtain the desired load torque. At steady state, the drive system input power and other relevant data were measured;
(iv) Increase the supply frequency by a small increment, and adjust the PWM modulation depth so that the same machine working point was reached.
(v) Repeat step (iv) until the defined machine working points could no longer be met.
(vi) Change the frequency ratio, and repeat the steps of (iii) - (v);

Given an induction machine drive delivering a particular output power, many different combinations of supply voltage and frequency are possible. This is clearly illustrated in Fig. 6.6, where the same machine operating point, and thus a constant output power, is achieved from several different settings of supply voltage and frequency.

6.3.2 Measuremental results with constant power control

The tests were performed at two machine working points, (7Nm, 970rpm) and (10Nm, 635rpm), or equivalent to output powers of 710W and 665W, respectively. In each case, the control variables, i.e. frequency ratio, machine supply voltage and machine supply frequency, were adjusted, whilst the machine operating point was fixed.

Measurement results at machine operating point (7Nm, 970rpm)

A series of results were taken with the modulation frequency ratio set to 9, 27 and 45. The performance of the dynamometer constant power control is shown respectively in Fig 6.7(a), Fig 6.8(a) and Fig 6.9(a); the drive system power loss against the machine speed slip in Fig 6.7(b), Fig 6.8(b) and Fig 6.9(b); the drive system power loss against machine supply voltage in Fig. 6.7(c), Fig. 9.8(c) and Fig. 6.9(c); the drive system power loss against machine supply frequency in Fig. 6.7(d), Fig. 6.8(d) and Fig. 6.9(d); and the combination of supply voltage and frequency for minimum loss drive and for constant flux drive modes in Fig 6.7(e), Fig 6.8(e) and Fig 6.9(e). The detailed measured data is given in Appendix F.

Measurement results at machine operating point (10Nm, 635rpm)

The modulation frequency ratio was again set to 9, 27 and 45 for the tests. The performance of the dynamometer constant power control is shown respectively in Fig. 6.10(a), Fig 6.11(a) and Fig 6.12(a); the drive system power loss against the machine speed slip in Fig 6.10(b), Fig 6.11(b) and Fig 6.12(b); the drive system power loss against machine supply voltage in Fig. 6.10(c), Fig. 9.11(c) and Fig. 6.12(c); the drive system power loss against machine supply frequency in Fig. 6.10(d), Fig. 6.11(d) and Fig. 6.12(d); and the combination of supply voltage and frequency for minimum loss drive and for constant flux drive modes in Fig 6.10(e), Fig 6.11(e) and Fig 6.12(e). The detailed measured data is given in Appendix F.

6.3.3 Summary of experimental investigation

From the above experimental results the following conclusions can be deduced, which will be used for the development of the drive system loss minimisation control strategies.

(a) Although the induction machine output power was indirectly controlled by the dynamometer armature terminal voltage, the performance of the constant power control was very satisfactory;

(b) At partial load the conventional rated flux control does not give minimum loss in an induction machine drive system, however, by operation of reduced voltage and slightly higher frequency, maximum efficiency can be realised;

(c) The smaller the load torque, the greater is the reduction of voltage needed to achieve the maximum drive system efficiency;

(d) The minimum loss occurs when the machine is operating at approximately the rated slip;

(e) The source harmonic distortion had a limited effect on the combination of the voltage and frequency which gave machine the maximum efficiency, or in other words, the selection of the optimal voltage and frequency is relatively independent of the inverter switching frequency.

(f) The optimal efficiency control will not cause rotor overheating since at partial load the rotor loss is still lower than the rated value.

6.4 Development of system loss minimisation scheme

Since the induction machine is a major user of electric energy, its efficient operation have attracted a lot of attention. Initial published work has concentrated on mains supplied machines operating at constant speed, for example in 1977 Nola proposed a method of improving the efficiency of induction machines operating at partial load by reducing the stator voltage and thus reducing the air-gap flux level. The purpose of this flux reduction was to achieve a better balance between the machine copper loss and iron loss. However, the efficiency improvement turned out to be only marginal [Famouri 1991]. With the introduction of variable speed drives, the adjustment of supply frequency provides an extra degree of freedom for regulating the air-gap flux level, thus enabling a machine to operate over its complete range with the maximum efficiency. It has been suggested that if a model of the induction machine including saturation, stray loss and skin effect can be obtained, the best

combination of machine voltage and frequency can be calculated over the complete speed and load range using a feedforward efficiency optimisation procedure [Kirschen 1984, Chen 1992]. To avoid the difficulties of accurately modelling the machine loss, and to include the inverter loss in the system, feedback optimal efficiency control strategies have also been proposed [Kirschen 1987, Green 1982], in which the machine voltage and frequency are adjusted by monitoring the directly measured input power to the drive. Although it has been commonly recognised that the switching frequency in the drive should also be adjusted to balance the machine harmonic loss and the inverter switching loss, no work has been published in this area, possibly because of the difficulty of modelling machine harmonic loss in a feedforward controller and the complexity of adjustment in the feedback controller.

In the following section, a simple loss model of the PWM inverter fed induction machine system is derived and is used to obtain the minimum loss. A number of assumptions, based on the outcome of experimental observations and the analysis, are then applied to simplify the calculation procedure in order to make it suitable to implementing in a practical controller. Following from this, a simple adjustment rule for feedback loss minimisation is proposed.

In the development of the loss model the following dimensionless parameters are used,

$$k_T = T_m / T_{me} \tag{6.2}$$

$$k_{f_r} = f_r / f_e \tag{6.3}$$

$$k_v = V / V_e \tag{6.4}$$

$$k_f = f / f_e \tag{6.5}$$

$$R = f_s / f \tag{6.6}$$

where (k_T , k_{f_r}) define the machine operating point, k_v is the supply fundamental voltage, k_f is the supply frequency and R is the switching to fundamental frequency ratio. T_m and T_{me} are the machine torque and rated torque; V and V_e are the machine fundamental voltage and rated

voltage; f, f_r and f_e are the stator frequency, rotor frequency and the rated stator frequency; and f_s is the inverter switching frequency.

6.4.1 Induction machine loss model

The total losses in an inverter fed induction machine can be considered as being composed of fundamental and harmonic loss components. By fundamental loss it is meant the loss due to the fundamental voltage and current supplied to the machine by the inverter, whilst the harmonic loss is that induced by the harmonic components in the machine supply.

6.4.1.1 Induction machine fundamental losses

In an efficiently controlled induction machine, the speed slip will be maintained at a relatively low value for the purpose of balancing the iron loss and rotor copper loss, even when the load is light. This allows a simplified version of induction machine phase equivalent circuit to be used to calculate the machine losses. Further, if the machine is assumed to operate only over the linear region of its torque-slip characteristic,

$$T_m = \frac{3p}{2\pi f} \cdot \frac{V^2}{R_2'/s} \tag{6.7}$$

where p is the machine number of pole pairs, s is the machine speed slip, and R_2' is the equivalent rotor resistance.

Since the control of the induction machine will usually act to maintain a high power factor, the magnetising current component of the stator current can be neglected, particularly when the machine is operating at reduced airgap flux. Thus, the stator current is approximately given by,

$$I = \frac{V}{R_2'/s} \tag{6.8}$$

(a) Machine fundamental copper loss

The machine copper loss at a particular stator current, I, is equal to,

$$P_R = (\frac{I}{I_e})^2 P_{R_e} \tag{6.9}$$

where P_{R_e} is the copper loss and I_e the current at the rated condition.

Since

$$s = \frac{k_T k_f}{k_v^2} s_e \tag{6.10}$$

$$\frac{I}{I_e} = \frac{k_T k_f}{k_v} \tag{6.11}$$

then the copper loss will be expressed in terms of the dimensionless variables, Eqns. (6.2) - (6.6),

$$P_R = (\frac{k_T k_f}{k_v})^2 P_{R_e} \tag{6.12}$$

(b) Machine fundamental iron losses

Iron losses consist of core loss and stray load loss. Core loss which occurs mainly in the stator core is approximately proportional to the flux density squared and to the square root of frequency cubed [Chalmers 1968],

$$P_{I,C} = (\frac{\Phi}{\Phi_e})^2 (\frac{f}{f_e})^{1.5} P_{Ie,C} \tag{6.13}$$

where Φ is the machine air-gap flux and Φ_e is the rated air-gap flux. $P_{Ie,C}$ is the machine core loss at the rated condition.

Stray load loss is caused by the load current m.m.f.s, and appears mainly as end-leakage effects in an unskewed induction machine. As discussed in Chapter 4 the end-leakage loss is proportional to the flux density squared and to the square root of frequency cubed. If all other features were held constant, the stray load loss would be approximately proportional to the square of the electric loading [Chalmers 1965], a relationship which has also recently been experimentally verified [Baholo 1997]. Thus,

$$P_{I,s} = k_f^2 \left(\frac{\Phi}{\Phi_e}\right)^2 \left(\frac{f}{f_e}\right)^{1.5} P_{Ie,s} \tag{6.14}$$

where $P_{Ie,s}$ is the machine stray load loss at the rated condition.

Since,

$$\frac{\Phi}{\Phi_e} \approx \frac{k_v}{k_f} \tag{6.15}$$

then the machine fundamental iron loss is determined in terms of the dimensionless variables,

$$P_I = P_{I,c} + P_{I,s}$$

$$= \frac{k_v^2}{\sqrt{k_f}} \left(P_{Ie,c} + k_f^2 P_{Ie,s} \right) \tag{6.16}$$

6.4.1.2 Induction machine harmonic loss

The harmonic loss model developed in Chapter 4 considered the individual effects of each harmonic in the machine current spectrum. However, it was also shown that the waveform THD figure was a good indication of the machine harmonic loss, and has been used to develop a generalised model for machine harmonic loss.

(a) Machine harmonic copper loss

$$P_{R,har} = 3\sum_{n=2}^{\infty} I_n^2 R_e$$

$$= 3\sum_{n=2}^{\infty} (\sqrt{\frac{3}{2}}\frac{V_n}{nX})^2 R_e$$

$$\approx 9\frac{V_{1,rms}^2 R_e}{X^2}\sum_{n=2}^{\infty}(\frac{V_{n,rms}}{n V_{1,rms}})^2$$

$$= 9\frac{R_e V_e^2}{X_e^2}\cdot\frac{k_v^2}{k_f^2}\cdot THD^2 \qquad (6.17)$$

where R_e is the machine resistance and X_e is the machine leakage reactance at the rated condition. The waveform THD varies with the frequency ratio R and the modulation depth M. The THD associated with vector space PWM can be expressed approximately as [Appendix G],

$$THD^2 = \frac{1}{R^2}(b_1'' M^3 + b_2'' M^2 + b_3'' M + b_4'') \qquad (6.18)$$

where

$$\begin{cases} b_1'' = 0.124 \\ b_2'' = 0.258 \\ b_3'' = -1.015 \\ b_4'' = 0.788 \end{cases} \qquad (6.19)$$

and

$$M = \alpha k_v \qquad (6.20)$$

α is determined by the machine rated voltage and the inverter d.c. link voltage. For example, in the case of the Δ connected 26kW induction machine, where $V_e = 153\ V$ and $V_d = 216\ V$, $\alpha = 1.15$.

Thus,

$$P_{R,har} = 9\frac{R_e V_e^2}{X_e^2} \cdot \frac{k_v^2}{k_f^2 R^2} (b_1' k_v^3 + b_2' k_v^2 + b_3' k_v + b_4') \tag{6.21}$$

where

$$\begin{cases} b_1' = 0.189 \\ b_2' = 0.341 \\ b_3' = -1.167 \\ b_4' = 0.788 \end{cases} \tag{6.22}$$

(b) Machine harmonic iron loss

The load dependent stray load losses would be slightly larger with harmonics present. However, they are usually small and are taken to be the same as with sinusoidal excitation [Klingshirn 1968]. The harmonic core losses are assumed to be dominated by the end-leakage and skew-leakage effects. The harmonic iron loss may thus be expressed as,

$$P_{I,har} = \sum_{n=2}^{\infty} C_i f_n i_n^2 P_I \tag{6.23}$$

where P_I is the machine fundamental iron loss, and

$$C_i = 8.0 \times 10^{-4} \tag{6.24}$$

$$f_n = n f \tag{6.25}$$

$$i_n = \frac{I_n}{I} = \sqrt{3}\frac{V_n}{n V_1} \cdot \frac{R_2'}{s X} \tag{6.26}$$

Thus,

$$P_{I,har} = \sum_{\substack{n=2 \\ n \neq triplen}}^{\infty} C_i \, nf \cdot (\sqrt{3} \, \frac{V_n}{n V_1})^2 \cdot (\frac{R_2'}{s X})^2 P_I$$

$$= 3 \, C_i f \cdot (\frac{R_2'}{s X})^2 P_I [\sum_{\substack{n=2 \\ n \neq triplen}}^{\infty} n \cdot (\frac{V_n}{n V_1})^2]$$

$$= 3 \, C_i \cdot kf f_e \cdot \frac{R_2'^2}{X_e^2 \, s_e^2} \cdot \frac{k_v^4}{k_f^2 \, k_f^4} \cdot P_I \cdot THDI^2 \qquad (6.27)$$

where the harmonic distribution parameter THDI is defined as,

$$THDI = \sqrt{\sum_{\substack{n=2 \\ n \neq triplen}}^{\infty} n (\frac{V_n}{n V_1})^2} \qquad (6.28)$$

which for a particular PWM method can again be expressed as a function of the frequency ratio and the normalised fundamental voltage [Appendix G],

$$THDI^2 = \frac{1}{R} (a_1' k_v^3 + a_2' k_v^2 + a_3' k_v + a_4') \qquad (6.29)$$

where for vector space PWM,

$$\begin{cases} a_1' = -1.942 \\ a_2' = 5.581 \\ a_3' = -5.883 \\ a_4' = 2.396 \end{cases} \qquad (6.30)$$

Therefore,

$$P_{I,har} = 3\,C_i f_e \cdot \frac{R_2^{',2}}{X_e^2\, s_e^2} \cdot \frac{k_v^4}{k_f^2\, k_f^3} \cdot \frac{k_v^2}{\sqrt{(k_f}} (P_{Ie,c} + k_f^2\, P_{Ie,s}) \cdot THDI^2$$

$$= 3\,C_i f_e \cdot \frac{R_2^{',2}}{X_e^2\, s_e^2} \cdot \frac{k_v^6}{\sqrt{k_f^7}} \cdot (\frac{P_{Ie,c}}{k_f^2} + P_{Ie,s}) \cdot THDI^2$$

$$= 3\,C_{ie} \cdot \frac{k_v^6 (a_1' k_v^3 + a_2' k_v^2 + a_3' k_v + a_4')}{R\sqrt{k_f^7}} \cdot (\frac{P_{Ie,c}}{k_f^2} + P_{Ie,s}) \qquad (6.31)$$

where

$$C_{ie} = C_i f_e \cdot \frac{R_2^{',2}}{X_e^2\, s_e^2} \qquad (6.32)$$

6.4.2 Inverter loss model

Although the different PWM strategies used can influence inverter loss as shown in Chapter 4, the effect is relatively small. Therefore, for simplicity a loss formula based on natural PWM, Eqn. (4.37), will be used to model inverter loss,

$$P_{INV} = [\frac{3}{\pi} (V_{T_o} + V_{d_o}) I_m + \frac{3}{4} (k_T + k_D) I_m^2]$$

$$+ [\frac{3}{4} (V_{T_o} - V_{D_o}) I_m \cos\varphi + \frac{2}{\pi} (k_T - k_D) I_m^2 \cos\varphi]\, M$$

$$+ R_f [\frac{3}{2} \alpha_1 V_d I_m^2 + \frac{6}{\pi} (\alpha_2 V_d + \alpha_3) I_m + 3\,\alpha_4 V_d] \qquad (6.33)$$

The power factor $\cos\varphi$ may be considered as a constant, the value being dependent on the machine power rating.

Since for a Δ connected machine,

$$I_m = \sqrt{6}\, I$$

$$= \sqrt{6} \cdot \frac{V}{R_2'/s}$$

$$= \sqrt{6}\, I_e \cdot \frac{k_T\, k_f}{k_v} \tag{6.34}$$

and

$$M = \alpha\, k_v \tag{6.35}$$

the inverter loss can be written in terms of the dimensionless variables as,

$$P_{INV} = \frac{1}{k_v^2} [\, C_1\, k_T\, k_f\, k_v + C_2\, k_f^2\, k_f^2 + C_3\, k_T\, k_f\, k_v^2$$

$$+ C_4\, k_f^2\, k_f^2\, k_v + C_5\, k_f^2\, k_f^3\, R + C_6\, k_T\, k_f^2\, k_v\, R + C_7\, k_f\, k_v^2\, R\,] \tag{6.36}$$

where C_1 , $\cdots$, C_7 are constants, determined from,

$$C_1 = \frac{3\sqrt{6}}{\pi} (\, V_{T_o} + V_{D_o}\,)\, I_e \tag{6.37}$$

$$C_2 = \frac{9}{2} (\, K_T + K_D\,)\, I_e^2 \tag{6.38}$$

$$C_3 = \frac{3\sqrt{6}}{4} (\, V_{T_o} - V_{D_o}\,) \cdot I_e\, \alpha\, \cos\varphi \tag{6.39}$$

$$C_4 = \frac{12}{\pi} (\, K_T - K_D\,) \cdot I_e^2 \cdot \alpha\, \cos\varphi \tag{6.40}$$

$$C_5 = 9\, \alpha_1\, V_d f_e\, I_e^2 \tag{6.41}$$

$$C_6 = \frac{6\sqrt{6}}{\pi} (\, \alpha_2\, V_d + \alpha_3\,) f_e\, I_e \tag{6.42}$$

$$C_7 = 3\, \alpha_4 f_e\, V_d \tag{6.43}$$

6.4.3 System loss minimisation

The total loss in the traction drive is thus,

$$P_{sys} = P_R + P_I + P_{R,har} + P_{I,har} + P_{INV} \tag{6.44}$$

which is a function of machine supply voltage, supply frequency and inverter switching frequency, i.e.,

$$P_{sys} = h\,(\,k_v\,,\,k_f\,,\,R\,) \tag{6.45}$$

The requirement for efficient control of the inverter fed induction machine drive is to minimise the system loss P_{sys} under the constraints of the required load and speed (T_m, n), expressed in their equivalent dimensionless form (k_T , k_{f_r}). The constraint of torque k_T is automatically included in the total loss, P_{sys}, expression, whereas that of speed k_{f_r} can be described as,

$$k_{f_r} = \frac{f_r}{f_e} \approx k_f - \frac{k_T\,k_f^2}{k_v^2}\,s_e \tag{6.46}$$

The minimum system loss can be determined analytically by defining an Euler-Lagrange equation,

$$L \equiv h\,(\,k_v\,,\,k_f\,,\,R\,) + \lambda\,(\,k_{f_r} - k_f + \frac{k_T\,k_f^2}{k_v^2}\,s_e\,) \tag{6.47}$$

where λ is the Lagrange multiplier.

and solving,

$$\begin{cases} \dfrac{\partial L}{\partial k_v} = 0 \\ \dfrac{\partial L}{\partial k_f} = 0 \\ \dfrac{\partial L}{\partial R} = 0 \end{cases} \tag{6.48}$$

and the adjoint equation,

$$\frac{\partial L}{\partial \lambda} = k_{f_r} - k_f + \frac{k_T k_f^2}{k_v^2} s_e = 0 \tag{6.49}$$

Using this method the required machine voltage, the machine frequency and the PWM frequency ratio (discritised into triplen odd value), which maximise the system efficiency, can be found. However, due to their complexity the above equations can only be solved off-line numerically.

6.4.4 A simple drive system loss minimum control strategy

The loss minimisation strategy would be practically feasible only if the control variables could be obtained reasonably easily. In the following, the previous theoretical and experimental findings will be used to simplify the above expressions in order to design an easily implemented loss minimisation strategy.

Since the minimum machine loss usually occurs at a speed slip close to the rated, the optimisation process can be simplified by assuming rated slip,

$$s \approx s_e \tag{6.50}$$

Thus, Eqns. (6.49) and (6.46) reduce to,

$$k_v = \sqrt{k_T k_f} \tag{6.51}$$

$$k_f = \frac{1}{1 - s_e} k_{f_r} \tag{6.52}$$

If it is assumed that the torque varies with speed squared, which is approximated the case for a vehicle travelling on a level road,

$$k_T \approx k_f^2 \tag{6.53}$$

the required voltage would be,

$$k_v = k_f^{3/2} \tag{6.54}$$

The relationship given by Eqn. (6.51) represents an operating state at which the machine copper loss and iron loss are approximately balanced.

By defining a factor k_w, equal to the inverter switching frequency normalised to the rated machine supply frequency,

$$k_w = \frac{f_s}{f_e} = \frac{f R}{f_e} = k_f R \tag{6.55}$$

then the drive system loss equation can be written as,

$$\begin{aligned} & h\,(k_v, k_f, k_w) \\ & = k_v^2 P_{Re} + k_v \sqrt{k_T}\,(P_{Ie,c} + k_f^2 P_{Ie,s}) \\ & + \frac{1}{k_w^2}(b_1 k_v^5 + b_2 k_v^4 + b_3 k_v^3 + b_4 k_v^2) \\ & + \frac{\sqrt{k_f^5}}{k_w}(a_1 k_v^5 + a_2 k_v^3 + a_3 k_v^2 + a_4 k_v)\left(\frac{P_{Ie,c}}{k_f^2} + P_{Ie,s}\right) \\ & + \frac{1}{k_v^2}(C_1 k_v^3 + C_2 k_v^4 + C_3 k_v^4 + C_4 k_v^5 + C_5 k_v^4 k_w + C_6 k_v^3 k_w + C_7 k_v^2 k_w) \end{aligned} \tag{6.56}$$

where

$$b_i = 9 \frac{V_e^2 R_e}{X_e^2} b_i' \tag{6.57}$$

$$a_i = 3\, c_i f_e \frac{R_2'}{X_e^2 s_e^2} a_i' \tag{6.58}$$

Solving for the minimum loss, i.e.,

$$\frac{\partial h}{\partial k_w} = 0 \tag{6.59}$$

then,

$$(C_5 k_v^2 + C_6 + C_7) k_w^3 - (P_{Iec}\sqrt{k_T} + P_{Ies}\sqrt[5]{k_T}) \cdot (a_1 k_v^4 + a_2 k_v^3 + a_3 k_v^2 + a_4 k_v) k_w -$$

$$- 2 (b_1 k_v^5 + b_2 k_v^4 + b_3 k_v^3 + b_4 k_v^2) = 0 \qquad (6.60)$$

or

$$k_w^3 - p\, k_w - q = 0 \qquad (6.61)$$

where

$$p = \frac{a_1 k_v^4 + a_2 k_v^3 + a_3 k_v^2 + a_4 k_v}{C_5 k_v^2 + C_6 k_v + C_7} \cdot (P_{Iec}\sqrt{k_T} + P_{Ies}\sqrt[5]{k_T}) \qquad (6.62)$$

$$q = \frac{2 (b_1 k_v^5 + b_2 k_v^4 + b_3 k_v^3 + b_4 k_v^2)}{C_5 k_v^2 + C_6 k_v + C_7} \qquad (6.63)$$

The Eqn. (6.61) can be solved as,

$$k_w = \begin{cases} \sqrt[3]{\frac{q}{2} + \sqrt{\frac{q^2}{4} - (\frac{p}{3})^3}} + \sqrt[3]{\frac{q}{2} - \sqrt{\frac{q^2}{4} - (\frac{p}{3})^3}}\ , \ when\ \frac{q^2}{2} \geq (\frac{p}{3})^3 \\ 2\sqrt{\frac{p}{3}} \cos\frac{\theta}{3}\ ,\ \theta = atan\left(\sqrt{((\frac{p}{3})^3 - \frac{q^2}{4})/\frac{q}{2}}\right)\ ,\ when\ \frac{q^2}{4} < (\frac{p}{3})^3 \end{cases} \qquad (6.64)$$

Hence the optimum frequency ratio is determined using,

$$R = INT_{(triplen)} (\frac{k_w}{k_f}) \qquad (6.65)$$

However, it may be neccesary to include hysteresis band in the frequency ratio calculation to prevent system from cycling continuously between two different frequency ratios at certain speeds.

When the voltage reaches its maximum,

$k_v = 1$

$R = 1$

k_f is adjusted to let the machine operate at the required speed k_{f_r}. There is no efficiency optimisation in this case.

The above analysis has assumed that the optimal working point occurs when the induction machine operates at close to rated slip (s). This is confirmed by Table 6.1, where it is seen that the experimentally measured optimal point is closer to rated slip (s), than rated rotor slip frequency (f_r) suggested in the previous work by [Boys 1982, Famouri 1991]. However, a small improvement in efficiency may be possible by perturbing this working point.

Table 6.1 Experimentally obtained optimal speed slip (s) and rotor slip frequency (f_r).

Freqency ratio	n=970rpm, T_q=7Nm		n=635rpm, T_q=10Nm	
	s (%)	f_r (Hz)	s (%)	f_r (Hz)
45	5.08	1.75	5.74	1.42
33			5.23	1.15
27	4.87	1.80		
15	5.27	1.59		
9			5.22	1.19
Rated values	s^*=5.33%	f_r^*=2.67Hz	s^*=5.33%	f_r^*=2.67Hz

Because of the small deviation of the optimal speed slip from the rated one, an initial guess of the required voltage and frequency may be made using Eqns. (6.51) and (6.52). These pre-calculated voltage and frequency are then used to calculate the required switching frequency. Due to the discrete nature of the frequency ratio and the low sensitivity of the machine optimal working point to the harmonics, the calculated frequency ratio can be considered as close to the true optimal one. Finally, the required voltage and frequency are perturbed using the following strategy,

(i) Calculate k_w from Eqn. (6.64), and transform it into frequency ratio R;

(ii) Perturb the voltage k_v to meet the condition,

$$5\,b_1\,k_v^4 + (4\,b_2 + 4\,a_1\,k_w)\,k_v^3 + (3\,b_3 + 3\,C_4\,k_w^2 + 3\,a_2\,k_w)\,k_v^2$$

$$+ (2\,b_4 + 2\,C_5\,k_w^3 + 2\,d_2\,k_w^2 + 2s\,a_3\,k_w)\,k_v + (d_1\,k_w^2 + a_4\,k_w) = 0 \qquad (6.66)$$

(iii) Perturb the frequency k_f using,

$$k_f = \frac{k_v^2}{k_T} \qquad (6.67)$$

6.4.5 Verification of the loss minimisation strategy

The loss model and the loss minimisation control, Eqns. (6.51), (6.52) and (6.64), were tested on the experimental 3kW inverter fed induction machine drive system. The theoretically optimised control variables, in comparison with those obtained from experiments, are given in Table 6.2. and a good agreement is obtained between the voltage and frequency figures. However, due to lack of anticipation during the tests sufficient data was not available to collaborate the frequency ratio figure. Nevertheless, it can be observed from Fig. 6.13 that when the frequency ratio is 45 for the experiment of machine operating at (7Nm,970rpm), the system loss is approaching a minimum.

Table. 6.2 Predicted and tested optimal control variables for the 3kW inverter fed induction machine drive.

		Voltage (V)	Frequency (Hz)	Frequency ratio
Working point (10Nm, 635rpm)	Predicted	112.6	22.20	87
	Measured	108.0	22.48	-
Working point (7Nm, 970rpm)	Predicted	116.8	34.10	51
	Measured	112.2	34.08	~ 45

The Fortran program used for the calculation of the optimal control variables is given in Appendix H for reference, together with the parameters used.

The drive system efficiency improvement by replacing the rated flux controller with the optimal control has also been confirmed by experiments on the 3kW induction machine drive system, as shown in Table 6.3. The optimal control realised an efficiency improvement of between 9 and 3% compared to rated flux control.

Table 6.3 Experimental comparison of drive system efficiency for constant flux control and optimal control.

Machine speed (rpm)	Machine load (Nm)	Modulation depth	Frequency ratio	Drive system efficiency (%)	
				Flux constant control	Optimal control
970	7	0.35	45	66	75
635	10	0.5	9	44	47
635	10	0.5	45	62	67

6.5 Feedback loss minimisation control methods

Feedback energy efficient control is attractive since it can be accomplished without using a complex loss model. An example of feedback loss minimisation control is the so-called auto energy saving function available in recent models of inverters used in industrial drives [dpa 1996]. The control principle is to very slowly perturb the voltage being applied to the motor, and to monitor d.c. link current to achieve a minimum value. More advanced techniques have been proposed which incorporate the feedback loss minimisation control with flux vector control [Kirschen 1987] or direct torque control [Casadei 1995]. In these methods, an internal field orientation torque control loop and a speed regulator are employed to maintain the load and speed requirements, whilst the d-axis component of the stator current, i.e. the rotor flux, is adapted to minimise the drive system input power. Since flux changes create disturbances in the torque, the response time of the torque control loop has to be designed to be much faster

than the time constant governing the flux variation. However, it was found that tuning of the controller had a significant impact on the efficiency of the drive system. In addition, the inverter loss was treated more or less the same way as the windage and friction losses, and there was no mechanism to minimise this component of loss.

In some applications such as electric vehicle drives, the dynamic response is not a major concern and it may not be necessary to apply the complex flux vector control or the direct torque control methods. A simple feedback loss minimisation control method may be appropriate such as that proposed as in Fig. 6.14. Here, the machine speed demand is set by the vehicle driver interface, and the machine load is determined automatically by driving conditions. The machine supply frequency is varied to obtain a minimum inverter d.c. link current. The machine supply voltage (or PWM modulation depth) is adjusted in order to maintain the demand speed. The obtained optimal voltage and frequency are then used to calculate the optimal switching frequency as described in the previous feedforward optimisation strategy. Due to its discrete nature, the frequency ratio is not sensitive to small perturbations in the supply frequency and the frequency ratio may only need to be adjusted when the supply voltage and frequency are relatively stable.

The feedback loss minimisation strategies are only effective when the system is operating in the steady state, i.e. the machine stays in a working point for some time. In comparison, feedforward loss minimisation strategies can be used in transient state as well as in steady state, because it will always follow the defined machine working points. This is particularly useful in an electric vehicle drive, as the demand torque needs to be continually varied to adjust the vehicle speed to account for road and traffic conditions.

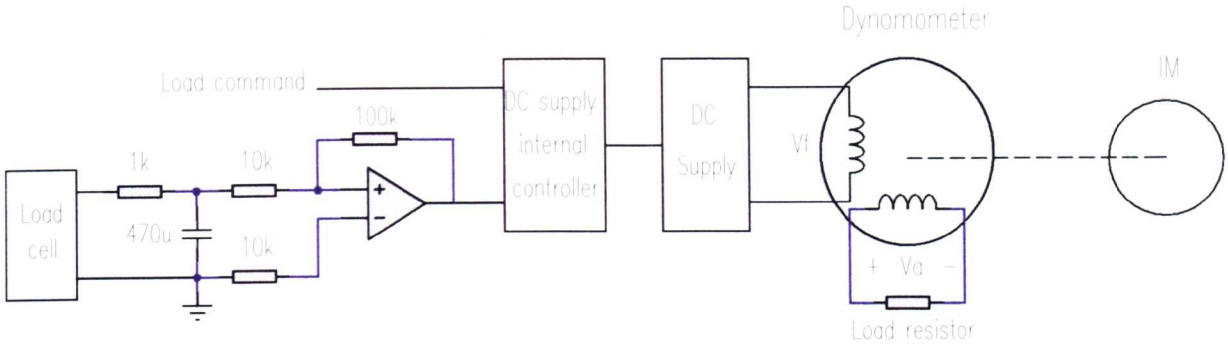

Fig 6.1 Schematic of method used to achieve constant load torque control from the dynamometer.

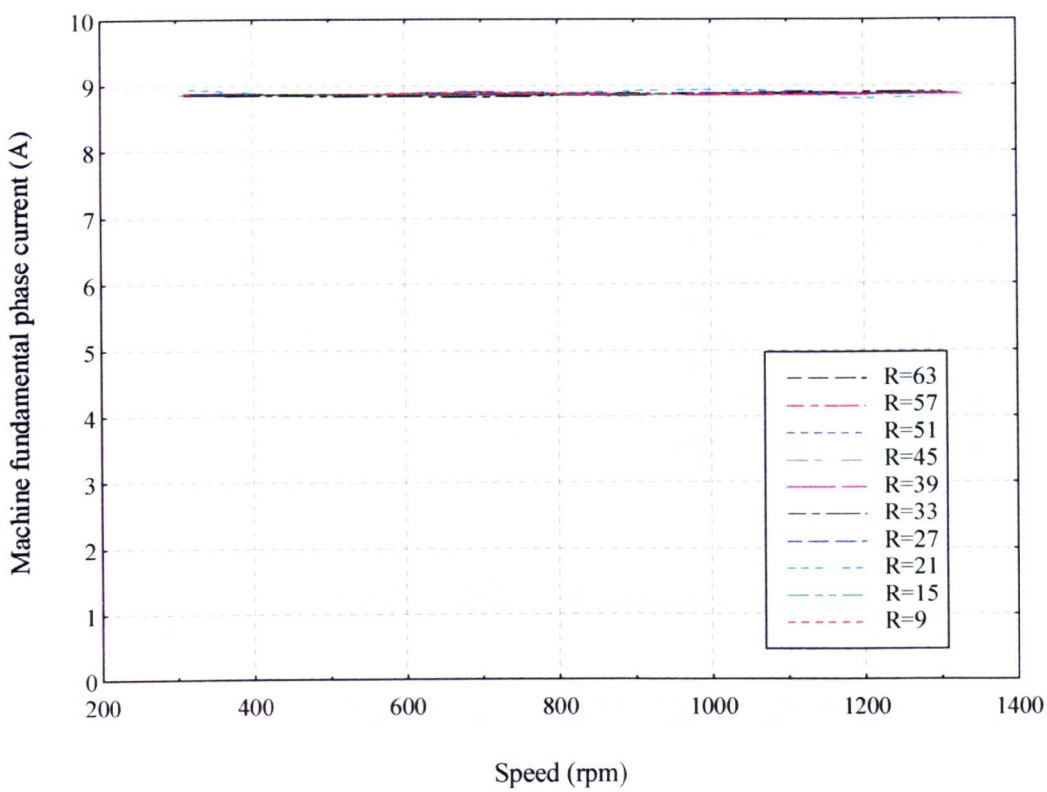

Fig 6.2 Plot of machine input current under constant torque control over a range of speed and inverter switching frequencies.

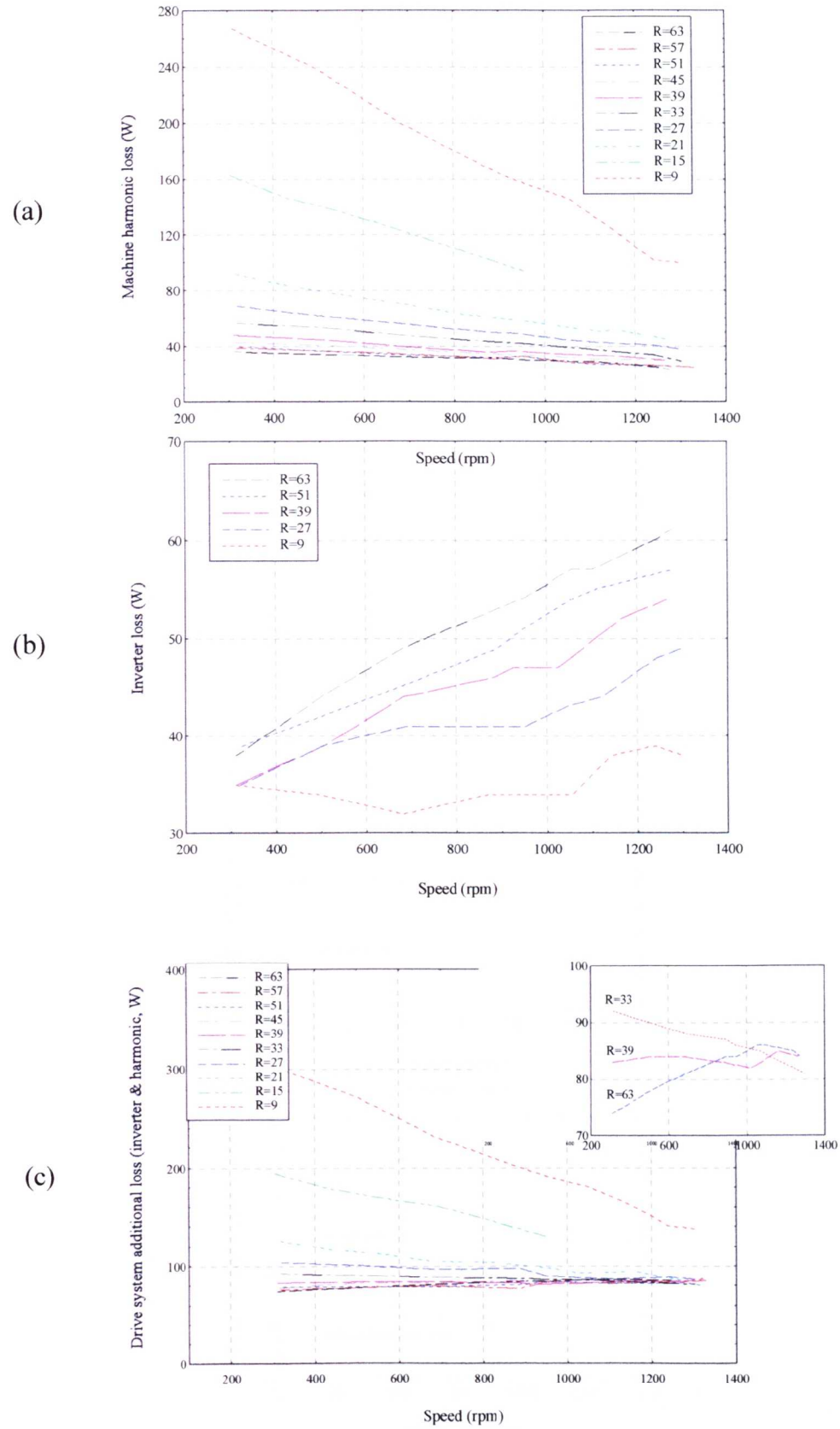

Fig 6.3 Measured 3kW drive loss at constant torque and different machine speeds and PWM frequency ratios. (a) Machine harmonic loss, (b) inverter loss, (c) total system additional loss.

(a)

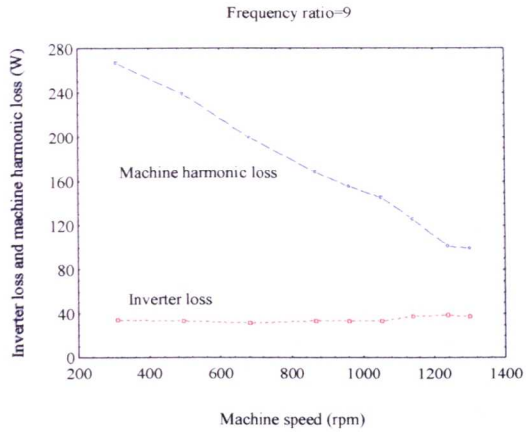

(b)

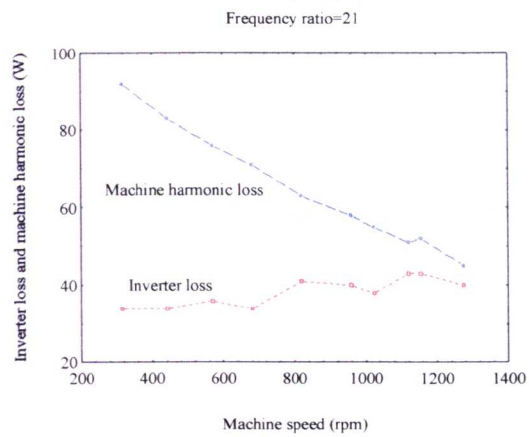

(c)

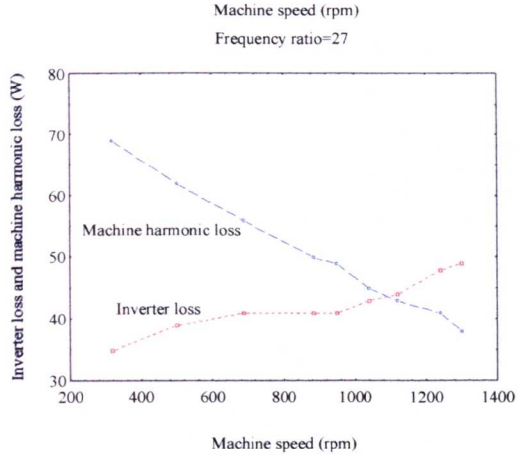

(d)

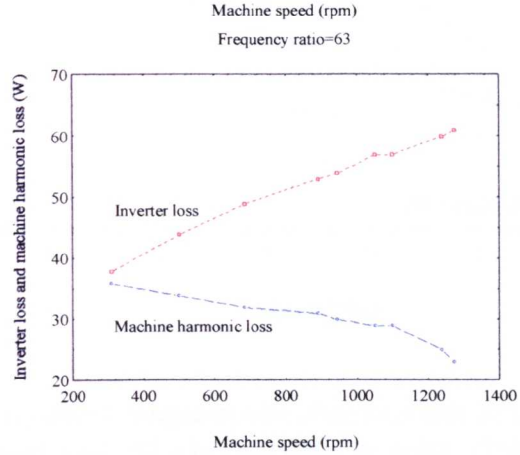

Fig 6.4 Comparison of machine harmonic loss and inverter loss at different PWM frequency ratios. (a) ratio 9, (b) ratio 21 , (c) ratio 27 , and (d) ratio 63 .

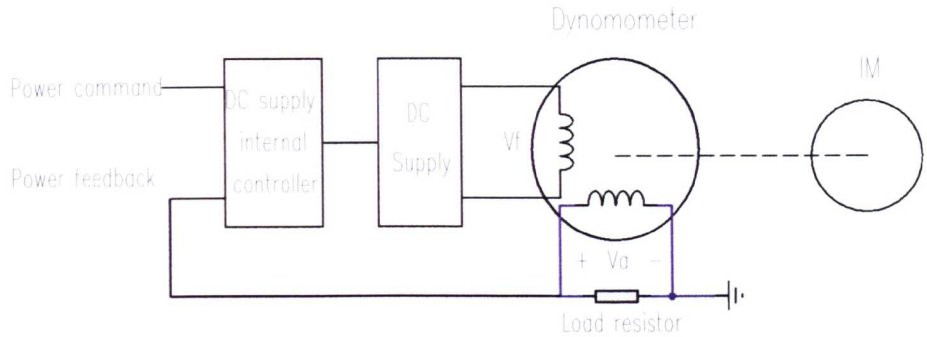

Fig. 6.5. Constant power control of the dynamometer.

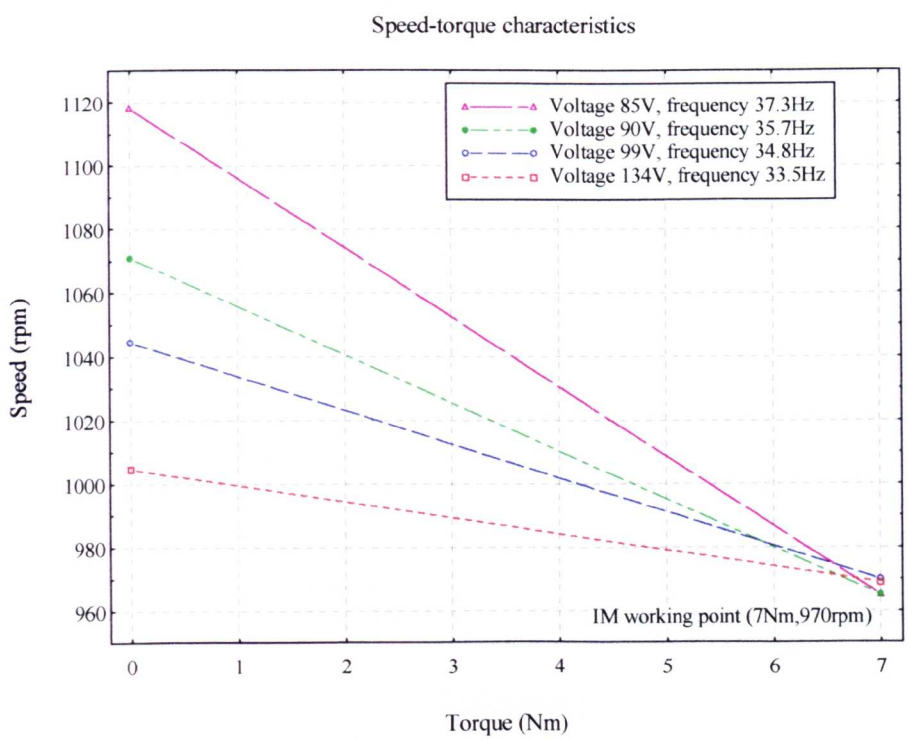

Fig 6.6 3kW induction machine torque-speed characteristic at constant output power and variable voltage and frequency. Machine operating point: (7Nm, 970rpm) and PWM frequency ratio: 9.

(a)

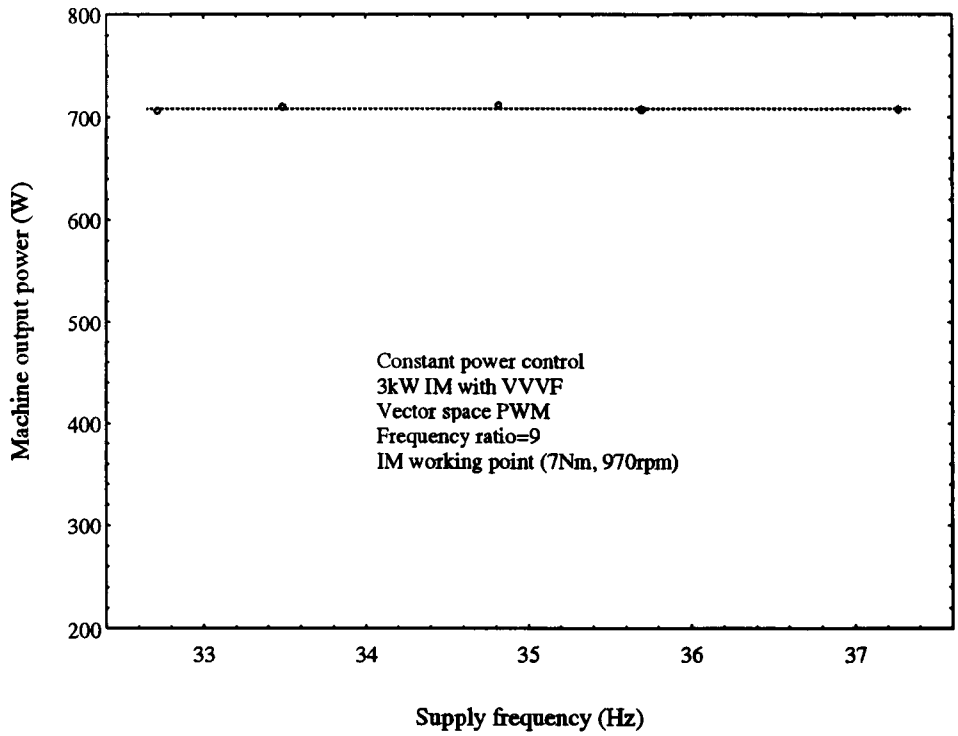

(b)

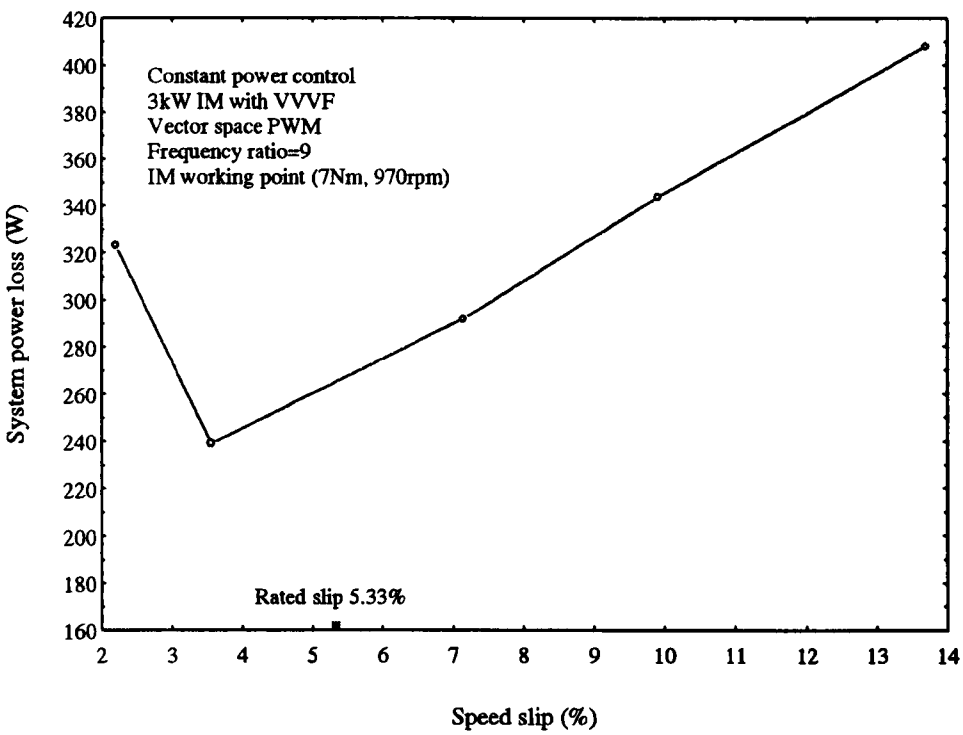

Fig 6.7 Measurement results under constant power control at 35% full load. The frequency ratio is 9. (a) Constant power control performance, (b) the drive system power loss against machine speed slip.

(c)

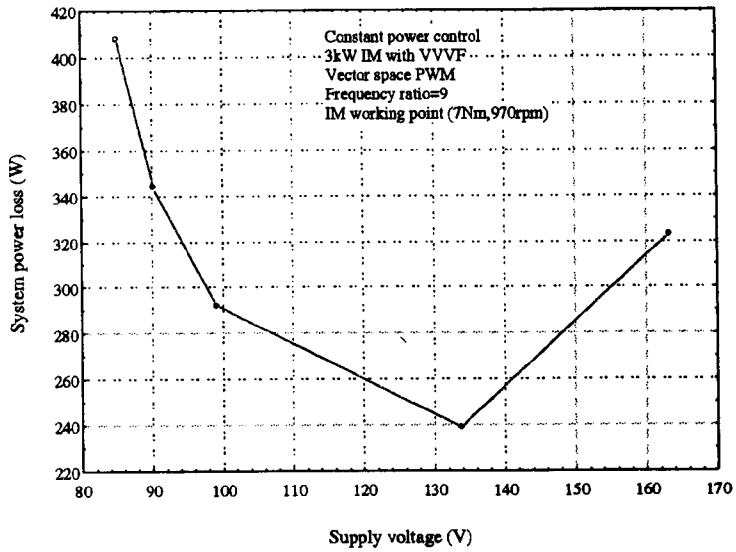

(d)

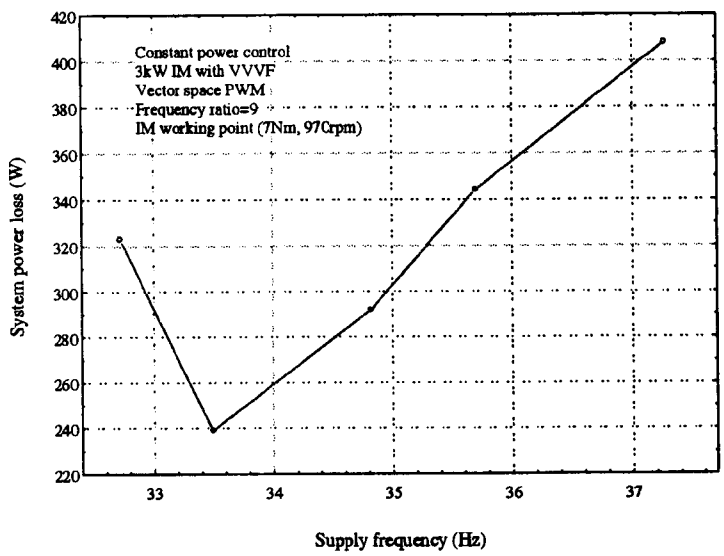

(e)

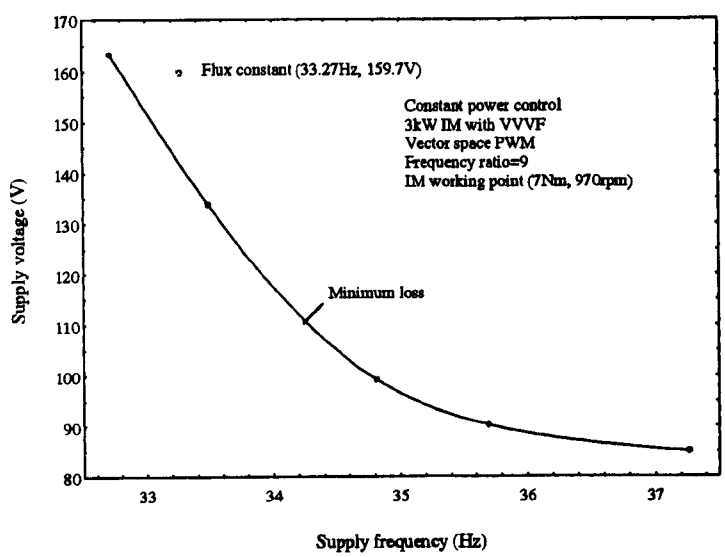

Fig 6.7 Measurement results under constant power control at 35% full load. The frequency ratio is 9. (c) The drive system power loss against machine supply voltage, (d) the drive system power loss against machine speed, (e) the combinations of supply voltage and frequency for minimum loss and for flux constant drive modes.

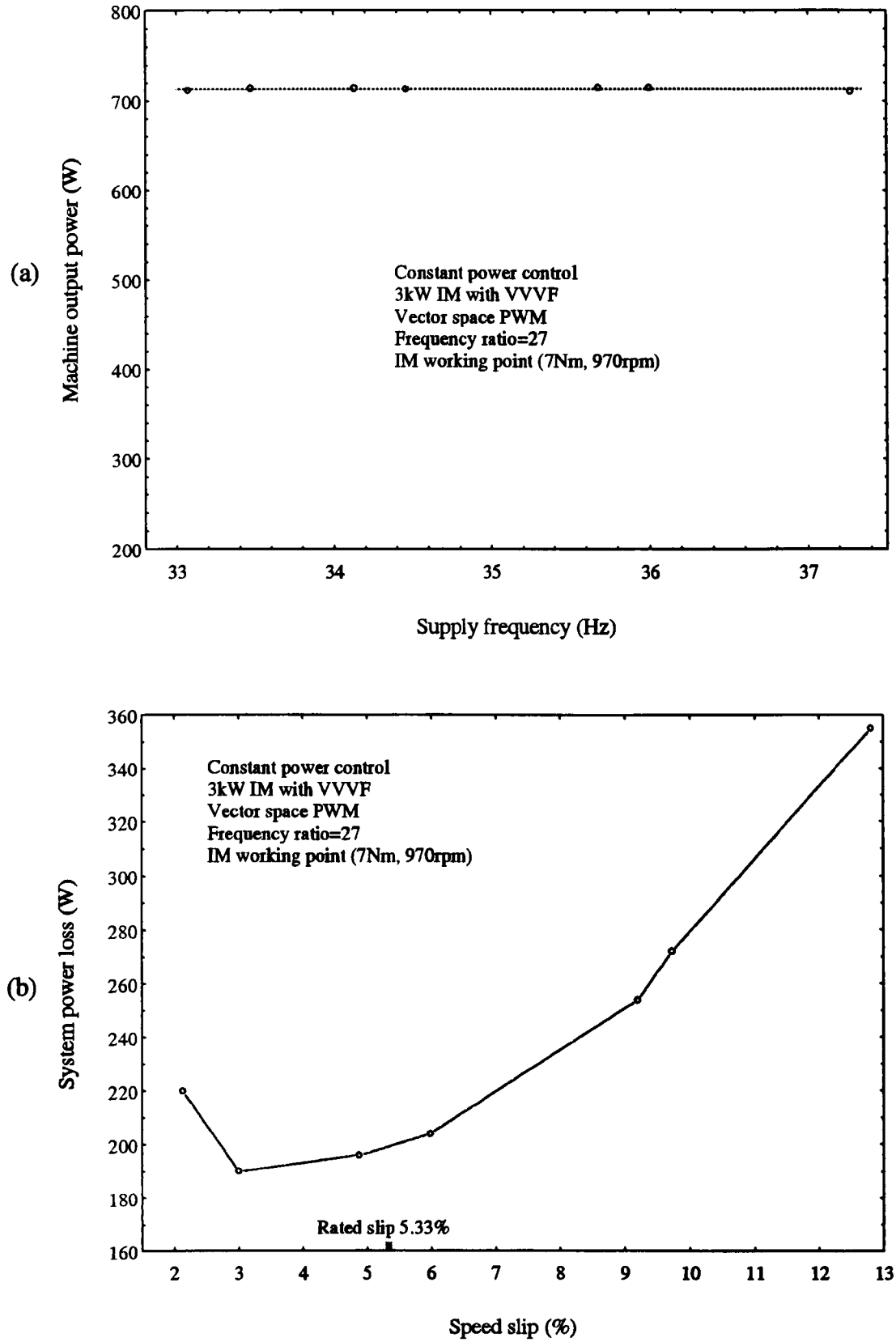

Fig 6.8 Measurement results under constant power control at 35% full load. The frequency ratio is 27. (a) Constant power control performance, (b) the drive system power loss against machine speed slip.

(c)

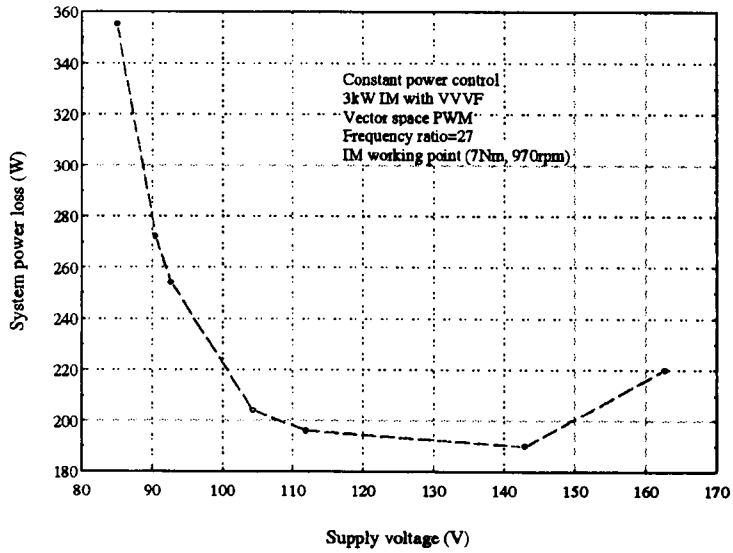

(d)

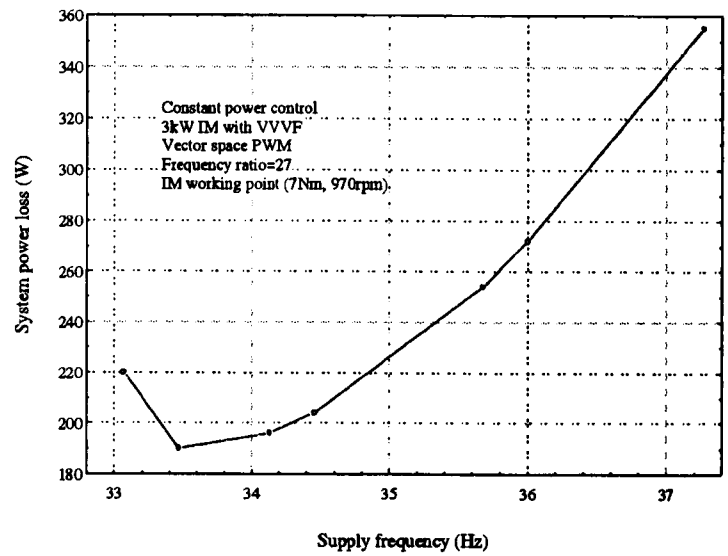

(e)

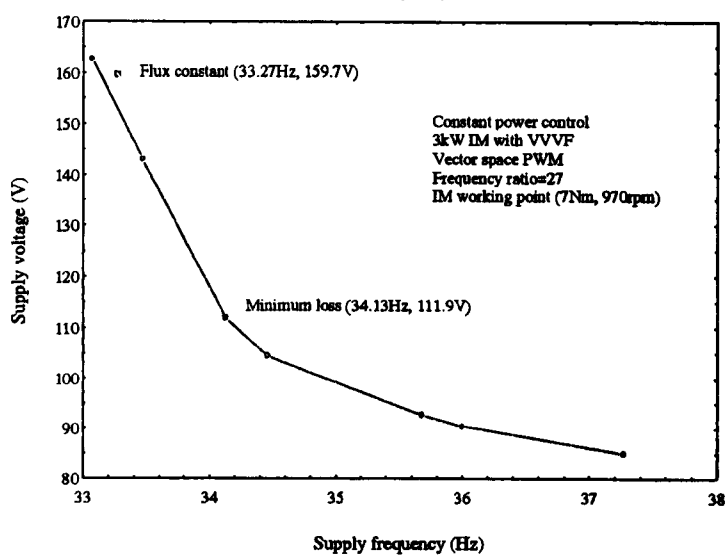

Fig 6.8 Measurement results under constant power control at 35% full load. The frequency ratio is 27. (c) The drive system power loss against machine supply voltage, (d) the drive system power loss against machine speed, (e) the combinations of supply voltage and frequency for minimum loss and for flux constant drive modes.

(a)

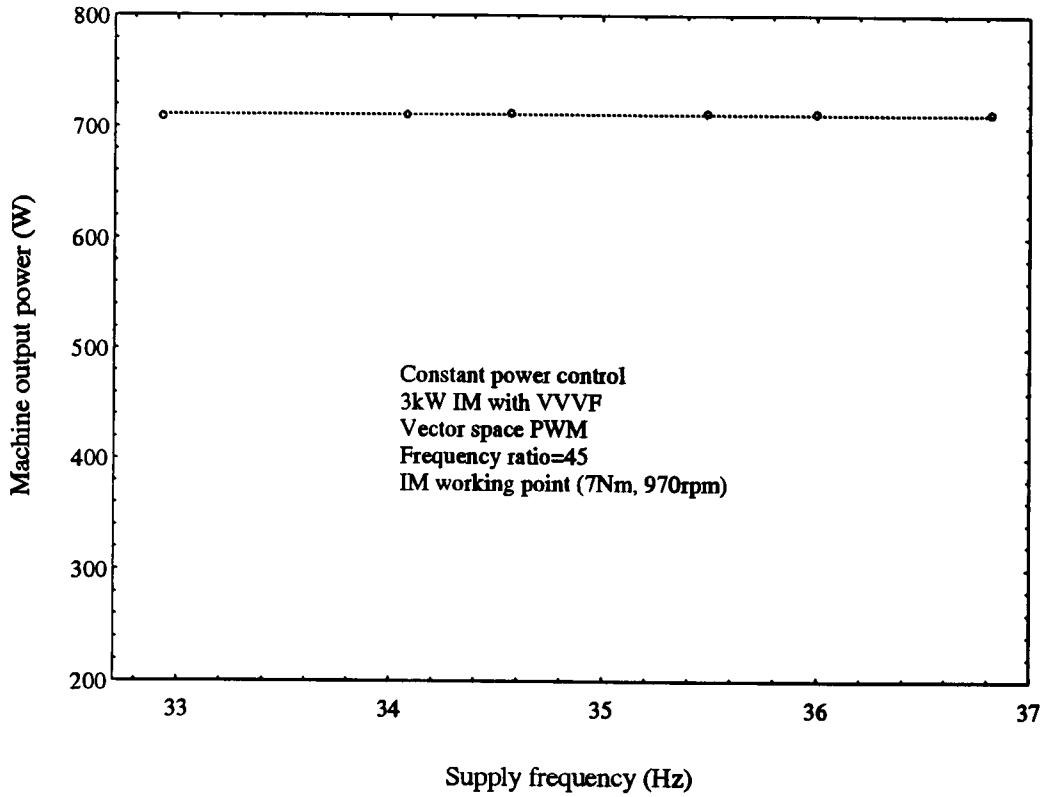

(b)

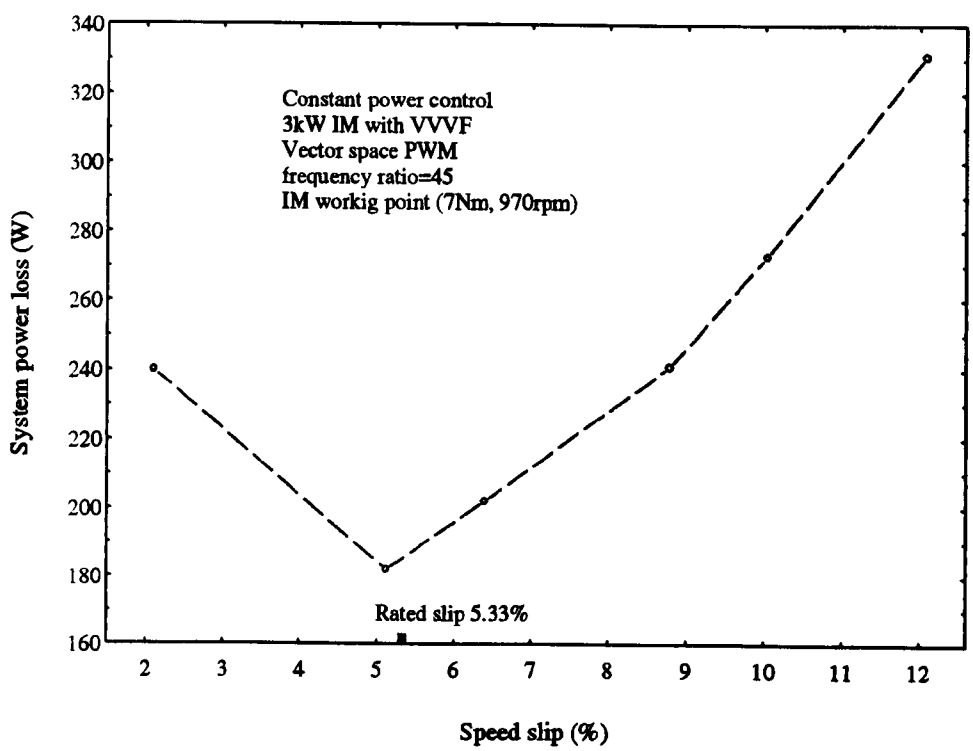

Fig 6.9 Measurement results under constant power control at 35% full load. The frequency ratio is 45. (a) Constant power control performance, (b) the drive system power loss against machine speed slip.

(c)

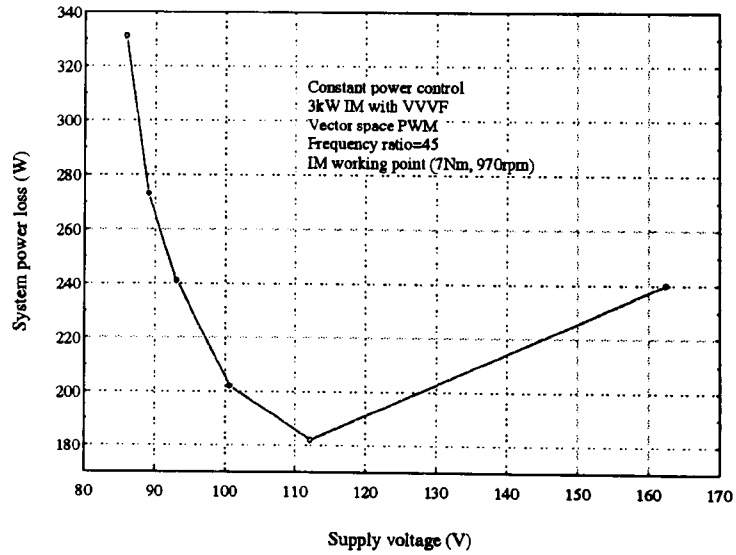

(d)

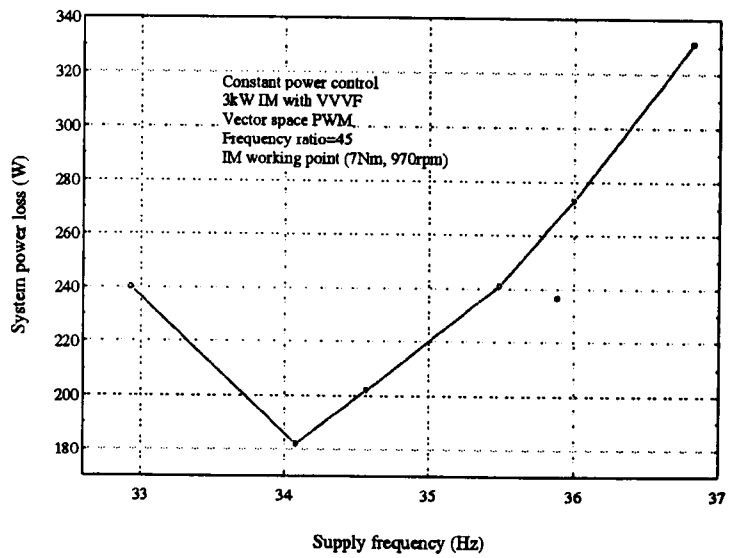

(e)

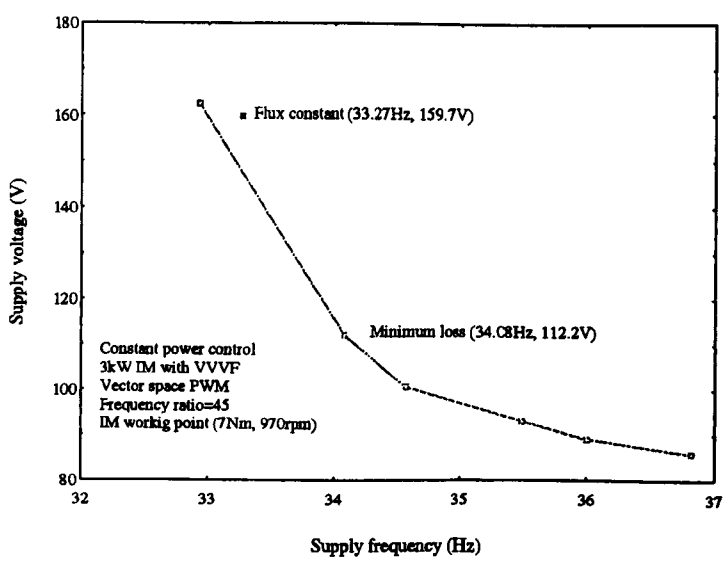

Fig 6.9 Measurement results under constant power control at 35% full load. The frequency ratio is 45. (c) The drive system power loss against machine supply voltage, (d) the drive system power loss against machine speed, (e) the combinations of supply voltage and frequency for minimum loss and for flux constant drive modes.

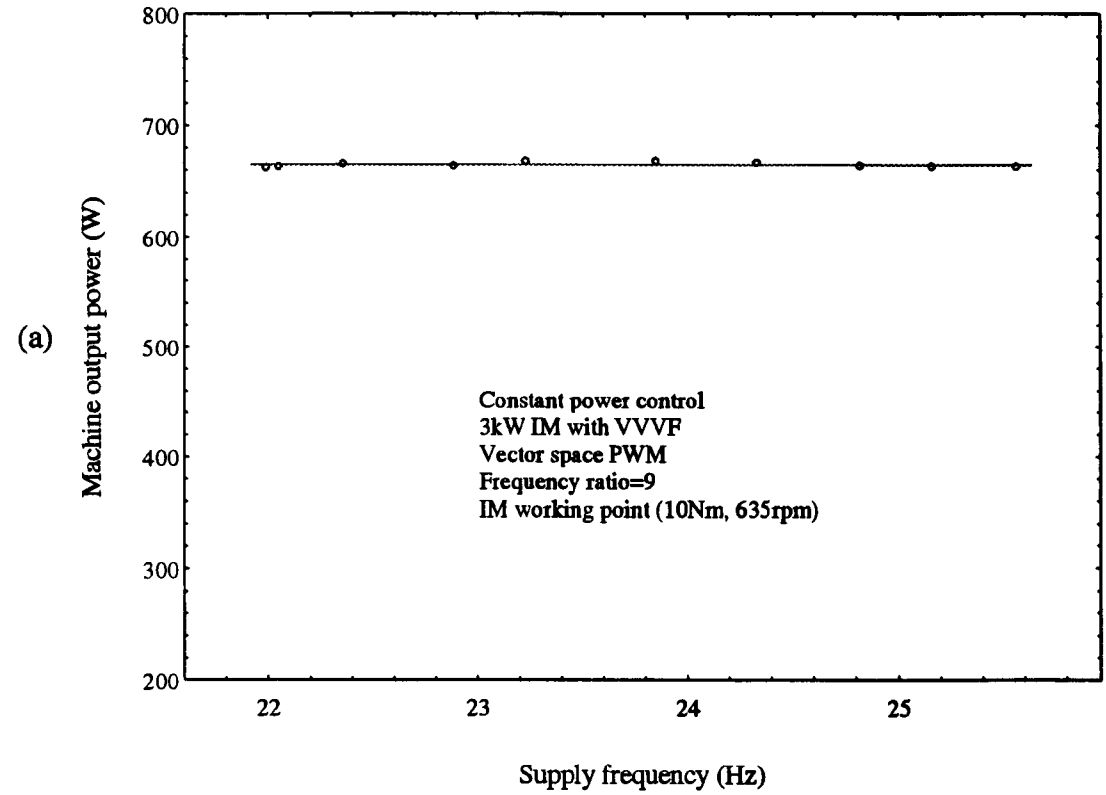

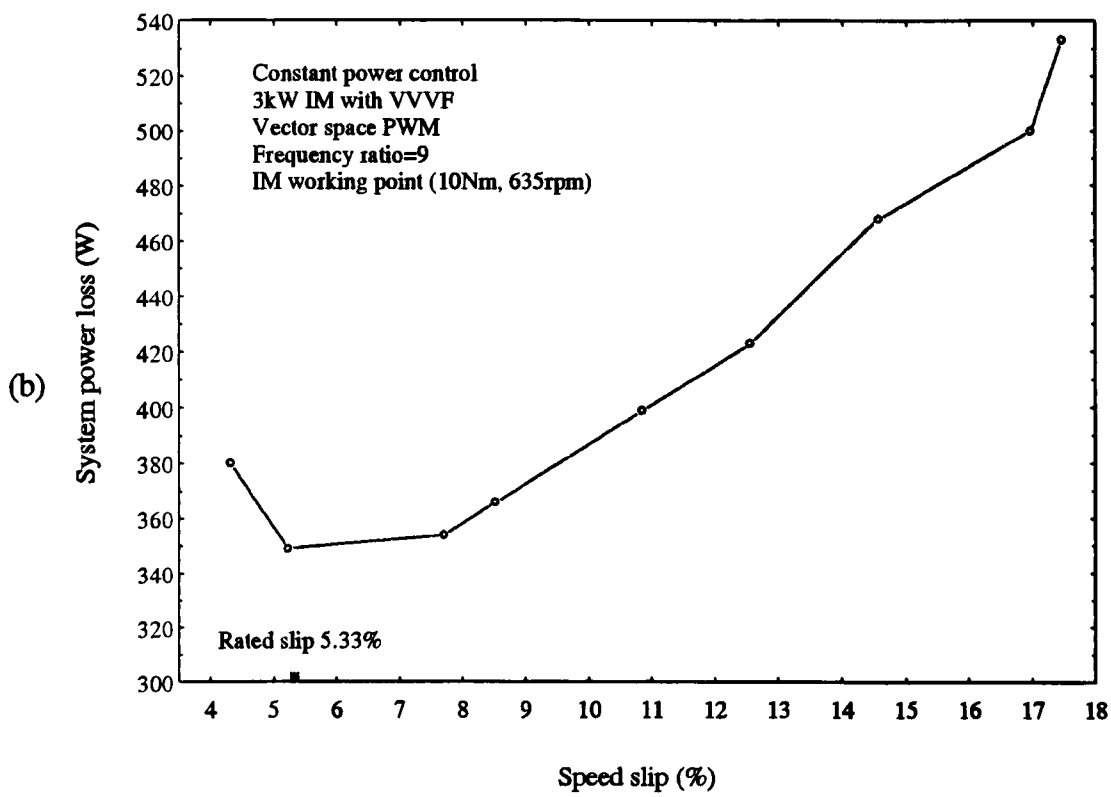

Fig 6.10 Measurement results under constant power control at 50% full load. The frequency ratio is 9. (a) Constant power control performance, (b) the drive system power loss against machine speed slip.

(c)

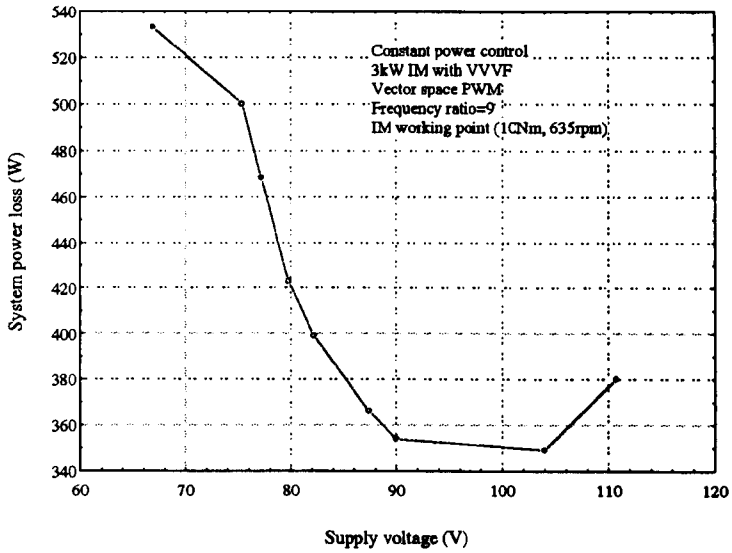

(d)

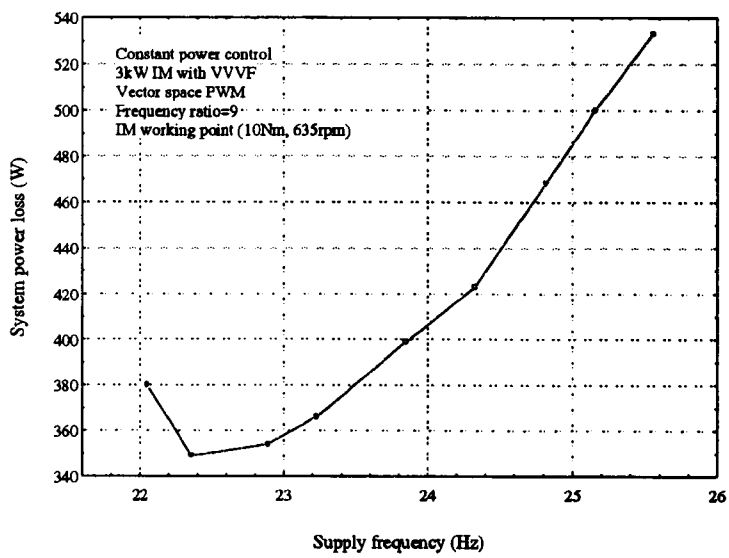

(e)

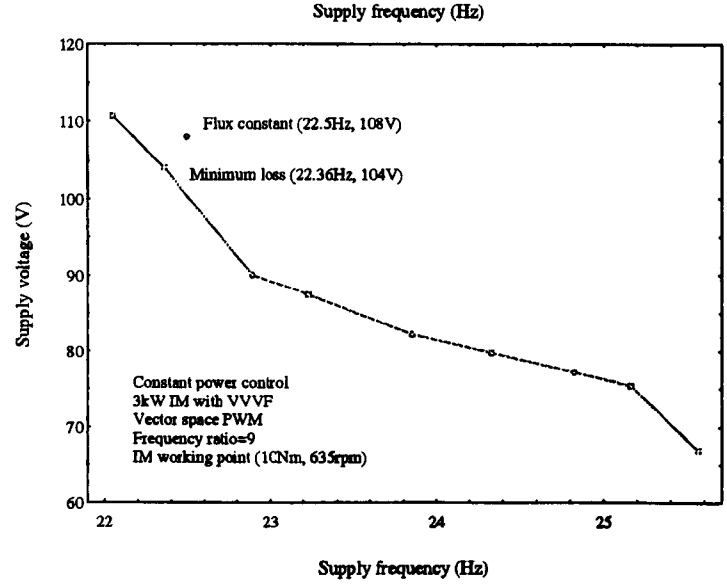

Fig 6.10 Measurement results under constant power control at 50% full load. The frequency ratio is 9. (c) The drive system power loss against machine supply voltage, (d) the drive system power loss against machine speed, (e) the combinations of supply voltage and frequency for minimum loss and for flux constant drive modes.

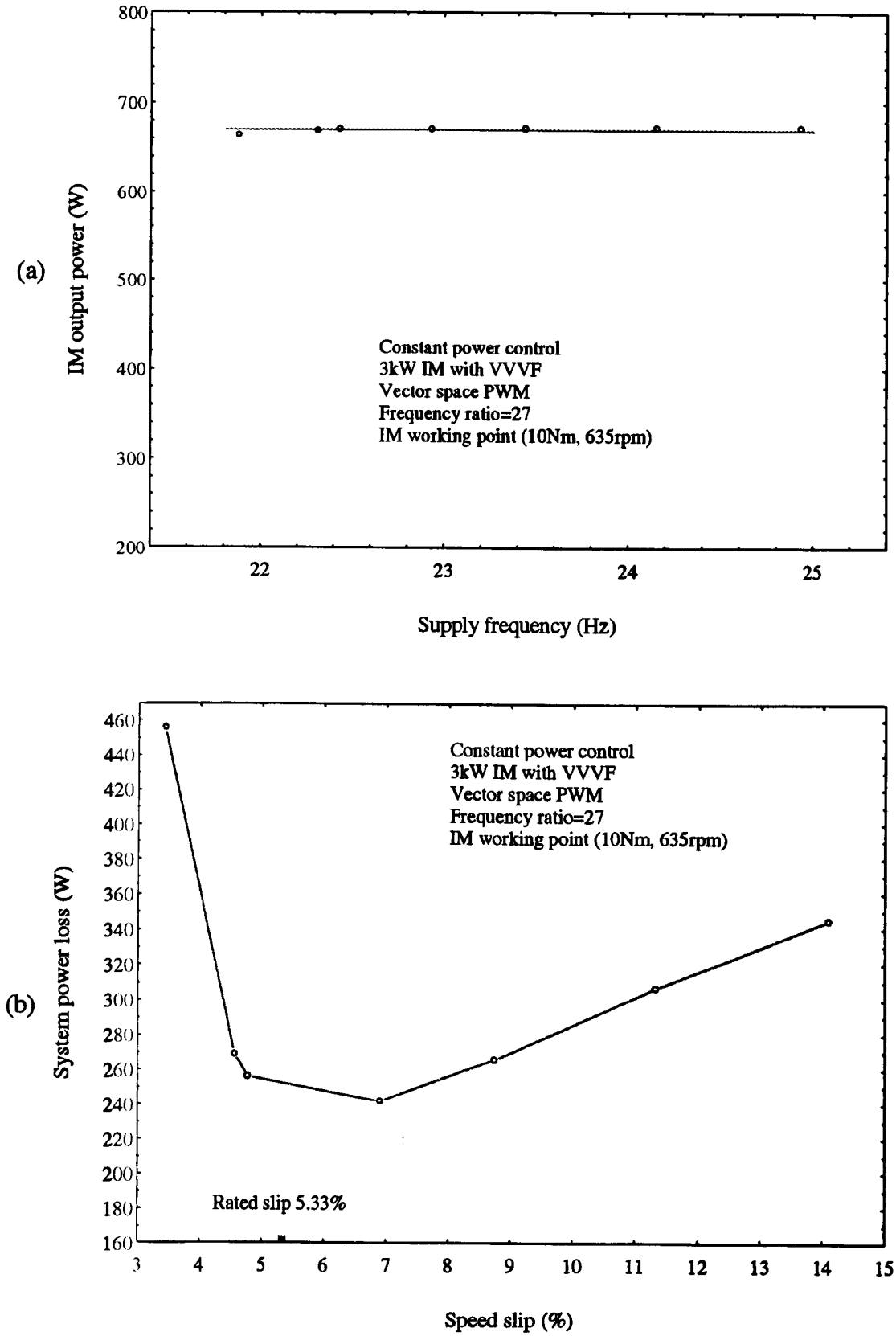

Fig 6.11 Measurement results under constant power control at 50% full load. The frequency ratio is 27. (a) Constant power control performance, (b) the drive system power loss against machine speed slip.

(c)

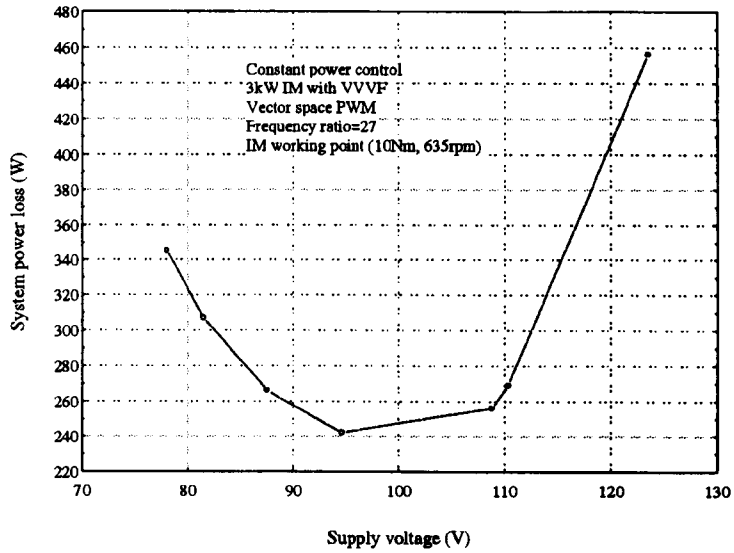

(d)

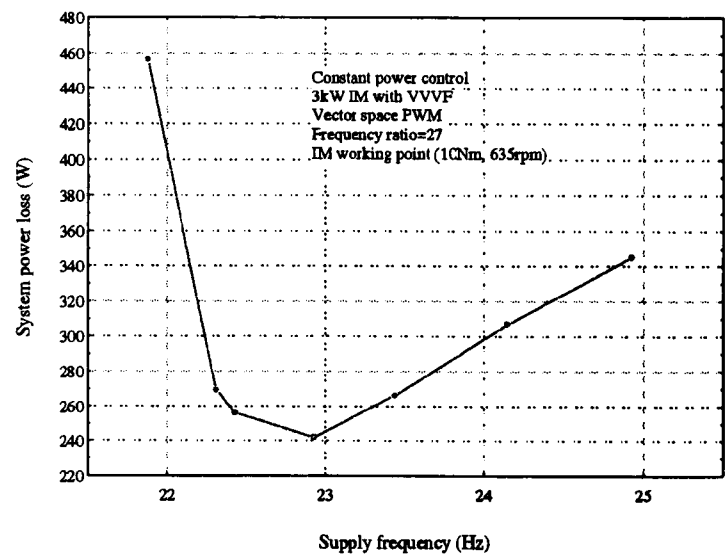

(e)

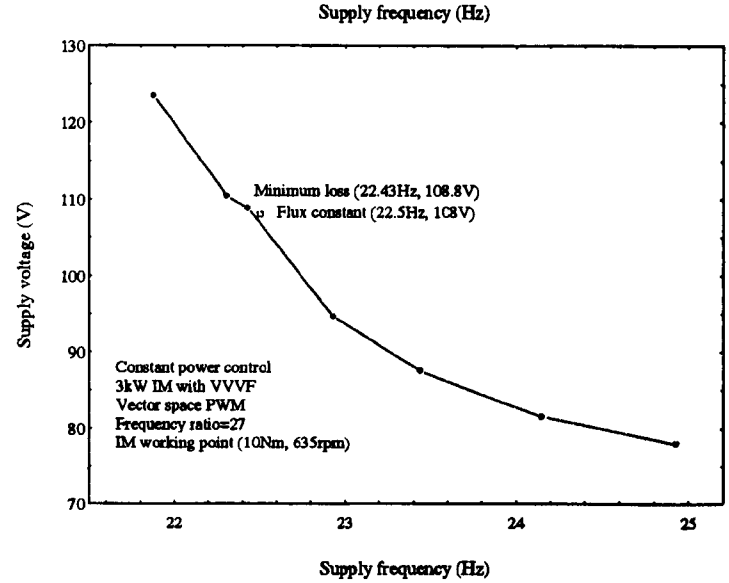

Fig 6.11 Measurement results under constant power control at 50% full load. The frequency ratio is 27. (c) The drive system power loss against machine supply voltage, (d) the drive system power loss against machine speed, (e) the combinations of supply voltage and frequency for minimum loss and for flux constant drive modes.

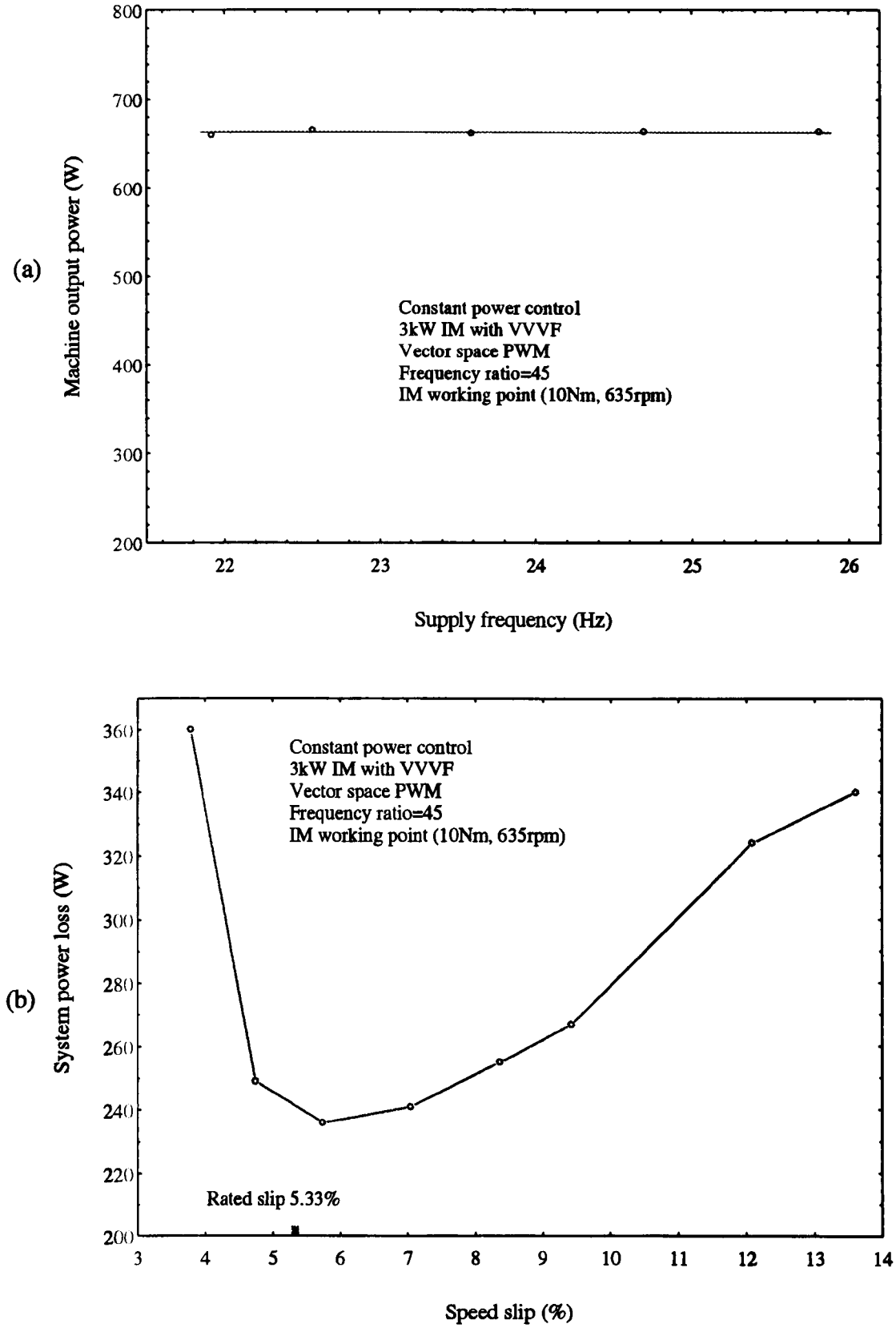

Fig 6.12 Measurement results under constant power control at 50% full load. The frequency ratio is 45. (a) Constant power control performance, (b) the drive system power loss against machine speed slip.

(c)

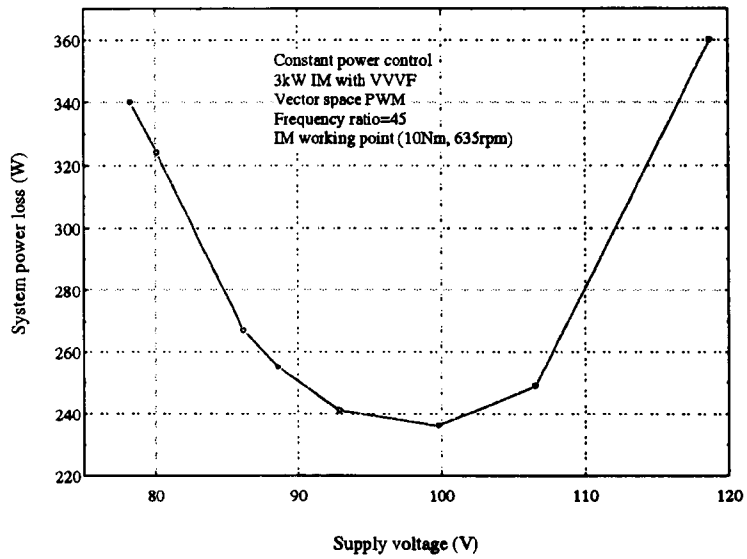

(d)

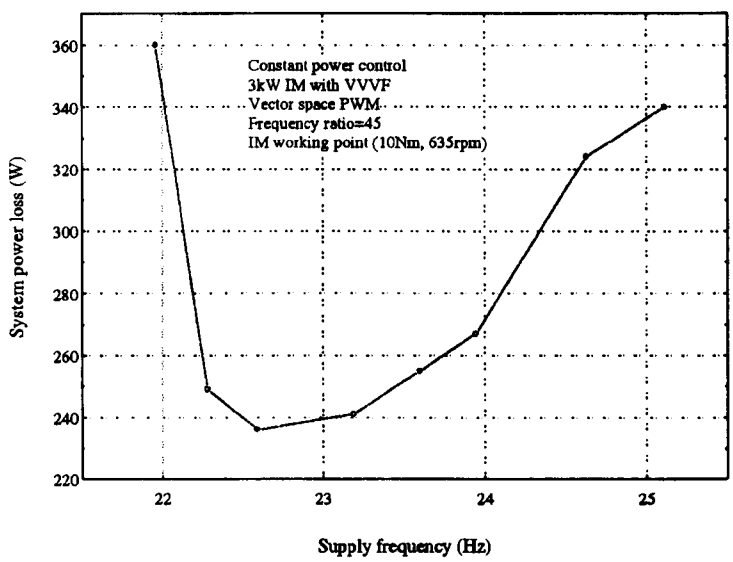

(e)

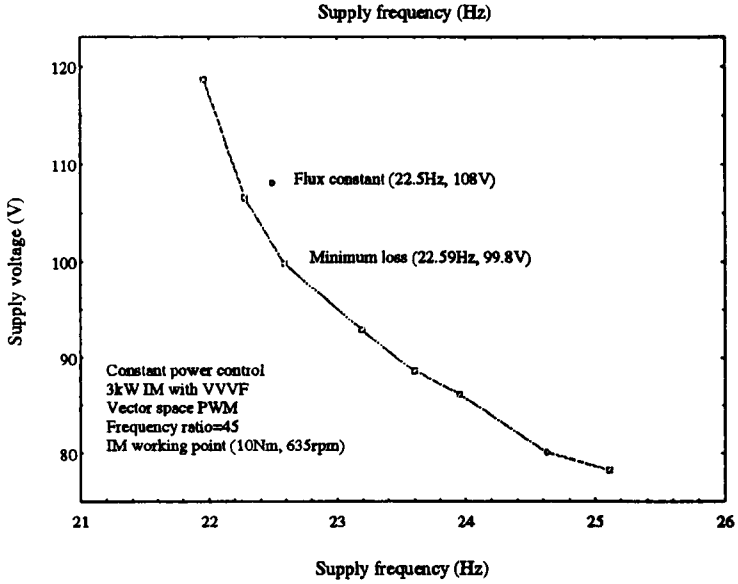

Fig 6.12 Measurement results under constant power control at 50% full load. The frequency ratio is 45. (c) The drive system power loss against machine supply voltage, (d) the drive system power loss against machine speed, (e) the combinations of supply voltage and frequency for minimum loss and for flux constant drive modes.

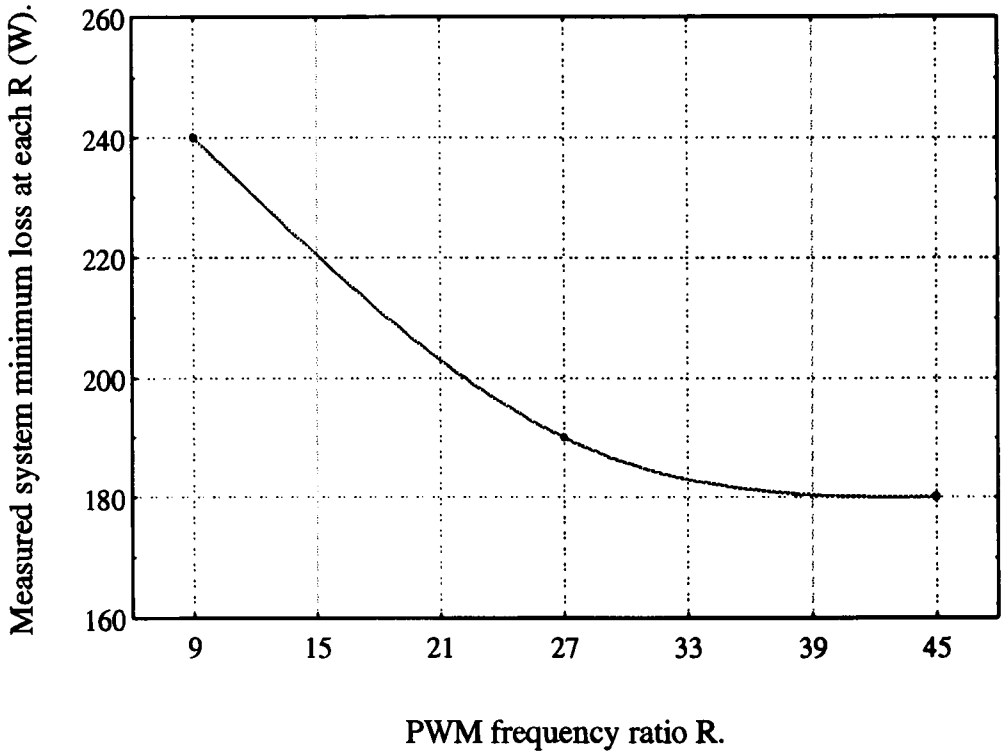

Fig. 6.13. Measured drive system minimium loss at different PWM frequency ratios. Machine operating point is (7Nm, 970rpm).

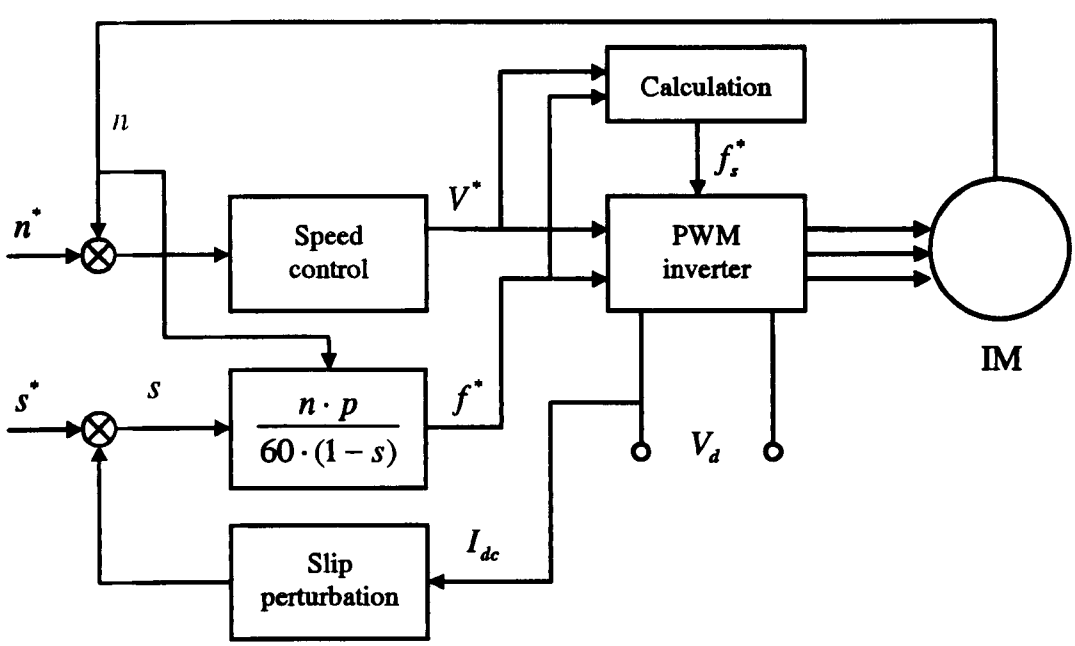

Fig. 6.14. A simple feedback drive system loss minimisation control scheme.

7. Case Study of the Loss Minimisation Control Strategy Applied to a Small Urban Electric Vehicle

The proposed feedforward loss minimisation control strategy will be applied to an electric vehicle drive for a typical urban travel. The adjustment of the control variables will be illustrated, in contrast to the selections in the conventional induction machine control, i.e. constant flux mode, and the potential energy saving will be demonstrated. Unfortunately, due to the unavailability of the 26kW drive system and a suitable dynamometer, the above investigations have been limited to a theoretical study.

7.1 Representative electric vehicle urban travel analysis

7.1.1 Fiat Elettra

The Fiat Elettra is a four seater electric vehicle derived from Fiat Cinquecento. Fig. 7.1 shows the general layout of the vehicle. The drive batteries are distributed along the vehicle floor pan. The traction motor and power converter are located at the rear, near the wheels. Some of the specifications of this vehicle are given in Table. 7.1.

Table 7. 1. Specifications of FIAT Cinqucento Elettra.

Gross vehicle weight	m	1420	kg
Overall gear ratio	n_g	7.3	
Wheel radius	r	0.256	m
Drag coefficient	C_d	0.315	
Rolling resistance coefficient	C_f	0.009	
Frontal area	A_f	1.75	m^2
Voltage of battery pack	V_d	216	V
Weight of drive battery		360	kg
Transmission efficiency	η	0.9	
Top speed		100	km/h
Acceleration time		0 to 50 km/h - 8s; 0 to 80 km/h - 15s	
Maximum incline		25	%

The battery pack is formed from 18, 12V 60Ah lead-acid monoblock which are linked in series to give a total battery voltage of 216V. The nominal stored energy of the battery is 13kWh and the total weight is about 400 kg. The 26kW induction machine drive described in the previous chapters has been designed for Fiat Elettra and was specified to have a performance which would enable the vehicle to have an acceleration from 0 to 50 km/h in 8 seconds, and a top speed of 100 km/h.

7.1.2 ECE15 driving cycle

Standard driving cycles are used to compare the performance of similar vehicles. In the case of electric vehicles, often driving cycles are used to determine the offline specifications of the traction system and to gauge the likely range of the vehicle for a particular mode of driving, viz. urban and suburban.

One of the standard driving cycles used in Europe is the ECE15 electric vehicle cycle, as shown in Fig. 7.2 [Ferraris 1995]. The cycle represents urban travel in a "stop-start" environment, with variable speed and variable acceleration/deceleration demands. Upon completion of each cycle the vehicle will have travelled 1.108 km at an average speed of 20 km/h.

7.1.3 Modelling of vehicle motion

Based on the driving cycle, i.e. ECE15, the required power and torque for the traction machine of the Fiat Cinqucento Elettra can be identified [Harson 1994].

The vehicle dynamics are expressed as,

$$\frac{dv}{dt} = \frac{1}{m}(F - F_d - F_r - F_g) \tag{7.1}$$

where,

F - the force produced by the vehicle

F_d - the force due to aerodynamic drag,

$$F_d = \frac{1}{2} \rho \, C_d A_f v^2 \tag{7.2}$$

F_r - the force due to the rolling resistance of the tyre,

$$F_r = C_f mg \cos(\theta) \cdot sgn(v) \tag{7.3}$$

F_g - the climbing force,

$$F_g = mg \sin(\theta) \tag{7.4}$$

mg is the weight of the vehicle, v is the velocity of the vehicle, θ is the vehicle incline, and ρ is the density of air ($\rho = 1.225\ kg\ m^{-3} = 12.017\ Nm^{-3}\ at\ 15^{o}\ C$).

The torque requirement on the motor, T_m, is therefore found using,

$$T_m = \frac{F}{\eta \, n_g} \cdot r \tag{7.5}$$

where r is the wheel radius, n_g is the overall gear ratio, and η is the gearbox transmission efficiency.

The required motor output power is,

$$P = T_m \cdot n_g \, \frac{v}{r} \tag{7.6}$$

Clearly the required machine torque and power are not only determined by the driving cycle but also the road inclination. For simplicity, only the case when the vehicle is running on a level road is considered, and the required traction motor torque and power for the ECE15 cycle are given in Fig 7.3 and Fig 7.4, respectively. It is observed that the power profile has a number of large peaks that last for a short periods of time, and that the torque varies over a wide range.

Often when a traction machine is designed, the maximum continuous torque required by the vehicle and the maximum speed that the vehicle has to achieve are considered as the main criteria [Schofield 1993b]. However, in the actual operation, the machine will have a highly variable load and speed, and the realisation of a high efficiency over the full operation range is important to electric vehicle drives.

7.2 Comparison of traction system efficiency under constant flux and loss minimisation controls

The losses in traction system of previously described electric vehicle driving the ECE15 urban cycle on a level road were calculated, firstly when the machine was controlled under conventional constant flux control, and then under the proposed loss minimum control strategy. The range of machine operating state is shown in Fig. 7.5.

7.2.1 Constant flux control

A converter switching frequency of 5kHz, has been used for the PWM drive. The machine air-gap flux was controlled at the rated level by setting V/f to be approximately constant. The calculated drive system losses when the vehicle was driving over an urban cycle, namely the machine fundamental copper loss, machine fundamental iron loss, machine harmonic losses, inverter conduction loss, inverter switching loss and the drive system total loss, are shown in Fig. 7.6 (a), (b) and (c). It is observed that the machine copper loss and iron loss are poorly balanced, especially when the speed and load are relatively low. Also, in some conditions the inverter switching loss is excessive in comparison with the machine harmonic loss.

7.2.2 Loss minimisation control

Under the proposed loss minimisation control strategy the optimised control variables, viz. machine voltage, machine frequency, and inverter switching frequency (or frequency ratio), are shown in Fig. 7.7 (a) and (b), respectively. It is observed that the machine voltage and frequency on longer have a constant linear relationship, and the resultant machine fundamental

copper loss, machine fundamental iron loss and inverter conduction loss, are in a better balance, as shown in Fig. 7.8 (a). The optimised inverter switching frequency is in a region of 2kHz, varying according to machine operating speed as well as load, and the corresponding frequency ratio can be as low as 1, 9 and 15. The balance of machine harmonic loss and inverter switching loss, is shown in Fig. 7.8 (b). The resultant drive system total loss is shown in Fig. 7.8 (c).

A comparison of the estimated losses in the drive system for the constant flux control and loss minimisation control, when the vehicle is driving over an urban cycle, is shown in Fig. 7.9. It is observed that there is a significant saving of energy in a wide machine operating range when the optimal control is applied. However, there are occasions when the total losses for the two controls are fairly close. This is because the machine is operating close to its rated state, which has been optimised for efficiency.

The potential energy saving and driving range extension by using the loss minimisation control in replacement of the constant flux control are given in Table 7.2.

Table 7.2 Energy saving and driving range extension by loss minimisation control

Total traction energy per cycle	234Wh
Loss per cycle under constant flux control	43Wh
Loss per cycle under loss minimisation control	29Wh
Energy saving per cycle	14Wh
Loss reduction	32%
Driving range extension	5.3%

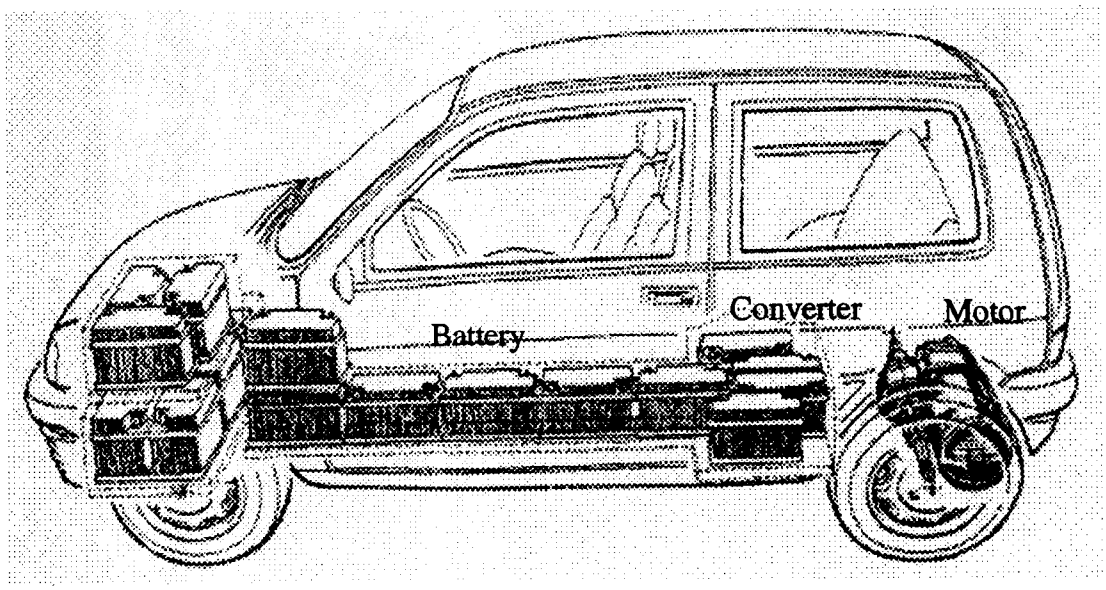

Fig. 7.1. General layout of Fiat Elettra vehicle.

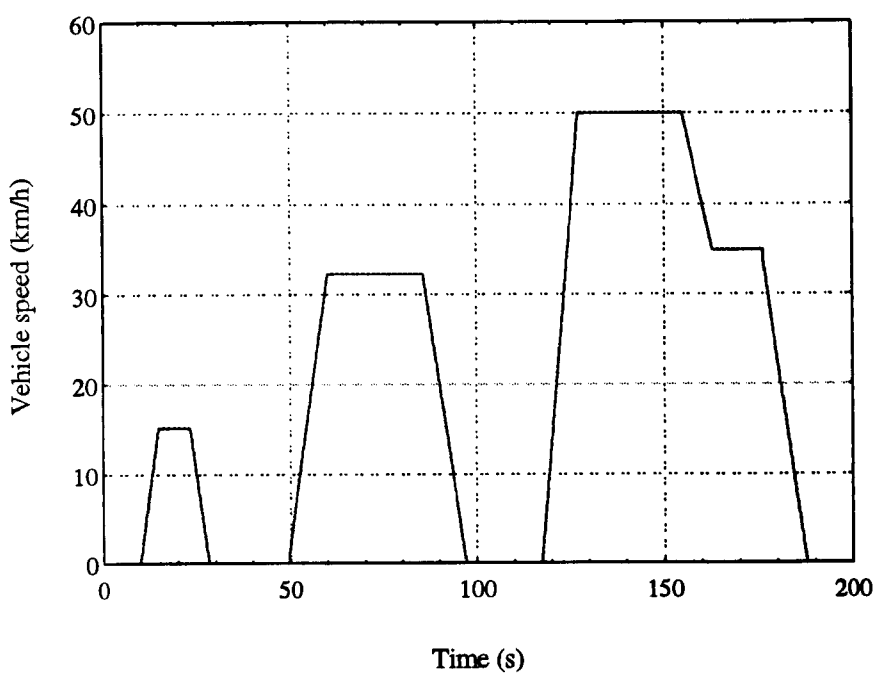

Fig 7.2 ECE15 urban driving cycle.

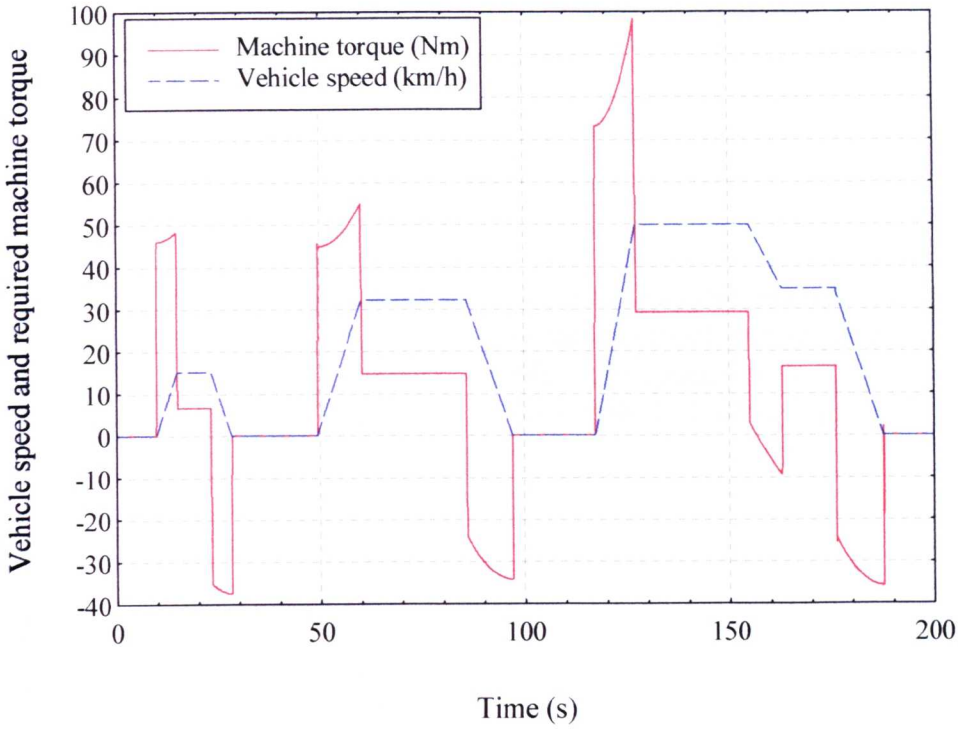

Fig. 7.3. Required machine torque for urban driving over ECE15 cycle.

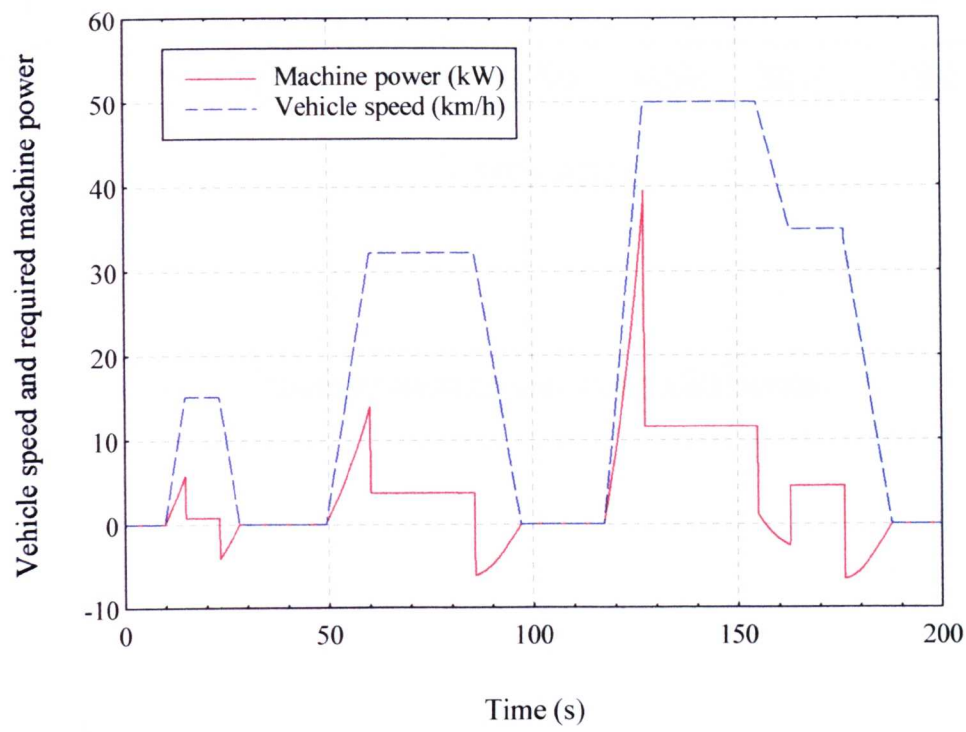

Fig. 7.4. Required machine power for urban driving over ECE15 cycle.

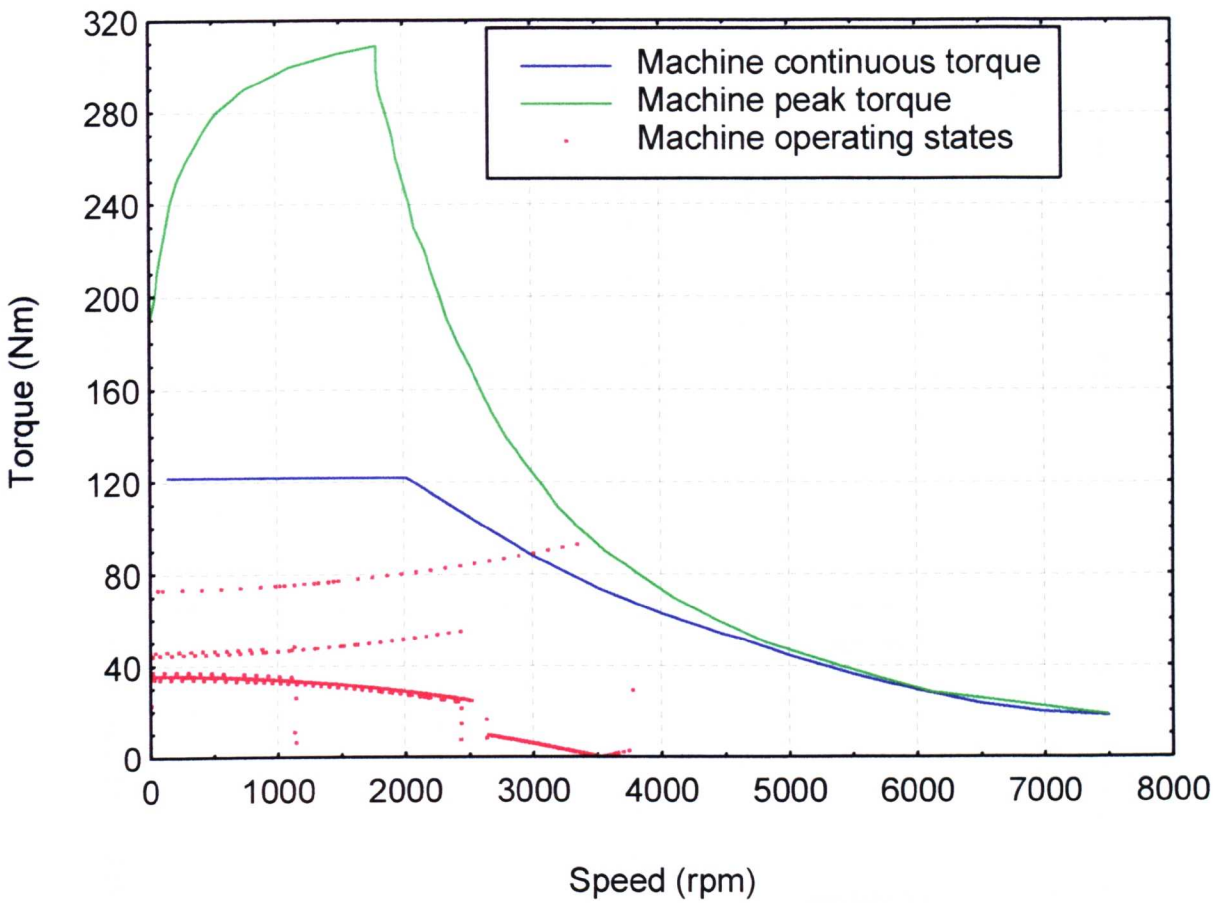

Fig. 7.5. Machine operating state over ECE15 cycle.

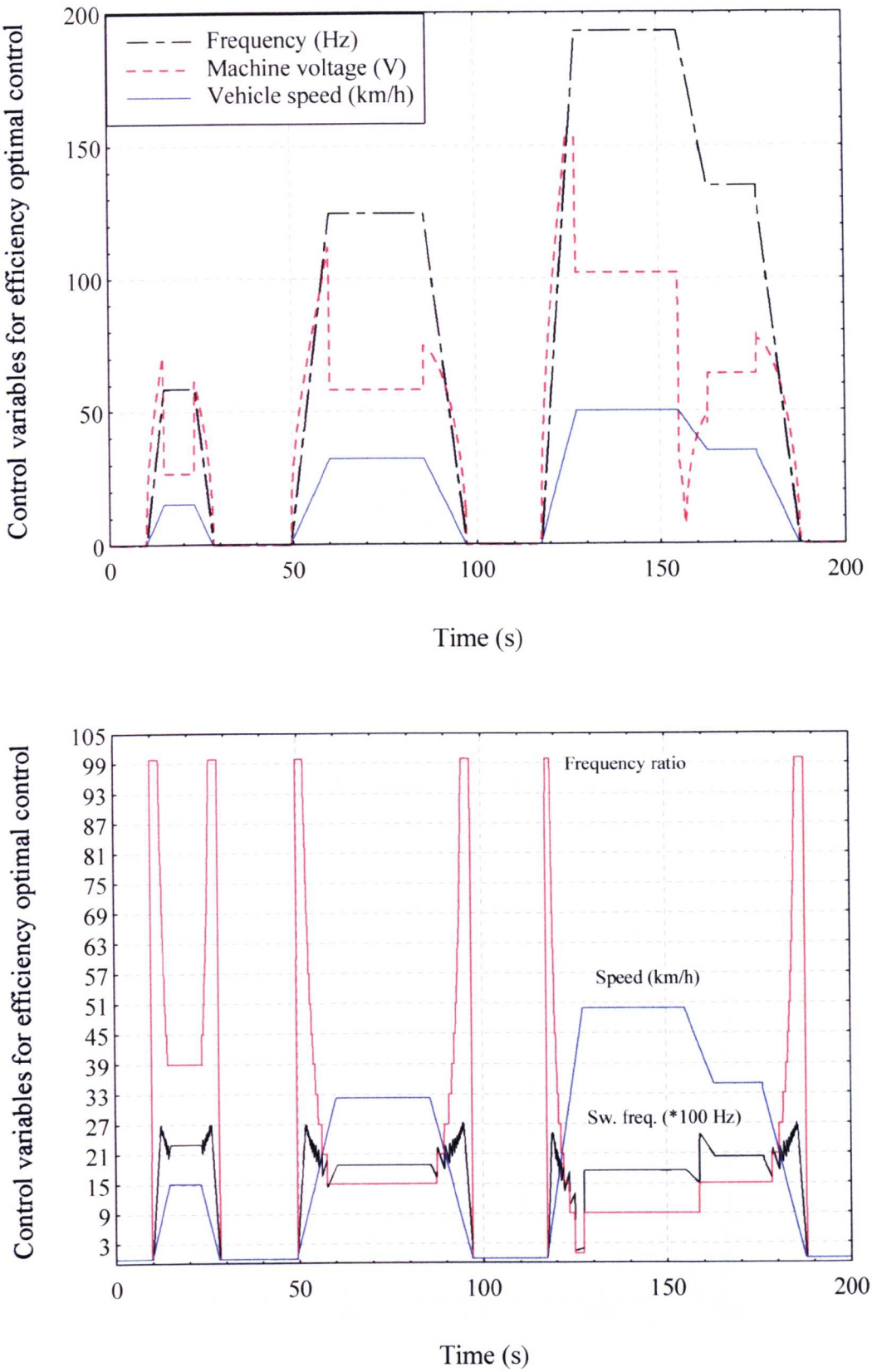

Fig. 7.6. Electric vehicle drive system energy efficiency optimal control variables, viz. machine supply voltage, machine supply frequency, inverter switching frequency (frequency ratio).

(a)

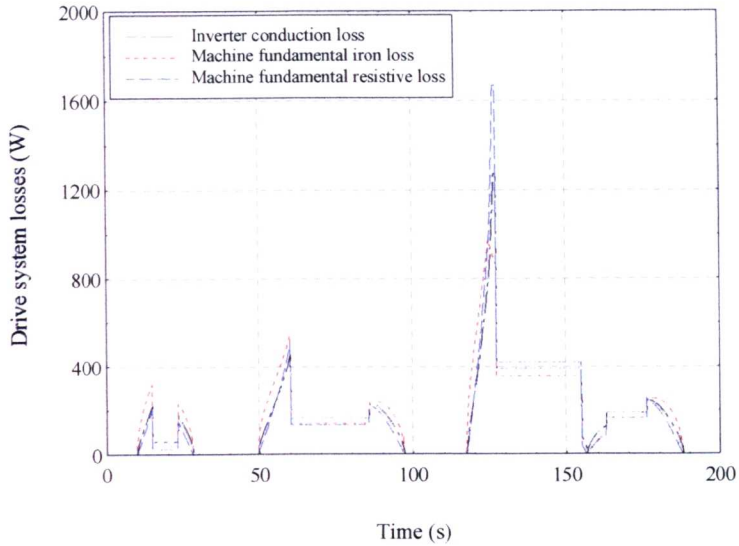

(b)

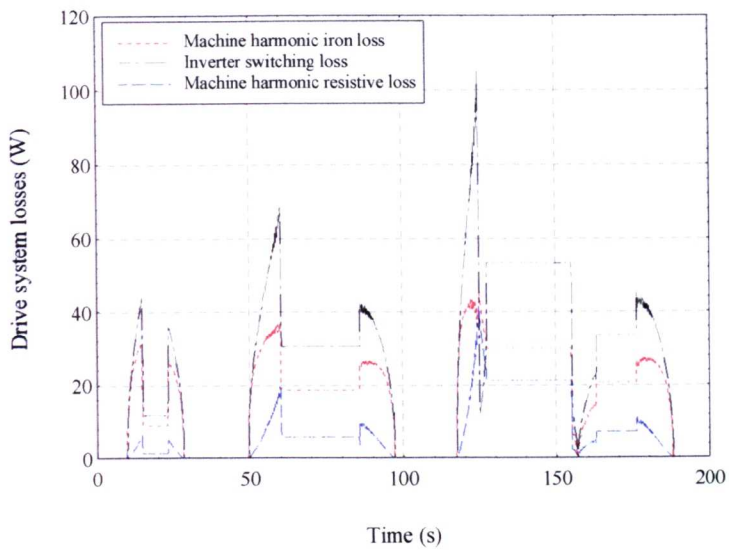

(c)

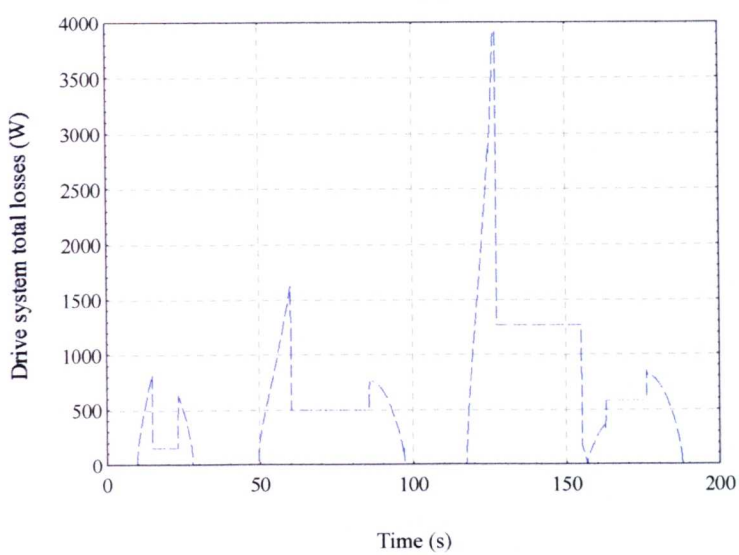

Fig. 7.7.Simulation of electric vehicle drive system losses when the energy efficiency optimal control is applied. (a) Machine fundamental resistive and iron losses, and inverter conduction loss. (b) Machine harmonic resistive and iron losses, and inverter switching loss. (c) Drive system total losses.

(a)

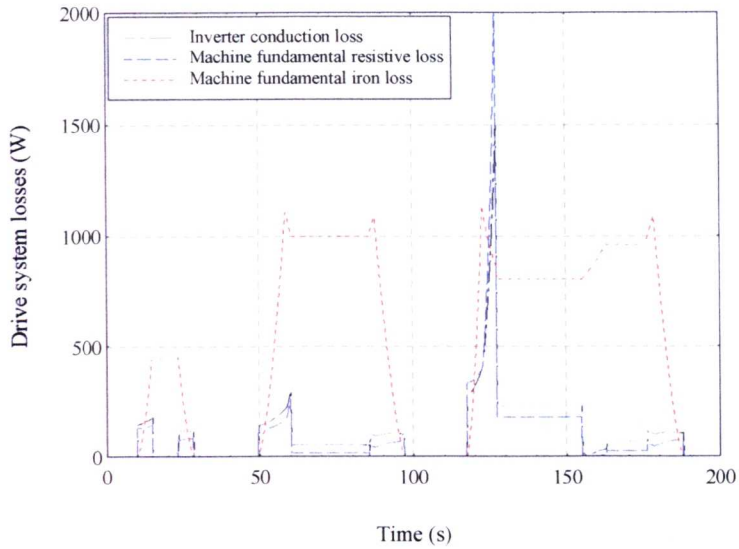

(b)

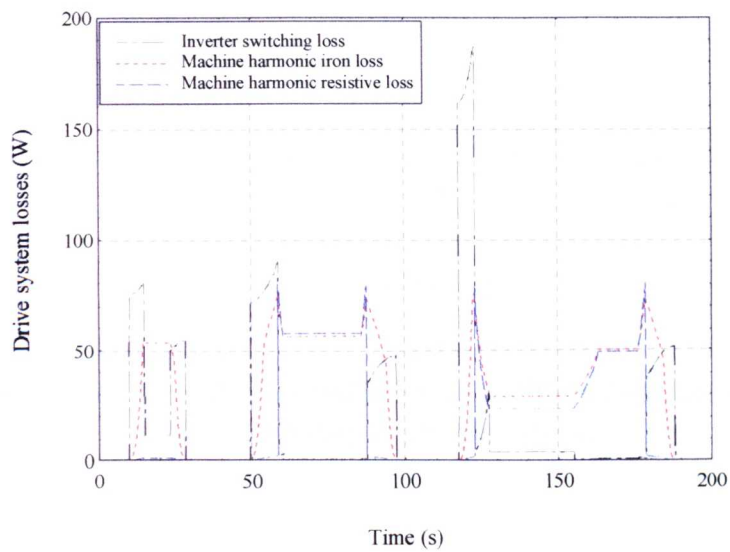

(c)

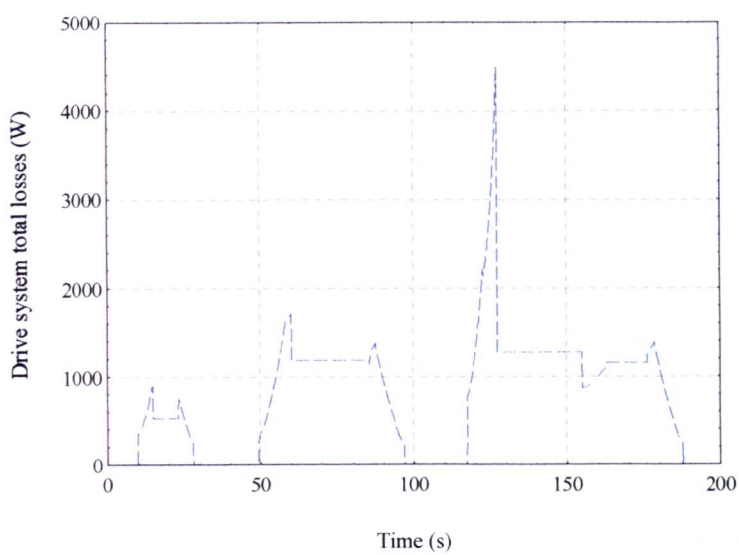

Fig. 7.8. Electric vehicle drive system losses when the constant flux control is applied. with 5kHz switching frequency. (a) Machine fundamental resistive and iron losses, and inverter conduction loss. (b) Machine harmonic resistive and iron losses, and inverter switching loss. (c) Drive system total losses.

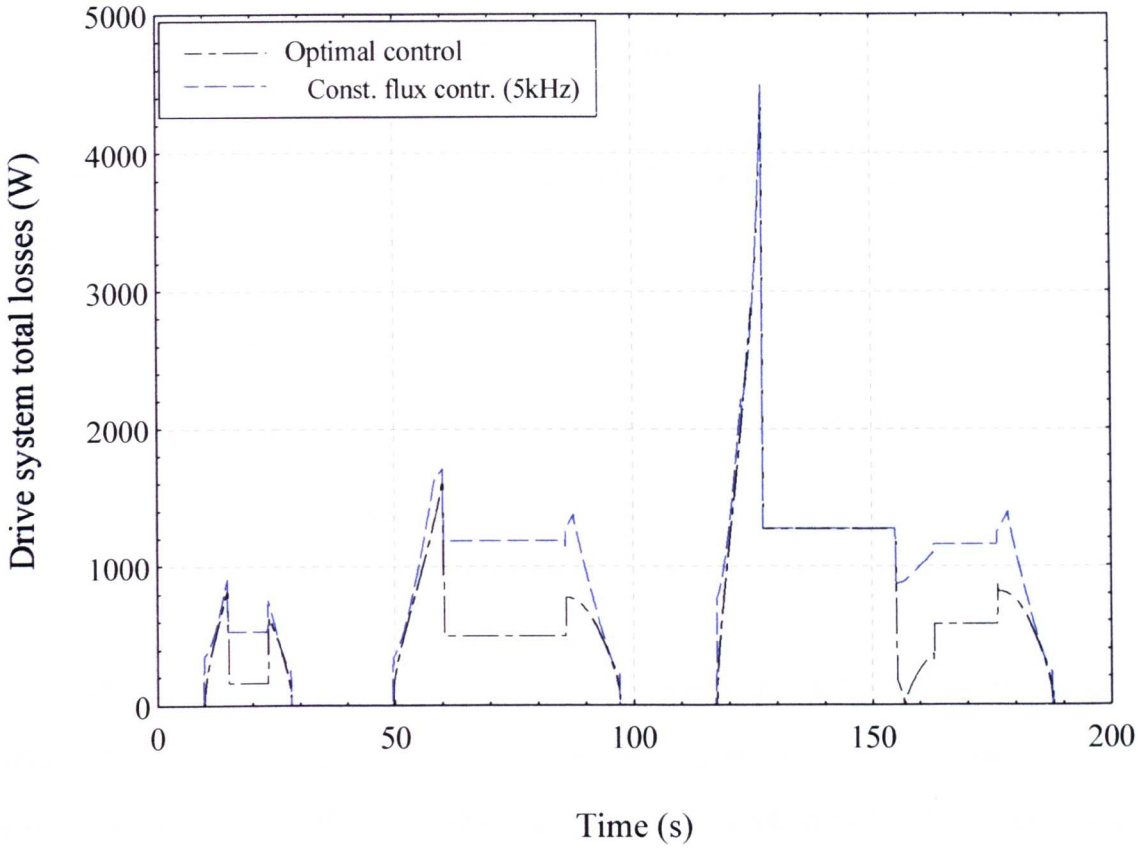

Fig. 7.9. Comparison of drive system losses between different control methods when the vehicle is driving in an urban cycle.

8. Conclusions

The thesis has presented an energy efficient control scheme for an electric vehicle drive system which features the following elements,

A 26kW high efficiency induction machine

A high efficiency hard-switched voltage source IGBT inverter

A gear changing, vector space pulse width modulator

A minimal loss controller

The 26kW induction motor was the subject of previous research and has been used in the thesis as being representative of a state of the art traction machine. The machine has been rated to be capable of propelling a small urban vehicle, similar to the Fiat Cinquecento, at a maximum speed of 100km/hr and with an acceleration of 0-50km/hr in 8 seconds.

Based on this traction motor and vehicle specification, the most appropriate combination of power electronic inverter, pulse width modulation switching strategy and overall drive system control have been researched, in order to achieve maximum efficiency from the drive system. High efficiency being an essential requirement of an electric vehicle drive train, in order to make maximum use of the limited energy storage capabilities in the battery.

8.1 Use of paralleled IGBTs to improve inverter efficiency

A soft-switched inverter will tend to have a lower efficiency than a comparable hard-switched inverter when the switching frequency is relatively low, say 1-5 kHz. This is due to the loss overhead within the additional resonant components being greater than the improvements in switching loss. In addition, a soft-switched inverter is much more complex in construction and control. As a result conventional six-switch full bridge hard-switched inverter topology is likely to give the best efficiency for an electric vehicle drive.

At the battery voltages typical of electric vehicles (216V in this case) the most suitable power semiconductor devices are IGBTs. In the design of an IGBT inverter, a careful selection of the power component ratings and parameters is necessary in order to minimise the conduction loss and switching loss when operating at an appropriate switching frequency. Observations from power component data sheets and experimental measurements have shown that the conduction voltage drop and switching times of an IGBT increases with conducting current. Thus, both the conduction loss and switching loss can be reduced by limiting the individual device maximum current by paralleling a number of IGBTs per switch. Paralleling devices can also bring other benefits to the system, as it allows smaller and cheaper components to be used, whilst increasing the power dissipation capability. The efficiency improvement through the use of paralleling IGBTs will diminish as more devices are used and a compromise will be reached when the increased cost and complexity outweighs the improved efficiency.

However, the advantages of IGBT paralleling operation can only be guaranteed if the current sharing among the paralleled devices is good. Experiments have shown that hard paralleled IGBTs will exhibit a good steady-state current sharing when placed in close thermal proximity on a common heatsink, and have a performance which compares favourably with paralleled MOSFETs. Since turn-off loss dominates in the IGBT switching loss, and the IGBT turn-off time is insensitive to the gate series resistance, it has been shown that the gate resistors can be used to match the switching characteristics of the paralleled IGBTs. A significant improvement of transient current sharing has been clearly shown by experiments through the use of properly selected gate resistances.

8.2 Influence of pulse-width-modulation (PWM) strategies on drive efficiency and performance

PWM methods can be classified into voltage controlled feedforward strategies and closed-loop current (flux, etc.) feedback methods such as hysteresis control. In electric vehicle applications where the requirements in terms of dynamic response are moderate, feedforward voltage

controlled PWM is preferred since the switching patterns for a given depth of modulation are predefined. This allows a more direct control of the harmonic content of output current waveform for a given inverter switching frequency.

The following seven different PWM strategies, together with the quasi-square wave switching scheme, have been considered in the thesis,

(a) Natural sampling. The traditional analogue method of implementing PWM where a sinusoidal modulating signal is compared against a triangular signal.

(b) Asymmetrical regular sampling PWM. The pulse widths are derived from sampled values of the sinusoidal modulating waveform. Each pulse edge is determined from a new sample thus requiring a sampling rate of twice the pulse frequency.

(c) Sub-optimal regular sampled PWM. Identical to asymmetrical regular sampling except a modulating waveform of a sine function plus 0.25 p.u. third harmonic is used.

(d) Adjustable PWM. An enhanced version of the regular sampling PWM which, through the use of an interpolative algorithm, allows the harmonic content of the PWM waveform to be varied.

(e) Vector space PWM. This method uses a rotating space vector representation of the required three phase voltages to decompose the output into three of eight possible inverter switching states. The durations of the selected states are determined using a voltage time integral invariant method, to get a circular rotating field for the machine.

(f) Optimal harmonic minimisation PWM. The positions of the switching edges of the pulse waveform are pre-calculated to give minimum harmonic distortion.

(g) Optimal harmonic elimination PWM. The positions of the switching edges of the pulse waveform are pre-calculated to eliminate certain number of selected harmonics.

Analysis of the voltage spectrums of the various PWM methods has highlighted that the harmonic magnitudes are effected not only by the amplitude but also the phase of the modulating signal. Whilst it is necessary to adjust the amplitude of the modulating wave to control the fundamental voltage, the phase can be used to control the PWM performance, i.e. the phase angle is selected to ensure a minimum harmonic distortion in the modulation process during the steady-state operation, or alternatively the phase angle is adjusted to maintain the output fundamental voltage and thus allow a smooth transition during changes in the switching frequency ratio. The effectiveness of this PWM performance control strategy by employing the modulating phase angle in a ratio change has been demonstrated by experiments on an inverter fed induction machine drive system, in which the fundamental voltage and frequency were unaffected by a sudden change in inverter switching frequency.

The influence of a particular PWM strategy on drive system efficiency was gauged through experiments on an inverter fed 3kW induction machine drive in the laboratory. The tests were based on the assumption that if the machine is operating at a fixed working point, the machine fundamental loss, inverter loss and mechanical loss will be unchanged, and when controlled under different PWM methods the difference in total drive system loss will reflect only the difference in the machine harmonic loss. The system loss was calculated from the difference of input and output powers and had an estimated accuracy of 4% of the total measurement loss, as confirmed by a more accurate calorimeter based loss measurement method. A study of the effect of the various PWM methods on machine harmonic loss has shown that the simple THD (total-harmonic-distortion) term is a valuable method for assessing the different PWM strategies.

The effects of the various PWM strategies on machine torque ripple have been experimentally investigated based on a simple measurement method of using the inverter d.c. link current spectrum distribution.

The various PWM methods have also been assessed in terms of their capability for voltage control, effect on the inverter loss, other harmonic effects in the machine such as acoustic noise, and ease of implementation. A comparison of the various PWM strategies against these performance indicators is given in Table. 8.1, where an index of "1-5" or "E" is used, with "5" being the best, and "E" representing an equal or almost equal rating between different PWM strategies.

Compared to the analogue circuit based natural PWM, digital PWM methods have better harmonic performance and capability of using the d.c. link voltage. The off-line optimal harmonic minimisation PWM has the lowest harmonic distortion, whilst the optimal harmonic elimination PWM is capable to eliminate several harmful harmonic components in the output, however, they both suffer from the complexity of pulse pattern generation and practical implementation. Among the on-line PWM methods, adjustable PWM gives the best harmonic performance such as reduced total harmonic distortion and eliminated low order harmonics, although it tends to take more execution time in a DSP. The vector space and sub-optimal PWM methods have almost identical harmonic performance, and both exhibit lower level of harmonic distortion than the regular sampling PWM and are capable to extend the linear modulation range by 15% above the d.c. link voltage. However, vector space PWM is more time and memory efficient in digital implementation, and additionally features the simplicity of realisation in a gear changing PWM modulator. All PWM strategies give similar performance in terms of inverter loss and machine acoustic noise.

Table 8.1 Assessment of PWM strategies

PWM	Voltage control		THD	Inverter loss	Machine harmonic loss	Machine torque ripple			Machine acoustic noise	Implementation	
	Range	Linearity				6th	12th	18th		Memory	Excu. time
Natural PWM	1.0	E	1	E	1	2	3	3	E	-	-
Regular PWM	1.0	E	2	E	2	3	3	3	E	4	3
Sub-optimal PWM	1.15	E	3	E	3	3	3	3	E	3	3
Adjustable PWM	1.15	E	4	E	4	4	3	3	E	3	2
Vector space PWM	1.15	E	3	E	3	3	3	3	E	5	4
Opt. har. elimination	1.27	E	1	E	1	5	1	4	E	1	5
Opt. har. minimisation	1.27	E	5	E	5	2	3	2	E	1	5

8.3 A digital PWM modulator

Of the many possible hardware formats that have been proposed to digitally implement feedforward PWM, the four-counter structure is the most widely accepted since it is able to achieve the required pulse accuracy whilst needing only a moderate amount of external hardware. In line with the current trends of digital system integration to minimise component count to reduce cost and to increase reliability, a customised digital PWM modulator has been developed based on two integrated circuits, a TPC1020A FPGA (Field Programmable Gate Array) and a TMS320E15 DSP (Digital Signal Processor) microcontroller. The modulator was capable of generating three phase PWM at inverter switching frequencies of up to 6kHz, with a resolution of approximately 0.01degrees for the pulse edges for a 50Hz fundamental.

The hardware of the modulator was designed to be able to accommodate all the PWM methods examined. An application program has been developed which allowed on-line selection of PWM method and the various PWM parameters such as switching frequency, depth of modulation and modulation wave phase, etc. In addition a dedicated program for vector space PWM has also been implemented, which features a simple and flexible gear changing algorithm.

The performance of the PWM modulator, with application of various PWM methods, has been evaluated experimentally on an inverter fed 3kW induction machine drive, under the conditions of no-load and 60% load. The performance of the modulator, as well as the inverter, have been demonstrated by comparisons of the ideal spectrum distributions of PWM processes with those measured at the modulator output, the inverter gate driver output, the inverter output and the machine phase current. The results indicated that the digital modulator introduces negligible addition distortion, whereas the inverter operation increases the waveform THD by 3% from the ideal, primarily as a result of a need to introduce a deadtime between the switching of the power semiconductors.

8.4 PWM inverter induction machine drive loss minimisation control strategy

A total system loss model has been developed based on three system control variables: machine supply voltage, machine supply frequency and inverter switching frequency. The model was then applied to determine the optimum values of these three control variables that would give minimum system loss at a particular machine operating point. For real time implementation, the control strategy has been simplified by combining the system loss minimisation procedure with some engineering approximations. The control strategy has been verified by experiments on 3kW induction machine drive system, where the theoretically and experimentally obtained three control variables were in a good agreement.

Finally the minimum loss control has been applied to the representative 26kW electric vehicle traction drive to demonstrate the benefits of employing the technique.

8.4.1 Induction machine loss model

The methodology proposed by [Buck 1984] has been employed to provide a model of the loss in an induction motor. In the method the machine fundamental copper loss and iron loss at variable speed and variable load are calculated based on the machine nominal loss at the rated condition. The machine nominal loss is also used for machine harmonic loss calculations, where from a knowledge of spectrum distribution of the inverter output voltage, the harmonic loss is obtained by superposition of losses produced by separate harmonics. Skin and leakage effects are included in the model based on empirical data, the machine power rating and geometry.

Since the inverter output pulse pattern is determined by the modulation process only, two terms, total-harmonic-distortion (THD) and iron loss related total-harmonic-distortion (THDI), have been introduced to model the machine total harmonic copper loss and iron loss, which can be expressed as a function of the modulation depth and frequency ratio for a particular PWM strategy.

The machine harmonic loss model has been verified indirectly by comparing the calculated and measured machine harmonic loss on a laboratory 3kW induction machine drive.

8.4.2 Inverter loss model

The conduction loss in a converter can be simply determined from the semiconductor saturation characteristics, the supply voltage and output current. However, the modelling of switching loss is a much more complex process, because of the dependency of switching characteristics on the circuit layout and control. Instead of modelling individually the switching-on and -off losses on the individual IGBTs and anti-parallel diodes, an IGBT and diode pair per pulse model has been considered, and for this a simple experimental scheme has been proposed to determine the coefficients in the model. It has been observed from both analysis and experiments that an IGBT inverter loss has a quadratic relationship with conducting current, a linear relationship with d.c. link voltage and a linear relationship with switching frequency. This switching loss model has been validated by experiments, and gave a more accurate loss prediction than a previously published loss model [Casanellas 1994], i.e. within 10% of measured loss compared to 30% in the case of an H-bridge operating at 120V d.c. link voltage, 45A conducting current and 10kHz switching frequency.

8.4.3 The necessity of relatively low switching frequency

Whilst high PWM frequency ratio is beneficial to the machine because of the reduced harmonic effect, it will result in a higher switching loss in the inverter. A simulation using the parameters of the 26kW inverter fed induction traction drive has shown that, at the rated load, the optimum inverter switching frequency for the lowest machine harmonic loss and inverter switching loss varied with machine speed, and is in the range of 1~2kHz. The relative increase and decrease, or vice versa, of the machine harmonic loss and inverter switching loss, has also been clearly shown by the experiments on a constant torque controlled 3kW induction machine, when the frequency ratio was adjusted. For example, at 75% of the full load, the optimal inverter switching frequency ratio was around 45.

8.4.4 The necessity of reduced flux operation

The electric and magnetic loadings of an induction machine are usually chosen to give the highest efficiency at close to the maximum rated working point. However, the balance of electric and magnetic losses may not be ideal in the case of operations at variable speeds and variable loads. For example, at light loads it will be beneficial to reduce the air-gap flux to lower iron loss with corresponding increase in copper loss, so as to get an improved overall efficiency. The optimal induction motor operation modes were investigated using a test method, which allowed the supply voltage and frequency to be varied whilst the machine output power was maintained at the pre-specified working point. A typical test result with a 3kW inverter fed induction machine drive showed that at a partial load of 35% and a frequency ratio of 45, the system efficiency can be improved by 9% by reducing the flux below the rated value.

It has also been observed that varying the supply harmonic content by adjusting the inverter switching frequency ratio has a limited influence on the optimal flux level. A machine operating with reduced flux is also less noisy.

8.4.5 Loss minimisation control applied to an electric vehicle drive

The benefits of proposed energy efficient control strategy was simulated based on a 26kW induction motor traction drive fitted to a Fiat Cinqucento Elettra driving through an ECE15 cycle. For comparison, the performance of the traction system was also simulated under the conventional rated machine flux control and a fixed inverter switching frequency of 5kHz. From the derived machine required power and torque, it was found that for the majority of the time, the machine is operating at partial load. The optimal loss control achieved a much better balance of the losses, and better overall efficiency compared with the conventional constant flux control. The calculated optimal switching frequency had a mean of around 2kHz, fluctuating according to the machine working conditions, with occasionally the inverter reverting to quasi-square control. The results indicated that over the ECE15 cycle, the traction

system loss would be reduced by 30% and the driving range can be extended by over 5% if the loss minimisation control was used instead of the conventional constant flux and fixed switching frequency control.

8.5 Future work

Further experiments are required on a high power electric vehicle drive system, to validate the necessity of using relatively low switching frequency and to verify the loss model and the system loss minimisation strategy. To improve the dynamic performance of the drive system, the loss minimisation process may be incorporated with a feedback control to obtain an energy efficient direct torque control. This would form the basis of an energy efficient controller dedicated to electric vehicle applications.

Typically an induction machine is designed, such that it has the highest efficiency at close to the maximum rated working point. However, in applications such as electric vehicles, it may be more appropriate to design a machine which has maximum efficiency at part load working point. The resultant machine may be smaller in size and weight, although it must be capable of withstanding short periods of overload. A much lower value of rotor resistance is tolerable in an adjustable frequency drive, as high torques can be obtained very easily by reducing the excitation frequency to a low value when starting the drive. Design changes in this area would lead to reductions in the harmonic losses and indeed the fundamental 'slip losses' could also be reduced. Besides the design factors of electric and magnetic loadings, the effect of harmonic content in the converter supply should be considered in the machine design stage. For example, the stator might be improved by using thinner laminations and "litz" type windings distributed throughout a larger number of shallower slots, along with a high grade of insulation.

References

Adcock P L, et. al (1995). "How beneficial are EVs to the environment?". Electric & Hybrid Vehicle Technology '95. pp 232-237.

Ahmed M M, et. al. (1986). "Electrical instability in a voltage source inverter-fed induction motor drive at constant speed". IEE-B, 133(4). pp. 299-307.

ALABC (1995). "A new generation in lead-acid". Electric & Hybrid Vehicle Technology '95. pp. 81-84.

Alger P L (1970). "The nature of induction machines". Gordon & Breach.

Antably A and Klemen D (1995). "Wheel drivemotors for electric and hybrid electric bus applications". CICEM'95, HangZhou, China. pp. 956-960.

Baker K (1997). "Waiting for the revolution". Electric & Hybrid Vehicle Technology '97. pp. 10-17.

Belmans R M, et.al (1987). "Analysis of the audible noise of three-phase squirrel-cage induction motors supplied by inverters" IEEE Trans. on Industry Applications. IA-23(5). pp. 842-847.

Bitsche O (1994). "Fully integrated electric vehicle control unit". EVS-12, Dec.5-7, California, USA.

Black R S (1953). "Modulation theory", Van Nostrand. pp.266-276.

Boglietti A, et al (1994a). "Induction motor design criteria for traction application". ICEMA'94. pp. 543-548.

Boglietti A (1994b). "PWM inverter fed induction motors losses evaluation". Electric Machines and Power Systems, 22. pp. 439-449.

Boholo B, et. al (1994). "An automated calorimetric method of loss measurement in electrical machines". Journal of Magnetism and Magnetic Materials, Vol. 133. pp. 433-436.

Boholo B (1997). "Accurate measurement and prediction of iron losses in three-phase cage induction motors". PhD thesis. University of Sheffield.

Bonino M and Brusaglino G (1995). "Traction system management strategies for FIAT's electric vehicles". EVT'95, Paris. pp. 494-507.

Bose B K and Szczesny P M (1988). "A microcomputer-based control and simulation of an advanced IPM synchronous machine drive system for electric vehicle propulsion". IEEE Trans. Industrial Electronics, 35(4). pp 547-558.

Bose B K (1990). "An adaptive hysteresis-band current control technique of a voltage-fed PWM inverter for machine drive system". IEEE Trans. on Industrial Electronics, 37(5). pp. 402-408.

Bowes S R (1975a). "New sinusoidal pulse-width-modulated inverter". IEE Proc. 122(11). pp. 1279-1285.

Bowes S R and Bird B M (1975b). "Novel approach to the analysis and synthesis of modulation processes in power convertors". Proc. IEE, 122(5). pp. 507-512.

Bowes S R, et. al. (1982). "Transient performance of inverter systems". IEE-B, 129(6). pp.301-314.

Bowes S R and Midoun A (1985). "Suboptimal switching strategies for microprocessor-controlled PWM inverter drives". IEE Proc. B. 132(3). pp. 133-148.

Bowes S R and Midoun A (1986). "A new PWM switching strategy for microprocessor-controlled inverter drives". IEE Proc. B. 133(4). pp. 237-254.

Bowes S R and Clark P R (1992). "Transputer-based optimal PWM control of inverter drives". IEEE-IA, 28(1). pp. 81-88.

Bowes S R (1994). "Novel real-time harmonic minimised PWM control for drives and static power converters". IEEE Trans. on Power Electronics, 9(3). pp. 256-262.

Boys J T and Walton S J (1985). "A loss minimised sinusoidal PWM inverter". IEE Proc. B. 132(5). pp 260-268.

Boys J T and Walton S J (1988). "Scalar control: an alternative AC drive philosophy". IEE Proc. B. 135(3). pp. 151-158.

Boys J T and Handley P G (1990). "Harmonic analysis of space vector modulated PWM waveforms". IEE Proc. B. 137(4). pp 197-204.

Boys J T and Handley P G (1992). "Spread spectrum switching: low noise modulation technique for PWM inverter drives". IEE Proc. B. 139(3). pp. 252-260.

Boys J T and Miles M J (1994). "Empirical thermal model for inverter-driven cage induction machines". IEE Proc. B. 141(6). pp. 360-372.

Broeck V D, et.al (1986). "Analysis and realisation of a pulsewidth modulation based voltage space vectors". IEEE-IAS Ann. Mtg. 1986, pp244-251. Also, IEEE Trans. IA-24(1), 1988 . pp. 142-150.

Broeck V D (1992). "Analysis of the voltage harmonics of PWM voltage fed inverters using high switching frequencies and different modulation functions". European Trans. on Electrical Power Eng. 2(6). pp. 341-350.

Buck F G De (1979). "Losses and parasitic torques in electric motors subjected to PWM waveforms". IEEE Trans. IA-15(1).

Buck F D, Gistelinck P and Backer D D (1983). "Loss-optimal PWM waveforms for variable-speed induction-motor drives". IEE Proc. B. 130(5). pp. 310-319.

Buck F D, Gistelinck P and Backer D D (1984). "A simple but reliable loss model for inverter-supplied induction motors". IEEE Trans. on Industry Applications. 20(1). pp. 190-202.

Buckley G W (1995). "Making the switch". Electric & Hybrid Vehicle Technology '95. pp. 162-165.

Buja G B and Indri G B (1977). " Optimal pulse-width-modulation for feeding AC motors". IEEE Trans. Industry Applications, Vol. IA-13, 1977. pp. 38-44.

Butler O I and Birch T S (1971). "Comparison of alternative skew-effect parameters of cage induction motors". Proc. Inst. Elec. Eng. Vol. 118. pp. 879-883.

Cade M (1994). "Improvement of induction machine stability by modulation techniques". IEE Proc. Electr. Appl. 141(6). pp. 347-352.

Casadei D, Serra G and Tani A (1995). "Direct flux and torque control of induction machine for electric vehicle applications". IEE Conf. Pub. No 412, Proc. EMD, 11-13 September. pp 349-353.

Casanellas F (1994). "Losses in PWM inverters using IGBTs". IEE Proc. B 141(5). pp. 235-239.

Casanellas F (1995). "Correspondence: losses in PWM inverters using IGBTs". IEE Proc. B 142(4). pp. 285-288.

Chalmers B J (1965). "Electromagnetic problems of A.C. machines". Chapman and Hall Ltd.

Chalmers B J and Sarkar B R (1968). "Induction-motor losses due to nonsinusoidal supply waveforms". IEE Proc. 115(12). pp. 1777-1782.

Chang L C (1993). "Recent developments of electric vehicles and their propulsion systems". IEEE Aerospace and Electronic Systems Magazine. 8(12). pp 3-6.

Chang L C (1994). "Comparison of AC drives for electric vehicles - a report on experts' opinion survey". IEEE Aerospace Electronic and Systems Magazine. 9(4). pp. 7-11.

Chen C C and Chau K T (1993). "A new PWM algorithm for battery-source three-phase inverters". Electric Machines and Power Systems. Vol. 20. 1993. pp. 43-54.

Chen C C and Chau K T (1995). "Challenges of electric vehicle technology". CICEM'95, HangZhou, China. pp. 34-41.

Chen C C, et. al (1997). "Soft switching inverters in electric vehicles". EVS-14, Dec. 15-17, 1997, Orlando, Florida USA.

Chen C C (1998). "Electric vehicle development strategy and key technology - an overview".

Chen S and Yeh S N (1992). "Optimal efficiency analysis of induction motors fed by variable-voltage and variable-frequency source". IEEE Trans. on Energy Conversion. 7(3). pp. 537-543.

Chokhawala R S, Catt J and Pelly B R (1995). "Gate drive considerations for IGBT modules". IEEE Trans. on Industry Applications. 31(3). pp. 603-611.

Famouri P and Cathey J J (1991). "Loss minimisation control of an induction motor drive". IEEE Trans. on Industry Applications. 27(1). pp. 32-37.

Ferraris P, et. al. (1995). "New design of high performance induction motor drive train for European city-car". EVT'95, Paris. pp. 447-456.

Farnell (1990). Instruction and service manual for AP series 500W systems power supplies. Farnell, 1990.

Garcia G O and Mendes J C, et.al (1994). "An efficient controller for an adjustable speed induction motor drive". IEEE Trans. on Industry Applications. 41(5). pp. 533-539.

Garcia-Otero S and Devaney M (1994). "Minimisation of acoustic noise in variable speed induction motors using a modified PWM drive". IEEE Trans. on Industry Applications. 30(1). pp. 111-115.

Gosden D F. "Which motor for an EV drive - induction or PM AC?". Inter. Conf. on Electrical Machines. Australia. Vol. 2, pp. 279-284.

Grant D A and Seidner R (1981). "Ratio changing in pulse-width-modulated inverters". IEE Proc. B. 128(5). pp 243-248.

Green R M and Boys J T (1982). "Inverter AC-drive efficiency". IEE Proc. B. 129(2). pp. 75-81.

Grudkowski T W and Polly E C (1995). "Advanced flywheel technology". Electric & Hybrid Vehicle Technology'95. pp. 138-143.

Handley P G and Boys J T (1992). "Practical real-time PWM modulators: an assessment". IEE Proc. B, 139(2), 1992. pp. 96-102.

Harson A (1994). "Vehicle layout and simulation". The University of Sheffield report.

Harson A, Mellor P H and Howe D (1995). "Design considerations for induction machines for electric vehicle drives". IEE Conf. Pub. No 412, Proc. EMD, 11-13 September 1995. pp. 16-20.

Heller B and Hamata V. "Harmonic field effects in induction machines"

Holtz J, et. al. (1986). "High-speed drive system with ultrasonic MOSFET PWM inverter and single-chip microprocessor control". IEEE-IAS Ann. Mtg. 1986. pp. 12-17.

Holtz J (1992). "Pulsewidth modulation - a survey". IEEE Trans. on Industrial Electronics. 39(5). pp. 410-420.

Holtz J (1994a). "Pulsewidth modulation for electronic power conversion". Proceedings of the IEEE, 82(8). pp. 1195-1214.

Holtz J and Beyer B (1994b). "Optimal pulsewidth modulation for AC servos and low-cost industrial drives". IEEE-IA, 30(4). pp. 1039-1047.

Hong C G, et. al. (1991). "Characteristics of a squirrel cage induction motor". IEE-B, 138(3). pp. 115-124.

Horowitz P and Hill W (1994). "The art of electronics". Cambridge University Press. 1994.

Howe D and Mellor P H (1994). "Flywheel electro-mechanical battery for electric vehicles (feasibility study)". The University of Sheffield report.

Howe D, Mellor P H and Peel D (1995). " High speed electro-mechanical energy storage systems for electric vehicles". Invited paper, IEEE/KTH Stockholm Power Tech Conference. Stockholm, Sweden, June. pp. 50-56"

HP 36550A signal analyser operating manual. 1988.

IGBT designer's manual. International Rectifier. 1994.

Janky P (1998). "High efficiency for induction motor drives". PCIM Intelligent Motion, May. pp. 109-119.

Jobing R, et. al. (1994). "Digital implementation of bus clamped space vector modulation". IEEE Trans. on Energy Conversion, 9(2). pp. 344-348.

Kahlen H (1995). "Technological steps in the electric vehicle drivetrain development". EVT'95, Paris. pp. 328-339.

Kellaway M and Shemmans D (1996). "Integrating power control". Electric & Hybrid Vehicle Technology'96. pp.171-176.

Kim H G, et.al (1984). "Optimal efficiency drive of a current source inverter fed induction motor by flux control". IEEE Trans. on Industry Applications. IA-20(6). pp. 1453-1459.

Kirschen D S, Novotny D W and Suwanwisoot W (1984). "Minimizing induction motor losses by excitation control in variable frequency drives". IEEE Trans. on Industry Applications. 20(5). pp. 1244-1250.

Kirschen D S, Novotny D W and Lipo T A (1987). "Optimal efficiency control of an induction motor drive". IEEE Trans. on Energy Conversion. 2(1). pp. 70-76.

Klingshirn E A and Jordan H E (1968). "Polyphase induction motor performance and losses on nonsinusoidal voltage sources". IEEE Trans. on Power Apparatus and Systems. 87(3). pp. 624-631.

Kolar J W et.al. (1991). "Influence of the modulation method on the conduction and switching losses of a PWM converter system". IEEE Trans. IA-27(6). pp. 1063-1075.

Kusko A and Galler D (1983). "Control means for minimisation of losses in ac and dc motor drives". IEEE Trans. Ind. Appl. Vol. IA-19. pp. 561-570.

Lee J A and Sun Y Y (1988). "Novel sinusoidal pulsewidth modulation schemes for voltage-source inverters with fluctuating input voltage". IEEE Trans. on Industrial Electronics, 35(2). pp. 284-291.

Le-Huy H, et.al (1994). "Analysis and implementation of a real-time predictive current controller for permanent-magnet synchronous servo drives". IEEE Trans. on Industrial Electronics, Vol. 41, No.1. pp.110-117.

Letor R (1992). "Static and dynamic behaviour of paralleled IGBT's". IEEE Trans. on Industry Applications. 28(2). pp. 395-402.

Lipo T A and Krause P C (1969). " Stability analysis of a rectifier-inverter induction motor drive". IEEE Trans. App. Syst. Vo. 88, Jan. pp. 56-66.

Locher R and Arnold M (1996). "Three stages in electric drive evolution". Electric & Hybrid Vehicle Technology'96. pp. 153-154.

Loh W K and .Renfrew A C (1986). "Optimised microelectronic power control of an AC drive for an electric vehicle". IEE-B, 133(4). pp. 291-298.

Manz L B (1995). "The motor designer's viewpoint of an adjustable speed drive specification". IEEE Industry Applications Magazine, Jan/Feb. pp.16-21.

Mclachlan N W (1955). "Bessel functions for engineers". Oxford Press.

Mellor P H (1991a). "A 300V, 40A high frequency inverter pole using paralleled FREDFET modules". Power Semiconductor Applications.

Mellor P H et.al. (1991b). "Reduction of spectral distortion in Class D amplifiers by an enhanced pulse width modulation sampling process". IEE Proc. G 138(4). pp. 441-447.

Mellor P H, et. al. (1992). "Digital sampling process for audio class D, PWM, power amplifiers", IEE Electronics Letters, 28 (1). pp. 56-58.

Mellor P H (1993). "An adjustable sinusoidal PWM sampling process for a.c. drives". Proc. 5th Euro. Conf. on Power Electronics and Applications. Vol.4. pp 231-235.

Mellor P H, Allen T and Howe D (1997). "Operational experience of a hub-mounted, electric drive system for a high-performance all-electric racing vehicle". EVS-14, Dec. 15-17, 1997, Orlando, Florida USA.

Mertens A (1992). "Harmonic distortion in three-phase inverters controlled by synchronous sigma-delta-modulation". ETEP, 2(6). pp.351-358.

Mesha L K and Evans P D (1989). "Analysis od on-state losses in PWM inverters". IEEE Proc. B 136(4). pp. 189-195.

Michel H and Raible C (1999). "Bursting with power". PCIM Europe Power Electronic, No. 3, 1999. pp. 36-37.

Mohan N, et. al. (1995). "Power electronics, converters, applications and design". John Wiley & Sons Inc. 1995.

Murai Y, et. al. (1987). "New PWM method for fully digitised inverters". IEEE-IA, 23(5). pp. 887-893.

Murphy J N and Egan M G (1983). "A comparison of PWM strategies for inverter-fed induction motors". IEEE Trans. on Industry Applications. 19(3). pp. 363-369.

Nash J N (1997). "Direct torque control, induction motor vector control without an encoder". IEEE Trans. IA-33(2). pp. 333-341.

Niekerk H R (1986). "Drive system design philosophy for mass minimisation of battery-powered vehicles". IEE Proc. B. 133(2). pp 49-53

Novotny D W and Lipo T A (1996). "Vector control and dynamics of AC drives". Oxford science publications. 1996.

O'Brien W A (1993). "Electric vehicles (EVs): A look behind the scenes". IEEE AES Systems Magazine, May. pp. 38-41.

Patel H S and Hoft R G (1973). "Generalised techniques of harmonic elimination and voltage control in thyristor inverters: Part 1 - Harmonic elimination". IEEE Trans. IA-9(3). pp. 310-317.

Philips (1991). Power semiconductor applications.

Pitel I J (1981). "Spectral errors in the application of pulsewidth modulated waveforms", IEEE Trans on Industry Applications, IA-17(3), pp. 289-295.

Plunkett A B and Plette D L (1977). "Inverter-induction motor drive for traction cars". IEEE Trans. Industry Application. IA-13(1). pp 26-37.

Pollmann A J (1986). "Software pulsewidth modulation for μp control of AC drives". IEEE Trans. IA-22(4). pp. 691-696.

Puttgen H B, et. al (1993). "Adjustable speed drive performance evaluation methods". 5th EPE Conference, Brighton, 1993. pp. 247 - 252.

Ramshaw R S (1994). Power Electronics semiconductor switches. Chapman & Hall.

Rajashekara K (1994). "History of electric vehicles in General Motors". IEEE Trans. Industry Applications. 30(4). pp. 897-904.

Rendell D (1994). "A report on the design and operation of a clamped resonant link for loss-less switching in inverter drives". The University of Sheffield report.

Rendell D (1996). "Seminar on: soft-switching resonant link converters". The University of Sheffield.

Robertson S D T and Hebbar K M (1971). "Torque pulsations in induction motors with inverter drive". IEEE Trans. Ind. Gen. Appl. 7(2). pp.318-323.

Schofield N, Mellor P H and Howe D (1993a). "An integrated low cost torque sensor for the direct control of a brushless DC traction motor". 26th International Symposium on Automotive Technology and Automation - Electric, hybrid and alternative fuel vehicles: progress in technology & infrastructure. Aachen, Germany, 13th -17th Sept. 1993. No. 93EL082.

Schofield N, Mellor P H and Howe D (1993b). "Design and testing of a prototype brushless dc traction motor for a hybrid electric vehicle". 26th International Symposium on Automotive Technology and Automation - Electric, hybrid and alternative fuel vehicles: progress in technology & infrastructure. Aachen, Germany, 13th -17th Sept. 1993. No. 93EL084.

Schmid M (1995). 'Design and analysis of a compact high-efficiency PWM converter for a hybrid vehicle".

Shimizu H (1998). "EV efficiency tops ICEV performance". Electric Vehicle Progress, 20(2). pp. 7.

Simpson R W (1996). "Improving the efficiency of motors". Electric & Hybrid Vehicle Technology'96. pp. 149-150.

Sutherland P E (1995). "Harmonic measurements in industrial power systems". IEEE Trans. on Industry Applications. 31(1). pp. 175-183.

Tahara M, et. al. (1994) "Performances of electric vehicle". 12th Int. Electric Vehicle Symp, California, USA. pp. 89-100.

Takahashi I and Noguchi T (1986). "A new quick-response and high-efficiency control strategy of an induction motor" IEEE Trans. IA-22(5). pp. 820-827.

Tan F D, et al (1995). "A practical approach for magnetic core-loss characterization". IEEE Trans. on Power Electronics. (2). pp. 124-.

Taufiq J A, et. al. (1986). "A novel algorithm for generating near optimal PWM waveforms for ac traction drives". IEE-B, 133(2). pp. 85-91.

Texas Instruments (1991), "TMS320C1x User's guide". Texas Instruments. 1991.

Texas Instruments (1992). "FPGA development systems". Texas Instruments. 1992.

Theocharis J and Petridis V (1990). "Spectral erros in 3-l PWM schemes", Int. J. Electronics, 69(4), pp. 451-465.

Timar P L and Lai J C S (1994). "Acoustic noise of electromagnetic origin in an ideal frequency-converter-driven induction motor". IEE Proc. B. 141(6). pp. 341-346.

Tomazic G (1994). "Considerations regarding the comparison of traction batteries". IEEE AES Systems Magazine, April. pp. 37-41.

Trzynadlowski A M and Blaabjerg F, et al (1994a). "Random pulse width modulation techniques for converter-fed drive system - a review". IEEE Trans on Industry Applications. 30(5). pp. 1166-1175.

Trzynadlowski A M and Legowski S (1994). "Minimum-loss vector PWM strategy for three-phase inverters". IEEE Trans. on Power Electronics, 9(1). pp. 26-34.

Turner D R and Binns K J, et. al (1991). "Accurate measurement of induction motor losses using balance calorimeter". IEE Proc. B. 138(5). pp.233-242.

Tzou Y Y and Hsu H J (1997). "FPGA realisation of space-vector PWM control IC for three-phase PWM inverters". IEEE Trans. on Power Electronics. Vol. 12, No.6. pp. 953-963.

Umeda M, Hashimoto S, et. al (1995). "Permanent magnet motor for EV". PEDS'95. IEEE Catalogue No. 95TH8025, pp. 792-796.

Weijer C J and Schmal D (1996). "Hybrid vehicles - system studies and development". Electric & Hybrid Vehicle Technology'96. pp.177-180.

Williamson S and Cann R G (1984). "A comparison of PWM switching strategies on the basis of drive system efficiency". IEEE Trans. Industry Applications, Vol. IA-29, No.6, 1984. pp. 1460-1472.

Winter U (1998). "Comparison of different drive system technologies for electric vehicles". EVS-15, Brussels 1998. pp. 77-90.

Wouk V (1995). "Hybrids: then and now". IEEE Spectrum, July 1995. pp. 17-21.

Wu Z Y (1994). "Determination of losses in a voltage source hard-switched IGBT inverter". The University of Sheffield report.

Wu Z Y, Mellor P H and Howe D (1995). "A DSP and FPGA based digital PWM modulator for AC traction drives". CICEM'95, Hangzhou, China, 1995. pp. 850-854.

Wu Z Y, Mellor P H and Howe D (1996). "Steady-state and transient performance control of PWM inverter drives". Intelligent Motion, PCIM'96, Nurnberg, Germany, 1996. pp. 339-350.

Vezzini A, et. al (1994). "Performance optimization for the electrical drive system of the hybrid III - passenger car". EVS-12.

Voltech (1994a). PM3000A Universal power analyser user manual. Voltech, 1994.

Voltech (1994b). The technology of PWM motor drives - measuring power, efficiency, torque and speed. Voltech Application handbook.

Zach F C (1989). "Comparison of voltage and current spectra using optimized forms of inverter pulsewidth modulation". IEEE Trans. on Power Electronics, 4(1). pp. 64-72.

Zhang C H, et.al (1995). "Analysis of control mode for asynchronous motor speed control by frequency control". CICEM'95, Hangzhou, China. pp.90-93.

Zuckerberger A and Alexandrovitz A (1986). "Determination of commutation sequence with a view to eliminating harmonics in microprocessor-controlled PWM voltage inverter". IEEE Trans. on Industrial Electronics, 33(3). pp. 262-270.

[Appendix A] Equipment Specifications

A.1 3 kW induction machine

Table A.1. Specifications of the 3kW induction machine

Output power	P_{out}	3	kW
Base speed (full load speed)	n	1420	rpm
Base frequency	f	50	Hz
Efficiency	η	81	%
Power factor	cos φ	80	
Phase voltage	V	240	V
Phase current	I	6.5	
pole pairs	p	2	
Rated torque	T_e	20	Nm
Pull out torque	T_m	300	%
Connection		Δ	

Table A.2. Electric parameters of the 3KW induction machine

Stator resistance	$R_{s,dc}$	1.966	Ω
Rotor resistance	$R_{r,dc}$	1.60	Ω
Nominal leakage reactance	X_{nom}	6.94	Ω

The characteristic of the machine is shown in Fig A.1.

A.2 3kW DC dynamometer

Table A.3. Specifications of the 3kW shunt d.c. machine

Power (kW)	Voltage (V)	Current (A)	Speed (rpm)
3	200	17.8	2250

A.3 Data sheet of IGBT IXSH40N60

Table A.4 IXSH40N60 maximum ratings

Parameter	Symbol	Rating	Unit
Collector-emitter voltage	V_{CES}	600	V
Gate-emitter voltage continuous	V_{GES}	±20	V
Collector current continuous (T_C=25^oC)	I_{C25}	75	A
Collector current pulsed	I_{CM}	150	A
Switching safe operation area	SSOA	80A @ 0.8×V_{CES}	
Total power dissipation	P_C	300	W
Operating and storage temperature	T_j & T_{STG}	-55 to +150	^oC

The IGBT has a low collector leakage current (max. 1mA), a low conduction voltage drop, and its saturation characteristics is shown in Fig. A.2. The IGBT can operate at switching speeds up to 30kHz. Its turn-on time is about 0.225 μs, and the turn-off time is much longer than the turn-on time. The dependency of the turn-off fall time on collector current and on gate series resistance are shown respectively in Fig A.3 and Fig A.4.4.

A.4 Diode DSEI2X61-06C

Table A.5 Specifications of DSEI2X61-60C

Parameter	Symbol	Rating	Unit
Repetitive peak reverse voltage	V_{RRM}	600	V
Average forward current	$I_{(AVE)}$	120	A
Forward voltage	V_F (max.)	1.9	V
Reverse recovery time	T_{rr}	35	ns

A.5 Load inductor

Inductance: 393 μH at 1kHz, 389 μH at 10 kHz.

Current rating: 200A

Resistance:

$$R = 33.8 + 0.166T \qquad \text{(A.1)}$$

where T is the temperature in Centigrade (^{o}C)

A.6 PM3000A universal power analyser

The PM3000A has 6 isolated input channels (3 voltages and 3 currents). Each channel has its own signal amplifier, filter and analogue-to-digital converter. The sampling is under the direct control of a microprocessor, and is taken simultaneously for all channels (no phasing errors). The sampled data is sent to the microprocessor via pulse transformer based isolations, thus allowing the PM3000A extremely high common mode rejection, and is processed in the microprocessor. The calculated voltage, current and power for each channel, and the computed fundamental components of the voltage and current and any other required harmonics, are then transferred to the interface processor for further processing such as averaging and for display in the front screen. These results are also available to the printer, and to the IEEE and the RS232 interfaces.

The PM3000A can operate in several modes, however, the most interest one is the "PWM motor drive" mode. In this mode, the data is sampled at high rate, and the total quantities, including all harmonic and carrier components, are computed in real time. At the same time, the sampled data is digitally filtered to provide low frequency measurements such as "fundamental" and measurement of output frequency. Since both low and high frequency signals result from the same measurement, this technique allows the high frequency measurements to be synchronised to the low frequency signal, which is the only way of providing high frequency measurement results that are both accurate and stable.

Some specifications for electrical parameter measurements are as follows,

Current

Internal shunts

Measuring range: 0.05 to 200 Apk (30A rms)

Accuracy: ± 0.05 % *rdg*

Bandwidth: 0 to 100 kHz

Voltage

Measuring range: 0.5 to 2000 Vpk (1400 rms)

Accuracy: ± 0.05 % *rdg*

Bandwidth: 0 to 100 kHz

Frequency

Measuring range: 5 Hz to 1 MHz

Accuracy: ± 0.1 %

Power

Measuring range: 25 mW to 400 kW (peak)

Accuracy (sine wave): $\pm [(V_{rdg} \times A_{error}) + (A_{rdg} \times V_{error})]$

Power factor

Measuring range: 0 to ± 1.000

Accuracy: ± 0.002

Impedance

Measuring range: 0.0001 ohms to 9.999 Mohms

Accuracy: ± 0.5 % *rdg*

A. 7 HP 35660A signal dynamic analyser

The HP 35660A Dynamic Signal Analyser is actually two instruments in one - a network analyser (two-channel spectrum measurements) and a spectrum analyser. It includes the functions of data input, calculation, and presentation of harmonic data on an oscilloscope screen. Its main specifications are as follows,

Amplitude

Input range: +27 to -51 dBV (31.7 Vpk to 3.99 mVpk)

Common mode input range: ±4*V* peak (floating mode)

Input range increment: 2dB

Harmonic distortion response range: -70dB

Amplitude accuracy: ±0.5*dB* (±0.003% of input range)

Frequency

Measurement range: 488 μ*Hz* to 102.4 kHz (single channel mode), 244 μ*Hz* to 51.2kHz (dual channel mode)

Accuracy: ±0.003% of frequency reading

Resolution: Span/400

Noise

Narrow span is recommended to prevent instrument noise. Time averaging function can be used to cancel out random noise.

Windows

Windowing is used to provide filtering in the time domain and bandwidth control in the frequency domain. Windowing techniques are, a) flat top - gives a good record of

amplitude, but spreads the pulse, so that two peaks close together in frequency tend to merge; b) hanning and hamming - picks out adjacent frequencies accurately, but distorts the pulse amplitude.

A. 8 Torque measurement

Load cell

Range: 0 ~ 20 Nm

Accuracy: ± 0.03% *of rated load*

Strain gauge amplifier

Accuracy: ± 0.005% *of reading*

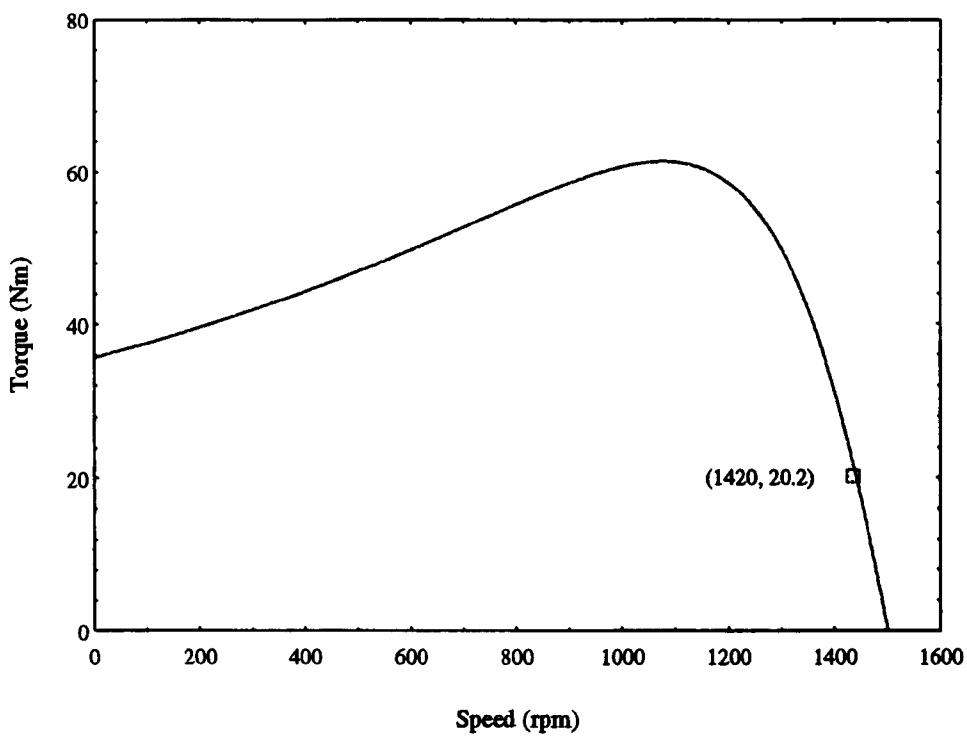

Fig. A.1 Torque-speed characteristics of the 3 kW induction machine.

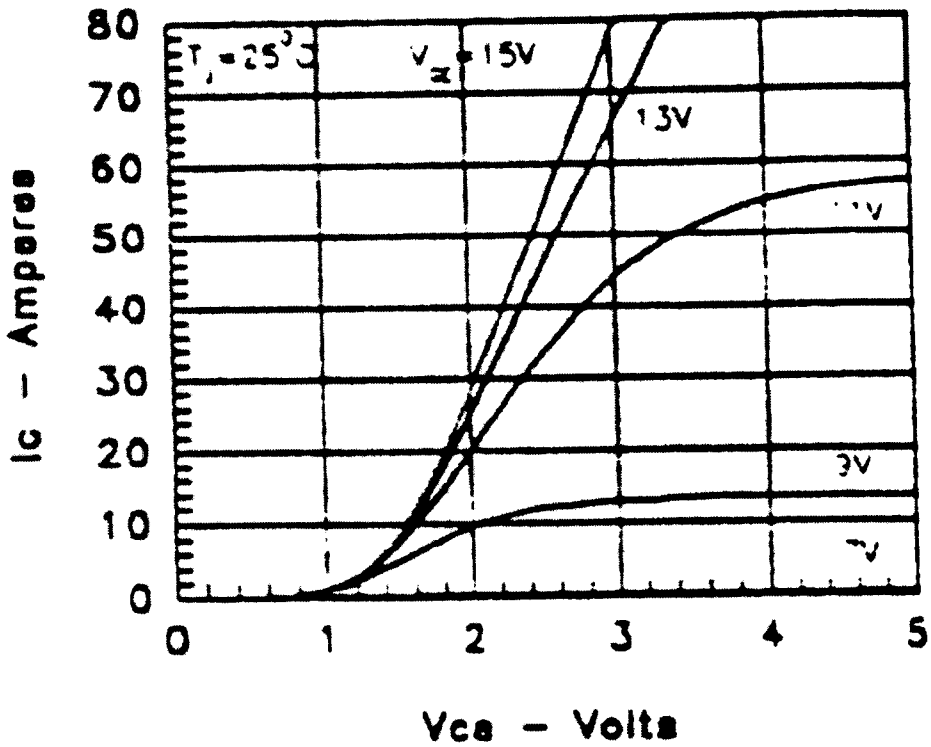

Fig. A.2 Saturation characteristics of IGBT IXSH40N60.

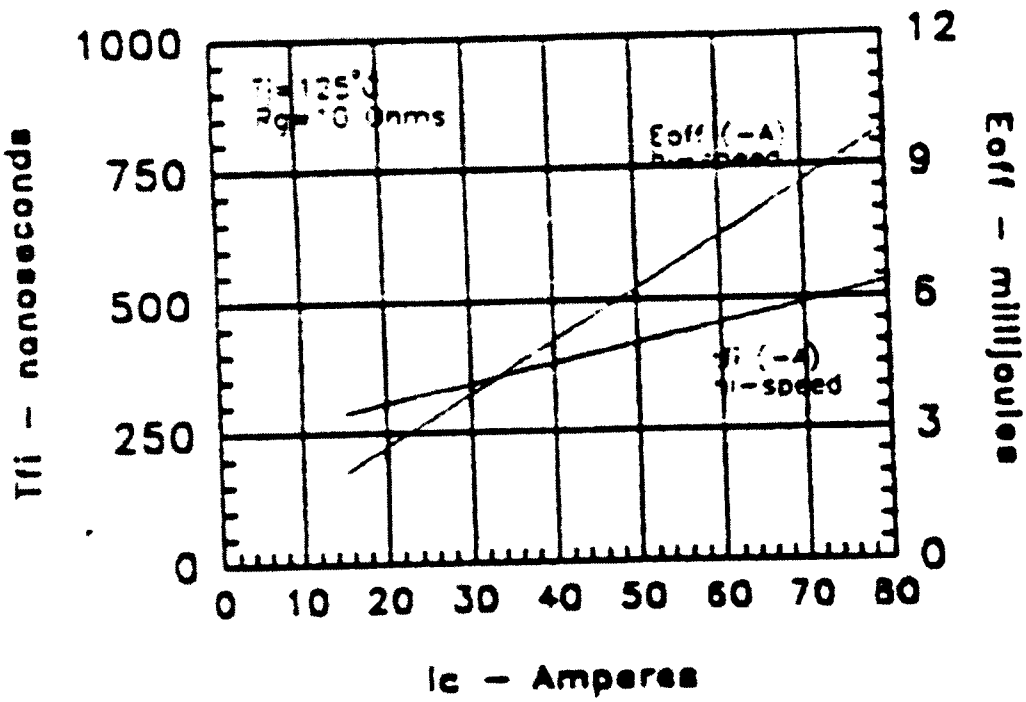

Fig. A.3 Dependency of turn-off energy per pulse and fall time on collector current.

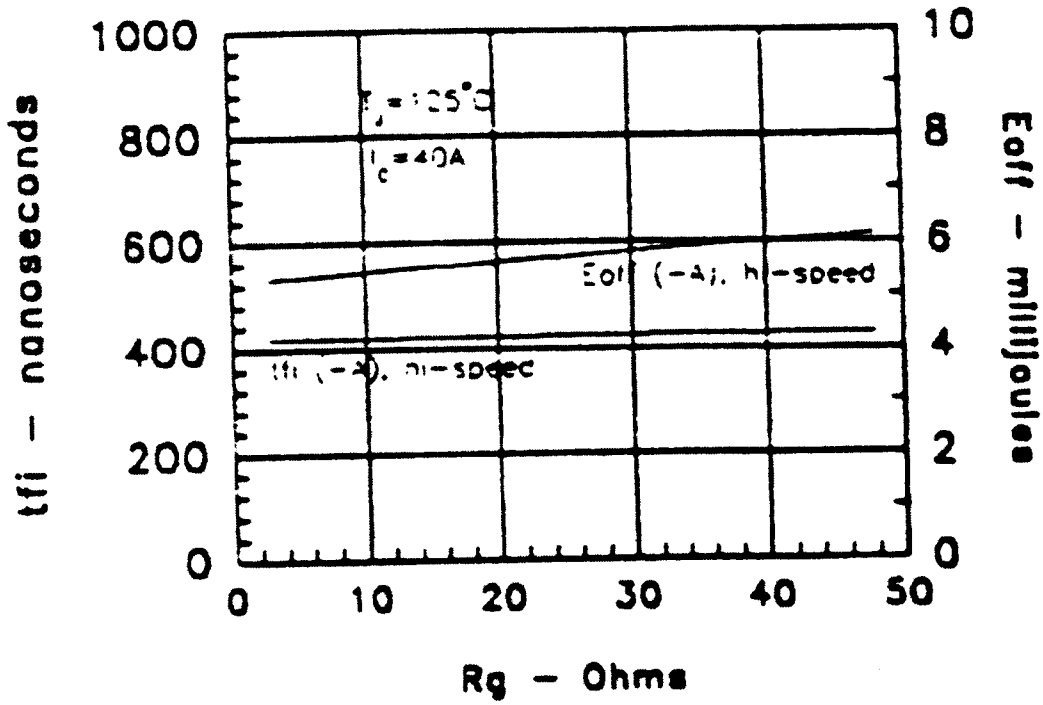

Fig. A.4 Dependency of turn-off energy per pulse and fall time on gate resistance.

[Appendix B] Current Sharing Performances of Paralleled MOSFETs

MOSFETs are supposed very suitable for paralleling operation because of their positive temperature coefficient. To follow the normal exercise, two MOSFETs were hard connected in parallel, driven from the same source (Fig B.1). The MOSFET used was BUK455-60A ($V_{DS} = 60V$, $I_{\max} = 41A$), and the fast recovery diode was MBR20100 ($I_{(AVE)} = 20A$, $V_{RRM} = 100V$)

The measured current sharing waveform with a switching frequency of 5kHz is shown in Fig B.2. It is observed that the MOSFETs have a very good steady state current performance, whilst there are some high peaks in the transient current sharing.

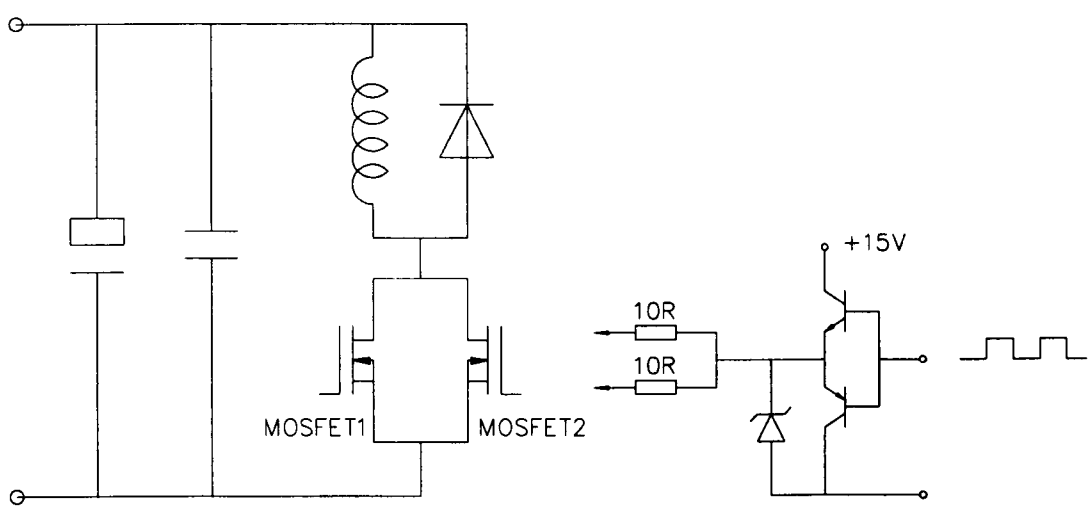

Fig. B.1 Circuit for MOSFETs paralleling operation tests.

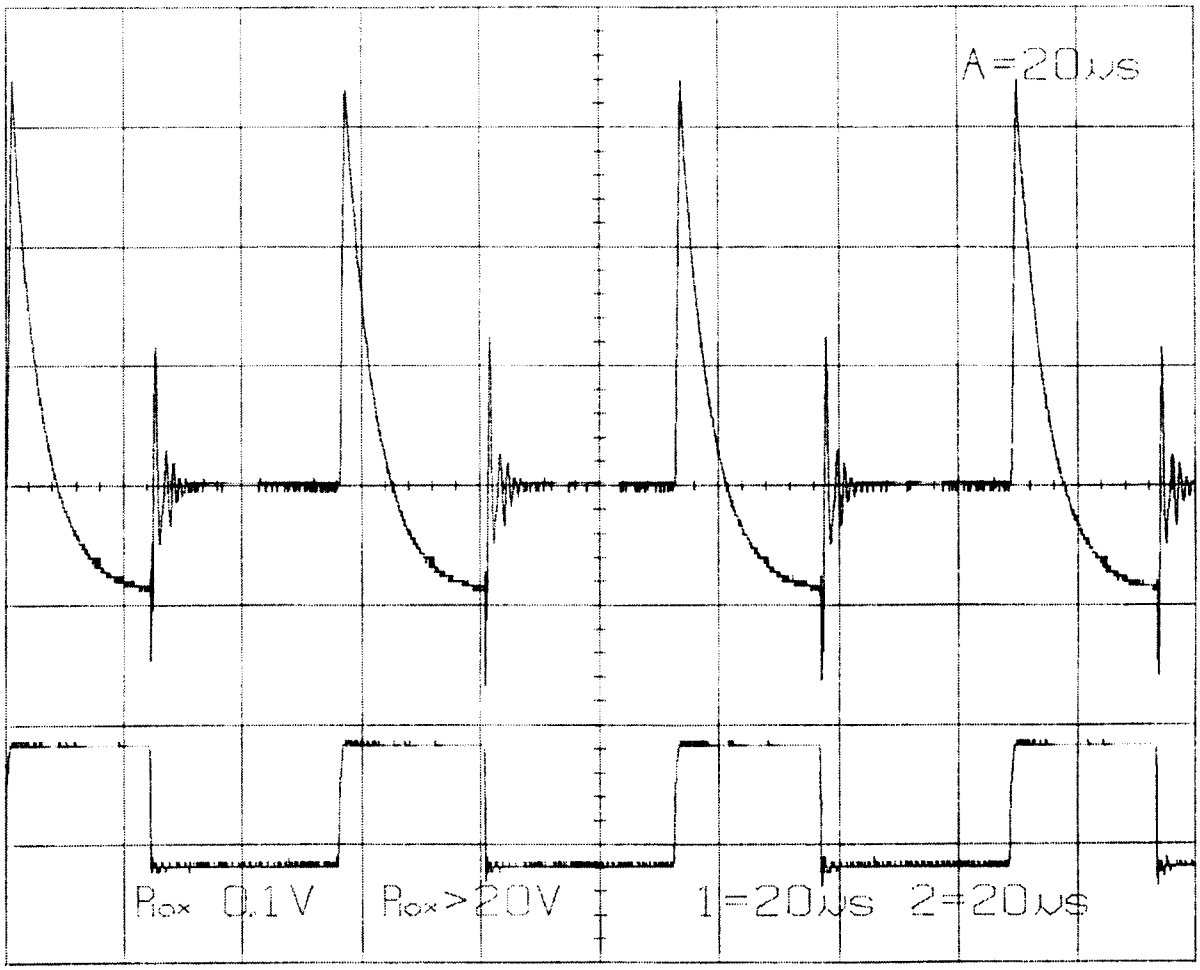

Fig. B.2 Current sharing performance for MOSFETs paralleling operation.

[Appendix C] Derivation of Full Spectral Distribution for Sub-optimal PWM Process

Following the graph illustration by Black [Black 1953], a width modulated pulse train can be represented by a three-dimensional configuration (Fig. C.1). The θ-axis of the graph represents a time scale which has been normalised to the pulse width modulation carrier frequency ω_s, such as $\theta = \omega_s t$. Similarly the Φ-axis represents a time scale normalised to the fundamental frequency of the modulating signal ω, where $\Phi = \omega t + \delta$, and δ is the phase angle of the modulating wave. The third axis represents the pulse amplitude $f(\theta, \Phi)$, which has a value of either 0 or H, and has a width along θ-axis given by, e.g.

$$\Omega(\Phi) = \pi k (1 + M \cos \Phi) \tag{C.1}$$

where M is the modulation depth, and k is a constant dependent on the modulation process, for example, when the pulses are obtained by single sided modulation, k=1; and when the pulses are formed by double sided modulation, $k = \frac{1}{2}$.

$f(\theta, \Phi)$ represents a flat shape of height H and of a width within 2 π. If this shape is repeated every 2 π along θ-axis, then $f(\theta, \Phi)$ will have a diagram of infinite paralleled walls. Thus, with the travelling of θ and Φ, an edge of one of the walls (e.g. trailing edge) will be intersected within every 2 π along θ-axis. If one pulse is defined at each intersection, then a pulse train will be obtained.

From above discussion, it is obvious that the pulse train pattern is dependent on the locations of the intersections, i.e. how the shape of the walls is defined and in which way the θ and Φ travel. In the natural PWM, the shape is given by Eqn. (C.1), and

$$\begin{cases} \theta = \omega_s t \\ \Phi = \omega t + \delta \end{cases} \tag{C.2}$$

In the case of regular sampling sub-optimal PWM, the pulse width function $\Omega(\Phi)$ is defined as,

$$\Omega(\Phi) = \pi k [\, 1 + M(\cos\Phi + \beta \cos 3\Phi)\,] \tag{C.3}$$

and the modulation variables are given by,

$$\begin{cases} \theta = \omega_S t \\ \Phi = \dfrac{|\,\theta\,|_{2\pi}}{R} + \delta \end{cases} \tag{C.4}$$

where β is the third harmonic factor, R is the PWM frequency ratio, and $|\,\theta\,|_{2\pi}$ denotes the nearest multiples of 2π in angle θ.

If a variable is defined as,

$$\overline{\Phi} = \omega t + \delta = \Phi + \frac{1}{R}(\theta - |\,\theta\,|_{2\pi}) \tag{C.5}$$

then the pulse width function is,

$$\Omega(\theta, \overline{\Phi}) = \pi k [\, 1 + M(\cos(\overline{\Phi} - \frac{\theta - |\,\theta\,|_{2\pi}}{R}) + \beta \cos 3(\overline{\Phi} - \frac{\theta - |\,\theta\,|_{2\pi}}{R}))\,] \tag{C.6}$$

This is a periodic function of θ and $\overline{\Phi}$, with a period of 2π for both variables.

Therefore, the pulse train can be expressed by double Fourier series as,

$$f(\theta, \overline{\Phi}) = \sum_{m=-\infty}^{\infty} \sum_{n=-\infty}^{\infty} K_{mn}\, e^{j(m\theta + n\overline{\Phi})} \tag{C.7}$$

where

$$K_{mn} = \frac{1}{4\pi^2} \int_0^{2\pi} \int_0^{2\pi} f(\theta, \overline{\Phi})\, e^{-j(m\theta + n\overline{\Phi})}\, d\theta\, d\overline{\Phi} \tag{C.8}$$

Since the leading edges and trailing edges of the pulse train have a sort of symmetry, they can be transformed from each other. Thus, in the following a pulse formation process with single side modulated will be discussed first, and the spectral distribution for the double sided modulation will be subsequently obtained.

C.1 Single sided modulation (trailing edge)

The pulse train $f(\theta, \overline{\Phi})$ is described as,

$$f(\theta, \overline{\Phi}) = \begin{cases} H, 0 \le (\theta - |\theta|_{2\pi}) \le \Omega \\ 0, \textit{otherwise} \end{cases} \tag{C.9}$$

where the pulse width function in the integral interval of $0 \le \theta < 2\pi$ is,

$$\Omega = \pi k\, [\, 1 + M(\cos\Phi + \beta \cos 3\Phi)\,]$$

$$= \pi k\, [\, 1 + M(\cos(\overline{\Phi} - \frac{\theta}{R}) + \beta \cos 3(\overline{\Phi} - \frac{\theta}{R}))\,] \tag{C.10}$$

and the constant $k = 1$

The coefficients K_{mn} are determined as,

$$K_{mn} = \frac{H}{4\pi^2} \int_0^{2\pi} \int_0^{\pi k[1 + M(\cos\Phi + \beta\cos 3\Phi)]} e^{-j(m\theta + n\overline{\Phi})}\, d\theta\, d\overline{\Phi}$$

$$= \frac{H}{4\pi^2} \int_0^{2\pi} \int_0^{\pi k[1 + M(\cos\Phi + \beta\cos 3\Phi)]} e^{-j(m\theta + n(\Phi + \frac{\theta}{R}))}\, d\theta\, d\Phi \tag{C.11}$$

After some manipulations, the following equations are obtained,

$$K_{m0} = A \cdot J_0(a)\, J_0(b) \tag{C.12}$$

and when $n \neq 0$

$$K_{mn} = A \cdot e^{-jn\pi/2} \cdot \sum_{q=-\infty}^{\infty} J_{n-3q}(a)\, J_q(b) \tag{C.13}$$

where

$$A = \frac{Hj}{2\pi\,(m+\frac{n}{R})}\, e^{-j\pi k\,(m+\frac{n}{R})} \tag{C.14}$$

$$a = \pi k M\,(m+\frac{n}{R}) \tag{C.15}$$

$$b = \pi k M \beta\,(m+\frac{n}{R}) \tag{C.16}$$

and $J_n(z)$ is the Bessel function of the first kind, defined as,

$$J_n(z) = \frac{e^{-jn\pi/2}}{2\pi} \int_0^{2\pi} e^{jz\cos\Phi}\, e^{jn\Phi}\, d\Phi \tag{C.17}$$

Put

$$\begin{cases} \theta = \omega_s t \\ \Phi = \omega t + \delta \end{cases} \tag{C.18}$$

into the double Fourier series of Eqn. (C.7), the spectral distribution of the trailing edge modulated sub-optimal PWM is obtained as follows,

$$f(t) = \frac{H}{\frac{\pi}{R}} \sum_{q=-\infty}^{\infty} J_{1-3q}\left(\frac{\pi M}{R}\right) J_q\left(\frac{\pi M \beta}{R}\right) \cdot \cos\left(\omega t + \delta - \frac{\pi}{R}\right)$$

$$- \sum_{n=2}^{\infty} \sum_{q=-\infty}^{\infty} \frac{H}{\frac{n\pi}{R}} J_{n-3q}\left(\frac{\pi n M}{R}\right) J_q\left(\frac{\pi n M \beta}{R}\right) \cdot \sin\left(n\,(\omega t + \delta) - \frac{n\pi}{R} - \frac{n\pi}{2}\right)$$

$$+\sum_{m=1}^{\infty}\sum_{n=-\infty}^{\infty}\sum_{q=-\infty}^{\infty}\frac{(-1)^{m+1}H}{\pi\,(m+\frac{n}{R})}J_{n-3q}\left(\pi M\,(m+\frac{n}{R})\right)J_q\left(\pi M\beta\,(m+\frac{n}{R})\right)$$

$$\cdot\sin\left(n\left(\omega t+\delta\right)+m\,\omega_s t-\frac{n\pi}{R}-\frac{n\pi}{2}\right) \qquad \text{(C.19)}$$

C2. Double sided sub-optimal modulation

This is a PWM process where oversampling is employed to give separate samples for each pulse edge. The double Fourier series can be constructed using the above results for single sided modulation in such a way as,

$$f(\theta,\Phi)=f(\theta,\overline{\Phi})+f(-\theta,-\overline{\Phi}+\frac{\pi}{R})$$

$$=\sum_{m=-\infty}^{\infty}\sum_{n=-\infty}^{\infty}2\,K_{mn}\,e^{j\frac{n\pi}{2R}}\cos\left(m\theta+n\overline{\Phi}-\frac{n\pi}{2R}\right) \qquad \text{(C.20)}$$

where the constant $k=\frac{1}{2}$.

Similarly as for the single sided modulation, the spectral distribution for the asymmetric double sided sub-optimal PWM is obtained as follows,

$$f(t)=\frac{2H}{\frac{\pi}{R}}\sum_{q=-\infty}^{\infty}J_{1-3q}\left(\frac{\pi M}{2R}\right)J_q\left(\frac{\pi M\beta}{2R}\right)\cos\left(\omega t+\delta-\frac{\pi}{2R}\right)$$

$$+\sum_{n=2}^{\infty}\sum_{q=-\infty}^{\infty}\frac{2H}{n\pi}J_{n-3q}\left(\frac{\pi n M}{2R}\right)J_q\left(\frac{\pi n M\beta}{2R}\right)\sin\left(\frac{n\pi}{2}\right)\cos\left(n\left(\omega t+\delta\right)-\frac{n\pi}{2R}\right)$$

$$+\sum_{m=1}^{\infty}\sum_{n=-\infty}^{\infty}\sum_{q=-\infty}^{\infty}\frac{2H}{\pi\,(m+\frac{n}{R})}J_{n-3q}\left(\frac{\pi M}{2}(m+\frac{n}{R})\right)J_q\left(\frac{\pi M\beta}{2}(m+\frac{n}{R})\right)$$

$$\cdot \sin\left(\frac{\pi}{2}\left(m+\frac{n}{R}\right)\right)\cos\left(n\left(\omega t+\delta\right)+m\,\omega_s t-\frac{n\pi}{2R}\right) \qquad \text{(C.21)}$$

When the pulse height is H=2, which is equivalent to the case when the PWM pulses are normalised as ± 1, the amplitude of the kth harmonic will be,

$$|V_k| = \sum_{q=-\infty}^{\infty} \frac{4\,J_{k-3q}\left(\frac{\pi k M}{2R}\right) J_q\left(\frac{\pi k M \beta}{2R}\right)}{\frac{\pi k}{R}}$$

$$-\sum_{m=1}^{\infty}\sum_{q=-\infty}^{\infty} \frac{4\,J_{k-3q}\left(\frac{\pi M}{2}\left(m+\frac{k}{R}\right)\right) J_q\left(\frac{\pi M \beta}{2}\left(m+\frac{k}{R}\right)\right)}{\pi\left(m+\frac{k}{R}\right)} \qquad \text{(C.22)}$$

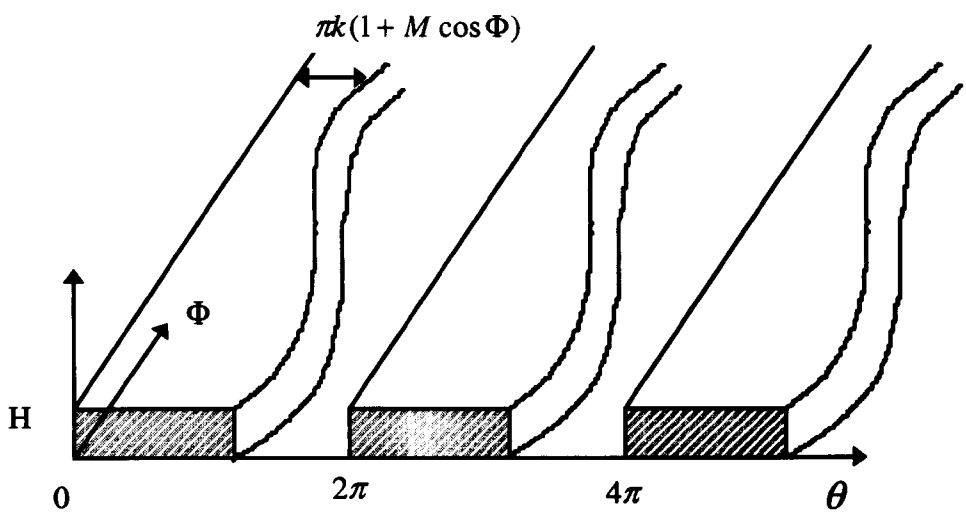

Fig. C.1 Graphic representation of a modulation process.

[Appendix D] Development of a Digital Three Phase Modulator

D.1. DSP TMS320E15

DSP TMS320E15 is among the first generation of the TMS320 family, and is a 16/32-bit single-chip digital signal processor. Since the appearance of it and other members in the early 80s, the powerful instruction set, inherent flexibility, high-speed number-crunching capabilities and innovative architecture have made this high-performance, cost-effective processor the ideal solution to many applications.

Key Features

Instruction cycle timing: 200ns
144-/256-word on-chip data RAM
1.5K-/4K-word on-chip program ROM
4K-word on-chip program EPROM
EPROM code protection for copyright security
4K-word total external memory at full speed
16-bit bi-directional data bus at 50-Mbps transfer rate
32-bit ALU/accumulator
16-×16-bit parallel multiplier with a 32-bit product
0- to 16-bit barrel shifter
On-chip clock generator
Eight input and eight output channels
Single 5V supply
Device packaging: 40-pin DIP
Technology: CMOS

Pinouts and Signal Descriptions

TMS320E15 (Top view)

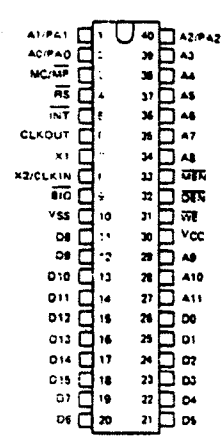

Table D-1. TMS320E15 signal descriptions

SIGNAL	I/O/Z	DESCRIPTION
A11 MSB A10 - A3 A2/PA2 A1/PA1 A0/PA0 D15 MSB D14 - D1 D0 LSB	O I/O/Z 	Program memory address bus A11(MSB) through A0(LSB) and port address PA2(MSB) through PA0(LSB). Address A11 through A0 are always active and never go to high impedance. During executive of IN and OUT instructions, pins A2 through A0 carry the port addresses, whilst pins A11 through A3 are always driven low. Parallel data bus D15(MSB) through D0(LSB). The data bus is always in the high-impedance state except when $\overline{WE}$ is active (low).
$\overline{BIO}$	I	External polling input. Polled by BIOZ instruction. If low, the device branches to the address specified by the instruction.
$\overline{DEN}$	O	Data enable for device input data. When active low, $\overline{DEN}$ indicates that the device will accept data from the data bus. $\overline{DEN}$ is only active during the first cycle of the IN instruction. When $\overline{DEN}$ is active, $\overline{MEN}$ and $\overline{WE}$ will always be inactive.
$\overline{INT}$	I	External interrupt input. The interrupt signal is generated by applying a negative-going edge to the $\overline{INT}$ pin. The edge is used to latch the interrupt flag register (INTF) until an interrupt is granted by the device. An active low level will also be sensed.
MC/$\overline{MP}$	I	Memory mode select pin. High selects the microcomputer mode, in which 4K words of on-chip program memory are available. A low on the pin enables the microprocessor mode. In this mode, the entire memory space is external, i.e., addresses 0 through 4095.
$\overline{MEN}$	O	Memory enable. $\overline{MEN}$ will be active low on every machine cycle except when $\overline{WE}$ and $\overline{DEN}$ are active. $\overline{MEN}$ is a control signal generated by the device to enable instruction fetches from program memory. $\overline{MEN}$ will be active on instructions fetched from both internal and external memory.
$\overline{RS}$	I	Reset input for initialising the device. When held at an active low for a minimum of five clock cycles, $\overline{WE}$, $\overline{DEN}$ and $\overline{MEN}$ are forced high; and, the data bus is not driven. The program counter (PC) and the address bus are then synchronously cleared after the next complete clock cycle from the falling edge of $\overline{RS}$. Reset also disables the interrupt, clears the interrupt flag register, and leaves the overflow mode register unchanged. The device can be held in the reset state indefinitely.
$\overline{WE}$	O	Write enable for device output data. When active low, $\overline{WE}$ indicates that data will be output from the device on the data bus. $\overline{WE}$ is only active during the first cycle of the OUT instruction and the second cycle of the TBLW instruction. When $\overline{WE}$ is active, $\overline{MEN}$ and $\overline{DEN}$ will always be inactive (high).
CLKOUT	O	System clock output (1/4 crystal/CLKIN frequency). Duty cycle is 50%.
Vcc	I	5-V supply pin
Vss	I	Groud pin
X1	O	Crystal output pin for internal oscillator. If the internal oscillator is not used, this pin should be left unconnected.

DSP development tool

The TMS320C1x Evaluation Module (EVM) is a low-cost development board for TMS32010/C10/C15/E15 devices, used for full-speed in-circuit emulation and hardware debugging. It consists of a single board that enables a designer to evaluate certain characteristics of the processor to determine if it meets the requirements of an application.

The powerful firmware package of the TMS320C1X EVM contains a debug monitor, assembler/reverse assembler, and software communication via three EIA ports. The three EIA ports allow the EVM to communicate with a designer's terminal, a host computer, a printing device or audio cassette. In addition, the EVM also supports an onboard PROM utility for programming TMS2764 EPROMs and for programming TMS320E15/E17 with supplement of an EPROM adapter socket.

The EVM assembles source code is created on a host computer or on the EVM's text editor. The EVM has a one-pass assembler, which resolves both forward and reverse labels and converts the incoming text into executable code. Object code produced by the EVM assembler is stored in memory. The reverse assembler converts object code back to assembly language mnemonics, and the patch assembler allows modification of the code.

The DSP development system is shown in Fig. D.1.

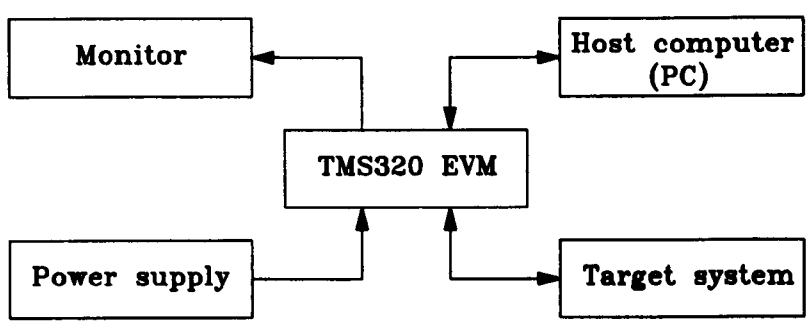

Fig. D.1. DSP development system.

D.2 FPGA technique

FPGA stands for field programmable gate array. The Texas Instrument (TI) series (e.g. TPC1020A) are fabricated using the TI silicon-gate CMOS process. The process features polysilicon gate, source, drain elements, and two levels of copper-doped-aluminium metallization to reduce internal resistance and enhance performance. These field-programmable devices combine gate-array flexibility with desktop programmability. This combination allows

the designer to avoid fabrication cycle times and nonrecurring engineering charges associated with conventional mask-programmed gate arrays. The FPGAs are unique in that the arrays are fabricated, tested and shipped to the user for programming. The FPGA contains user-configurable inputs, outputs, logic modules, and minimum-skew clock driver with hardwired distribution network. The FPGA also includes on-chip diagnostic probe capabilities and security fuses to protect the proprietary design. The FPGA architecture is detailed in Fig.D.2.

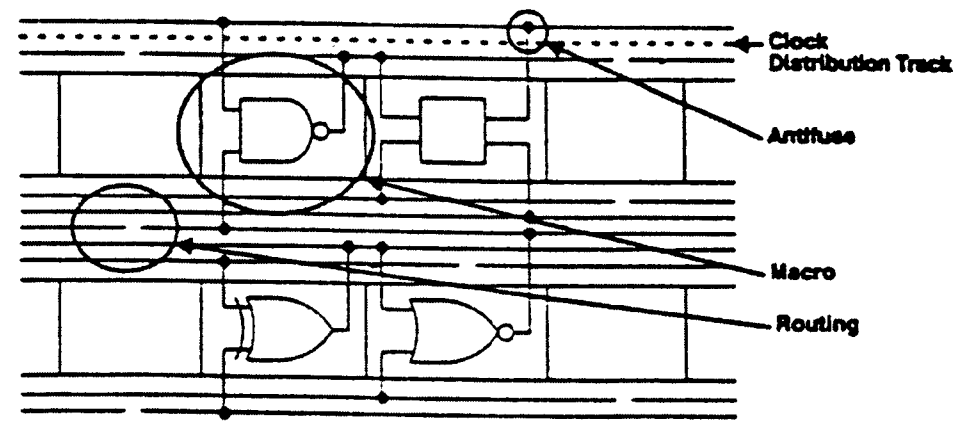

Fig. D.2. Architecture detail of an FPGA.

The **antifuse** provides programmability to the device. It is normally an open device which becomes conductive when a large voltage or current is applied to it. The size of the antifuse is very small and is up to 19 times smaller than other types of programmable elements such as EPROM or SRAM. The unprogrammed resistance of the antifuse is greater than 100MΩ and the programmed resistance is approximately 500Ω..

The rectangular array of **logic modules** contain generic logic circuits. These circuits can be programmed to perform a variety of functions. The **macro** functions implemented in the logic modules are generated in several ways. They come from TI-supplied hard and soft macro libraries or can be created by the user.

The **routing tracks** run horizontally between the logic modules and vertically over them, with an antifuse at each intersection. These tracks connect the macro functions implemented in the logic modules.

The **clock distribution network** consists of an assigned input pin and row buffers to provide additional drive for the large fan-out requirements of the clock signal. The network can connect to any logic module but only to clock and gated inputs of sequential macro functions.

The **I/O** function can be programmed as either input, output, 3-state, or bi-directional. Inputs can be driven by CMOS or TTL levels and output levels are compatible with standard CMOS and TTL specifications.

The profile of the TPC1020A FPGA is given in Table D.2. In Fig.D.3 are its pinouts and terminal functions.

Table D.2 TPC1020A profile

Capacity	Gate-array equivalent gates	2000
	TTL equivalent packages	53
CMOS process		1.2μm
Logic modules		547
Flip-flops (maximum)		273
Antifuses		186000
Horizontal tracks		22
Vertical tracks		13
User I/Os (maximum)		69

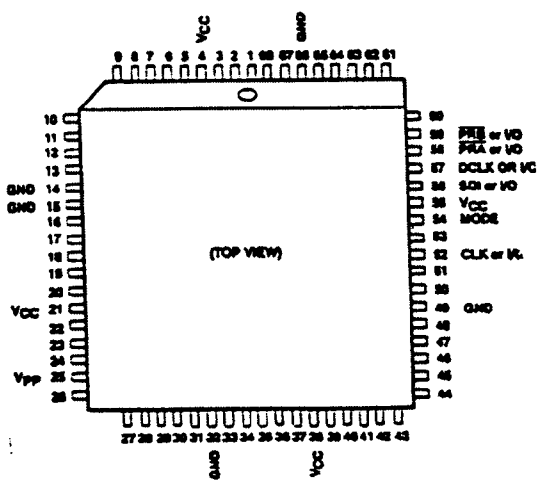

V_{cc} - supply voltage
V_{pp} - programming voltage
GND - ground
I/O - input/output
CLK - clock
DCLK, SDI, PRA, PRB - diagnostic terminals
MODE - control of diagnostic terminals

Fig. D.3 TPC1020A pinouts

D.3 Design of four 12-bit counters

Development support

The Texas Instruments Action Logic System (TI-ALS) is a high-productivity Computer Aided Engineering (CAE) development tool for implementing TI Field-Programmable -Gate -Array

(FPGA) designs. The designs can be captured and devices programmed at the designer's desk, when utilising a supported design system in conjunction with TI-ALS and TI FPGAs. The TI-ALS consists of software and hardware added into an existing CAE environment to provide a FPGA design library and device programming. The FPGA design process is shown in Fig. D.4.

The process is carried out in two steps: environment design process and TI-ALS design process. In the environment process, the gate array design package "*WORKVIEW*", in conjunction with the TPC series macro libraries, is used to design the function logic circuit. Then, the prelayout (and also the postlayout) simulations of the design can be performed, and the design is verified. When the environment design process is complete, the TI-ALS files (.adl, .crt, .ipf) are exported to the TI-ALS, and the design is ready to be processed in the TI-ALS to create the files needed for programming the FPGA.

The TI-ALS process is entered using the command

als ***file***

The **Project** function makes selection of FPGA type (e.g. 1020A) and package (e.g. 68 PLCC).

The **Pin Edit** allows the user to manually assign the device labelled pins to the package pin numbers (locations).

The schematic can be checked using **Validation** to assure that design parameters are met. One of the usual errors is excessive fanouts.

With **Place and Route**, all unassigned I/Os are automatically assigned for maximum performance and routability. Optimisations are possible for the specific design with special attention paid to critical paths.

After place and route is completed with no errors, the **Extract** program calculates net delays and module delays for each net in the design, so that the specific postlayout timing information is obtained.

The **Export** function permits the designer to back annotate the host system's delay files with FPGA postlayout timing data for use with the host system's simulator. Min/Max delay values reflecting the operating condition (voltage, temperature, and speed) can be specified by the designer, for example,

export tempr:com voltr:com speed:standard

The data from the place and route routine is used in the **Fuse** function to generate a fuse file that maps the fusing sequence and locations. This file will be utilised to program the FPGA device.

The TI-ALS reads the fuse file and **Activator** hardware applies programming pulses in sequence. Each antifuse is verified, and a check on surrounding antifuse assures correct device functionality.

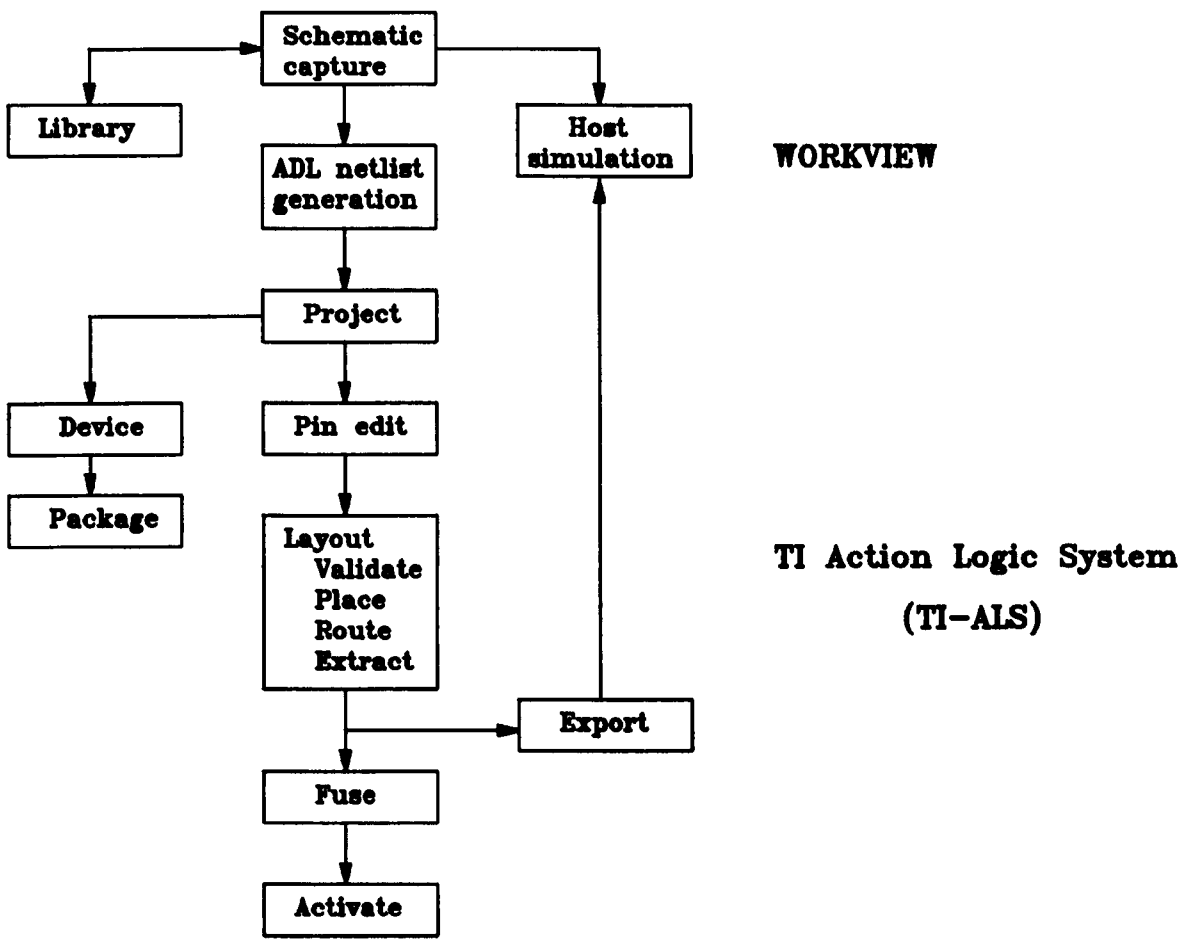

Fig. D.4 FPGA design process.

Design of the four 12-bit counters

The 68-pin PLCC packaged TPC1020A FPGA was used for the counters. Since there are only 2000 equivalent gates in this FPGA, firstly a special 12-bit counter was designed and created as a macro (Fig. D.5). Then this macro was used to design the four 12-bit counters (Fig. D.6). Before this circuit was programmed into the FPGA device, it was validated functionally working using

prelayout simulation and device working using postlayout simulation. The command program for the simulations and the simulated results are omitted here.

The programmed FPGA device can be used in the same way as other TTL chips and may be named as "Quadruple 12-bit counters". The signal description of this chip is given in Table D.3.

Table D.3 Signal description of the Quadruple 12-bit counters

Signal	Pin	I/O/Z	Description
D12(MSB	22	I	12-bit parallel data inputs
D11	20	I	
D10	18	I	
D9	16	I	
D8	26	I	
D7	24	I	
D6	63	I	
D5	62	I	
D4	61	I	
D3	48	I	
D2	46	I	
D1(LSB)	44	I	
OUT0	12	O	Counter count down to zero signals, active low.
OUTA	29	O	
OUTB	33	O	
OUTC	37	O	
LD01	7	I	Load signals for 12-bit counter 0
LD02	8	I	
LD03	9	I	
LDA1	3	I	Load signals for 12-bit counter A
LDA2	5	I	
LDA3	6	I	
LDB1	68	I	Load signals for 12-bit counter B
LDB2	1	I	
LDB3	2	I	
LDC1	64	I	Load signals for 12-bit counter C
LDC2	65	I	
LDC3	67	I	
CLOCK	52	I	Counters clock signal
VDD		I	5-V supply
GND		I	Ground

It is noticed that each counter has three load signals. This is due to the limitation of the number of fanouts in the FPGA. In applications, these three signals are connected together.

The key features of the Quadruple 12-bit counters are,

- Count down mode
- Immediate loading of the counter values with load signal, not controlled by the clock.
- Once loaded the counters are allowed to count down to zero and are then held at zero until they are reloaded.

D.4 Digital three phase PWM modulator

Descriptions

The schematic of the three phase digital PWM modulator is shown in Fig. D.7, and in Fig. D.8 is a photo of the built modulator. The applied DSP program contains eight PWM strategies, which is selected in the program initialisation stage. Once a PWM and its frequency ratio are selected the process will be repeated ad-infinitum. During the processing other PWM parameters can be adjusted by the setting switches. The arrangement is as follows,

Switch 1 (SW1):

b11 - b0 - switching frequency
b15 - b12 - pulse width limit

Switch 2 (SW2):

b9 - b0 - modulation depth
b15 - b10 - third harmonic factor or zero vector ratio

Switch 3 (SW3)

b2 - b0 - frequency ratio
b7 - b0 - sampling factor
b12 - b8 - phase angle
b15 - b13 - PWM mode selection

To prevent the short circuit, a pulse dropping scheme was designed to limit the minimum output pulse width, although in practice the narrow-width pulses are effectively absorbed by the delay circuit in the gate drivers. The pulse dropping algorithm is as follows,

If the calculated pulse width is less than the minimum pulse width set by the inputs then set the pulse width to zero; if the calculated pulse width is greater than the sample time minus the minimum pulse width limit then set the pulse width to equal the sample time. Other necessary explanations are given by statements in the program

Applied DSP program for PWM implementations (omitted)

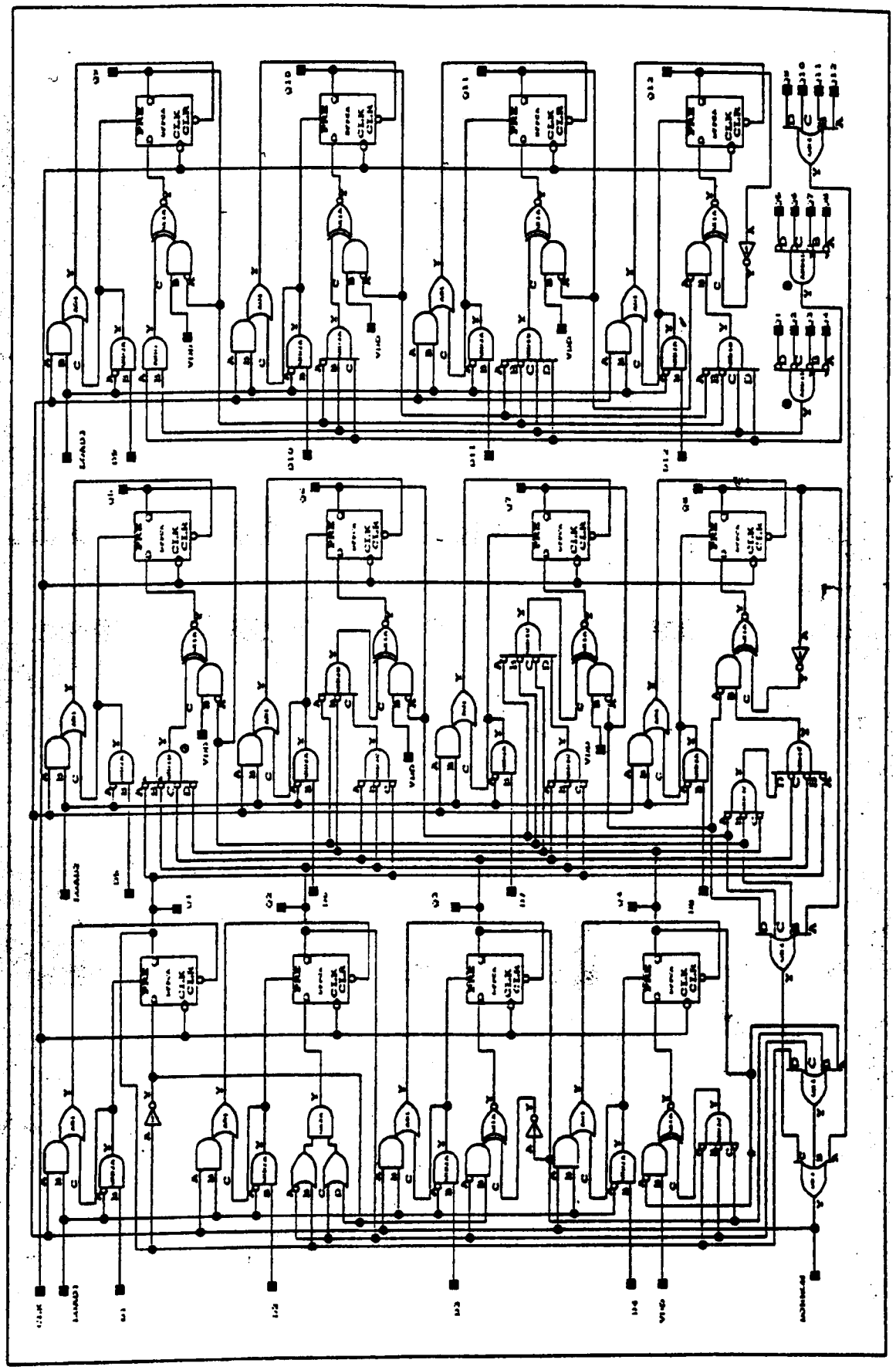

Fig. D.5. Logic circuit of a 12-bit counter for FPGA.

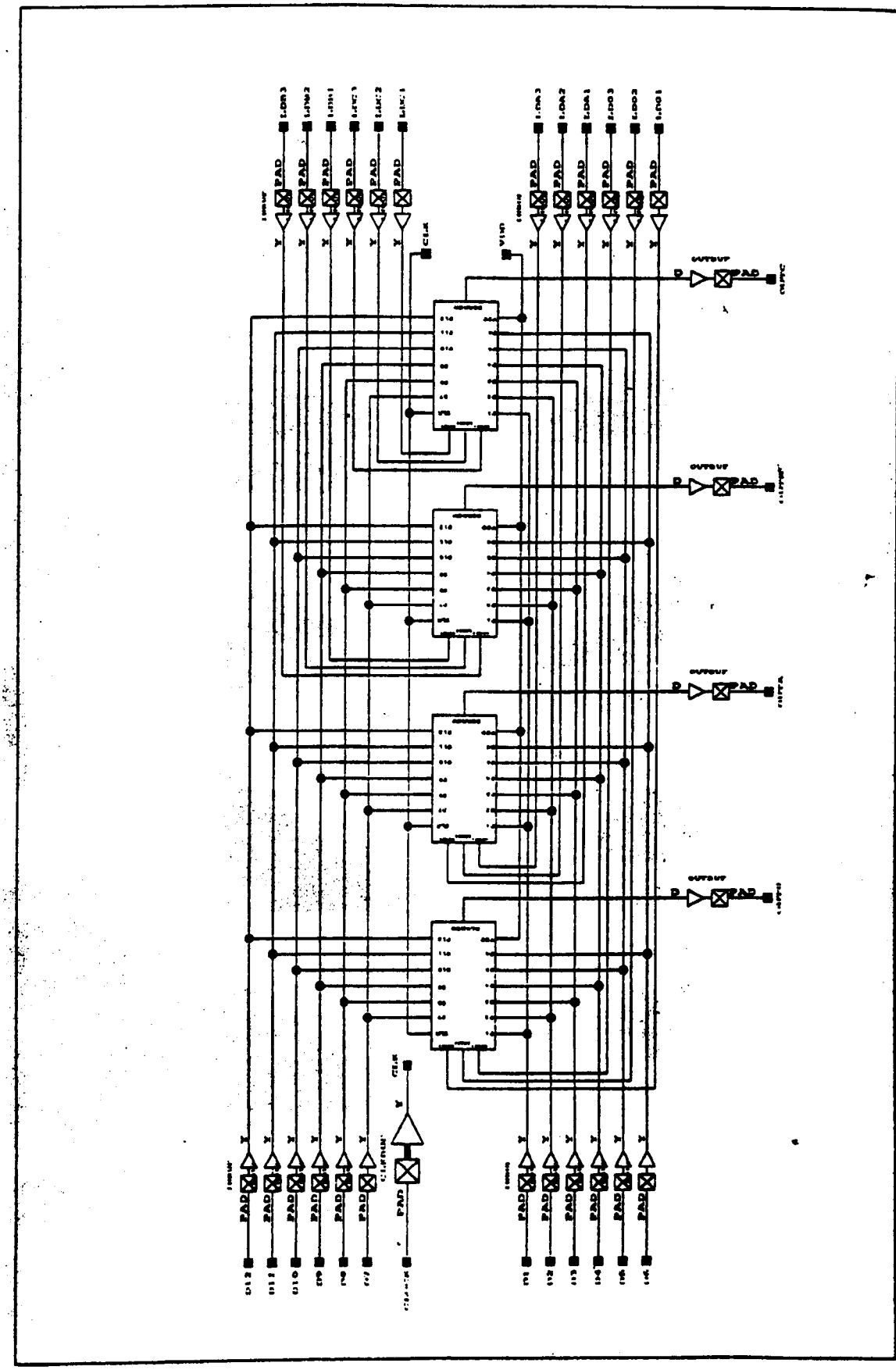

Fig. D.6. Logic circuit of the 12-bit counters for FPGA.

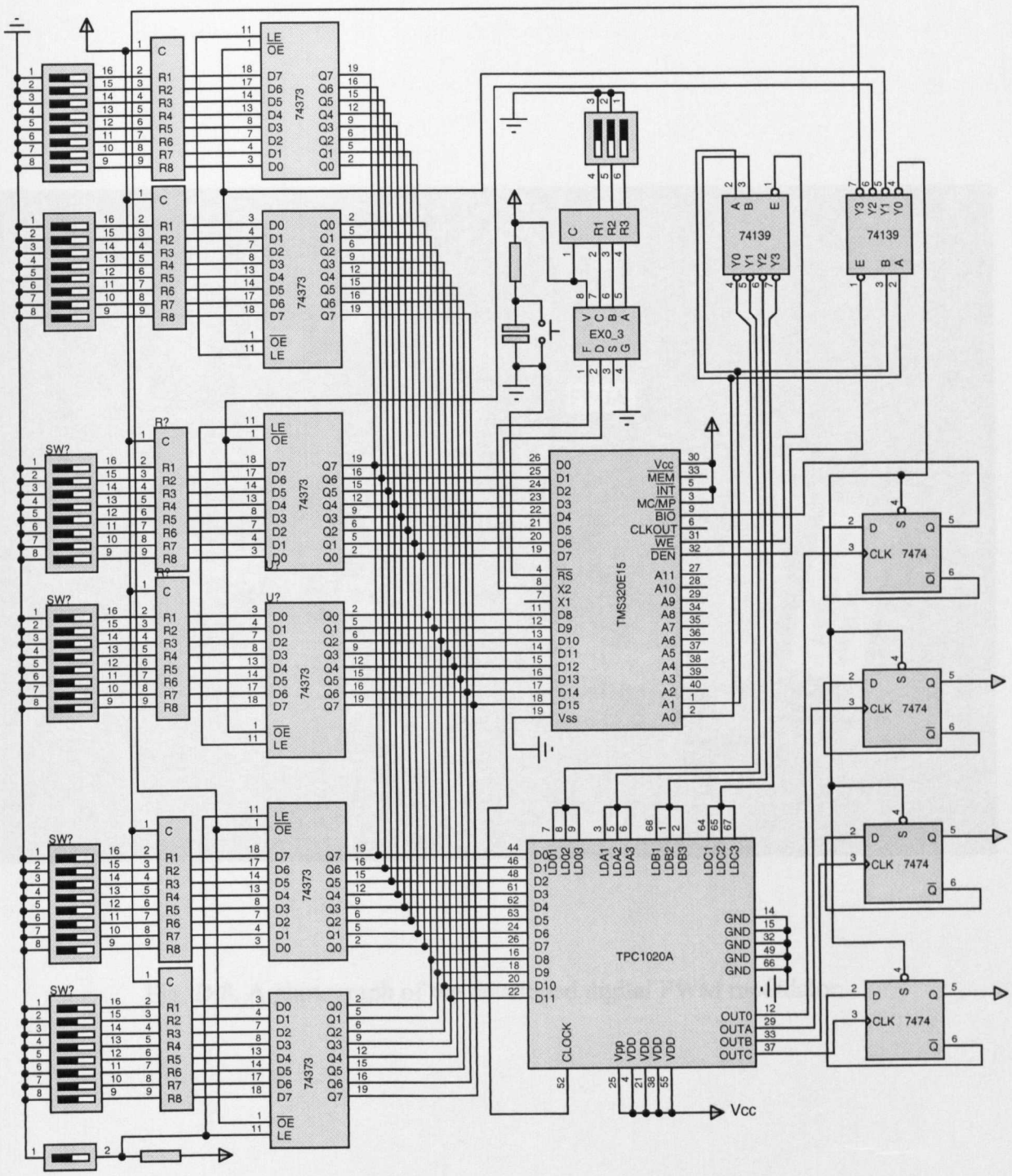

Fig. D.7. Schematic of the three phase digital PWM modulator.

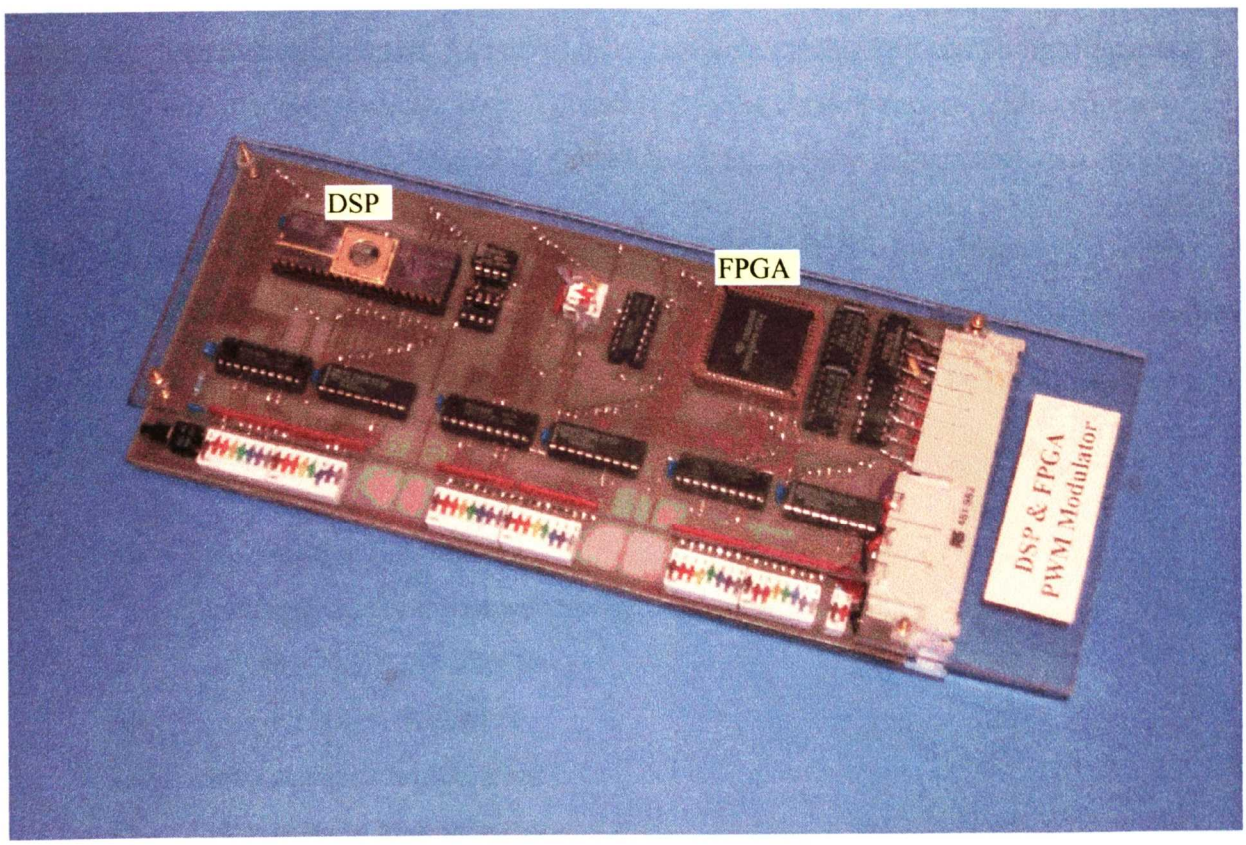

Fig. D.8. A photograph of the developed digital PWM modulator.

[Appendix E] Inverter Loss Measurement Results for Loss Model Determination

The three H-bridges derived from the three phase inverter, $T_1T_3T_4T_6$, $T_1T_5T_4T_2$ and $T_3T_5T_6T_2$, have been used for loss measurements. The experiments have been undertaken for the following three circumstances,

(A) Variable load current I_L; and fixed d.c. supply voltage and switching frequency.
(B) Variable d.c. supply voltage V_d; and fixed load current and switching frequency.
(C) Variable switching frequency f_s; and fixed d.c. supply voltage and load current.

The test results on H-bridge T_1 T_3 T_4 T_6 are given in Table E.1 (a), (b) and (c), respectively for the circumstances of (A), (B) and (C). Table E.2 (a), (b) and (c) are the test results on H-bridge T_1 T_5 T_4 T_2, and Table E.3 (a), (b) and (c) on H-bridge T_3 T_5 T_6 T_2. In these tables, the terms are defined as follows,

V_d - inverter d.c. link voltage
I_L - load current (or the power device conducting current)
f_s - inverter switching frequency
I_d - inverter d.c. link current
T_{R_L} - load inductor temperature
R_L - resistance in load inductor
P_{IN} - inverter input power (or d.c. link power)
P_{R_L} - resistive loss in load inductor
P_{INV} - inverter power loss

Table E.1 (a) H-bridge $T_1T_3T_4T_6$, $V_d = 60\ V$, $f_s = 10\ KHz$

$I_L\ (A)$	0	3.0	9.3	16.5	24.3	30.3	38.4	45.0	51.3
$I_d\ (A)$	0.09	0.12	0.56	1.14	1.95	2.67	3.87	5.00	6.20
$T_{R_L}\ (^oC)$	30	30	30	30	30	31	32	34	37
$R_L\ (m\Omega)$	39.1	39.1	39.1	39.1	39.1	39.2	39.2	39.4	39.9
$P_{IN}\ (W)$	5.4	10.1	33.5	68.4	117.0	160.2	232.2	300.0	372.0
$P_{R_L}\ (W)$	0.2	0.6	3.6	10.8	23.3	36.2	58.0	80.0	105.2
$P_{INV}\ (W)$	5.2	9.5	29.9	57.6	93.7	124.0	174.2	220.0	266.8
$I_L\ (A)$	0	-3.0	-9.9	-17.4	-25.5	-34.2	-43.2	-48.9	
$I_d\ (A)$	0.09	0.15	0.61	1.23	2.14	3.30	4.76	5.80	
$T_{R_L}\ (^oC)$	30	36	35	35	36	36	38	40	
$R_L\ (m\Omega)$	39.1	39.8	39.6	39.6	39.8	39.8	40.1	40.4	
$P_{IN}\ (W)$	5.4	9.0	36.6	73.8	128.4	198.0	285.6	348.0	
$P_{R_L}\ (W)$	0.2	0.6	4.1	12.2	26.1	46.8	75.0	96.8	
$P_{INV}\ (W)$	5.2	8.4	32.5	61.6	102.3	151.2	210.6	251.2	

Table E.1 (c) H-bridge $T_1T_3T_4T_6$, $I_L = 45\ A$, $V_d = 60\ V$

$f_s\ (kHz)$	4	6	8	10	12	14	16	18
$I_d\ (A)$	4.65	4.75	4.90	5.00	5.15	5.25	5.50	5.70
$T_{R_L}\ (^oC)$	42	47	49	51	55	55	55	54
$\Delta I\ (A)$	18.5	12.3	9.3	7.4	6.2	5.3	4.6	4.1
$R_L\ (m\Omega)$	40.8	41.6	41.9	42.3	42.9	42.9	42.9	42.8
$P_{IN}\ (W)$	279.0	285.0	294.0	300.0	309.0	315.0	330.0	342.0
$P_{R_L}\ (W)$	83.8	84.7	85.1	85.8	87.0	87.0	87.0	86.8
$P_{INV}\ (W)$	195.2	200.3	208.9	214.2	222.0	228.0	243.0	255.2

Table E.1 (b) H-bridge $T_1T_3T_4T_6$, $I_L = 45\ A$, $f_s = 10\ KHz$

$I_L(A)$	45	45	45	45	45	45	45	45	45	
$V_d\,(V)$	29.5	36.1	40.4	48.1	56.5	68.1	86.0	105.7	114.8	
$I_d\,(A)$	9.85	8.15	7.30	6.25	5.40	4.55	3.80	3.20	3.00	
$T_{R_L}\,(^oC)$	39	41	44	45	46	47	48	51	52	
$R_L\,(m\Omega)$	40.3	40.6	41.1	41.3	41.4	41.6	41.8	42.3	42.5	
$P_{IN}\,(W)$	290.6	294.2	294.9	300.6	305.1	309.8	326.8	338.2	344.4	
$P_{R_L}\,(W)$	81.6	82.2	83.2	83.6	83.8	84.2	84.6	85.6	86.1	
$P_{INV}\,(W)$	209.0	212.0	211.7	217.0	221.3	225.6	242.2	252.6	258.3	
$I_L(A)$	-45	-45	-45	-45	-45	-45	-45	-45	-45	-45
$V_d\,(V)$	29.3	34.5	40.8	50.2	59.0	68.0	80.8	95.0	108.2	116.9
$I_d\,(A)$	10.00	8.50	7.25	6.00	5.15	4.58	3.94	3.44	3.13	2.93
$T_{R_L}\,(^oC)$	62	62	61	60	59	57	56	55	54	53
$R_L\,(m\Omega)$	44.1	44.1	43.9	43.8	43.6	43.3	43.1	42.9	42.8	42.6
$P_{IN}\,(W)$	293	293.2	295.8	301.2	303.8	311.4	318.4	326.8	338.7	342.5
$P_{R_L}\,(W)$	89.3	89.3	88.9	88.7	88.3	87.7	87.3	86.9	86.7	86.3
$P_{INV}\,(W)$	203.7	203.9	206.9	212.5	215.5	223.7	231.1	239.9	252.0	256.2

Table E.2(a) H-bridge T_1 T_5 T_4 T_2, $V_d = 60\ V$, $f_s = 10\ kHz$

I_L (A)	0	3.0	8.4	13.2	21.3	27.3	33.0	39.0	42.3	47.7	51.3	57.0	62.4	68.1
I_d (A)	0.07	0.19	0.51	0.88	1.70	2.40	3.20	4.12	4.72	6.00	6.70	8.00	9.40	11.00
T_{RL} (^oC)	26	26	26	26	27	28	30	31	33	36	42	46	52	59
R_L ($m\Omega$)	38.7	38.7	38.7	38.7	38.8	38.9	39.1	39.2	39.3	39.8	40.0	41.4	42.4	43.6
P_{IN} (W)	4.2	10.2	30.6	52.8	102.0	144.0	192.0	247.2	283.2	360.0	402.0	480.0	564.0	660.0
P_{RL} (W)	0.2	0.5	2.9	6.9	17.8	29.2	42.7	59.8	70.5	90.7	105.4	134.7	165.3	202.4
P_{INV} (W)	4.0	9.7	27.7	45.9	84.2	114.8	149.2	187.4	212.7	269.3	296.6	345.3	398.7	457.6

I_L (A)	0	-3.0	-9.3	-15.9	-21.0	-26.7	-32.1	-40.5	-46.5	-52.2	-57.3	-63.3
I_d (A)	0.07	0.14	0.55	1.10	1.63	2.30	3.05	4.40	5.60	6.90	8.20	9.70
T_{RL} (^oC)	26	37	35	35	35	36	37	38	41	45	49	55
R_L ($m\Omega$)	38.7	39.9	39.6	39.6	39.6	39.8	39.9	40.1	40.6	41.4	41.9	42.9
P_{IN} (W)	4.2	8.4	33.0	66.0	97.8	138.0	183.0	264.0	336.0	414.0	492.0	582.0
P_{RL} (W)	0.2	0.5	3.6	10.2	17.6	28.5	41.3	65.0	88.0	113.0	137.7	172.1
P_{INV} (W)	4.0	7.9	29.4	55.8	80.2	109.5	141.7	198.1	248.0	301.0	354.3	409.9

Table E.2(b) H-bridge T_1 T_5 T_4 T_2, $I_L = 45\,A$, $f_s = 10\,kHz$

$I_L(A)$	45	45	45	45	45	45	45	45	45
$V_d\,(V)$	30.0	40.0	50.7	57.7	63.4	78.6	89.4	111.6	117.0
$I_d\,(A)$	9.60	7.30	5.80	5.20	4.90	4.05	3.66	3.06	2.95
$T_{R_L}\,(^oC)$	37	39	41	41	41	43	44	44	47
$R_L\,(m\Omega)$	39.9	40.3	40.6	40.6	40.6	40.9	41.1	41.1	41.6
$P_{IN}\,(W)$	288.0	292.0	294.1	300.0	310.7	318.3	327.2	341.5	345.2
$P_{R_L}\,(W)$	86.4	85.5	85.5	85.0	85.0	85.0	85.5	85.0	86.4
$P_{INV}\,(W)$	201.6	206.5	208.6	215.0	225.7	233.3	241.7	256.5	258.8
$I_L(A)$	-45	-45	-45	-45	-45	-45	-45	-45	-45
$V_d\,(V)$	29.0	33.4	39.4	52.0	68.3	80.5	91.3	106.6	117.5
$I_d\,(A)$	10.00	8.75	7.40	5.75	4.50	3.90	3.55	3.15	2.95
$T_{R_L}\,(^oC)$	42	43	43	44	44	46	46	48	48
$R_L\,(m\Omega)$	40.8	40.9	40.9	41.1	41.1	41.4	41.4	41.8	41.8
$P_{IN}\,(W)$	290.0	292.2	291.6	299.0	307.4	315.6	324.1	335.8	346.6
$P_{R_L}\,(W)$	89.4	89.6	89.6	89.6	90.0	90.4	90.4	90.0	90.4
$P_{INV}\,(W)$	200.6	202.6	202.0	209.4	217.4	225.2	233.7	245.8	256.2

Table E.2(c) H-bridge T_1 T_5 T_4 T_2, $I_L = 45\,A$, $V_d = 60\,V$

$f_s\,(kHz)$	4	6	8	10	12	14	16	18
$I_d\,(A)$	4.60	4.78	4.92	5.05	5.14	5.25	5.40	5.55
$T_{R_L}\,(^oC)$	35	36	39	42	42	43	44	47
$R_L\,(m\Omega)$	39.6	39.8	40.3	40.8	40.8	40.9	41.1	41.6
$P_{IN}\,(W)$	276.0	286.8	295.2	303.0	308.4	315.0	324.0	333.0
$P_{R_L}\,(W)$	87.5	87.8	88.5	89.3	89.2	89.1	89.6	90.4
$P_{INV}\,(W)$	188.5	199.0	206.7	213.7	219.2	225.9	234.4	242.6

Table E.3(a) H-bridge T_3 T_5 T_6 T_2, $V_d = 60\ V$, $f_s = 10\ kHz$

$I_L\ (A)$	0	3.0	8.4	11.7	15.9	21.3	27.6	32.1	36.3	42.3	48.0
$I_d\ (A)$	0.09	0.17	0.51	0.74	1.08	1.63	2.46	3.05	3.59	4.56	5.60
$T_{R_L}\ (^oC)$	24	24	24	24	25	25	26	27	29	32	34
$R_L\ (m\Omega)$	38.6	38.6	38.6	38.6	38.7	38.7	38.8	39.0	39.2	39.3	39.4
$P_{IN}\ (W)$	5.4	10.2	30.6	44.4	64.8	97.8	147.6	183.0	215.4	273.6	336.0
$P_{R_L}\ (W)$	0.2	0.5	2.9	5.4	9.8	17.7	29.6	40.2	51.6	70.3	91.0
$P_{INV}\ (W)$	5.2	9.7	27.7	39.0	55.0	80.1	118.0	142.8	163.8	203.3	245.0
$I_L\ (A)$	0	-3.0	-6.0	-12.0	-17.1	-22.2	-24.9	-30.3	-36.0	-41.7	-47.7
$I_d\ (A)$	0.09	0.16	0.34	0.78	1.20	1.75	2.05	2.75	3.60	4.55	5.60
$T_{R_L}\ (^oC)$	24	38	37	36	34	35	36	36	37	39	41
$R_L\ (m\Omega)$	38.6	40.1	39.9	39.8	39.4	39.6	39.8	39.8	39.9	40.3	40.6
$P_{IN}\ (W)$	5.4	9.9	20.4	46.5	72.0	105.0	123.0	165.0	216.0	273.0	336.0
$P_{R_L}\ (W)$	0.2	0.5	1.6	5.9	11.7	19.7	24.8	36.7	51.9	70.2	92.6
$P_{INV}\ (W)$	5.2	9.4	18.8	40.6	60.3	85.3	98.2	128.3	164.1	202.8	243.4

Table E.3(c) H-bridge , T_3 T_5 T_6 T_2, $I_L = 45\ A$, $V_d = 60\ V$

$f_s\ (kHz)$	4	6	8	10	12	14	16	18
$I_d\ (A)$	4.65	4.75	4.95	5.05	5.20	5.36	5.55	5.65
$T_{R_L}\ (^oC)$	34	36	38	41	46	47	49	52
$R_L\ (m\Omega)$	39.4	39.8	40.1	40.6	41.4	41.6	41.9	42.4
$P_{IN}\ (W)$	279.0	285.0	297.0	303.0	312.0	321.6	333.0	339.0
$P_{R_L}\ (W)$	80.9	81.1	81.5	82.4	83.9	84.3	84.9	86.0
$P_{INV}\ (W)$	198.1	203.9	215 .5	220.6	228.1	237.3	248.1	253.0

Table E.3(b) H-bridge , T_3 T_5 T_6 T_2, $I_L = 45\,A$, $f_s = 10\,kHz$

$I_L(A)$	45	45	45	45	45	45	45	45	45	45	45
$V_d\,(V)$	29.6	34.8	38.8	50.6	57.4	70.1	88.5	102.6	121.0		
$I_d\,(A)$	10.00	8.60	7.75	6.00	5.35	4.54	3.74	3.31	2.92		
$T_{R_L}\,(^oC)$	39	43	46	47	49	49	50	52	54		
$R_L\,(m\Omega)$	40.3	40.9	41.4	41.6	41.9	41.9	42.1	42.4	42.8		
$P_{IN}\,(W)$	296.0	299.3	300.7	303.6	307.1	318.2	331.0	339.6	353.3		
$P_{R_L}\,(W)$	81.6	82.8	83.8	84.2	84.8	84.8	85.2	85.9	86.7		
$P_{INV}\,(W)$	214.4	216.5	216.9	219.4	222.3	233.4	245.8	253.7	266.6		
$I_L(A)$	-45	-45	-45	-45	-45	-45	-45	-45	-45	-45	-45
$V_d\,(V)$	29.6	32.6	38.3	43.2	51.1	58.0	69.6	77.6	87.5	100.5	117.7
$I_d\,(A)$	9.95	8.95	7.70	6.90	5.90	5.25	4.50	4.13	3.74	3.35	2.96
$T_{R_L}\,(^oC)$	52	38	40	42	43	44	47	48	49	51	52
$R_L\,(m\Omega)$	42.4	40.3	40.8	40.9	41.1	41.6	41.8	41.9	42.3	42.4	42.4
$P_{IN}\,(W)$	294.5	291.8	294.9	298.1	301.5	304.5	313.2	320.5	327.2	336.7	348.4
$P_{R_L}\,(W)$	85.9	81.8	82.6	82.8	83.2	84.2	84.6	84.8	85.6	85.9	85.9
$P_{INV}\,(W)$	208.6	210.0	212.3	215.3	218.3	220.3	228.6	235.7	241.6	250.8	262.5

[Appendix F] Experimental Results for Machine Constant Torque Control and Constant Power Control

F.1 Constant torque control

Table F.1 Constant torque control measurements. Frequency ratio R=9. Torque T_m=15Nm.

f (Hz)	12.50	18.66	25.12	31.49	34.84	37.75	40.62	44.00	46.12
n (rpm)	310.6	496.9	683.3	869.6	963.5	1055.0	1142.7	1240.0	1302.3
Δn (rpm)	64.4	62.9	70.3	75.1	81.7	77.5	75.9	80	81.3
V_d (V)	318	316	320	319	318	315	315	312	314
I_d (A)	3.41	4.37	5.14	6.00	6.38	7.01	7.39	7.80	8.08
P_{dc} (W)	1083	1379	1646	1915	2028	2202	2324	2434	2534
V_{fund} (V)	60.2	88.70	112.3	135.0	145.7	161.4	174.4	183.1	190.0
I_{fund} (A)	8.86	8.86	8.88	8.86	8.86	8.87	8.86	8.86	8.89
$P_{IM,fund}$ (W)	781	1106	1414	1712	1838	2022	2160	2293	2386
P_{IM} (W)	1048	1345	1614	1881	1994	2168	2286	2395	2496
P_{out} (W)	488	780	1073	1366	1513	1657	1794	1947	2045
$P_{IM,har}$ (W)	267	239	200	169	156	146	126	102	110
P_{INV} (W)	35	34	32	34	34	34	38	39	38
P_{sys} (W)	595	599	573	549	515	545	530	487	489

In the table,

$$P_{out} = T_m \cdot \frac{2\pi}{60} n \tag{F.1}$$

$$P_{IM,har} = P_{IM} - P_{IM,fund} \tag{F.2}$$

$$P_{INV} = P_{dc} - P_{IM} \tag{F.3}$$

$$P_{sys} = P_{dc} - P_{out} \tag{F.4}$$

Table F.2 Constant torque control measurements. Frequency ratio R=15. Torque T_m=15Nm.

f (Hz)	12.46	16.79	20.66	25.75	34.60
n (rpm)	304.2	424.8	539.6	695.2	955.4
Δn (rpm)	69.6	78.9	80.2	78.2	82.6
V_d (V)	319	316	317	316	314
I_d (A)	3.14	3.77	4.34	5.10	6.25
P_{dc} (W)	1000	1194	1373	1612	1968
V_{fund} (V)	62.3	78.0	94.2	115.5	145.4
I_{fund} (A)	8.86	8.87	8.86	8.85	8.86
$P_{IM,fund}$ (W)	805	1012	1202	1451	1838
P_{IM} (W)	968	1161	1340	1573	1932
P_{out} (W)	478	667	847	1092	1500
$P_{IM,har}$ (W)	163	147	138	122	94
P_{INV} (W)	32	33	33	39	36
P_{sys} (W)	522	527	526	520	468

Table F.3 Constant torque control measurements. Frequency ratio R=21. Torque T_m=15Nm.

f (Hz)	12.43	16.77	20.96	25.12	29.27	34.41	36.58	39.66	40.78	44.66
n (rpm)	317.1	443.8	570.8	682.1	821.2	961.7	1025.4	1122.3	1156.9	1277.3
Δn (rpm)	55.8	59.3	58	71.5	56.9	70.6	72	67.5	66.5	62.5
V_d (V)	317	321	317	318	320	321	320	321	321	320
I_d (A)	2.96	3.53	4.21	4.83	5.39	5.96	6.30	6.92	6.98	7.65
P_{dc} (W)	938	1133	1336	1530	1726	1914	2022	2220	2240	2452
V_{fund} (V)	67.5	83.5	102.9	113.0	134.6	144.0	153.0	172.7	177.2	201.5
I_{fund} (A)	8.94	8.86	8.86	8.91	8.89	8.93	8.92	8.91	8.80	8.81
$P_{IM,fund}$ (W)	812	1016	1224	1425	1622	1816	1929	2126	2145	2367
P_{IM} (W)	904	1099	1300	1496	1685	1874	1984	2177	2197	2412
P_{out} (W)	498	697	896	1071	1290	1510	1610	1762	1817	2006
$P_{IM,har}$ (W)	92	83	76	71	63	58	55	51	52	45
P_{INV} (W)	34	34	36	34	41	40	38	43	43	40
P_{sys} (W)	440	436	440	459	436	404	412	458	423	446

Table F.4 Constant torque control measurements. Frequency ratio R=27. Torque T_m=15Nm.

f (Hz)	12.47	18.79	25.06	31.72	34.18	37.05	39.71	43.82	45.77
n (rpm)	320.0	502.9	689.0	886.0	951.4	1041.7	1120.8	1241.9	1302.5
Δn (rpm)	54.1	60.8	62.8	65.6	74	69.8	70.5	72.7	70.6
V_d (V)	322	322	322	321	322	322	321	321	320
I_d (A)	2.813	3.751	4.707	5.650	5.890	6.440	6.870	7.360	7.790
P_{dc} (W)	907	1210	1515	1819	1895	2070	2200	2361	2498
V_{fund} (V)	64.9	89.2	115.4	140.3	143.7	160.7	170.4	183.0	196.6
I_{fund} (A)	8.88	8.87	8.87	8.84	8.88	8.88	8.90	8.86	8.87
$P_{IM,fund}$ (W)	803	1109	1418	1721	1805	1982	2113	2272	2411
P_{IM} (W)	872	1171	1474	1771	1854	2027	2156	2313	2449
P_{out} (W)	502	790	1082	1391	1494	1636	1760	1950	2045
$P_{IM,har}$ (W)	69	62	56	50	49	45	43	41	38
P_{INV} (W)	35	39	41	48	41	43	44	48	49
P_{sys} (W)	405	420	433	428	401	434	440	411	453

Table F.5 Constant torque control measurements. Frequency ratio R=33. Torque T_m=15Nm.

f (Hz)	12.54	18.79	25.41	31.86	33.64	37.67	43.72	45.76
n (rpm)	316.2	509.4	698.3	897.1	943.8	1066.0	1238.1	1301.9
Δn (rpm)	60	54.3	64	58.7	65.4	64.1	73.5	70.9
V_d (V)	320	318	318	316	316	315	314	314
I_d (A)	2.779	3.80	4.75	5.72	5.92	6.68	7.53	7.95
P_{dc} (W)	890	1220	1512	1811	1871	2101	2360	2492
V_{fund} (V)	62.8	92.7	116.7	141.3	144.5	165.6	183.2	195.5
I_{fund} (A)	8.85	8.83	8.82	8.87	8.86	8.87	8.89	8.89
$P_{IM,fund}$ (W)	798	1108	1424	1724	1785	2016	2278	2411
P_{IM} (W)	854	1161	1471	1767	1827	2055	2312	2440
P_{out} (W)	497	800	1097	1409	1482	1674	1945	2045
$P_{IM,har}$ (W)	56	53	47	43	42	39	34	29
P_{INV} (W)	36	59	41	44	44	46	48	52
P_{sys} (W)	393	420	415	402	389	427	415	447

Table F.6 Constant torque control measurements. Frequency ratio R=39. Torque T_m=15Nm.

f (Hz)	12.54	18.98	25.06	31.84	33.39	36.63	41.25	44.80	46.63
n (rpm)	310.6	504.8	682.3	883.5	928.3	1025.0	1162.9	1267.9	1322.7
Δn (rpm)	65.6	64.5	69.5	71.7	73.4	73.9	74.6	76.1	76.2
V_d (V)	318	316	315	314	313	312	313	313	313
I_d (A)	2.80	3.81	4.78	5.76	5.96	6.49	7.13	7.66	7.96
P_{dc} (W)	890	1204	1509	1808	1863	2018	2232	2402	2486
V_{fund} (V)	62.3	89.5	113.2	138.2	142.6	155.8	172.7	187.2	193.3
I_{fund} (A)	8.88	8.86	8.90	8.87	8.86	8.85	8.85	8.85	8.86
$P_{IM,fund}$ (W)	807	1120	1425	1725	1782	1936	2147	2318	2399
P_{IM} (W)	855	1165	1465	1761	1819	1971	2180	2348	2434
P_{out} (W)	488	793	1072	1388	1458	1610	1827	1992	2078
$P_{IM,har}$ (W)	48	45	40	36	37	35	33	30	35
P_{INV} (W)	35	39	44	47	44	47	52	54	52
P_{sys} (W)	402	411	437	420	405	408	405	410	408

Table F.7 Constant torque control measurements. Frequency ratio R=45. Torque T_m=15Nm.

f (Hz)	12.55	18.82	25.08	31.33	34.20	39.33	44.90	46.64
n (rpm)	315.2	502.3	687.9	871.7	953.1	1106.0	1272.1	1323.3
Δn (rpm)	61.3	62.3	64.5	68.2	72.9	73.9	74.9	75.9
V_d (V)	318	317	317	316	317	315	314	314
I_d (A)	2.77	3.75	4.74	5.66	5.98	6.82	7.68	7.94
P_{dc} (W)	880	1190	1501	1792	1895	2152	2407	2496
V_{fund} (V)	62.2	88.8	114.9	137.9	145.1	165.8	187.1	193.6
I_{fund} (A)	8.86	8.87	8.87	8.87	8.86	8.88	8.86	8.88
$P_{IM,fund}$ (W)	802	1107	1418	1707	1812	2069	2322	2408
P_{IM} (W)	845	1148	1456	1742	1846	2100	2352	2441
P_{out} (W)	495	789	1080	1369	1497	1737	1998	2079
$P_{IM,har}$ (W)	43	41	38	35	34	31	30	33
P_{INV} (W)	35	42	45	50	49	52	55	55
P_{sys} (W)	385	401	421	423	398	415	409	417

Table F.8 Constant torque control measurements. Frequency ratio R=51. Torque T_m=15Nm.

f (Hz)	12.55	24.56	31.98	33.98	37.57	39.21	45.13	46.66
n (rpm)	323.8	674.4	891.9	947.7	1054.4	1104.8	1277.9	1323.8
Δn (rpm)	52.7	62.4	67.5	71.7	72.7	71.5	76	76
V_d (V)	317	315	314	315	315	315	313	313
I_d (A)	3.38	4.66	5.76	5.98	6.56	6.86	7.76	7.97
P_{dc} (W)	879	1466	1811	1880	2066	2155	2432	2497
V_{fund} (V)	64.6	112.6	139.3	143.6	159.1	167.9	187.8	192.9
I_{fund} (A)	8.86	8.86	8.88	8.86	8.87	8.85	8.88	8.88
$P_{IM,fund}$ (W)	800	1387	1730	1796	1983	2072	2339	2407
P_{IM} (W)	840	1421	1762	1829	2012	2100	2365	2437
P_{out} (W)	509	1059	1401	1489	1656	1735	2007	2079
$P_{IM,har}$ (W)	40	34	32	33	29	27	26	30
P_{INV} (W)	39	45	49	51	54	55	57	60
P_{sys} (W)	370	407	410	391	410	420	415	418

Table F.9 Constant torque control measurements. Frequency ratio R=57. Torque T_m=15Nm.

f (Hz)	12.54	24.56	32.00	34.07	37.66	39.32	46.78
n (rpm)	317.5	669.2	889.2	953.8	1059.4	1109.4	1330
Δn (rpm)	58.7	67.6	70.8	68.3	70.4	70.2	73.4
V_d (V)	318	318	317	318	315	316	317
I_d (A)	2.79	4.60	5.72	5.95	6.56	6.86	7.90
P_{dc} (W)	887	1463	1806	1883	2068	2167	2500
V_{fund} (V)	63.9	111.6	138.7	144.3	160.6	169.4	195.2
I_{fund} (A)	8.88	8.86	8.86	8.86	8.86	8.87	8.86
$P_{IM,fund}$ (W)	811	1383	1729	1799	1985	2085	2415
P_{IM} (W)	850	1418	1760	1832	2013	2113	2440
P_{out} (W)	499	1051	1397	1498	1664	1743	2089
$P_{IM,har}$ (W)	39	35	31	33	28	28	25
P_{INV} (W)	37	45	46	51	55	54	60
P_{sys} (W)	388	412	409	385	404	424	411

Table F.10 Constant torque control measurements. Frequency ratio R=63. Torque T_m=15Nm.

f (Hz)	12.40	18.82	24.97	32.03	34.07	37.47	39.27	43.86	45.10
n (rpm)	310.4	501.7	684.2	892.3	947.1	1054.2	1102.1	1239.6	1276.4
Δn (rpm)	61.6	62.9	64.9	68.6	75	69.9	76	76.2	76.6
V_d (V)	321	322	322	322	323	321	318	315	315
I_d (A)	2.71	3.70	4.63	5.63	5.85	6.54	6.75	7.49	7.69
P_{dc} (W)	872	1190	1493	1815	1891	2100	2140	2362	2426
V_{fund} (V)	62.6	89.4	114.0	139.9	144.2	163.8	164.5	182.6	188.2
I_{fund} (A)	8.85	8.86	8.87	8.85	8.86	8.87	8.86	8.87	8.87
$P_{IM,fund}$ (W)	798	1112	1412	1731	1807	2014	2054	2277	2342
P_{IM} (W)	834	1146	1444	1762	1837	2043	2083	2302	2365
P_{out} (W)	486	788	1075	1402	1488	1656	1731	1947	2005
$P_{IM,har}$ (W)	36	34	32	31	30	29	29	25	23
P_{INV} (W)	38	44	49	53	54	57	57	60	61
P_{sys} (W)	386	402	418	413	403	444	409	415	421

F.2 Constant power control

Table F.11 Constant power control measurements. Frequency ratio R=45. T_m=7Nm

n=970rpm.

f (Hz)	32.93	34.08	34.57	35.49	36.00	36.82
n (rpm)	967.1	970.4	970.8	971.2	971.7	971.2
s (%)	2.10	5.08	6.39	8.78	10.03	12.08
V_d (V)	325	322	322	322	321	321
I_d (A)	2.92	2.76	2.84	2.96	3.07	3.25
P_{dc} (W)	949	893	914	953	986	1043
V_{fund} (V)	162.4	112.2	100.7	93.1	89.1	85.9
I_{fund} (A)	7.03	5.56	5.97	6.69	7.09	7.71
$P_{IM,fund}$ (W)	876	827	847	890	915	958
P_{IM} (W)	907	860	880	921	947	988
P_{out} (W)	709	711	712	712	712	712
$P_{IM,har}$ (W)	31	34	33	31	32	30
P_{INV} (W)	41	33	34	32	39	55
P_{sys} (W)	240	182	202	241	273	331

Table F.12 Constant power control measurements. Frequ. ratio R=27. T_m=7Nm, n=970rpm.

f (Hz)	33.07	33.47	34.13	34.46	35.68	36.00	37.27
n (rpm)	971	974	974	972	972	975	975
s (%)	2.13	3.00	4.87	5.98	9.19	9.72	12.80
V_d (V)	328	328	327	326	327	327	328
I_d (A)	2.85	2.75	2.77	2.81	2.97	3.02	3.25
P_{dc} (W)	932	904	910	917	968	987	1066
V_{fund} (V)	162.7	143.0	111.9	104.4	92.7	90.5	85.0
I_{fund} (A)	6.96	5.45	5.51	5.80	6.67	6.93	8.04
$P_{IM,fund}$ (W)	876	821	825	841	894	910	985
P_{IM} (W)	921	870	877	890	940	955	1030
P_{out} (W)	712	714	714	713	715	715	711
$P_{IM,har}$ (W)	45	49	52	48	46	44	45
P_{INV} (W)	11	34	34	27	28	32	36
P_{sys} (W)	220	190	196	204	254	272	355

Table F.13 Constant power control measurements. Frequ. ratio R=15. T_m=7Nm, n=970rpm.

f (Hz)	33.92	34.60	34.85	35.80	36.57
n (rpm)	964	967	965	965	972
s (%)	5.27	6.84	7.70	10.15	11.40
V_d (V)	324	325	324	325	324
I_d (A)	2.87	2.94	2.96	3.10	3.22
P_{dc} (W)	932	957	959	1007	1044
V_{fund} (V)	108.6	100.3	95.9	89.4	88.0
I_{fund} (A)	5.60	5.99	6.28	7.04	7.33
$P_{IM,fund}$ (W)	827	850	864	913	938
P_{IM} (W)	908	927	940	985	1014
P_{out} (W)	707	709	707	707	713
$P_{IM,har}$ (W)	80	77	76	72	76
P_{INV} (W)	24	30	19	22	30
P_{sys} (W)	225	248	252	300	331

Table F.14 Constant power control measurements. Frequ. ratio R=9. T_m=7Nm, n=970rpm.

f (Hz)	32.72	33.49	34.82	35.70	37.27
n (rpm)	960	969	970	965	965
s (%)	2.20	3.55	7.14	9.90	13.69
V_d (V)	322	321	324	323	322
I_d (A)	3.18	2.95	3.10	3.24	3.47
P_{dc} (W)	1029	950	1003	1048	1115
V_{fund} (V)	163.2	133.8	99.1	90.2	85.0
I_{fund} (A)	7.29	5.33	6.06	6.85	7.99
$P_{IM,fund}$ (W)	885	817	856	899	982
P_{IM} (W)	993	928	976	1012	1092
P_{out} (W)	706	710	711	704	707
$P_{IM,har}$ (W)	108	111	120	113	110
P_{INV} (W)	36	22	27	36	23
P_{sys} (W)	323	239	292	344	408

Table F.15 Constant power control measurements. Frequ. ratio R=9. T_m=10Nm, n=635rpm.

f (Hz)	21.99	22.05	22.36	22.89	23.23	23.85	24.33	24.82	25.16	25.56
n (rpm)	631.7	632.9	635.8	633.8	637.5	637.9	638.3	636.2	626.7	632.9
s (%)	4.24	4.32	5.22	7.70	8.52	10.84	12.55	14.56	16.97	17.46
V_d (V)	320.4	320.4	320.3	320.5	321.0	321.5	320.8	320.7	319.7	320.3
I_d (A)	3.22	3.26	3.17	3.18	3.22	3.32	3.40	3.53	3.64	3.73
P_{dc} (W)	1031	1043	1015	1018	1034	1067	1090	1131	1163	1196
V_{fund} (V)	108.9	110.7	104.0	90.0	87.4	82.2	79.8	77.2	75.4	66.9
I_{fund} (A)	7.41	7.65	6.78	6.73	6.88	7.37	7.74	8.25	8.87	7.87
$P_{IM,fund}$ (W)	836	848	820	833	848	885	912	951	1001	
P_{IM} (W)	1008	1022	986	1000	1013	1045	1066	1104	1154	1158
P_{out} (W)	662	663	666	664	668	668	667	664	663	663
$P_{IM,har}$ (W)	172	174	166	167	165	160	154	153	153	
P_{INV} (W)	23	21	29	18	21	22	24	27		38
P_{sys} (W)	369	380	349	354	366	399	423	468	500	533

Table F.16 Constant power control measurements. Frequ. ratio R=15. T_m=10Nm, n=635rpm.

f (Hz)	22.26	22.86	23.49	23.81	24.36	24.98	26.12	26.95
n (rpm)	625.8	620.0	628.3	624.2	629.6	634.2	636.2	637.5
s (%)	6.29	9.59	10.84	12.61	13.85	15.37	18.81	21.15
V_d (V)	325.3	325.5	325.8	325.9	325.9	325.3	325.2	324.8
I_d (A)	2.89	3.03	3.08	3.13	3.26	3.36	3.61	3.86
P_{dc} (W)	939	987	1004	1016	1060	1093	1172	1254
V_{fund} (V)	94.4	83.0	81.7	77.6	77.2	76.8	75.1	74.6
I_{fund} (A)	6.61	7.16	7.34	7.93	8.19	8.40	9.29	10.17
$P_{IM,fund}$ (W)	809	853	872	912	939	962	1041	1131
P_{IM} (W)	914	960	974	1007	1031	1055	1132	1242
P_{out} (W)	655	649	658	654	659	664	666	668
$P_{IM,har}$ (W)	105	107	102	95	92	93	91	111
P_{INV} (W)	24	27	9	30	29	38	40	12
P_{sys} (W)	284	338	362	346	401	429	506	586

Table F.17 Constant power control measurements. Frequ. ratio R=27. T_m=10Nm, n=635rpm.

f (Hz)	21.88	22.31	22.43	22.93	23.44	24.15	24.93	24.89
n (rpm)	633.8	638.8	640.8	640.4	641.7	642.5	642.5	645.8
s (%)	3.44	4.56	4.77	6.90	8.74	11.32	14.09	13.51
V_d (V)	318.6	318.9	318.6	318.7	318.5	319.2	319.4	318.9
I_d (A)	3.51	2.94	2.91	2.86	2.94	3.07	3.19	3.20
P_{dc} (W)	1120	938	927	913	938	980	1018	1022
V_{fund} (V)	123.5	110.4	108.8	94.6	87.5	81.5	78.0	79.0
I_{fund} (A)	10.84	7.37	7.10	6.60	6.90	7.51	8.14	8.00
$P_{IM,fund}$ (W)	1016	846	837	828	853	896	943	940
P_{IM} (W)	1081	908	899	887	910	950	999	993
P_{out} (W)	664	669	671	671	672	673	673	676
$P_{IM,har}$ (W)	65	62	62	59	57	54	56	53
P_{INV} (W)	39	30	28	26	28	30	19	29
P_{sys} (W)	456	269	256	242	266	307	345	346

Table F.18 Constant power control measurements. Frequ. ratio R=33. T_m=10Nm, n=635rpm.

f (Hz)	21.94	22.32	22.85	23.32	23.91	24.38	25.09
n (rpm)	634.1	634.6	636.7	638.3	650.8	653.8	652.9
s (%)	3.66	5.23	7.08	8.76	9.27	10.61	13.26
V_d (V)	322	323.3	323.7	325.4	324.3	324.4	324.3
I_d (A)	3.22	2.88	2.86	2.92	2.94	3.00	3.17
P_{dc} (W)	1034	934	926	953.5	954.0	974	1023
V_{fund} (V)	118.3	106.7	94.5	88.4	87.4	84.3	79.2
I_{fund} (A)	9.19	7.03	6.70	6.97	7.01	7.28	7.94
$P_{IM,fund}$ (W)	942	948	847	867	873	896	945
P_{IM} (W)	996	901	898	918	922	942	990
P_{out} (W)	665	665	667	668	681	684	684
$P_{IM,har}$ (W)	54	47	51	51	49	46	45
P_{INV} (W)	38	33	28	36	32	32	33
P_{sys} (W)	369	269	259	286	272	289	339

Table F.19 Constant power control measurements. Frequ. ratio R=45. T_m=10Nm, n=635rpm.

f (Hz)	21.96	22.28	22.59	23.19	23.60	23.95	24.63	25.11
n (rpm)	633.8	636.7	638.8	646.7	648.8	650.8	649.6	650.8
s (%)	3.79	4.74	5.74	7.04	8.36	9.42	12.08	13.61
V_d (V)	322	321.8	322.4	322.6	323.7	324	321.6	320
I_d (A)	3.18	2.85	2.81	2.82	2.89	2.93	3.13	3.19
P_{dc} (W)	1024	916	905	918	934	949	1004	1022
V_{fund} (V)	118.7	106.6	99.8	92.9	88.6	86.2	80.1	78.3
I_{fund} (A)	9.36	7.04	6.67	6.71	6.91	7.09	7.86	8.17
$P_{IM,fund}$ (W)	937	841	834	843	860	875	930	954
P_{IM} (W)	979	882	874	882	900	913	966	989
P_{out} (W)	664	667	669	677	679	681	680	682
$P_{IM,har}$ (W)	42	41	41	39	40	38	36	35
P_{INV} (W)	45	34	31	36	34	36	38	33
P_{sys} (W)	360	249	236	241	255	267	324	340

Table F.20 Constant power control measurements. Frequ. ratio R=45. T_m=10Nm, n=635rpm.

f (Hz)	21.92	22.57	23.59	24.69	25.81
n (rpm)	630.4	635.6	632.1	634	634
s (%)	4.14	6.13	10.68	14.40	18.12
V_d (V)	320	320	319	319	318
I_d (A)	2.98	2.78	2.96	3.19	3.47
P_{dc} (W)	952	888	944	1017	1105
V_{fund} (V)	114.1	97.5	81.4	76.7	74.0
I_{fund} (A)	8.25	6.56	7.36	8.28	9.25
$P_{IM,fund}$ (W)	873	816	873	943	1021
P_{IM} (W)	915	856	912	980	1074
P_{out} (W)	660	666	662	664	664
$P_{IM,har}$ (W)	42	40	39	37	53
P_{INV} (W)	37	32	32	37	31
P_{sys} (W)	292	222	282	353	441

[Appendix G] Modelling of Harmonic Distortions for Vector Space PWM

The total harmonic distortion (THD) and the induction machine iron loss related total harmonic distortion (THDI) are respectively,

$$THD = \sqrt{\sum_{n=2}^{\infty} \left(\frac{V_n}{n V_1}\right)^2} \tag{G.1}$$

$$THDI = \sqrt{\sum_{n=2}^{\infty} n \left(\frac{V_n}{n V_1}\right)^2} \tag{G.2}$$

They are determined only by the spectrum distribution of a switching process. For the vector space PWM, their relationships with the modulation depth M and the frequency ratio R may be expressed as,

$$THD^2 = \frac{1}{R^2}\left(0.124\,M^3 + 0.258\,M^2 - 1.015\,M + 0.788\right) \tag{G.3}$$

$$THDI^2 = \frac{1}{R}\left(-1.277\,M^3 + 4.220\,M^2 - 5.116\,M + 2.396\right) \tag{G.4}$$

[Appendix H] FORTRAN Program of Loss Minimisation Control for 3kW Inverter Fed Induction Machine Drive

Initialisation

```
integer R,tt
real Ue,Fe,Ie,Te,Se,Pre,Piec,Pies,Re,Xe,et,Udc,Re2
real t,vl,sp,tq,Fr,R1
real Kv,Kf,Kt,Kw
real ap1,ap2,ap3,ap4,vt0,vd0,kdd,ktt,ci
real a1,a2,a3,a4,b1,b2,b3,b4,c1,c2,c3,c4,c5,c6,c7
real a10,a20,a30,a40
real p,q,U,F,a,b,sg1,sg2,ag
```

Machine and inverter parameters

```
Ue=240          ; Machine rated voltage
Fe=50
Ie=6.5          ; Machine rated current
Te=20.2         ; Machine rated torque
Se=0.05333      ; Machine rated speed slip
et=0.74         ; Machine efficiency
Udc=340         ; DC supply voltage
a10=-1.942      ; THD coefficients
a20=5.581
a30=-5.883
a40=2.396
b1=0.1886       ; THDI coefficients
b2=0.3412
b3=-1.1672
b4=0.788
ci=2.5e-03      ; Inverter loss model coefficients
ap1=1.1e-05
ap2=1.35e-04
ap3=4.9e-03
ap4=2.4e-03
vd0=0.90
kdd=0
vt0=1.20
ktt=0.039
Pre=409         ; Machine rated copper loss
Piec=335 ;      ; Machine rated iron loss
Pies=15
Re=3.7          ; Machine electrical parameters
Re2=1.74
Xe=6.93
```

Machine operating point

```
tq=7                    ; Machine torque
sp=970                  ; Machine speed
```

Loss minimisation control

U: machine supply voltage
F: machine supply frequency
R: PWM frequency ratio

```
Ie=Ue*Se/Re2
c1=2.339*(vt0+vd0)*Ie
c2=4.5*(ktt+kdd)*Ie*Ie
c3=2.113*(vt0-vd0)*et*Ie
c4=4.393*(ktt-kdd)*et*Ie*Ie
c5=9*ap1*Udc*Fe*Ie*Ie/1000
c6=4.678*(ap2*Udc+ap3)*Fe*Ie/1000
c7=3*ap4*Fe*Udc/1000
b1=3*b1*Re*Ue*Ue/(Xe*Xe)
b2=3*b2*Re*Ue*Ue/(Xe*Xe)
b3=3*b3*Re*Ue*Ue/(Xe*Xe)
b4=3*b4*Re*Ue*Ue/(Xe*Xe)
Fr=2*sp/60
Kt=tq/Te
Kf=1/(1-Se)*Fr/Fe
Kv=sqrt(Kt*Kf)
a1=a10*sqrt(Kt)*(Piec+Pies*Kt*Kt)*(ci/Xe/Xe*Fe*Re2/Se*Re2/Se)
a2=a20*sqrt(Kt)*(Piec+Pies*Kt*Kt)*ci*Fe*Re2**2/(Xe**2*Se**2)
a3=a30*sqrt(Kt)*(Piec+Pies*Kt*Kt)*ci*Fe*Re2**2/(Xe**2*Se**2)
a4=a40*sqrt(Kt)*(Piec+Pies*Kt*Kt)*ci*Fe*Re2**2/(Xe**2*Se**2)
p=1.0/(C5*Kv*Kv+C6*Kv+c7)*(a1*Kv**4+a2*Kv**3+a3*Kv**2+a4*Kv)
q=2.0/(C5*Kv*Kv+C6*Kv+c7)*(b1*Kv**5+b2*Kv**4+b3*Kv**3+b4*Kv**2)
if (q**2/4 .gt. (p/3)**3) then
 a=(q/2+sqrt((q*q/4-(p/3)**3)))
 b=(q/2-sqrt((q*q/4-(p/3)**3)))
 if (a .gt. 0.0) then
     sg1=1
 else
     sg1=-1
 end if
 if (b .gt. 0.0) then
     sg2=1
 else
     sg2=-1
 end if
 Kw=sg1*abs(a)**(1.0/3.0)+sg2*abs(b)**(1.0/3.0)
else
 ag=atan(sqrt((p/3)**3-q*q/4)*2/q)
```

```
  Kw=2*sqrt(p/3)*cos(ag/3)
end if
R=3*INT(Kw/Kf/3)
R1=R
if (R1/2 .eq. int(R1/2)) then
      R=R+3
else
end if
U=Kv*Ue
F=Kf*Fe
write(1,*)U,F,R,R*Kf*Fe/1000
end
```